

INFORMATION TO USERS

This manuscript has been reproduced from the microfilm master. UMI films the text directly from the original or copy submitted. Thus, some thesis and dissertation copies are in typewriter face, while others may be from any type of computer printer.

The quality of this reproduction is dependent upon the quality of the copy submitted. Broken or indistinct print, colored or poor quality illustrations and photographs, print bleedthrough, substandard margins, and improper alignment can adversely affect reproduction.

In the unlikely event that the author did not send UMI a complete manuscript and there are missing pages, these will be noted. Also, if unauthorized copyright material had to be removed, a note will indicate the deletion.

Oversize materials (e.g., maps, drawings, charts) are reproduced by sectioning the original, beginning at the upper left-hand corner and continuing from left to right in equal sections with small overlaps.

Photographs included in the original manuscript have been reproduced xerographically in this copy. Higher quality 6" x 9" black and white photographic prints are available for any photographs or illustrations appearing in this copy for an additional charge. Contact UMI directly to order.

**Bell & Howell Information and Learning
300 North Zeeb Road, Ann Arbor, MI 48106-1346 USA
800-521-0600**

UMI[®]

**IMPACT OF MICROPHYSICAL PARAMETERIZATIONS ON SIMULATED
STORM EVOLUTION AND REMOTELY-SENSED CHARACTERISTICS**

A Dissertation

by

SVETLA M. HRISTOVA-VELEVA

**Submitted to the Office of Graduate Studies of
Texas A&M University
in partial fulfillment of the requirements for the degree of**

DOCTOR OF PHILOSOPHY

December 2000

Major Subject: Atmospheric Sciences

UMI Number: 9994259

UMI[®]

UMI Microform 9994259

Copyright 2001 by Bell & Howell Information and Learning Company.

**All rights reserved. This microform edition is protected against
unauthorized copying under Title 17, United States Code.**

**Bell & Howell Information and Learning Company
300 North Zeeb Road
P.O. Box 1346
Ann Arbor, MI 48106-1346**

**IMPACT OF MICROPHYSICAL PARAMETERIZATIONS ON SIMULATED
STORM EVOLUTION AND REMOTELY-SENSED CHARACTERISTICS**

A Dissertation


by


SVETLA M. HRISTOVA-VELEVA


Submitted to Texas A&M University
in partial fulfillment of the requirements
for the degree of


DOCTOR OF PHILOSOPHY

Approved as to style and content by:



Michael I. Biggerstaff
(Chair of Committee)


Louis J. Wicker
(Member)


Benjamin Giese
(Member)


Thomas T. Wilheit
(Member)


Ping Chang
(Member)


Gerald R. North
(Head of Department)

December 2000

Major Subject: Atmospheric Sciences

ABSTRACT**Impact of Microphysical Parameterizations on Simulated Storm Evolution and
Remotely-Sensed Characteristics.****(December 2000)****Svetla M. Hristova-Veleva,****B.S., Sofia State University;****M.S., Texas A&M University****Chair of Advisory Committee: Dr. Michael I. Biggerstaff**

A non-hydrostatic, three-dimensional cloud model was used in conjunction with a radiative transfer model to study the sensitivity of the model-simulated storms and their remotely-sensed characteristics to the microphysical parameterizations used in the cloud model. Understanding the sensitivity of the cloud-radiation databases to the assumptions that went into their building is of particular importance since such cloud-radiation databases are extensively used in the development of algorithms for retrieval of rainfall and latent heating from microwave observations of precipitating systems. This study was conducted with the intent to shed more light on how the microphysical parameter choices affect not just a particular storm characteristic but the storm's micro- and macro-structure and evolution.

Three types of sensitivity tests were performed. The first evaluated sensitivity to the choice of microphysical parameterization scheme. For that purpose two microphysical schemes were compared - Tao's and Ferrier's. Both schemes share the

parameterizations. Their main differences are in the treatment of the cloud ice initiation processes and the subsequent growth of snow. The second test evaluated the sensitivity of modeled storms to the selection of ice aggregation parameters and to the assumed number of ice crystals that are activated at 0° C. The third test evaluated the sensitivity of simulated storms to the selection of the hydrometeor's descriptive parameters (density, terminal velocity, and particle size distributions).

The storm dynamics and remotely-sensed characteristics are affected by the microphysical parameterization philosophies and by the choice of microphysical parameters and hydrometeor descriptive parameters. Different storm characteristics show sensitivity to different microphysical assumptions. This finding suggests that by using coincidental observations of a variety of storm characteristics it would be possible to discriminate between simulations and to determine what microphysical setup produces storms that compare best to observations. Being able to reproduce the storm in its entirety will indicate that the complex intercorrelations between the different processes and scales are, indeed, properly represented by the model. This in turn, will give a high fidelity in the rainfall and latent heating retrieval algorithms using cloud model databases.

DEDICATION

To my husband, Omourtag, and my two beautiful daughters Biliانا and Kalina.

Without their love and inspiration I would have never finished this work,

I would have never gone this way...

To my mother and father, grandmother and aunt, to my mother-in-law.

I am forever thankful to them for always believing in me and encouraging me to pursue

my dreams.

ACKNOWLEDGMENTS

I would like to thank many people who helped me tremendously over the years ...

First and foremost, I would like to thank my committee chair Dr. Michael Biggerstaff for everything he taught me over the years, for all the ideas he shared with me, for sharing his vision and enthusiasm. I want to thank him for his support – financial and moral. I want to thank him for being a wonderful mentor and friend. I will be forever grateful to him for continuing to work with me even after I moved to Los Angeles during the last two and a half years of my research. He took time out of his busy schedule to come to Los Angeles several times so that he could spend time with me and give me advice and direction and keep me focussed. He always provided me with everything that I needed for my research.

I want to thank my committee members: Dr. Louis Wicker, Dr. Thomas Wilheit, Dr. Benjamin Giese, and Dr. Ping Chang for all the suggestions they gave me, for their thought-provoking questions, for their guidance and encouragement. I am especially thankful to Dr. Wicker for allowing me to use his cloud model in my research and for teaching me how to use it. His enthusiasm and enjoyment of the research have been contagious and stimulating.

I appreciate very much all the discussions which I've had with Dr. Brad Ferrier concerning microphysical processes and parameterizations. I am also thankful to him for letting me use his microphysical scheme in my research.

I am thankful to Dr. Christian Kummerow for giving me his radiative transfer model and for always being open for discussions and assistance.

I want to thank my GCR, Dr. G. Teetes, for stepping in on a very short notice.

I want to thank Jerry Guynes, Neil Smith and Gordon Carrie for their technical support, for teaching me so many things about computers and how to live with them.

I want to thank Mary Gammon, Jean Stanley, Pat Price and Barbara Straube for their readiness to help me with any administrative problem. I want to thank them for their friendliness and smiles.

I want to thank my colleague and friend Eun-Kyoung Seo for the many eye-opening discussions we had on our way.

I want to thank Dr. James Scoggins, Prof. John Griffiths, Dr. James McGuirk, Dr. Steve Lyons and Dr. Richard Orville for their help, support and encouragement when I first came to the United States.

I want to thank Dr. Edward Zipser and Mr. Otto Thiele for their constant support and belief in me. I deeply appreciate all the ideas and suggestions Dr. Zipser has given me over the years.

I want to thank Dr. Eastwood Im and Dr. Ziad Haddad from the Jet Propulsion Laboratory, Pasadena, California, for accepting me in their group and for providing me with an environment in which I could finish my research after I moved to Los Angeles. The discussions I've had with Dr. Haddad have been very stimulating and insightful. I also want to thank my office mates at the Jet Propulsion Laboratory, Jonathan Meagher, Dr. Marc Simard and Dr. Simone Tanelli for the many discussions we had and for their friendship.

I am very grateful to all the faculty in the Department of Atmospheric Sciences at Texas A&M University and to my fellow students for everything I learned from them. Their friendship made me feel at home so far from home and changed my life forever.

I want to thank my husband Omourtag and my two daughters Biliana and Kalina, I want to thank my friends for always being there for me and for always believing in me. Their support has been immense and I could hardly express the depth of my gratitude

I want to express my admiration of the dedication which my mother, grandmother and mother-in-law have shown to helping me in every possible way so that I could focus my efforts on my research. I thank them with all my heart!

This research was funded by NASA's Tropical Rainfall Measuring Mission under grant NAG-5-4776.

TABLE OF CONTENTS

	Page
ABSTRACT.....	iii
DEDICATION.....	v
ACKNOWLEDGMENTS.....	vi
TABLE OF CONTENTS.....	ix
LIST OF TABLES.....	xi
LIST OF FIGURES.....	xii
 CHAPTER	
I INTRODUCTION.....	1
II IMPACT OF MICROPHYSICAL SCHEMES ON SIMULATED STORM STRUCTURE, DYNAMICS, AND REMOTELY-SENSED CHARACTERISTICS. SIMULATION OF A MIDLATITUDE SQUALL LINE.....	13
1. Model description.....	13
a. Cloud model.....	13
b. Model setup and initialization.....	14
c. Radiative transfer model.....	16
d. Microphysical schemes.....	16
1) Microphysical differences.....	23
(i) Ice initiation and water vapor saturation adjustment.....	23
(ii) Autoconversion of cloud ice to snow	28
(iii) Graupel growth.....	29
(iv) Environmental modifications.....	30
2. Results and discussions.....	31
a. Overall storm structures and convective/stratiform/anvil separation ...	31
b. Mean hydrometeor profiles.....	38
1) Comparison among the three Tao simulations.....	39
2) Comparison among the three Ferrier simulations.....	46

CHAPTER	Page
3) Comparison between the Ferrier and Tao simulations under the same parameters.....	53
4) Comparison between the Ferrier and Tao simulations under the HI conditions.....	58
c. Mean vertical velocity and latent heating profiles.....	59
d. Impact on remotely-sensed characteristics.....	68
1) Radar reflectivity.....	69
2) Brightness temperatures.....	74
(i) Cumulative frequency distributions.....	74
e. Impact on storm structure and dynamics	83
3. Summary	106
III IMPACT OF PARTICLE TERMINAL VELOCITY AND SIZE	
DISTRIBUTION PARAMETERS ON SIMULATED STORM STRUCTURE, DYNAMICS AND REMOTELY-SENSED CHARACTERISTICS.	
SIMULATION OF A TROPICAL SQUALL LINE.....	116
1. Background.....	116
2. Experimental setup.....	120
a. Model setup and initialization.....	120
3. Results.....	125
a. Overview of the storm structure and the convective/stratiform partitioning.....	125
b. Mean vertical profiles over the convective and the stratiform areas....	140
c. Brightness temperatures relations.....	154
4. Summary.....	178
IV CONCLUSIONS.....	183
REFERENCES	193
VITA.....	201

LIST OF TABLES

TABLE	Page	
2.1	Density, terminal velocity and particle size distribution parameters for rain, snow and graupel that are used in the simulation of the midlatitude squall line. All parameters are common for the six sensitivity tests.....	18
2.2	Assumed number of cloud ice nuclei at 0° C (NCIO), autoconversion thresholds (QCWO and QCIO) and coalescence efficiency of snow removing ice (EIS) and that of graupel removing snow (ESG). The selected parameters are varied between the six simulations.....	20
3.1	Drop size distribution parameter for rain (Nor), density, terminal velocity and particle size distribution parameter for graupel (Nog) that are varied between the six simulations of the tropical squall line.....	122

.

LIST OF FIGURES

FIGURE		Page
2.1	The midlatitude environmental conditions used to initialize the cloud model: skew-T, log-P profile of temperature (red curve), and dewpoint (blue curve) in degree C, with path of an idealized parcel ascent given by the yellow curve.....	15
2.2	Radar reflectivity computed from the hydrometeor fields generated by the cloud model at 5:30 into the simulation time.....	32
2.3	Same as in Fig. 2.2 except for presented are the results of the convective / stratiform/ non-precipitating anvil separation.....	36
2.4	Convective (a), stratiform (b), anvil (c) and system (d) number of points between 5:40 and 7:50 simulation time. Presented are also the % convective area (e) which is the ratio of the convective area to the combined convective and stratiform area, and (f) the % convective rain as computed at the 3.8 km level.....	37
2.5	Mean vertical profiles of hydrometeors (g/m^3) over the convective (a)-(d) and the stratiform (e)-(h) area.....	40
2.6	Same as in Fig. 2.5 except for presented are the results from the three simulations that used Ferrier's microphysics (OF-HI, MF-LI and MF-HI).....	47
2.7	Same as in Fig. 2.5 except for presented are the results from the two simulations that were initialized with the exact same microphysical parameters but used different microphysical parameterization schemes (MT-LI and MF-LI).....	54
2.8	Mean vertical profiles of vertical velocity (m/s) computed over the mature stage (5:40-7:50) of the simulated storms for each of the six simulations and computed separately over the (a) convective and (c) stratiform regions. Mean vertical profiles of divergence (1/s) computed over the convective (b) and the stratiform (d) regions.....	60

FIGURE	Page
2.9 Same as in Fig. 2.8 except for presented are the area and time-averaged means of latent heating (a) and (c) and latent heating scaled by the average precipitation in the lowest 2 km – (b) and (d).....	61
2.10 Contoured frequency by altitude diagrams (CFADs – Yuter and Houze, 1995) of reflectivity for each of the six simulations: (a) MT–HI, (b) MT–LI, (c) OT–LI, (d) MF–HI, (e) MF–LI, (d) OF–HI. CFAD statistics were computed over the convective area and during the mature stage of the storm.	70
2.11 Same as in Fig. 2.10 except for CFAD statistics were computed over the stratiform area.....	71
2.12 Cumulative frequency distributions of brightness temperatures (Tbs)....	75
2.13 Contoured frequency liquid diagrams (CFLD) computed over the convective region.....	77
2.14 Same as in Fig. 2.13 except for statistics are computed over the stratiform regions of the six simulations.....	78
2.15 Scatterplots of the 37 GHz versus the 85.5 GHz brightness temperatures for each of the six simulations.....	81
2.16 Same as in Fig. 2.2 except for presented are the pressure perturbations from the initial conditions at 3 km altitude.....	84
2.17 Same as in Fig. 2.2 except for presented is the storm–relative flow at 3 km altitude.....	85
2.18 Same as in Fig. 2.2 except for presented is the storm–relative flow at 1 km altitude.....	87
2.19 Same as in Fig. 2.2 except for presented is the storm–relative flow at 7 km altitude.....	88

FIGURE	Page
2.20	Same as in Fig. 2.16 except for presented are the pressure perturbations at 7 hours and 20 minutes into the simulation time..... 90
2.21	Same as in Fig. 2.17 except for presented is the storm–relative flow at 7 hours and 20 minutes into the simulation time..... 92
2.22	Same as in Fig. 2.18 except for presented is the storm–relative flow at 7 hours and 20 minutes into the simulation time..... 93
2.23	Same as in Fig. 2.19 except for presented is the storm–relative flow at 7 hours and 20 minutes into the simulation time..... 94
2.24	Same as in Fig. 2.2 except for presented is the reflectivity field at 7 hours and 20 minutes into the simulation time..... 95
2.25	Reflectivity and storm–relative flow fields at 1.4 km (a) and 3.4 km (b) altitude as inferred from dual–Doppler analyses of the PRE–STORM squall line system observed on 28 May 1985..... 101
2.26	Cross–line and along–line storm–relative flow at 11:52 UTC as inferred from dual–Doppler analyses of the asymmetric squall line system observed on 28 May 1985 during PRE–STORM..... 103
2.27	Cross–line (left panels) and along–line (right panels) storm–relative flow at 7:20 hours into the MF–LI simulation..... 104
2.28	Same as in Fig. 2.27 except for the storm–relative flow at 5:30 hours into the simulation..... 105
2.29	Same as in Fig. 2.27 except for presented is the storm–relative flow produced by the MT–LI simulation..... 107
3.1	The tropical environmental conditions used to initialize the cloud model..... 123

FIGURE	Page
3.2 Radar reflectivity (in dBz) computed from the hydrometeor fields generated by the cloud model at 6 hours into the simulation time.....	126
3.3 Same as in Fig. 3.2 except for presented are the results of the convective / stratiform/ non-precipitating anvil separation.....	127
3.4 Contoured frequency by altitude diagrams of reflectivity for each of the six simulations presented in Fig. 3.2.....	129
3.5 Same as in Fig. 3.2 except for plotted are the potential temperature perturbations from the initial conditions at 500 m above sea level.....	133
3.6 Composite radar reflectivity (dBz) over the periods (a)2110–2120 UTC, (b) 2122–2130 UTC, (c) 2131–2137 UTC, (d) 2140–2146 UTC, (e) 2149–2156 UTC, and (f) 2200–2207 UTC from the P–3’s lower fuselage C–band radar, observed over the 22 February 1993 TOGA COARE squall line.....	135
3.7 Convective (a), stratiform (b), and anvil (c) number of points between 5 h 30 min and 7 h simulation time for each of the six simulations presented in Fig. 3.2. Presented is also the % convective area (d) which is the ratio of the convective area to the combined convective and stratiform area.....	138
3.8 Mean vertical profiles of hydrometeors (g/m^3) over the convective (a)–(d) and the stratiform (e)–(h) area for each of the six simulations presented in Fig. 3.2.	141
3.9 Mean vertical profiles of vertical velocity (m/s) computed over the mature stage of the simulated storms for each of the six simulations presented in Fig. 3.2. The means were computed separately over the (a) convective and (c) stratiform regions. Mean vertical profiles of divergence (1/s) computed over the convective (b) and the stratiform (d) regions.....	144

FIGURE	Page
3.10 Same as in Fig. 3.9 except for presented are the area and time-averaged means of latent heating (a) and (c) and latent heating scaled by the average precipitation in the lowest 2 km – (b) and (d).....	145
3.11 Same as in Fig. 3.4 except for presented are the CFADs of vertical velocity.....	149
3.12 Mean vertical profile of the latent heating (deg/h) computed over the combined convective, stratiform and non-precipitating anvil regions....	153
3.13 Convective area relationship between the model-produced near surface rain rate (mm/h) and the microwave brightness temperatures computed from the model hydrometeors at four frequencies: 10 GHz – (a); 19 GHz – (c); 37 GHz – (b), and 85 GHz – (d).....	155
3.14 Brightness temperature scatterplots for (a) 10.7 GHz vs. 19.35 GHz, (b) 10.7 GHz vs 85.5 GHz, (c) 19.35 GHz vs 85.5 GHz, (d) 10.7 GHz vs. 37.1 GHz, (e) 19.35 GHz vs. 37.1 GHz and (f) 37.1 GHz vs. 85.5 GHz. Data were observed by AMPR as it flew over the 22 February 1993 TOGA-COARE squall line system.....	160
3.15 Frequency distribution for each of the four microwave channels (10.7 GHz, 19.35 GHz, 37.1 GHz and 85.5 GHz) of the brightness temperatures observed by AMPR as it flew over the 22 February 1993 TOGA-COARE squall line system.....	161
3.16 Same as in Fig. 3.14 except for scatterplots of the brightness temperatures computed from the hydrometeor fields produced by each of the six simulations: (a) – 400_8_4_RHvt simulation; (b) – 400_8_4 simulation; (c) – 600_8_4 simulation; (d) – 600_22_10 simulation; (e) – 600_60_30 simulation; and (f) – 600_60_60 simulation.....	162

FIGURE	Page
<p>3.17 Same as in Fig. 3.15 except for frequency distribution of the brightness temperatures computed from the hydrometeor fields produced by each of the six simulations: (a) – the 400_8_4_RHvt simulation; (b) – the 400_8_4 simulation; (c) – the 600_8_4 simulation; (d) – the 600_22_10 simulation; (e) – the 600_60_30 simulation; and (f) – the 600_60_60 simulation. Statistics are computed over the combined convective and stratiform regions.....</p>	168
<p>3.18 Same as in Fig. 3.17 except for statistics are computed separately over the convective (a)–(d) and stratiform (e)–(h) regions. Presented are the data from three simulations: 600_8_4 (red), 600_22_10 (blue) and 600_60_30 (yellow).....</p>	176

CHAPTER I

INTRODUCTION

Several studies in the last two decades have shown that the four-dimensional distribution of latent heating by clouds has a direct impact on the structure of tropical circulations as well as on teleconnection patterns affecting midlatitude climate (Hartmann et al., 1984; DeMaria, 1985; Lau and Peng, 1987; Trenberth et al., 1988, Chen and Yen, 1991). Most of these studies used simplified models of the atmosphere with prescribed vertical heating profiles to examine the possible relationships between diabatic heating and the dynamics of the tropical atmosphere. Global circulation models (GCMs) which include detailed descriptions of the physical processes in the atmosphere as well as the interactions with the underlying surface will be the next tool to study the complex relationships. However, current GCMs have much coarser resolution than is necessary for resolving cloud-related processes and, thus, cannot for the time being account explicitly for the latent heating associated with these processes. Because of that, they have to rely on simplified convective-parameterization schemes which relate condensational-heating/evaporative-cooling and atmospheric dynamics. The representation of the net heating effect is complicated by the fact that two distinct processes should be accounted for (Tao et al., 1991): the release and redistribution of latent heat within the clouds (Houze, 1982; Johnson, 1984; Gallus and Johnson, 1991) and heating of the surrounding environment by the subsidence that accompanies the

This dissertation follows the style of *Journal of the Atmospheric Sciences*.

large upward mass fluxes in the clouds (Arakawa, 1971; Yanai et al., 1973). Convection resolving numerical models have been used extensively over the recent years to address many issues regarding the interaction between the cloud systems and their environment (Tao et al., 1991; Tao et al., 1993a, 1993b; Simpson and Tao, 1993; Schlesinger, 1994; Halverson et al., 1996).

Since the appropriate representation of the cloud-related tropical heating is crucial for the good performance of the global-scale models and their predictions of the short-term climate changes, the GCMs can apparently be improved by continuously assimilating diabatic heating estimates based on observations of cloud systems. Indeed, determining the four-dimensional distribution of the latent heating in the tropical atmosphere is the fundamental goal of the Tropical Rainfall Measuring Mission (TRMM). However, inferring the heating associated with the observed cloud systems is a complex problem. Cloud-resolving models are used to address the problem of relating satellite-observed brightness temperatures and radar reflectivities to the four-dimensional distribution of the hydrometeors and the diabatic heating associated with their production. Three main approaches have been proposed to infer the latent heating from the orbiting passive and active microwave observations. The first of these three approaches uses the fundamental difference between the heating profiles associated with convective versus stratiform precipitating regions (Houze, 1982 ; Johnson, 1984), to make a first-order approximation to the heating associated with the observed systems, by simply classifying the observed radar echoes as convective or stratiform and assigning to each the corresponding characteristic heating profile (Tao et al., 1993c). The inferred heating estimate can be further improved by constraining the net vertical

integral of the latent heating by the rainfall accumulation (Houze, 1982; Gallus and Johnson, 1991). Since this approach relies to a significant degree on diagnostically determined mean convective/stratiform (CS) profiles, it will likely produce heating estimates which agree well with the mean state of the atmosphere. However, the CS method only uses a tiny portion of the available information and, hence, its estimates will likely not reflect properly the spatial and temporal variability of the actual heating. Furthermore, the success of this approach depends critically on the proper discrimination between convective and stratiform rain. While this discrimination might be quite reliable with the TRMM satellite radar observations, it is much more difficult in the cases when only passive microwave measurements are available (the majority of the current and future missions).

The other two methods are superior because they use all of the available information and provide estimates based on relationships developed off-line between the observables and the vertical profiles of hydrometeors and latent heating. Such relationships are developed based on studying cloud-radiation databases and, while carrying the uncertainties associated with such databases, also have the advantage of quantitatively reflecting these uncertainties. Indeed, the development of realistic error models has been identified as one of the main thrusts of the rainfall remote-sensing research by the TRMM and AMSR science teams. In the first of these two other methods, hydrometeor profiles are first estimated from the observed brightness temperatures and reflectivity structures. The most physically sound approach in doing that is by using hybrid statistical-physical rainfall retrieval algorithms (Smith et al., 1992; Mugnai et al., 1993; Wilheit et al., 1994; Olson et al., 1996) that were developed

with the help of cloud–radiation databases and because of that provide a straightforward way of relating the upper–level hydrometeor structure of a precipitating cloud (the portion contributing the most to the emerging Tb’s) with the lower level microphysics (the portion controlling the surface rain), thus capturing the inherent complex intercorrelations of the microphysics from upper to lower atmosphere. The reliability of this approach is ultimately dependent upon the degree of microphysical sophistication incorporated in cloud model itself. In the next step, vertical latent heating profiles are deduced from the estimated hydrometeor profiles with the use of assumptions, for example such that the vertical fluxes of hydrometeors are exactly compensated for by condensation or evaporation (and deposition/sublimation in the presence of ice) (Tao et al, 1990; Tao et al., 1993c; Yang and Smith, 1999a, 1999b). The uncertainty in the resulting heating estimates is closely related to the uncertainty in determining the vertical profiles of hydrometeors. Hence, the accuracy of the estimated heating can only improve with more reliable estimates of the hydrometeor profiles. In the third approach, the latent heating profiles are directly “retrieved” from the observations, again based on relationships derived off–line from cloud–radiation databases (Olson et al., 1999). In this case, although the observations are not directly sensitive to the heating itself, they are sensitive to the hydrometeor profiles: the cloud–model physics are used to establish the connection between the two. Hence the accuracy of the estimates depends critically on the amount of detail accounted for in the database.

In short, cloud–resolving numerical models are the primary tool used to study and parameterize the net effect of cloud processes on the larger–scale environment resolved by the GCMs. Furthermore, cloud–scale models are used extensively in the

development of algorithms for retrieval of rainfall rates and heating profiles needed for the initialization stage of the GCMs. Hence, a good understanding of the behavior of the cloud-resolving models, which is still lacking, is important for improving the parameterization and initialization of the large-scale models. This, in turn, is crucial for better understanding and predicting the large-scale circulations and short-term climate changes (Simpson et al., 1988). Thus, an essential step toward achieving our goal of improving the long-term forecasts lies in evaluating the performance of the cloud-scale models by assessing the sensitivity of the modeled storms to the use of different models and parameterizations. Of them, the representation of the complex microphysical processes has probably the most crucial impact upon the modeled storms.

Recently, a number of bulk microphysical parameterizations have been developed by the modeling community. They span a wide range of sophistication depending upon the number of the predicted water and ice species, the number of the parameterized interactions between species and the number of predicted parameters of the distributions (e.g. single-moment schemes predicting only the mixing ratio of the species versus double-moment schemes predicting the size spectra as well). The most simple one is the water-only scheme developed by Kessler (1969) and describing warm-rain processes. However, the importance of ice microphysics to precipitation formation has long been recognized both theoretically as well as observationally. This prompted the development of a variety of parameterizations that include ice processes and range widely in the degree of complexity. The majority of cloud models, however, utilize single moment bulk microphysics schemes (predicting the mixing ratios only) with two or three ice categories.

Sensitivity tests to the inclusion of ice processes confirmed their strongly anticipated significance for the proper representation of the storm structure. The dynamics, kinematics, thermodynamics, and the distribution of water in the storm were strongly altered by the inclusion of ice processes in the simulation of a supercell storm (Johnson et al., 1993). More importantly, the ice-phase microphysical processes were found to be crucial for a realistic air flow and precipitation statistics in the stratiform regions of squall line systems (Tao et al., 1989a; Tao et al., 1993b; McCumber et al., 1991; Yang and Houze, 1995). Such regions often cover extensive areas and play important roles in determining the overall heat budgets. Moreover, the importance of ice-phase microphysics increases the longer a system persists (Tao et al., 1989a). Hence, a proper representation of the large, long-lived mesoscale systems, which have a significant impact on the large-scale environment, will be strongly hindered if the microphysical representation is not correct.

All this explains the attention which has recently been devoted to understanding the impact of the number of predicted ice species, their descriptive parameters (e.g. density of particles, intercept and slope parameters of the distributions) and terminal velocity on the simulated storms.

Generally, increasing the number of predicted ice species leads to increase in the contribution of the small particles to the total rain field. This increases the role of lighter precipitation, stimulates the development of stratiform cloud and associated mesoscale motions, and leads to the simulation of more realistic storm systems (McCumber et al., 1991; Tao et al., 1993a; Ferrier et al., 1995). The downside is that with the inclusion of just a few more categories, the number of processes to be

parameterized increases dramatically! This presents both computational as well as philosophical problems.

In the past few years, two microphysical parameterizations have been most widely used, the one developed by Rutledge and Hobbs (1983, 1984), referred hereafter as RH, and the other developed by Lin, Farley and Orville (1983) and referred as LFO. Both of these schemes use three-class ice parameterization (cloud ice, snow and graupel/hail) and predict only a single parameter (the mass of different hydrometeors) while specifying the intercept and the slope parameter of the distributions and the density of the hydrometeors. The major difference between them is that LFO uses hail for the large precipitating ice while RH uses graupel for this category. These choices affect both the microphysical processes, which are parameterized (hail-specific microphysical relations versus graupel specific), as well as the descriptive parameters, and the calculated terminal velocities. Modeling studies have shown that LFO parameterization is more representative of the microphysical processes in the midlatitudes because the midlatitude environments are supportive of generally stronger vertical velocities and, hence, larger hydrometeors (i.e. hail). RH, on the other hand, has shown to be more appropriate for representing the tropical types of convection and for simulating the characteristic mesoscale features of the stratiform areas. The use of graupel (in RH) instead of hail (in LFO) affects significantly the simulations mostly through the smaller terminal velocity, which allows the precipitating ice to enter the anvil region where it becomes an important constituent and contributes to the dynamic, thermodynamic and radar characteristics of the anvil in a way which agrees fairly well with observations (McCumber et al., 1991).

With the intention of providing guidance on how RH and LFO schemes should be used McCumber et al. (1991) incorporated them into a cloud model and contrasted the effects of the two schemes by simulating mostly tropical squall systems. The most important result of their study was that the simulation results were affected more significantly by the type of the large, precipitating ice particles than by differences in the way the microphysical processes were treated in each of the two schemes. They saw this as an encouraging result, which suggested that the two schemes are very similar and each of them could be easily modified to simulate either midlatitude or tropical convection by simply changing the descriptive parameters of the large-ice category.

A startling result of the comparison among simulations made with LFO, RH and Ferrier (1994) microphysics and variations in the descriptive parameters is that even though the variations in the surface rainfall (the net effect) are relatively small, there are significant differences in the vertical hydrometeor profiles, the relative importance of the microphysical processes and their vertical distribution (McCumber et al., 1991; Ferrier et al., 1995). This suggests that the produced heating profiles should be different for the different schemes since the vertical distribution of water and ice species is an indicator of the dominant microphysical processes (Tao et al., 1990; McCumber et al., 1991). Furthermore, these studies found that the partitioning of the total rainfall into convective or stratiform categories is sensitive to the microphysical parameterization. Thus, the relative contributions of the characteristic convective and stratiform heating profiles should vary among simulations utilizing different parameterizations and, hence, the net heating produced by the simulated storms (the large-scale effect) should vary.

The fact that the vertical hydrometeor profiles are sensitive to the microphysical assumptions is particularly significant in the light of understanding and interpreting the microwave observations which, in turn, are highly sensitive to the vertical microphysical structure of storms (Simpson et al., 1988; Smith et al., 1992; Mugnai et al., 1993). In particular, several studies have shown that the cloud water can alter to a significant degree the relationships between the emerging at the top of the atmosphere microwave brightness temperatures (BT) and the near surface rain rates (RR) (Mugnai and Smith, 1988; Smith and Mugnai, 1988; Adler et al., 1991). However, the question of what microphysical parameters control the cloud water production, and, thus modify the BT-RR relationships, has not been addressed.

All this prompts the necessity of more research to achieve better understanding of the sensitivity to the microphysical parameterizations of the storm's structure and evolution, impact on the large-scale environment, and the sensitivity of its simulated passive microwave features. Yet, only recently have numerical modeling studies begun to address some of these issues.

To summarize, previous research has addressed the sensitivity of some storm characteristics to three main issues concerning the microphysical parameterization: i) the basic inclusion of ice processes; ii) the role and relative importance of the different processes (e.g. condensation, evaporation, evaporative cooling, cooling by melting etc.); iii) the impact of the number and type of the predicted hydrometeors. Furthermore, the main differences between the large-scale impact of the midlatitude versus tropical convection have been explored by utilizing microphysical parameterizations with hydrometeor types representative of each of these environments (e.g. Simpson et al.,

1993). A majority of this research has been conducted using the Goddard Cumulus Ensemble (GCE) model (Tao et al., 1993a, 1993b). Due to computational limitations, the 3-D simulations were restricted to smaller domains and shorter integration times and because of that could not adequately reproduce many features associated with the stratiform region of mesoscale convective systems (Tao et al., 1989a). Most of the studies were conducted using the 2-D version of the model with a larger domain size. Even though sensitivity tests showed that the overall statistical properties of well-organized cloud systems are essentially the same between the 2-D and the 3-D simulations (Tao et al., 1993a), the use of a three-dimensional model domain is highly desirable in order to better represent the highly three-dimensional nature of convection and to fully capture all the scale interactions.

Sensitivity analyses related to the microphysical parameterizations which have not been done so far include: i). analyses of the sensitivity of storm's structure and dynamics to the modeled interactions between microphysical processes; ii). evaluation of the sensitivity of the large-scale effects of modeled convection (i.e. diabatic heating). The exact heating profile produced by the large mesoscale systems is a function of several factors: the proportions of the convective and stratiform areas; the intensity of the convective activity and, in particular, the intensity of the vertical motions and thus, the eddy heat flux convergence; the characteristics of the stratiform areas which can affect the upper-levels of the troposphere both through latent heat released during the growing stages as well as through long-wave absorption long after the deep convection has ceased. All this points to the importance of the proper representation of all three features listed above. iii) the sensitivity of the microwave characteristics of the modeled

storms to the microphysical parameterizations; iii). the use of 3-D models with large domains.

As already mentioned, cloud-radiation databases have been used extensively in the development of physically-based algorithms for retrieval of rainfall and latent heating profiles from passive and active microwave observations of storm characteristics. Panegrossi et al. (1998) illustrated that the microphysical details of the simulated storms strongly influence the retrievals that use such databases. They showed that rainfall retrievals are very dependent upon having a good agreement between measurement and model manifolds. More importantly, they pointed out that even a good match-up between the measurement and model manifolds does not guarantee that a single cloud-radiation database is appropriate for a given measurement! They suggested that, in order to have a good fidelity in the retrieval of both surface rain rate and hydrometeor profile structure, it is important that the simulated storms that are included in the database reproduce well the microphysical, macrophysical and environmental features of the storms that they represent.. However, very little has been done so far to investigate the simultaneous impact of microphysical assumptions on both the simulated storm structure and dynamics and on the simulated remotely-sensed storm characteristics that affect the rainfall retrievals using these simulations. Because of that the uncertainties associated with the rainfall retrievals remain still largely unknown even though we have the tools to develop the so needed error models. The importance of such efforts has been underscored by the rainfall remote sensing team of the soon-to-be-deployed AMSR mission which identified the development of realistic error models as one of the main thrusts of its research efforts. Because of that one of the main

motivations for this study has been to increase our understanding on the very important question about the impact of the microphysical parameterization schemes on the rainfall and heating retrievals. While in this study we will not look at the uncertainty of the retrievals, we address the same basic question by investigating the sensitivity of the simulated storm dynamics and microwave storm characteristics to the microphysical parameterizations. Our improved understanding on which are the microphysical parameters that control particular storm characteristics will be a very important guideline when using multi-sensor observational data from field campaigns to judge whether our cloud-radiation database is indeed representative of the micro-, macro- and environmental characteristics of the storms that were simulated.

CHAPTER II

IMPACT OF MICROPHYSICAL SCHEMES ON SIMULATED STORM STRUCTURE, DYNAMICS, AND REMOTELY-SENSED CHARACTERISTICS. SIMULATION OF A MIDLATITUDE SQUALL LINE

1. Model description

a. Cloud model

A three-dimensional non-hydrostatic cloud-resolving model (Collaborative Model for Multiscale Atmospheric Simulations – COMMAS) is used. It integrates the compressible equations of motion and uses a time-splitting technique (Klemp and Wilhelmson, 1978) to accommodate the sound waves by advancing certain terms with a separate smaller time step. The solution technique used in the model is described in Wicker and Wilhelmson (1995). From our perspective, the most important feature of this model is that it utilizes a unique adaptive-grid technique (Skamarock and Klemp, 1993). The model resolves both the highly 3-D structure of convection and the extensive mesoscale circulations by using multiple nested grids with different spatial resolution. Features not resolved on the coarser grids are resolved on the finer grids. Using this model will allow for accurate representation of different scales of motion (convective and mesoscale) and their interactions. Both the convective and the stratiform region play an essential role in determining the kinematics, dynamics and thermodynamics of the mesoscale systems and, hence, the proper representation of the

net effect of the mesoscale systems on their larger-scale environment would be significantly impaired if both convective and mesoscale contributions (and their relative importance) are not captured correctly.

b. Model setup and initialization

The model domain has a horizontal extent of 900x900 km and a vertical extent of 18 km. Three levels of grid refinement were used. The coarse grid had a horizontal resolution of 18 km. The refinement ratio is 3:1 resulting in a grid spacing of 2 km on the finest grid where convection is resolved. The vertical resolution is 200 m at the surface and stretching to 700 m at levels above 1 km.

The initial environment is horizontally homogeneous and is given by the thermodynamic sounding (Fig. 2.1) taken from Weisman and Klemp (1982). The initial winds are from west increasing from zero at the surface to 10 ms^{-1} at 2.5 km. This sounding represents a midlatitude continental environment with moderate Convective Available Potential Energy and weak vertical shear of the horizontal wind. Observational studies have indicated that such environments are conducive for the development of long-lived Mesoscale Convective Systems (MCSs). This types of systems are an important phenomenon that affects a great many areas around the world in both tropical and midlatitude environments. Since they transport vast amounts of mass, moisture and momentum, it would appear that they must play an important role in the global hydrological cycle. Moreover, studies, such as Fritsch and Maddox (1981), Maddox (1983), Augustine and Zipser (1987) and Cotton et al. (1989), have shown that MCSs greatly modify the environment in which they develop. The significant proportion of stratiform precipitation in addition to the convective precipitation produced by these

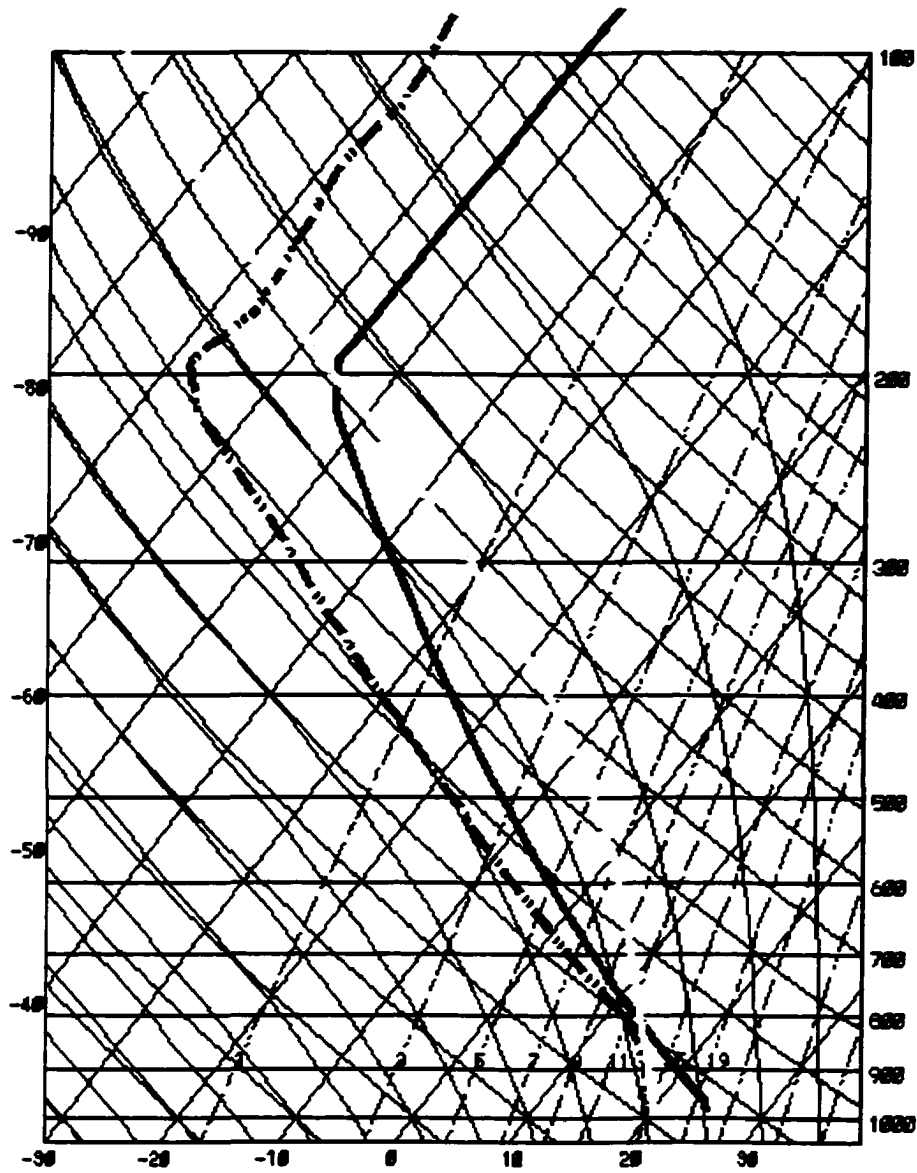


Figure 2.1. The midlatitude environmental conditions used to initialize the cloud model: skew-T, log-P profile of temperature (red curve), and dewpoint (blue curve) in degree C, with path of an idealized parcel ascent given by the yellow curve. The sounding is taken from Weisman and Klemp (1982)

systems makes them suitable for our sensitivity study since the proper understanding of the behavior of both of these regions is of crucial importance for both cloud modeling and for the development of precipitation and latent heating retrieval algorithms that use cloud-model generated databases.

Convection is initiated in the model by placing six warm bubbles in a north-south line. Each of the bubbles was 2.5° warmer than the environment and had 20 km horizontal and 2.8 km vertical dimensions. The bubbles were placed 40 km apart. Tests by Skamarock et al. (1994) showed that simulated storms are not particularly sensitive to the spacing, number, strength or size of the initial warm bubbles as long as they are large enough and their buoyancy is strong enough for them to survive ascent through the sheared environment. Hence, the simulated storms are not very sensitive to the initial perturbations when warm bubbles are used. However, as it will be discussed in Chapter III, the simulated storms appear to be very sensitive to the initiation of convection if cold perturbations are used!

c. Radiative transfer model

A radiative transfer model (Kummerow, 1993; Kummerow et al., 1988) is used to simulate the brightness temperatures (at five different frequencies and two polarizations) which are associated with the cloud-model produced hydrometeor structures. The data presented here were computed at nadir and over an ocean background. The ocean surface was assumed to be specular as suggested by Tesmer and Wilheit (1998). The temperature and the wind at the lowest model level were used to compute the surface emissivity. Microwave brightness temperatures were computed at five different frequencies and two polarizations.

d. Microphysical schemes

The purpose of this study is to examine the sensitivity of storm dynamics, brightness temperature relations, and latent heating to microphysical parameterizations used in simulations of deep convective storms. In contrast to previous studies that investigated the impact of vastly different paradigms like the inclusion of ice-phase microphysics (e.g. Tao and Simpson, 1989a,1993a; Johnson et al., 1993, Yang and Houze, 1995, Liu et al., 1997) or changes in the type or number of hydrometeor species represented in the parameterizations (e.g. McCumber et al., 1991), this study focused on two microphysical schemes that share the same basic paradigm.

Both schemes have a two-class liquid water (cloud water and rain) and three-class ice-phase (cloud ice, snow and graupel) set of parameterizations. The first one was taken from Tao and Simpson (1993a) and is a hybrid version of the Lin et al. 1983 parameterization. In the current application the scheme was altered by substituting graupel in place of hail in the high-density ice category following McCumber et al. (1991) who suggested that the use of graupel instead of hail leads to the simulation of much more realistic stratiform precipitation. The second scheme is a single-moment, three-ice version of Ferrier (1994). Both schemes assume monodisperse distributions for the non-precipitating cloud water and cloud ice and inverse exponential distributions for the precipitating hydrometeors of the form

$$N(D) = N_0 \exp(-\lambda D) \quad (1)$$

where N_0 is the intercept kept constant during the simulation and λ is the slope which is computed at each time step as a function of the model-predicted mixing ratios for each hydrometeor category. The choice of the intercept parameters was based on

observational studies. For rain, the size distribution given by Marshall–Palmer (1948) is used. The intercept parameters for snow and graupel were chosen based on the study by Houze et al. (1979). Table 2.1 lists parameters that are common to both schemes. As noted in Table 2.1, the fall speed formula in Ferrier (1994) was changed to be consistent with the Tao et al. (1993a) scheme. The hydrometeor descriptive parameters (i.e. density and distribution parameters) and their terminal velocities were purposely set to be the same in the two schemes in order to avoid their first–order impact on the simulated storms (McCumber et al., 1991) and to focus our attention on the impact of the differences in the treatment of the microphysical processes. Despite the described changes made to the original parameters in the two microphysical codes, the two simulations that resulted from their use will be referred hereafter as the "original Tao" (OT) and "original Ferrier" (OF).

Table 2.1. Density, terminal velocity and particle size distribution parameters for rain, snow and graupel that are used in the simulation of the midlatitude squall line. All parameters are common for the six sensitivity tests.

	Particle Density [kg/m ³]	Intercept Parameter No [m ⁻⁴]	Terminal Velocity $V = a \frac{\Gamma(4+b)}{6 \lambda^b} \left(\frac{\rho_o}{\rho}\right)^{0.5}$
Rain	1000	8x10 ⁶	a=842.0 b=0.80
Snow	100	3x10 ⁶	a=4.836 b=0.25
Graupel	400	4x10 ⁶	a=86.818 b=0.50

While both OT and OF share the same paradigm of bulk 3-ice parameterizations with identical hydrometeor descriptions, there are still a number of differences in the values of parameters used in the microphysical formulas as well as differences in how certain physical processes are modeled. Table 2.2 lists values for the most important differences in parameters between the two original schemes. One of the most striking differences is in the number of ice crystals assumed to be activated at 0 deg C (NCIO). OF sets this parameter to a value that is five orders of magnitude greater than OT. Previous research has pointed to the importance of the NCIO selection in particular (e.g. Bennetts and Rawlins, 1981; Rutledge and Hobs, 1984) and the ice initiation parameterization in general (Cotton et al., 1986; Meyers et al., 1992). As it will be shown later our study confirms the important impact that the NCIO selection has on the partitioning between the cloud ice and the cloud water production in the mixed phase regime and on the subsequent growth of the snow and graupel fields.

Many studies have recognized the importance of ice aggregation, especially in stratiform clouds. The parameterization of the aggregation processes depends to a significant degree on the coalescence efficiencies (the probability that two colliding particles will stick together) that are assumed in the microphysical scheme. Unfortunately, as in the case of the ice initiation parameters, observational and

Table 2.2 Assumed number of cloud ice nuclei at 0° C (NCIO), autoconversion thresholds (QCWO and QCIO) and coalescence efficiency of snow removing ice (EIS) and that of graupel removing snow (ESG). The selected parameters are varied between the six simulations.

	<i>Original Tao – Low Ice – OT-LI</i>	<i>Original Ferrier – High Ice – OF-HI</i>
NCIO	10^{-2} m^{-3}	619 m^{-3}
EIS	$1.\text{exp}(0.25\text{TC})$	$0.1\text{exp}(0.1\text{TC})$
ESG	$1.\text{exp}(0.09\text{TC})$	$0.1\text{exp}(0.1\text{TC})$
QCIO	0.0006 kg/kg	1.000 kg/kg
QCWO	0.002 kg/kg	0.001 kg/kg
	<i>Modified Tao – Low Ice – MT-LI</i>	<i>Modified Ferrier – Low Ice – MF-LI</i>
NCIO	10^{-2} m^{-3}	10^{-2} m^{-3}
EIS	0.1	0.1
ESG	0.1	0.1
QCIO	0.001 kg/kg	0.001 kg/kg
QCWO	0.001 kg/kg	0.001 kg/kg
	<i>Modified Tao – High Ice – MT-HI</i>	<i>Modified Ferrier – High Ice – MF-HI</i>
NCIO	10^7 m^{-3}	619 m^{-3} (NCIO _{max} = 10^7)
EIS	0.1	0.1
ESG	0.1	0.1
QCIO	0.001 kg/kg	0.001 kg/kg
QCWO	0.001 kg/kg	0.001 kg/kg

laboratory studies of the coalescence efficiencies are still insufficient and their sometimes contradictory results have not been able so far to provide clear guidance in the development of microphysical parameterizations. The difference in the choices for coalescence efficiencies in OT and OF (see Table 2.2) reflect that. In both OF and OT, the coalescence efficiency of snow removing ice (ESI) and that of graupel removing snow (ESG) have a temperature dependent equation in accordance with results reported by Hallgren and Hosler (1960) and Hosler and Hallgren (1960). However, OF and OT differ in their choices of EIS and ESG by an order of magnitude. While in OF the exponentially decreasing with colder temperatures EIS and ESG have a maximum value of 0.1 at 0 deg C, this value in OT is 1 indicating efficiency of 100%. Most laboratory results indicate much lower efficiencies near 0 deg C (Pruppacher and Klett, 1978). However, OT's selection follows that of Lin et al. (1983) who justified it with the fact that the laboratory experiments have been made in ice-saturation conditions while other studies (Hosler et al., 1957) have suggested that these efficiencies are considerably higher in ice-supersaturation conditions, the efficiencies increasing with increasing temperature. Lin et al. (1983) further supported their choice with the fact that: (i) their efficiencies approached laboratory results at colder temperatures where ice-saturation is more likely; (ii) efficiencies are highest near 0 deg C consistent with efficient aggregation in this region as manifested by the radar "bright band". The difference in choice of efficiencies between the two schemes should amount to OT having a much easier conversion of smaller and low-density ice particles into larger, higher density categories. A second difference between the two schemes is that while in OF the two coalescence efficiencies (EIS and ESG) are equal, in OT the coalescence efficiency for

snow removing ice is greater than the coalescence efficiency for graupel removing snow. In both schemes the coalescence efficiency for graupel removing ice is set to a constant value of 0.1.

Another parameter that affects cloud ice is the threshold used to trigger autoconversion from ice to snow (QCIO). The very large threshold value set in OF suggests that this process is only activated in the OT scheme. In reality, however, cloud ice is allowed to convert to snow in the OF scheme – just not through a single autoconversion procedure. Autoconversion thresholds for cloud water converting to rain are also different with OT requiring twice as much cloud water as OF.

To test the impact of the different parameter values versus the differences in parameterization philosophies, two sensitivity tests were conducted. In the first one, the parameters listed above were set to equivalent values in the two schemes (Table 2.2). The NCIO value of 10^{-2} m^{-3} has often been suggested as typical (Fletcher, 1962; Rutledge and Hobbs, 1984). Furthermore, NCIO of 10^{-2} m^{-3} produces 0.5 active nuclei per liter at -18 deg C , a normal atmospheric value in England as reported by Bennetts and Rawlins (1981) and, hence, an appropriate choice when simulating midlatitude convective storms. The coalescence efficiency values were set to be temperature independent and rather low (0.1) in closer agreement with the laboratory results of Hosler and Hallgren (1961). The simulations conducted with this set of parameters will be referred to as "Modified Tao–Low Ice" (MT–LI) and "Modified Ferrier–Low Ice" (MF–LI). The "Low Ice" will be used hereafter to refer to the choice of NCIO being equal to 10^{-2} m^{-3} . In the second test, the sensitivity to the NCIO selection was tested. All parameters remained the same except the NCIO which was set to very high value

(especially in the Tao simulation). These two simulations will be referred as "Modified Ferrier–High Ice" (MF–HI) and "Modified Tao–High Ice" (MT–HI) and "High Ice" will be used hereafter to refer to $\text{NCIO} > 600 \text{ m}^{-3}$.

To summarize: i) the two original runs represent extremes in the possible choices. OT–LI is set up in such a way as to favor the production of precipitation versus that of cloud ice. This includes the low NCIO, the easy conversion of cloud ice to snow as the result of the low QCIO and the fast collection of cloud ice and snow parameterized by the high collection efficiencies. OF–HI represents the opposite philosophy. Everything is set as to favor the production of cloud ice at the expense of precipitation; ii). the two modified Low Ice (LI) versions have parameters which are commonly used. As it will be shown they represent environment in which there are not enough cloud ice crystals to absorb all the vapor available above ice saturation. As a result, supercooled cloud water is produced; iii). the two modified High Ice (HI) simulations show the impact of the NCIO selection and represent environments in which enough cloud ice nuclei are present and supercooled cloud water is not produced.

1) Microphysical differences

There are numerous minor differences in the parameterizations of physical processes in the OT and OF schemes. Rather than enumerate them, the focus here is on the major differences relevant to the current set of simulations.

(i) Ice initiation and water vapor saturation adjustment

Tao's scheme

For grid points that are supersaturated with respect to ice in Tao's scheme, a

certain amount of the excess water vapor is converted into cloud ice. This happens in two steps.

In the first step cloud ice is initiated and grown by deposition in two different ways and then the final ice production rate is taken to be the minimum of the two. The two ways are as follows: i). in the first way, cloud ice is initiated in amounts such that the number concentration of active natural ice nuclei is equal to that given by

$$NCI = NCIO \exp(-0.6*TC) \quad (2)$$

where TC is the temperature in Celsius and NCIO is the assumed number concentration of cloud ice nuclei in m^{-3} at 0 deg C. This ice initiation rate is limited by the amount of water vapor above ice saturation and by the choice of NCIO. Next the cloud ice is grown by deposition and this rate is dependent upon the present supersaturation and upon the present amount of cloud ice. ii). in the second way, it is assumed that cloud ice nuclei are present in large enough quantities as to absorb all the water vapor above ice saturation and the ice initiation and depositional growth are computed following the saturation adjustment technique of Soong and Ogura (1973). As already stated, the minimum of the two ice–initiation/depositional–growth rates is taken. Hence, the ice–initiation/depositional–growth rate is limited by the ice initiation processes when the assumed NCIO is small but when the assumed NCIO is large, the rate is limited by the actual amount of water vapor above ice saturation. In that sense, assuming an extremely large NCIO (like in MT–HI) only assures that all of the ice–supersaturated water vapor will be used for ice initiation/deposition. Even such a high NCIO would not lead to depletion of the water vapor below ice saturation.

In the second step of cloud ice production the so-called water-ice saturation adjustment (Lord et al. 1984; Tao et al., 1989b) is applied. After accounting for the change in temperature associated with the phase change in the ice initiation step, a new saturation vapor pressure is computed using a mass-weighted average between water and ice values. The newly computed excess water vapor is then partitioned into both cloud ice and cloud water with the fraction converted to ice varying linearly with temperature from zero at 0° C to 1.0 at -40° C. In this manner, cloud ice is always generated in ice-saturated environments regardless of how low the assumed number of activated ice crystals (NCI and NCIO) could be! Cloud water is also produced even though the air might not be saturated with respect to water. Furthermore, since the saturation vapor pressure for ice is lower than that for water, the air will still be supersaturated with respect to ice even after the cloud ice/cloud water production step.

After modifying the temperature to account for the cloud ice/cloud water production, a new ice-saturation vapor pressure is computed. The excess water vapor is converted to snow through deposition. The temperature is readjusted to account for the additional phase change. Finally, the air is checked to see if it is still saturated with respect to water. If not, evaporation of rain is allowed to occur if rain is present.

It should be noted that evaporation of cloud water and sublimation of cloud ice in Tao's scheme are only performed if the initial vapor pressure entering the water-ice saturation adjustment procedure is less than the mass-weighted saturation vapor pressure and cloud water and cloud ice are available for evaporation/sublimation. Since this step occurs before the evaporation of rain, the Tao scheme tends to remove cloud water first before reducing the rain in subsaturated parcels.

Ferrier's scheme

In Ferrier's scheme, the cloud ice related processes depend more strongly on the NCIO parameter than they did in Tao's scheme. Cloud ice initiation is constrained to be the difference between what is already present and the maximum possible cloud ice mass where the maximum possible cloud ice mass is given by the product of the mass of an individual crystal (assumed to be 10^{-12} kg) and the smaller of two NCIs: that given by (2) or 10^7 m^{-3} . Hence, while Tao would continuously activate new cloud ice crystals in the presence of ice supersaturation, Ferrier would do that only if there are not enough crystals already there ("enough" being dependent on the choice of NCIO). Furthermore, the cloud ice depositional growth and the autoconversion from cloud ice to snow also depend upon the assumed NCI with the autoconversion working in such way as to assure that all cloud ice exceeding the maximum allowed in terms of NCI will be converted to snow. In considering these two processes, the number of active cloud ice nuclei (NCI) is assumed to be the minimum of three terms: the number of crystals given by (2), 10^7 m^{-3} , or the mass of cloud ice that is already present divided by the mass of an individual crystal. Hence, the smaller the assumed NCIO, the less cloud ice will be initiated and grown by deposition. While the trend is similar in Tao, the difference is that in Tao the depositional growth does not depend explicitly on the choice of NCIO. More importantly, Tao has an additional mechanism for cloud ice growth that is completely independent from the choice of NCIO.

After cloud ice deposition, the temperature is adjusted taking into account the phase changes from all depositional processes (vapor to ice, snow and graupel). It should be noted that depositional growth of graupel is only allowed in the Ferrier

scheme. From the new temperature, a water saturation vapor pressure is computed and compared to the air's vapor pressure. Any excess is converted into cloud water. If there is a deficit, unlike Tao, cloud water is evaporated last only after rain, melting snow and graupel are evaporated.

To summarize, the net effect of the differences in the Ferrier and Tao treatment of ice initiation and subsequent water vapor saturation adjustment is that cloud ice production should be favored in Tao while the production of supercooled cloud water should be favored in Ferrier. This happens because in Ferrier cloud ice is initiated only if there is not enough there already. Hence, as the cloud grows and the amount of cloud ice increases, the cloud ice initiation would actually decrease. In Tao cloud ice is generated *always* when there is ice-supersaturated water vapor, regardless of the present amounts of cloud ice and whether some of the cloud ice nuclei assumed to be in the environment have already been used. In other words, a continuous supply of cloud ice nuclei is assumed, this supply, though, being fixed by the NCIO assumptions. This difference in the philosophy of the ice initiation treatment should also lead to Tao using more of the ice-supersaturated water vapor during the convective growth and Ferrier leaving more of that water vapor available for later use (e.g. depositional growth in the stratiform region). The second difference between the two schemes is that Tao has a secondary mechanism for cloud ice production – the water-ice saturation adjustment. This mechanism also assures that cloud ice will be generated continuously, regardless of the assumed NCIO, as long as there is vapor above water saturation. As will be shown later, differences in how the cloud ice and supercooled cloud water are partitioned affect the growth of the other hydrometeors and, thus, the storm structure and its remotely–

sensed characteristics. Furthermore, where and how the supersaturated water vapor is condensed/deposited affects the area-averaged vertical profiles of latent heating.

(ii) Autoconversion of cloud ice to snow

Tao scheme

There are two methods by which cloud ice is converted to snow in the Tao scheme. The first is simply autoconversion when the cloud ice mixing ratio exceeds the QCIO threshold parameter (Table 2.2). The second method occurs during the Bergeron process for snow production. In addition to cloud water converting to snow to account for the differences in saturation vapor pressure for water and ice (the traditional Bergeron processes), a fraction of the cloud ice is converted into snow to parameterize the growth of ice crystals to precipitation sized particles through vapor deposition. No change in the water vapor mixing ratio is performed, however, since the depositional growth of the cloud ice happens at the expense of the cloud water.

Ferrier scheme

The conversion of cloud ice to snow via the Bergeron processes is also modeled in the Ferrier scheme, but only when cloud water is present. In Tao's formulation, the processes occurs with or without cloud water. The dependence on the presence of cloud water implies that the process is inactive if the temperature is less than -40°C in Ferrier's scheme but still active in Tao's scheme. As noted by Krueger et al. (1995), such an approach not to make the Bergeron processes subject to the presence of supercooled cloud water in fact acts as a crude fall-speed parameterization for cloud ice. Thus, in Tao cloud ice is continuously depleted and converted into snow while in Ferrier

this happens only when and where there is supercooled cloud water, and, hence, does not happen in simulations in which supercooled cloud water is not produced.

In the original Ferrier scheme, the autoconversion threshold for cloud ice converting to snow (QCIO in Table 2.2) effectively turns off the constant mass-based autoconversion. In its place, Ferrier uses a temperature dependent (NCI dependent) autoconversion threshold mentioned earlier. The values vary throughout the cloud. At upper levels the autoconversion threshold is typically an order of magnitude greater than the constant mass-based threshold used in OT scheme. Consequently, the production of snow would be more limited in OF compared to OT at these levels. At warmer temperatures, near the melting level, where the threshold approaches zero Ferrier will convert cloud ice to snow much more effectively. Furthermore, the autoconversion threshold is dependent upon the assumed NCI (NCIO) and the conversion is quicker for smaller NCI. It should be noted, however, that in Ferrier cloud ice is not even produced if the maximum allowed NCIs are already present. That means that the autoconversion will be activated only in cases when cloud ice amount grew above the maximum allowed due to depositional growth or advection. In that sense this additional autoconversion mechanism in Ferrier only assures that cloud ice mass will not exceed the maximum allowed (in terms of NCI).

(iii) Graupel growth

The Tao scheme is based on Lin et al. (1983) who were interested in simulating hail producing storms. As such, the Tao parameterization includes freezing of rain drops to produce high-density ice particles (graupel in the present case). Although not the dominant source of graupel production, this processes is not included in the Ferrier

scheme and could lead to differences in graupel amounts found in the Tao and Ferrier simulations.

To complicate matters, however, the Ferrier scheme includes two graupel growth processes not accounted for in the Tao scheme. The first is through the accretion of cloud water by snow. If the cloud water exceeds a threshold of 0.0005 kg/kg, the fraction of snow that would be associated with large snowflakes is assumed to convert to graupel during the cloud water accretion processes. The second graupel growth mechanism included in Ferrier, but not in Tao, is growth via vapor deposition in the saturation adjustment procedure.

Regardless of these differences, the primary graupel production processes are the accretion of snow and ice by rain and the primary growth processes are accretion of rain and cloud water by graupel and these processes are similar in both parameterization schemes.

(iv) Environmental modifications

Another important philosophical difference in the Tao and Ferrier schemes is when they perform modifications to the environmental temperature and water vapor mixing ratios. In Tao's scheme, the temperature is modified after each processes has been modeled. Assuming that the air parcel was initially supersaturated, this gives preference to the first few steps in the microphysical parameterization as subsequent steps will have less water vapor available and warmer environmental temperatures with correspondingly higher saturation vapor pressures and lower supersaturations.

In contrast, Ferrier's scheme allows all the processes, except for the condensation of cloud water, to compete for the available excess water vapor at the same temperature.

Condensation of cloud water is performed after the temperature and water vapor have been adjusted for all depositional growth processes. This reflects the nature of the traditional Bergeron processes which gives preference to the growth of ice over, and at the expense of, water in ice-supersaturated environments. According to Ferrier (1994), this eliminates the need for explicit parameterization of the Bergeron processes for cloud ice include in Lin et al. (1983) and also in Tao's scheme used here.

2. Results and discussions

a. Overall storm structures and convective/stratiform/anvil separation

The overall structure of the simulated storms can be seen in Fig. 2.2 which presents the maximum reflectivity in the column for each of the six runs at 5 hours and 30 minutes into the simulation. All six simulations produced squall line systems of the type leading-convective-trailing stratiform precipitation. Furthermore, all six simulations show some degree of asymmetry in the structure of the stratiform area with most of the echo confined to the north-central portion of the storm and a relative absence of stratiform precipitation behind the southern portion of the storm. Such storm organization, referred to as "asymmetric squall line", has often been observed in midlatitude storms and is attributed to the development of a stratiform-region Midlevel Convective Vortex (MCV) that forms in large CAPE (Convective Available Potential Energy) and weak vertical wind shear environments (e.g. Bartels and Maddox, 1991). Another common feature is the development of reflectivity notch at the rear echo boundary in association with bulging of the convective line downwind of the echo notch, a structure which has been documented by Smull and Houze (1985). However, a

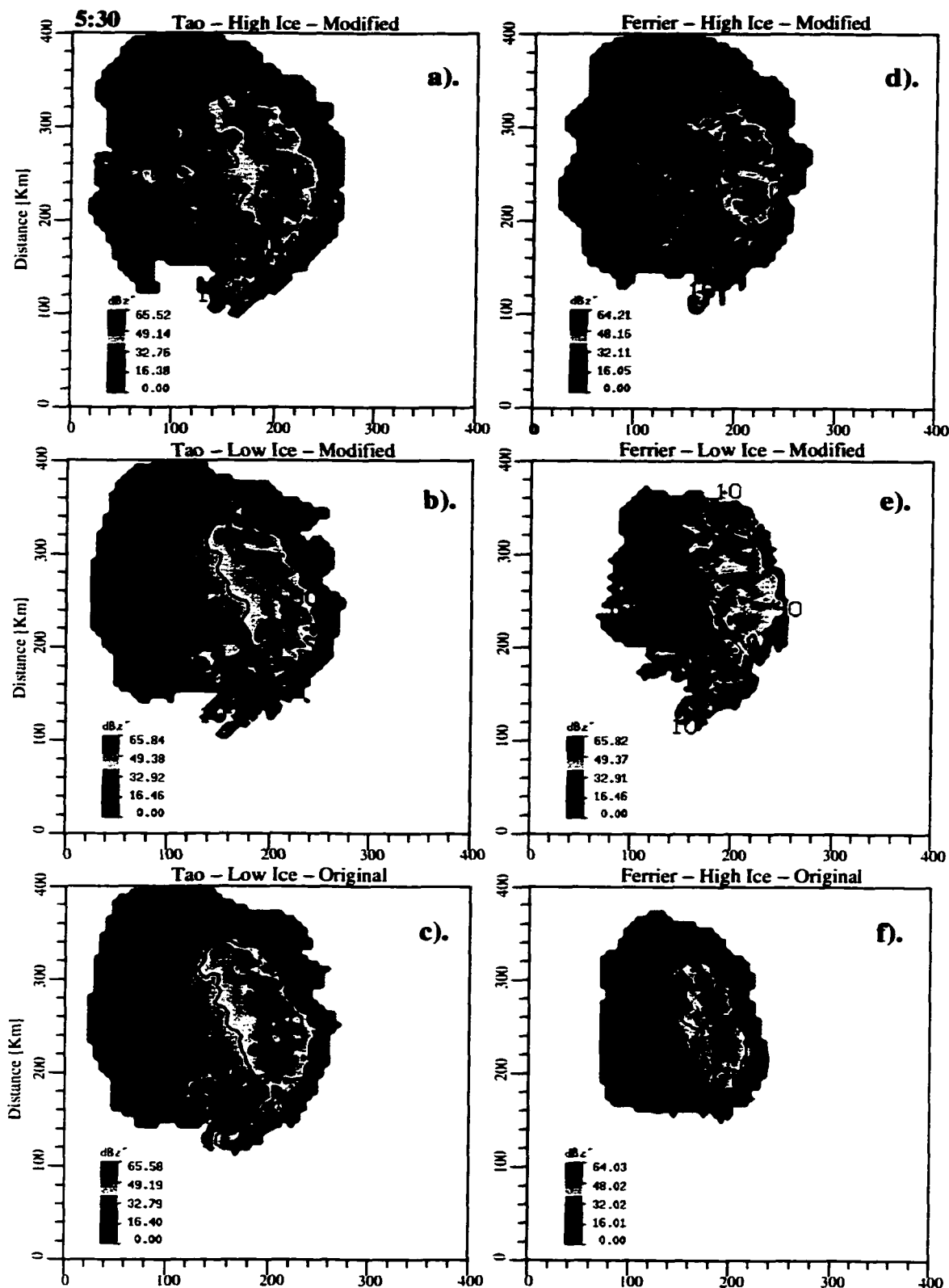


Figure 2.2. Radar reflectivity computed from the hydrometeor fields generated by the cloud model at 5:30 into the simulation time. Presented is the maximum reflectivity in each 6x6 km² column. Model domain is 400x400km². Each of the six panels presents the reflectivity field that corresponds to a particular model run: (a) MT-HI; (b) MT-LI; (c) OT-LI (d) MF-HI; (e) MF-LI; (f) OF-HI. See Table 2.2 for details on the setup for each of the six runs. Contour interval is 10.

quick inspection of the storm structure reveals that there are also significant differences among the simulations. Probably the most important difference is in the scale of the systems. While the three Tao simulations exhibit small variability in the scale, the three Ferrier simulations show a much stronger sensitivity to the choice of parameters. Indeed, an up-scale growth can be observed with OF-HI producing the smallest system and MF-HI producing the largest one which is comparable in size to the systems produced by Tao's microphysics. Furthermore, differences among the six simulations are observed in the scale and organization of the reflectivity cores, the orientation of the leading convective line and the tendency to develop secondary bands of convection. Apparently, the six microphysical realizations produce different storms, with different hydrometeor structures and different remotely-sensed characteristics. We will first describe the differences in the hydrometeors structures and relate them to the already discussed differences in the way the microphysical parameterizations work. Next, we will relate the differences in the remotely-sensed characteristics to the hydrometeor structures. Finally, we will look at the storm structure and evolution and, again, explain the observed differences among the six simulations by relating them to the hydrometeor structures.

Considering that different microphysical processes are dominant in convective versus stratiform clouds, the modeled squall line systems were first partitioned into convective, stratiform and non-precipitating anvil regions and the three regions were then analyzed separately in terms of their mean vertical profiles and frequency distributions of the remotely-sensed characteristics.

The convective/stratiform separation was performed for all grid points for which the maximum reflectivity in the column (maxdBz) was greater or equal to 15 dBz. The decision to exclude from the convective/stratiform classification these points for which the maximum reflectivity was less than < 15 dBz was based on the fact that, in the long run, we are interested in using the simulated convective/stratiform characteristics in the development and the improvement of algorithms for rainfall and latent heating retrievals from spaceborne observations (like that of TRMM) and the sensitivity of the only spaceborne precipitation radar is on the order of 15 dBz. All points with no surface precipitation but with maxdBz > 1 were classified as non-precipitating anvil. The convective/stratiform separation methodology that was used is similar to that suggested by Tao et al. (1993b). A grid point was considered convective if the maximum updraft exceeds 5 m/s or if cloud water is present (cloud water mixing ratio $> 0.2\text{g/kg}$) below the melting layer. These criteria are useful to identify regions with active convection aloft even if there is no surface precipitation, and regions in between the active convective cores which, even though less active, are still convective in the terms of their dominant microphysical processes. Furthermore, if a grid point was not convective but three of the surrounding four were, the grid point was also classified as convective. This resulted in more contiguous regions of convective and stratiform rainfall. The often-used background-exceedence criteria which identifies cores of more intense precipitation was not applied here since it often classified as convective areas of high gradients (e.g. the back of the stratiform area) which did not show convective characteristics otherwise. Finally, if a grid point had surface precipitation and was not convective, it was classified as stratiform.

Figure 2.3 illustrates how the convective/stratiform/anvil precipitation classification performed in the case of each of the six simulations at 5 hours and 30 minutes into the simulation. The statistics of the precipitation partitioning over the period 5:40 to 7:50 hours into the simulation are shown in Fig. 2.4. Figures 2.3 and 2.4 clearly illustrate several points: i). in Tao neither the size nor the relative proportions change much from one realization to another (weak sensitivity to the choice of parameters); ii) to the contrary, the variability in the size of the convective/stratiform/anvil and their relative proportions is quite significant in Ferrier; iii). Ferrier tends to produce smaller systems with larger percent convective area and larger percent convective rain. Especially outstanding in that sense is the OF-HI simulation which produced a system almost half the size of the systems produced by Tao. The MF-HI simulation produced a much larger system which compares very closely in size and proportions to the systems produced by Tao. MF-LI produced a system with intermediate characteristics. Hence, OF-HI and MF-HI represent the two extremes (in terms of system size) in the Ferrier simulations. Their setups differ in choices for the collection efficiencies and the threshold for autoconversion from cloud ice to snow (see Table 2.2) with OF-HI giving preference to the cloud ice production at the expense of the precipitation production. Apparently, this results in a much smaller system. This result clearly indicates the important role which the precipitation-generated cold pool plays in the upscale growth of the convective systems; iv). from a point of view of the systems size, Ferrier shows also significant sensitivity to the choice of the NCIO parameter while Tao does not. Indeed, when the NCIO parameter is decreased from that in MF-HI to that in MF-LI, the convective area in Ferrier does not

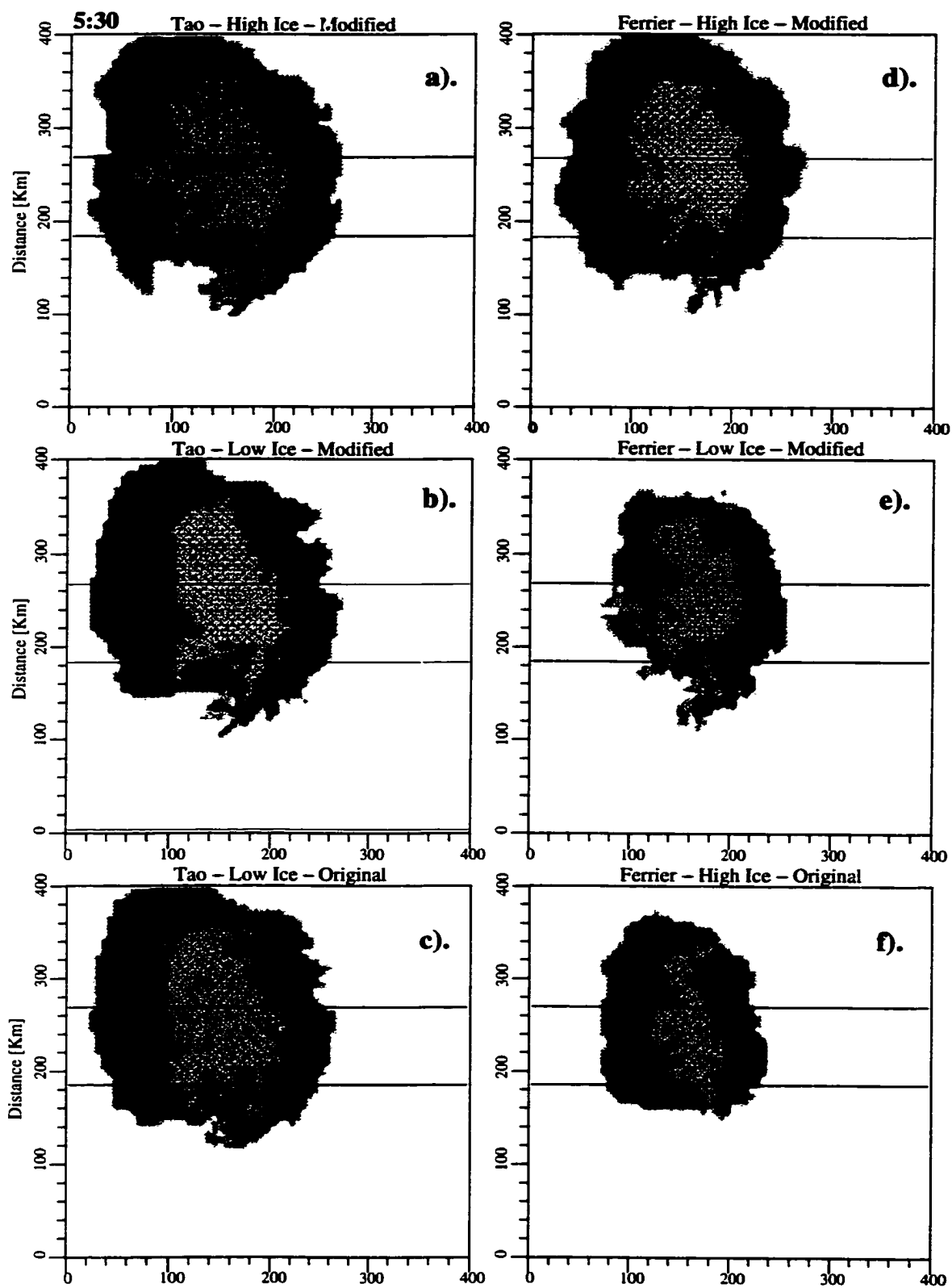


Figure 2.3. Same as in Fig. 2.2 except for presented are the results of the convective / stratiform / non-precipitating anvil separation. The convective region is plotted in black, the stratiform region - in light gray and the non-precipitating anvil - in darker gray.

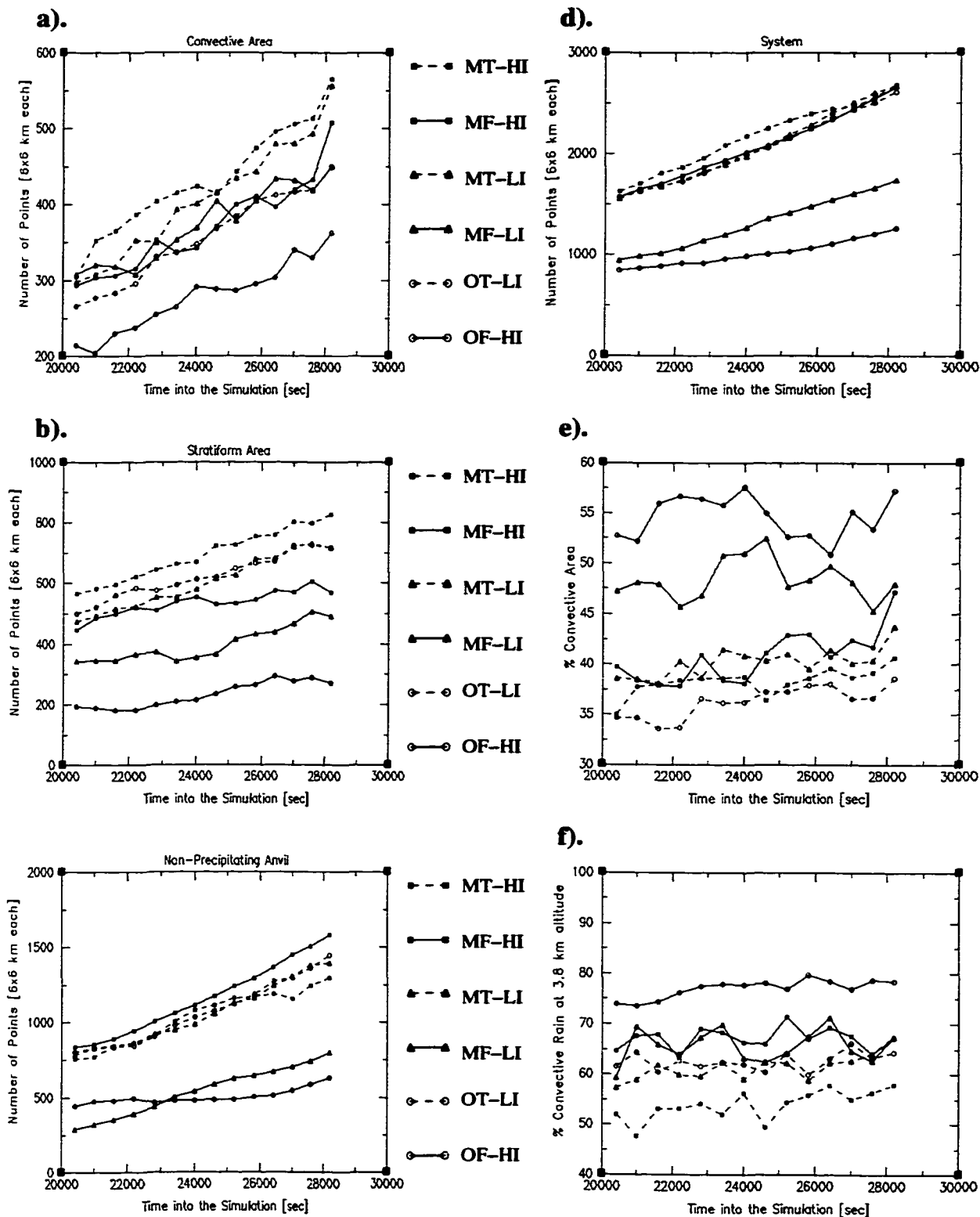


Figure 2.4. Convective (a), stratiform (b), anvil (c) and system (d) number of points between 5:40 and 7:50 simulation time. Presented are also the % convective area (e) which is the ratio of the convective area to the combined convective and stratiform area, and (f) the % convective rain as computed at the 3.8 km level.

change much in size but the stratiform and the anvil areas decrease significantly. Hence, in Ferrier the biggest system is produced when the cloud ice production is favored over that of supercooled cloud water and, when in addition to that, the collection efficiencies and the auto-conversion thresholds both stimulate quicker conversion of cloud ice into precipitating snow and graupel; v). finally, the percent convective area and percent convective rainfall of all six simulations compare reasonably well to the 40–60% of convective rain reported from observations of mesoscale convective systems. The only exception might be the OF–HI simulation which produced only about 25% of stratiform precipitation, still a reasonable even though somewhat smaller number.

b. Mean hydrometeor profiles

Area and time-averaged vertical profiles of each hydrometeor species were constructed from the model output over the convective and stratiform regions and encompassing the period 5:30–7:50 hours into the simulation. Hence, the mean cloud structures presented below represent the mature stage (Leary and Houze, 1979) of the storm.

In order to better separate the effects of the parameter choices from that of the differences in treatment of the microphysical processes we will compare the mean hydrometeor profiles in three ways: first, the three Tao simulations will be compared to each other; next the three Ferrier simulations will be compared; finally, the modified low-ice versions of Ferrier and Tao will be compared since these two simulations were ran with the exact same choice of parameters and all differences between them can be attributed to the differences in microphysical parameterization philosophy adopted by each of the two schemes.

The following clarification of terms is needed. Hereafter the term production (e.g. cloud ice production) will be used to describe the end result of a microphysical realization and to indicate the accumulated amounts of different hydrometeors. These amounts represent the time and space-averaged differences between the sources and the sinks for these hydrometeors. When we want to describe the source terms only, the term "production rate" will be used. In other words, when we say that one microphysical realization produces higher amounts of cloud ice, for example, than another that does not necessarily mean that its production rates are higher but simply means that the residual, the end result of the balance between sources and sinks is higher.

1) Comparison among the three Tao simulations

Figures 2.5a–h show the mean hydrometeor profiles in the convective and stratiform area of the three Tao simulations. Inspection of the cloud ice field reveals that the cloud ice production in the convective area depends only on the choice of the NCIO parameter (see Fig. 2.5a). Indeed, when the collection efficiencies and the autoconversion thresholds were changed between OT–LI and MT–LI the produced cloud ice did not change at all. When the NCIO was increased between MT–LI and MT–HI, the amount of cloud ice also increased, especially at levels below 7 km. Two things should be noted: i) the increase in cloud ice was not very big despite the 9 orders of magnitude increase in NCIO. This is a reflection of the fact that in the second (high NCIO) case the cloud ice production was limited by the amount of water vapor above ice-saturation. Furthermore, the fact that the increase was very small at upper levels also indicates that in Tao the cloud ice is not allowed to accumulate regardless of how much has been produced. Indeed, the continuous conversion of cloud ice into snow via

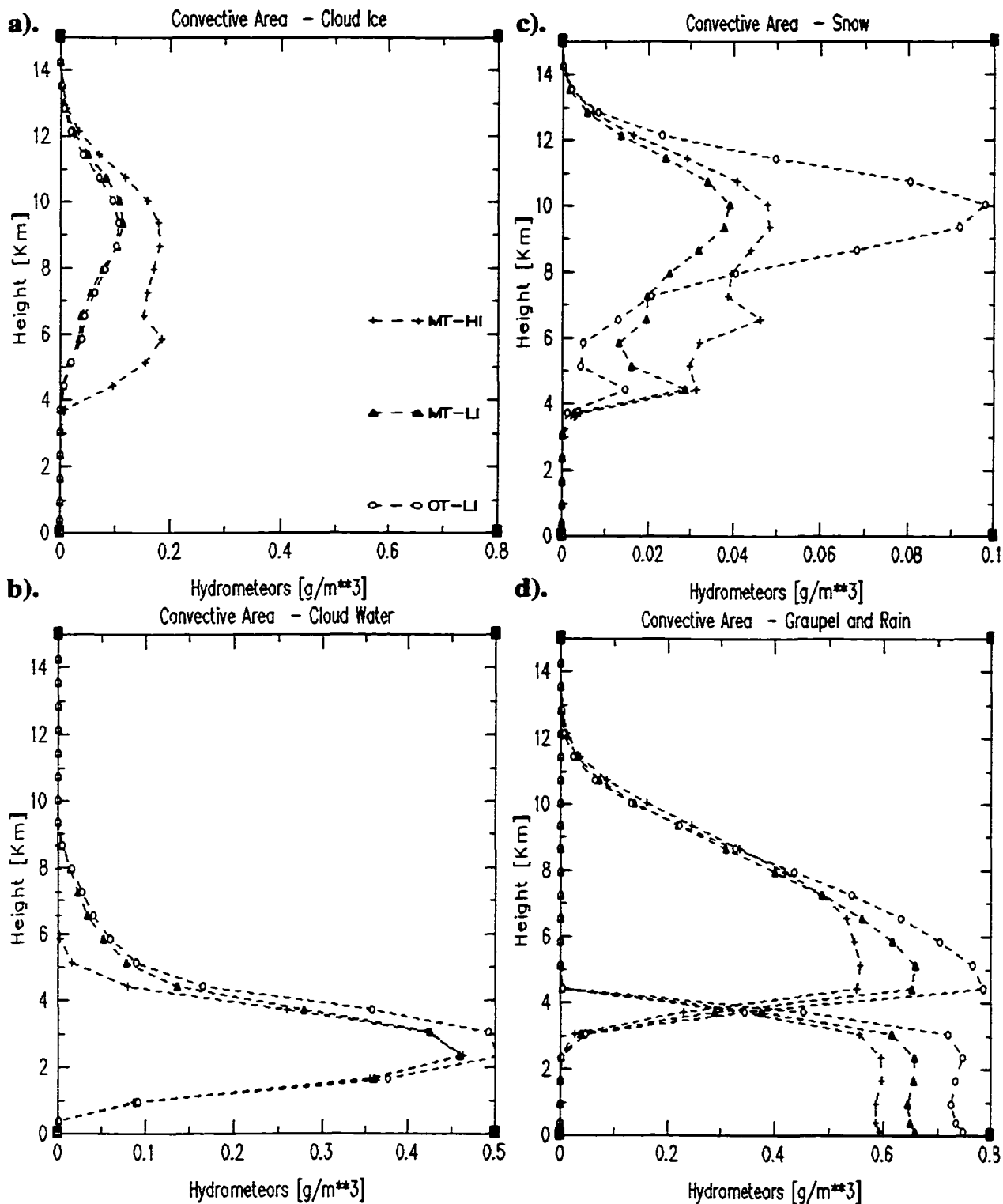


Figure 2.5. Mean vertical profiles of hydrometeors (g/m^3) over the convective (a)–(d) and the stratiform (e)–(h) area. The means were computed over the period from 5:40 to 7:50 hours model time that presents the mature stage of the simulated storms. The results from the three simulations that used Tao's microphysics (OT-LI, MT-LI and MT-HI), are presented in one plot in the following manner: (a) and (e) – cloud ice; (b) and (f) – cloud water; (c) and (g) – snow; and (d) and (h) – graupel and rain.

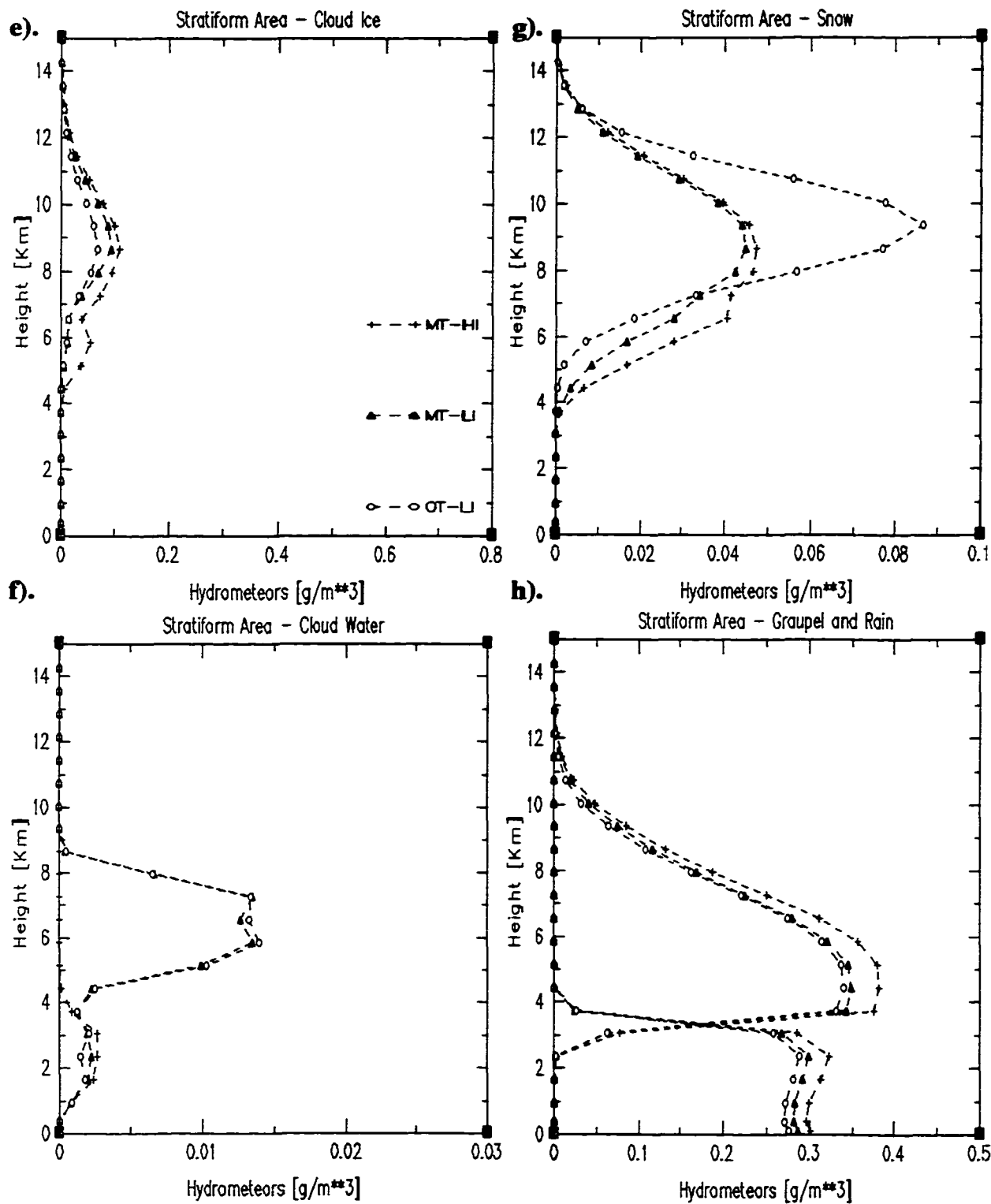


Figure 2.5. (Continued)

the Bergeron processes, which in Tao is allowed to happen at all levels and even in the absence of cloud water, represents a constant sink for cloud ice; ii) as already mentioned, the very large NCIO that was used in MT–HI simply represents an environment with sufficient amount of cloud ice nuclei to absorb all the excess water vapor provided by the updrafts. This apparently kept the vapor pressure below water saturation and, thus, prevented the condensation of supercooled cloud water in the mixed–phase regime (see Fig. 2.5b). While the supercooled cloud water production is affected mainly by the NCIO selection, the amount of cloud water below the freezing level is affected mostly by the choice of the threshold for autoconversion from cloud water to rain (QCWO). Indeed, the OT–LI simulation, which used a higher threshold for autoconversion (see Table 2.2) than the other two simulations, had more cloud water at levels below melting than the two other. Moreover, the two simulations which used an equal QCWO threshold (MT–LI and MT–HI), had also equal amounts of cloud water below melting.

Figure 2.5c reveals the complex structure of the area and time–averaged vertical profiles of the snow field. Clearly, the OT–LI simulation stands out with its high values and elevated peak (about 10 km altitude). Indeed, as it will be shown later, the OT–LI simulation produced the most upper–level snow from all six simulations. Hence, while increasing the NCIO values from MT–LI to MT–HI case (and the associated increase in cloud ice production) lead to an increase in the snow amounts, this increase was not very big and the shape of the profile remained rather unchanged. In contrast, when the collection efficiencies and the threshold value for autoconversion from cloud ice to snow (QCIO) were changed between MT–LI and OT–LI, both the magnitude and the shape of

the profile changed rather dramatically. In OT-LI the collection efficiency for snow collecting cloud ice was much higher than that in the other two simulations. This, in addition to an easier autoconversion from cloud ice to snow (as a result of the lower QCIO) apparently stimulated the production of snow. However, maybe even more important for determining the snow profile, is the fact that the collection efficiency for graupel collecting snow is temperature (and, hence, height) dependent as opposed to the constant collection efficiency used in the other two simulations. This temperature-dependent collection efficiency is lower than the constant one at temperatures $< -25^{\circ}\text{C}$ and higher at warmer temperatures, increasing rapidly from -0.2 at -17°C to 1 at 0°C . The -25°C is located at about 8.5 km in the convective area. Hence, the high values of snow at levels above 9 km and the dramatic decrease in the snow amounts at levels below 9 km can both be explained with a low collection efficiency for graupel collecting snow at upper levels and a sharp increase in the collection efficiency at levels closer to melting. This interpretation is further supported by the fact that in the two Tao simulations in which the snow to graupel collection efficiency was set to 0.1 (MT-LI and MT-HI) the higher concentrations of snow extended to lower altitudes than in the OT-LI run.

Another interesting feature of the mean convective area snow profiles is the tendency for multi-peak structure which is especially well illustrated in the two low NCIO (low cloud ice) cases. In these two cases, the lower-level peaks are found at altitudes just above melting where supercooled cloud water is abundant. Apparently, the two processes which are responsible for the production of the lower-level peaks are the

increase in the Bergeron growth for snow in the presence of cloud water and the accelerated growth of snow by riming (accretion of cloud water).

The convective area graupel and rain fields (Fig. 2.5d) show significant sensitivity to the choice of parameters. The precipitation is most intense when supercooled cloud water is produced and the collection efficiencies near freezing are high (OT-LI). Selecting lower values for the NCIO and the collection efficiencies (the MT-HI case) resulted in about 25% reduction of the maximum graupel and rain amounts (Fig. 2.5d). When only the collection efficiencies were decreased from the OT-LI values to the the MT-LI (keeping the OT-LI choice for NCIO), the resultant maximum graupel and rain amounts were decreased from the OT-LI values by ~18%. This indicates that both the collection efficiencies and the NCIO selection play a very important role in determining the mean intensity of the convective region. Furthermore, by altering the QCWO parameter the ratio of graupel-to-rain can be altered. Having lower QCWO facilitates the rain production at the expense of the graupel and changes the ratio in favor of more "warm rain" production (i.e. production of rain without production of graupel). However, note that this effect is very small, at least for the choice of QCWO values used here.

The stratiform area mean hydrometeor profiles (Figs. 2.5e-h) exhibit the same main features observed in the convective area. Again, low NCIO simulations that produced relatively smaller amounts of cloud ice in the mixed-phase regime had relatively high concentrations of supercooled cloud water. Of course, the weaker updrafts typically associated with stratiform rain regions (e.g. Biggerstaff and Houze

1991, 1993) created lower supersaturations and led to cloud water concentrations that were an order of magnitude less than those found in the convective region.

The mean snow profiles exhibit a more simple structure in the stratiform region (Fig. 2.5g) compared to the multi-peak distribution found in the convective region (Fig. 2.5c). Continuous growth of snow through vapor deposition and collection of cloud ice smoothed the vertical distribution in the stratiform region. Moreover, the Bergeron growth processes for snow and the accretional growth of snow were less active since the supersaturation rates and the cloud water contents were lower. Consequently, the snow distributions decrease monotonically from their upper-level peak values.

Note that the more intense the convective area precipitation (graupel and rain) the less intense the stratiform area precipitation (compare Figs. 2.5d and 2.5h). Hence, when the setup favors more fallout of condensate in the convective area, less is transported back into the stratiform area and its intensity decreases even though its size does not change much. On the other hand, the biggest and most intense stratiform area is produced when cloud ice production is favored over that of supercooled cloud water and, as a result of that the convective area precipitation is least intensive (MT-HI). In that case it is likely that more of the convectively produced cloud ice and snow are transported backward from the convective area and fall off as precipitation in the stratiform area. What might have also helped the increase in stratiform area size and intensity in the two modified cases (MT-LI and MT-HI) is that these two cases had also a higher collection efficiency for graupel collecting snow at upper levels (above the -25° C temperature level) where significant amounts of snow are being produced. This, coupled with the increased amounts of cloud ice and snow produced in the high NCIO

case (MT–HI) apparently led to the production of the biggest and most intense stratiform area. Interestingly, the increase in size of the stratiform area is associated with increase in size of the convective area as well, despite its weaker intensity. This suggests that the stratiform area precipitation, and the associated cold pool generation, play a significant role in determining the size of the system.

2) Comparison among the three Ferrier simulations

Figure 2.6 a–h presents the area and time–averaged mean hydrometeor profiles in the convective and stratiform area of the three Ferrier simulations. The first and most striking difference from the three Tao simulations is in the amount and the vertical distribution of the cloud ice (Fig. 2.6a). Ferrier produced large amounts of cloud ice with a single maximum located at ~10 km altitude. In contrast, Tao produced smaller amounts of cloud ice with a tendency for a more complex vertical profile (i.e. double maximum). Another, very important difference from the Tao simulations is that the three Ferrier runs show stronger sensitivity of the cloud ice to the choice of the microphysical parameters. Indeed, increasing the NCIO from the MF–LI values to that of MF–HI led not only to doubling of the maximum values but also to the production of a deeper layer of cloud ice (see the difference between the two profiles at levels below 8 km). The OF–HI run had practically no autoconversion to snow and very low upper–level collection efficiencies. Hence, the amount of cloud ice was only limited through the production restrictions (and ultimately by the NCIO selection which was also very high). Because of that, it is no surprise that OF–HI produced double the amount of the MF–HI case and an order of magnitude more cloud ice than the MT–LI run.

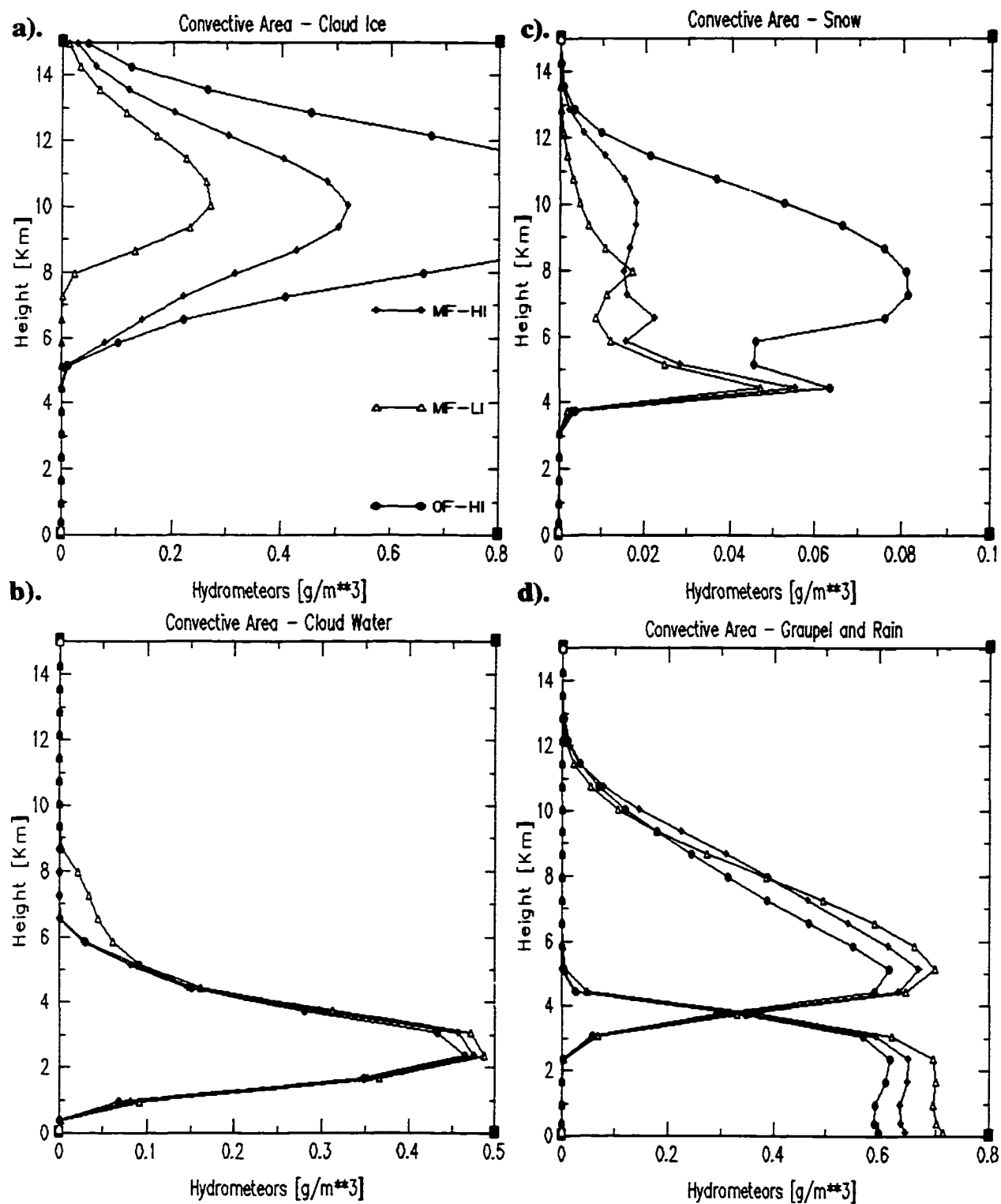


Figure 2.6. Same as in Fig. 2.5 except for presented are the results from the three simulations that used Ferrier's microphysics (OF-HI, MF-LI and MF-HI).

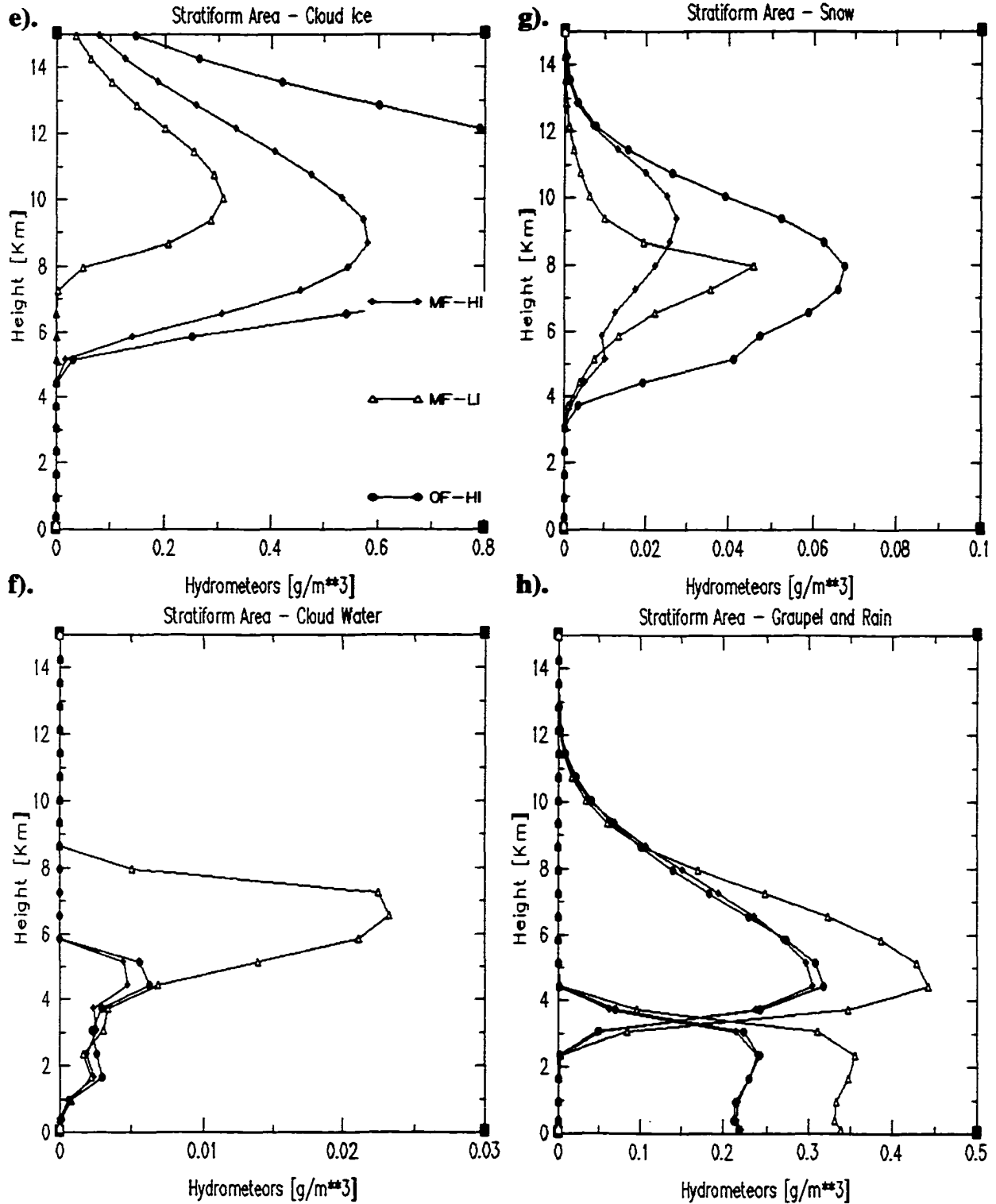


Figure 2.6. (Continued)

As in the three Tao simulations, the amount of the supercooled cloud water in Ferrier (Fig. 2.6b) was also controlled by the choice of the NCIO parameter. The selection of higher NCIO values assured that there will be enough ice crystals to absorb most of the available ice-supersaturated water vapor in the mixed-phase regime and to significantly decrease the condensation of cloud water (and even totally prevent the water condensation at levels above 6.5 km).

Inspection of the snow field (Fig. 2.6c) reveals that the OF-HI run produced the most upper-level snow of the three simulations despite the fact that the snow production rates were very inefficient (practically no autoconversion from cloud ice and very low efficiency for snow collecting ice). This clearly suggests that the high amounts of snow that were found in the OF-HI case are a reflection of low rates of conversion to graupel (small sink terms), namely the low efficiency for graupel collecting snow at upper levels. Indeed, this also explains why OF-HI produced also the least amounts of graupel and rain. Coming back to the snow field, when the upper-level collection efficiency for graupel collecting snow was increased (MF-HI), the amount of upper-level snow sharply decreased despite the increased production rate for snow (much lower threshold for autoconversion from cloud ice to snow and higher collection efficiency for snow collecting cloud ice). Incidentally, the decrease in the upper-level snow was accompanied by an increase in the graupel and rain amounts in the MF-HI case.

Modifying the NCIO parameter between MF-HI and MF-LI affected the snow profile more significantly only at levels above 8 km. The lower cloud ice production associated with the lower NCIO value in MF-LI resulted in lower amounts of snow at

these upper levels. This suggests that the primary mechanism for snow production at these levels is through autoconversion and collection of cloud ice. However, at levels below 8 km, where the cloud ice was not even produced in the MF-LI case, the snow field was not affected that strongly. This points to an efficient snow depositional growth processes at these levels, which apparently is able to use all of the ice-supersaturated vapor that is available and not used for cloud ice growth (since the assumed NCIO does not allow the presence of cloud ice at these levels). This is an example of how in Ferrier the different processes compete for the available water vapor.

It should be pointed that the snow profile showed variability from one simulation to another only at levels above 5 km. At levels closer to melting the snow amounts were rather high and very similar for all three Ferrier runs. The similarity is explained to a large degree by the fact that at levels closer to freezing all three Ferrier runs had very similar collection efficiencies. Indeed, even in Tao when the collection efficiencies were the same (MT-LI and MT-HI), the amount of snow at levels just above freezing was also the same. The relatively high values of snow at levels below 5 km are clearly related to the abundance of supercooled cloud water at these levels. This suggests that the Bergeron growth of snow and the accretion of cloud water by snow are the primary processes responsible for the snow production at these levels.

Again, as in Tao, the convective area graupel and rain (Fig. 2.6d) are most intense when supercooled cloud water is produced and the collection efficiencies are higher (MF-LI). The shape of the graupel profile is affected by the interplay (partitioning) among the cloud ice, supercooled cloud water and snow. When the autoconversion thresholds and collection efficiencies are set the same (MF-HI and MF-

LI), having more cloud ice leads to the production of more upper-level snow and less supercooled cloud water. This, in turn leads to increased graupel amounts at upper levels, due to the snow abundance, and decreased graupel amounts at levels closer to melting, where the absence of supercooled cloud water diminishes the graupel growth. Production of rain is highest when the production of graupel is maximized at levels closer to melting, and, hence, when supercooled cloud water is present.

Noteworthy is the fact that that the three Ferrier simulations did not differ much in their graupel production. This is likely due to the following two reasons: i) at levels close to freezing all three simulations had very similar collection efficiencies; ii) all three simulations produced significant amounts of supercooled cloud water at levels just above freezing (~ 5 km) since the choice of the NCIO was such that even the high value (619 m^{-3}) was not large enough to assure that no cloud water will be produced there. In Tao, on the other hand, the MT-HI case used a very large NCIO and the cloud water production was severely limited at levels just above freezing. The absence of supercooled cloud water clearly led to the very negligible graupel growth in the mixed phase regime in the MT-HI case that is evident from the flat maximum found between 5 and 7 km (Fig. 2.5d) as compared to the more peaked 5 km maximum found in all other simulations.

The stratiform area profiles (Fig. 2.6 e-h) exhibit the same main features and sensitivity in the cloud ice and the cloud water fields that were observed in the convective area. Furthermore, it should be pointed, that like in Tao the cloud water was found in very limited amounts. However, in contrast to the Tao stratiform area where the cloud ice was also in very limited amounts and showed almost no sensitivity to the

choice of parameters (the three simulations had almost the same amounts), in Ferrier the cloud ice shows sensitivity and is found in significant amounts that even exceed those found in the convective area.

The stratiform area snow field (Fig. 2.6g) gives an even better illustration (as compared to the convective area one) of the competition between the cloud ice and the snow depositional growth for the available vapor. Indeed, when cloud ice is produced in big amounts (MF–HI), snow production is increased but only at levels above 9 km. At lower levels, the snow production is higher when there is little cloud ice to compete with for the ice–supersaturated vapor. This leads to a peak at 8 km altitude and a sharp decrease below.

The stratiform area graupel and rain fields (Fig. 2.6h) present two somewhat unexpected results. The first one is that, unlike in Tao, a more intense convective area in Ferrier is not necessarily associated with less intense stratiform area! Indeed, the stratiform area is also most intense when the convective area is most intense, i.e. when supercooled cloud water is present (MF–LI). This most intense stratiform area is, however, intermediate in size between the OF–HI and the MF–HI realizations (see Fig. 2.4b). The associated anvil area is also very small (Fig. 2.4c). Hence, in Ferrier, the size and the intensity of the stratiform area depend not only upon the convective characteristics but are also determined by the growth processes which take place in the stratiform area itself. More specifically, in Ferrier, the additional processes for graupel formation (depositional growth of graupel and snow collecting cloud water and producing graupel) alter the structure of the stratiform area in such way that when supercooled cloud water is present, graupel is rather quickly generated and that leads to

the production of rather intense even though not very extensive stratiform area. Apparently, these additional growth mechanisms allow for quick precipitating out of the snow and this limits the extent of both the stratiform area and the non-precipitating anvil. The condensate falls out closer to the convective area and this likely leads to the production of comparatively strong cold pool that apparently is sufficient to force significantly large convective area.

The second point worth making is that the two HI cases (OF-HI and MF-HI) which had different collection efficiencies and auto-conversion rates produced stratiform areas with very different sizes but with the same intensity! Apparently, increasing the collection efficiencies and speeding-up the auto-conversion from cloud ice to snow in MF-HI helped increase the precipitating out of the condensate. But, with no-additional processes at play (no increase in the supercooled cloud water), the mean graupel and rain fields remained the same. Simply more cloud ice and snow were converted to graupel and rain and this lead to the increase in the area of stratiform precipitation.

3) Comparison between the Ferrier and Tao simulations under the same parameters

When run with the exact same set of microphysical parameters (MT-LI and MF-LI), the two schemes produce different simulations (Fig. 2.7a-h). In terms of mean convective area characteristics, the fundamental differences are in the amounts and the vertical distributions of cloud ice and snow. Tao produces a deeper layer of cloud ice that extends to lower levels than Ferrier. This can be attributed to the water-ice saturation adjustment technique used in Tao which always generates some cloud ice at

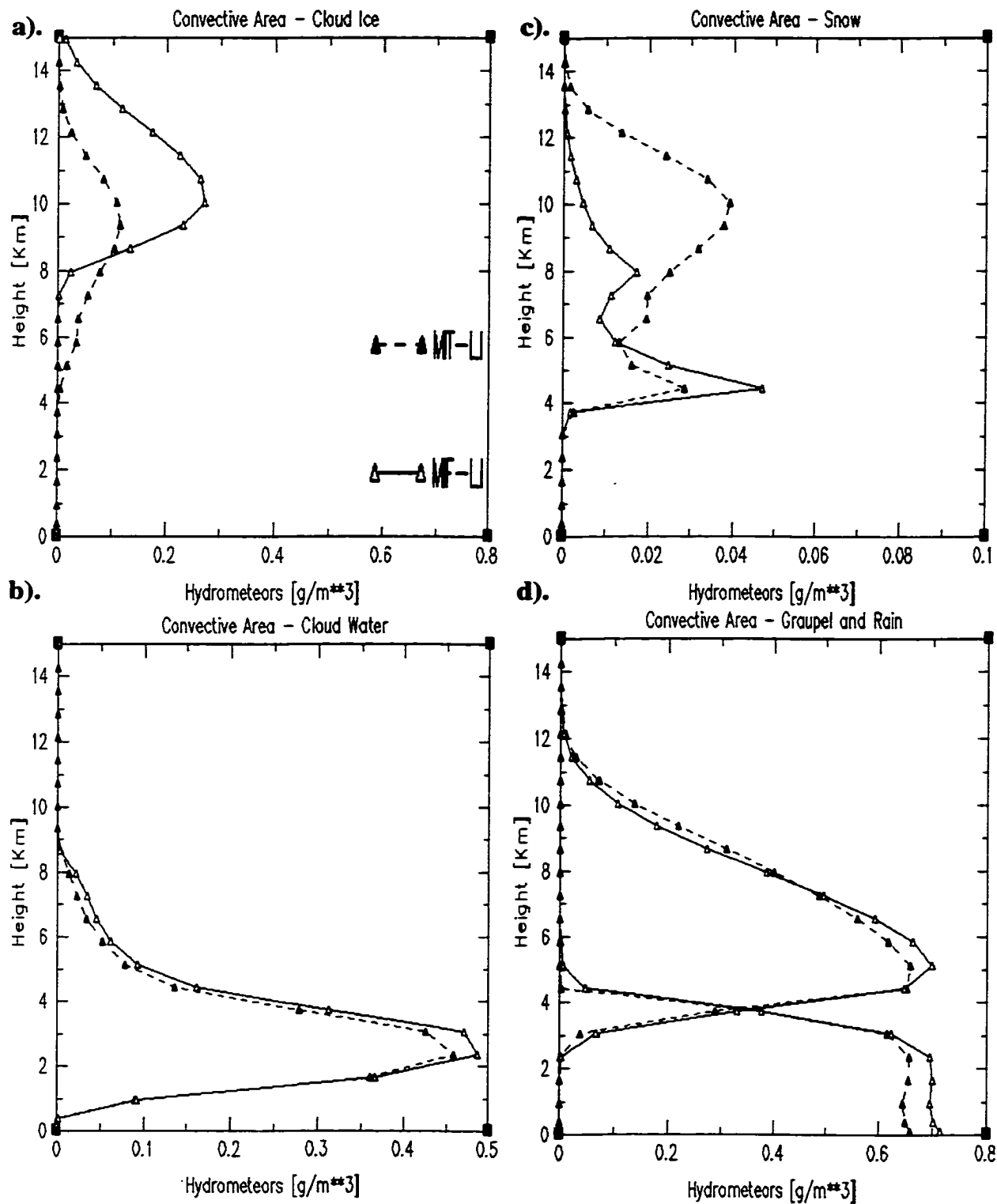


Figure 2.7. Same as in Fig. 2.5 except for presented are the results from the two simulations that were initialized with the exact same microphysical parameters but used different microphysical parameterization schemes (MT-LI and MF-LI).

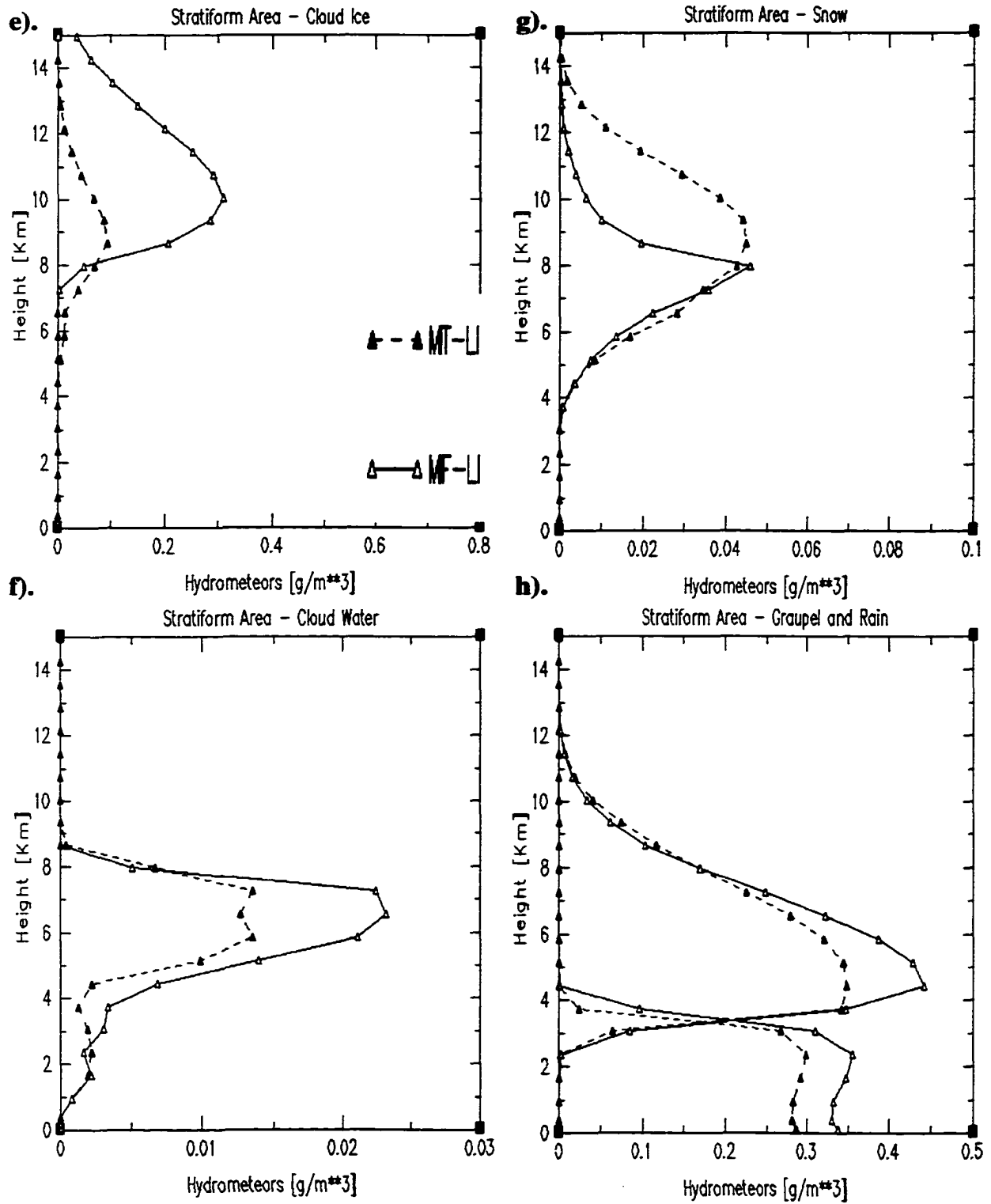


Figure 2.7. (Continued)

levels close to freezing even when the assumed NCIO is rather low (here 10^{-2} m^{-3}) and cloud ice should not be initiated according to the other mechanism for cloud ice initiation that is common between Ferrier and Tao. In contrast, in that case Ferrier does not generate or grow cloud ice at levels below 8 km.

While Tao has a deeper layer of cloud ice, the maximum amount of cloud ice is smaller in Tao but the upper-level snow amount is larger. Both of these features can be attributed to the Bergeron growth for snow which in Tao works without regard of whether or not cloud water is present and, hence, constantly converts cloud ice into snow. In Ferrier this growth happens only when cloud water is present and, because of that, is apparently very limited at levels above 8 km. At levels just above melting Ferrier produces more snow. This is probably aided by somewhat faster Bergeron growth rates in Ferrier (higher values of the temperature-dependent coefficients). However, the primary reason for the difference is that Ferrier likely produces more supercooled cloud water since it does not produce cloud ice in this region. With more cloud water being available, both the Bergeron growth of cloud ice to snow and the accretional growth of snow are further invigorated.

The convective area precipitation intensity is rather similar. Still, Ferrier produces slightly more precipitation than Tao at levels below 8 km and less at upper levels. This can again be attributed to the fact that Ferrier probably has higher production rates of supercooled cloud water than Tao (which is constantly producing cloud ice) and, hence, the graupel growth at lower levels is favored in Ferrier. On the other hand, the higher amounts of upper-level snow in Tao are probably responsible for

production of more upper-level graupel. Both the higher graupel and snow amounts at upper levels will lead to the simulation of higher upper-level reflectivity.

While the differences between the two microphysics in the stratiform area cloud ice and snow fields are similar to that in the convective area, the differences in the graupel, rain and the cloud water fields are more pronounced in the stratiform area as compared to that in the convective area. In particular, Ferrier produces significantly more intense precipitation and has almost double the amount of the supercooled cloud water found in Tao. This can be attributed to two factors. First, in Ferrier (MF-LI) less water vapor is used in the convective area since less cloud ice is produced and, hence, the water vapor is probably close to water saturation values at levels below 7 km. In MT-LI cloud ice is continuously produced at levels above freezing, leaving the water vapor at values closer to ice-saturation as compared to that in MF-LI and this should result in less water vapor being transported back in the stratiform area. Hence, MF-LI having more water vapor in the stratiform area is in a more favorable situation for additional cloud ice initiation and depositional growth in the stratiform area. This should lead to the release of more latent heat and the subsequent stronger vertical velocity and, hence, production of more supercooled cloud water. The increased supercooled cloud water and ice supersaturated vapor would, in turn, lead to increased growth of graupel, which in Ferrier should be even faster than that in Tao because of the two extra graupel growth mechanisms that Ferrier has. Second, in Tao (MT-LI) the area of the stratiform precipitation is bigger than that in MF-LI. This is likely due to the fact that in Tao the snow production is always larger (cloud ice is continuously grown and converted to snow via the Bergeron growth which works all the time) and,

hence there is larger area over which stratiform precipitation is produced. Hence, the smaller mean represents an average over larger but less intense area as compared to that in MF-LI.

4) Comparison between the Ferrier and Tao simulations under the HI conditions

The two modified high ice (HI) cases of Ferrier and Tao (MT-HI and MF-HI) cannot be closely compared since they used different NCIO in their closer to freezing levels, with Ferrier having lower NCIO between 0 and -10° C. This apparently led to the production of more supercooled cloud water and the subsequent enhanced production of graupel in the convective area of Ferrier MF-HI case as compared to MT-HI which has the lowest mean convective graupel amounts among all six simulations. Still, the differences in the mean convective rain rates of MT-HI and MF-HI are comparatively small.

Furthermore, the two simulations have rather comparable sizes of their convective, stratiform and non-precipitating anvil areas and of their convective area fraction. However, even though MF-HI produced the largest stratiform area of all three Ferrier simulations, MT-HI still produced a 20% larger stratiform area with about 36% more mean surface rain than MF-HI. Indeed, the convective rain fraction of MT-HI (~50%) is about 17% lower than that of MF-HI (close to 67%) – a further indication of the intensity of the MT-HI stratiform area. This can be to the fact that a lot less snow (and subsequent precipitation) is being produced in the MF-HI stratiform area as compared to that in MT-HI due to the differences in the treatment of the Bergeron processes.

Considering all six simulations, it is important to note that in terms of area-averaged surface rain, the net effect of the different microphysical parameterizations leads to about 25% variability in mean rainfall over the convective area and close to 50% variability in the mean stratiform rain. Even for the set of simulations in which the microphysical realizations created storms of nearly the same size (MT-HI and MF-HI), the mean stratiform rainfall differed by about 36%. Given the smaller size of the OF-LI storm and the weaker average rain amount, it is clear that quantitative precipitation forecast will be limited by uncertainty in cloud model microphysical parameterizations.

c. Mean vertical velocity and latent heating profiles

Figures 2.8a-d and 2.9a-d present the mean area and time-averaged profiles of vertical velocity, divergence and latent heating computed over the convective and stratiform regions of the six microphysical realizations.

A quick inspection of the convective area vertical velocity profiles (Fig. 2.8a) shows that the three Ferrier simulations exhibit higher variability than the three Tao runs. Furthermore, in Ferrier the intensity of the vertical velocity and the height of the velocity maximum appear to be related to the amount of cloud ice that is present. Indeed, the strongest and most elevated vertical velocity maximum is found in the simulation with the highest amount of cloud ice (OF-HI), while the weakest and lowest vertical velocity maximum is found in the simulation with the least amount of cloud ice (MF-LI). While the variability in the height of the maximum is not that big, the variability in the intensity is ~ 25%. In Tao, it appears that the height of the maximum is invariable and its intensity varies only by about 18%. Another difference from the Ferrier runs is that in Tao the strongest mean vertical velocities are not found in the

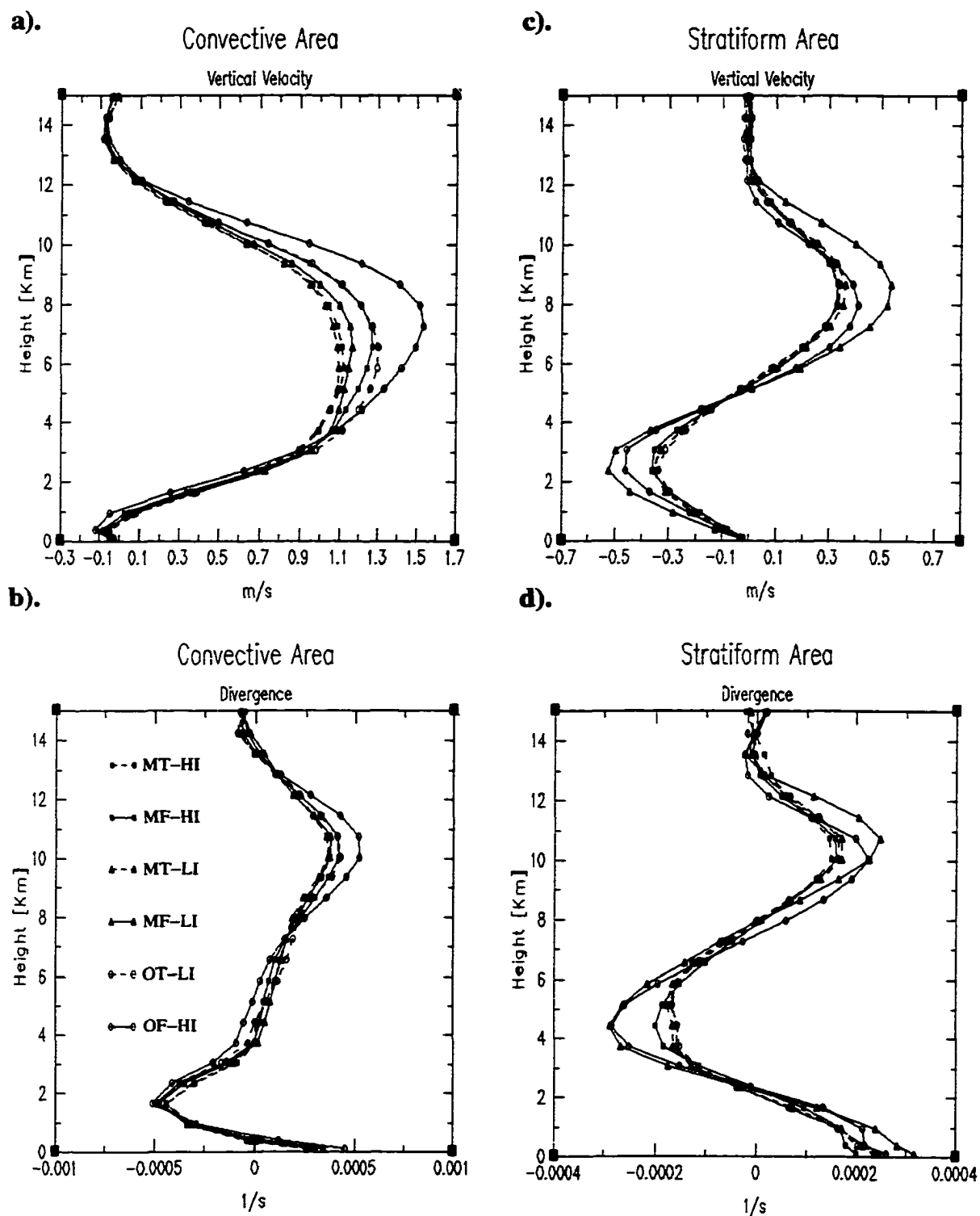


Figure 2.8. Mean vertical profiles of vertical velocity (m/s) computed over the mature stage (5:40–7:50) of the simulated storms for each of the six simulations and computed separately over the (a) convective and (c) stratiform regions. Mean vertical profiles of divergence (1/s) computed over the convective (b) and the stratiform (d) regions.

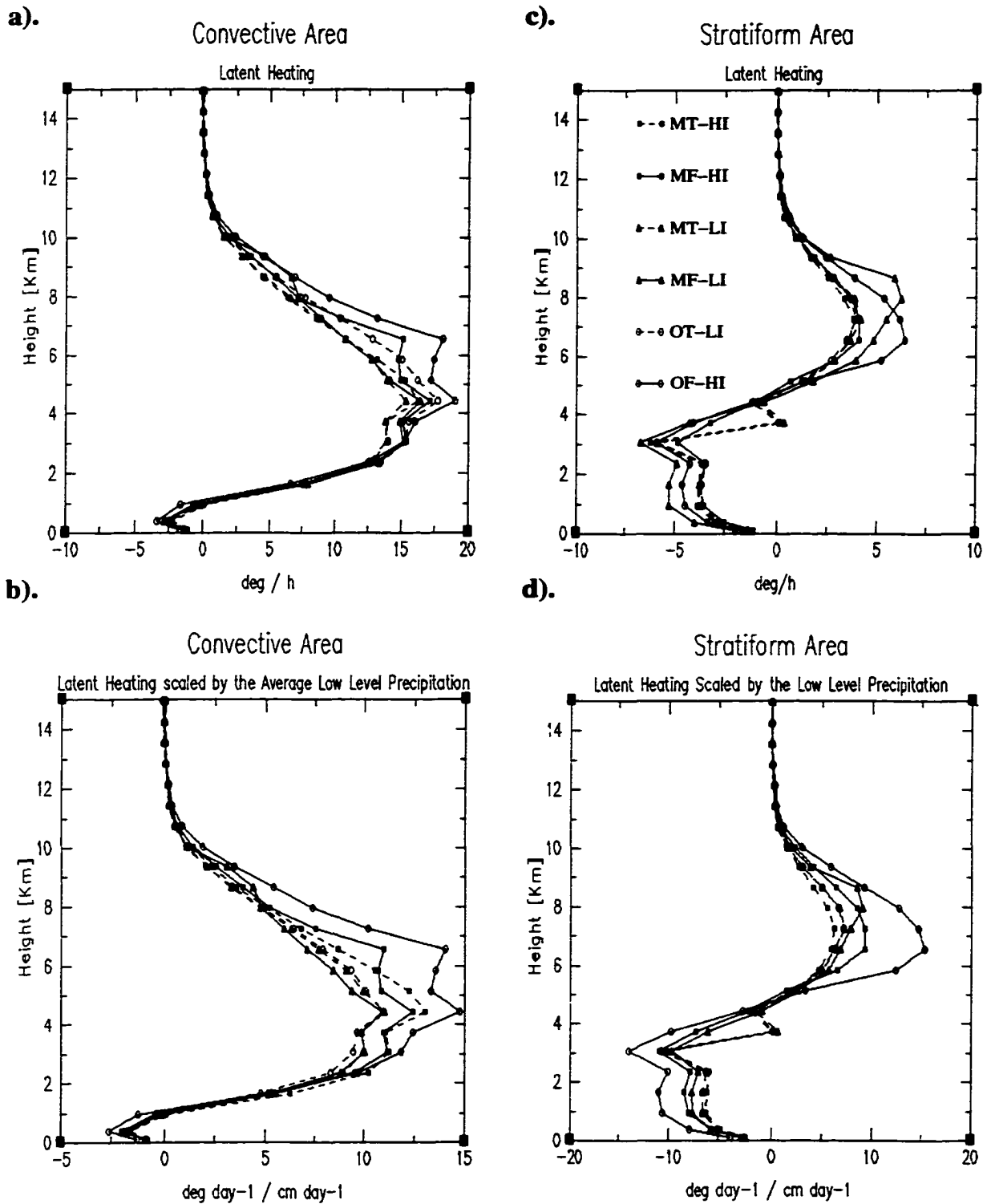


Figure 2.9. Same as in Fig. 2.8 except for presented are the area and time-averaged means of latent heating (a) and (c) and latent heating scaled by the average precipitation in the lowest 2 km – (b) and (d).

simulation with the most cloud ice (MT-HI) but in the simulation with the highest graupel production (OT-LI). The two modified Tao runs had almost identical mean vertical velocity profiles.

The stratiform area vertical velocity profiles (Fig. 2.8c) show again that Ferrier's scheme is much more sensitive to the choice of parameters than Tao's. An interesting point is that the low ice case simulation (MF-LI) that produced a somewhat lower-level vertical velocity maximum in the convective area is associated with a more elevated maximum in the stratiform area. This is an indication that in the MF-LI case the depositional growth of cloud ice is probably happening at upper levels and is also quite intense.

Considering all six simulations, OF-HI produced the most intense and elevated vertical velocity maximum in the convective area, while MT-HI and MT-LI produced the weakest. The difference in intensity was ~36%. In the stratiform area, MF-LI produced ~48% more intense mean vertical velocities than the three Tao simulations, including the one which was run with the exact same set of parameters. The MF-HI run came closest to the three Tao runs in terms of mean stratiform area vertical velocity. Note that it also produced the most similar system in terms of size. However, the mean stratiform precipitation intensity of MF-HI was much weaker than that of the three Tao runs.

The vertical velocity field in convective storms represents the response of the atmosphere to the buoyancy production that is associated with the latent heat released during the phase changes of water. Hence, an inspection of the mean latent heating profiles can provide a better appreciation of the causes for the differences in the mean

vertical velocity profiles and a more direct way of relating these differences to the way the microphysical parameterizations work. Furthermore, a good understanding of how the latent heating profiles are related to the hydrometeors fields which are associated with them is of crucial importance since these relationships form the basis for the retrieval of latent heating (and the so-needed vertical velocity and divergence fields) from remote-sensing observations of precipitation.

We will look at the latent heating profiles in two different ways – in terms of area and time-averaged (Figs. 2.9a and 2.9c, referred to as "mean profiles") and in terms of averages scaled by the mean precipitation in the lowest 2 km (Figs. 2.9b and 2.9d, referred to as "mean precipitation-scaled profiles"). Before we go on to discuss the details of the latent heating profiles we would like to point out that all six simulations produced the classically shaped convective and stratiform mean heating structures as described by Houze (1982). Comparison of the mean convective area latent heating profiles of the three Tao simulations shows that the largest area average is produced by the OT-LI case while the MT-LI case produces about 16% less heating at all levels (up to 2.5 deg/h difference at 5 km). The graupel production in both of these runs is aided significantly by the presence of supercooled cloud water. However, in the OT-LI case this processes is probably further invigorated by the higher efficiency of graupel collecting snow (as already discussed) and this more intense graupel production translates into higher heating rates. Here the increased latent heat release is directly associated with the production of precipitation size particles (graupel and rain). Because of that, when scaled by the low-level precipitation, the two runs (which also had the exact same mean cloud ice profiles) produce the exact same latent heating by unit near-

surface rain (Fig. 2.9b). This is not the case when the production of more cloud ice is allowed (in the MT–HI case). This increased production of cloud ice does not change by much the mean heating profile but it does increase the mean precipitation–scaled heating profile, reflecting the fact that latent heating is produced during the cloud ice growth even though precipitation–sized particles might not be produced. This point is further illustrated by the three Ferrier profiles. Indeed, as more cloud ice production is allowed in Ferrier (MF–LI compared to MF–HI compared to OF–HI), the difference between the mean precipitation–scaled heating profiles grows faster than that between the mean profiles. The three Ferrier runs show another feature not observed in Tao. While in Tao the shape of the heating profiles did not change between the simulations and only the magnitude did, in Ferrier both the magnitude and the shape changed. The simulations which had higher cloud ice amounts (MF–HI and OF–HI), also had a more complex convective heating profile with a secondary maximum found at the base of the cloud ice layer (~ 6 km altitude where cloud ice was rapidly increasing). Furthermore, this upper–level heating maximum was proportional in intensity to the amount of cloud ice at these levels. For example, the OF–HI simulation had a more intense upper–level heating than the MF–HI simulation, even though the two runs assumed the same NCIO and, hence, allowed for the same amount of cloud ice initiation. This clearly suggests that this upper–level maximum is related not only to the cloud ice initiation but also to its growth. Indeed, the OF–HI simulation resulted in significant accumulation of cloud ice at upper levels due to its low efficiency of conversion to snow, graupel and rain. This apparently facilitated a more intense cloud ice depositional growth and led to the increase of the latent heating both in terms of a mean and, even more so, in terms of a

precipitation–scaled mean.

The stratiform area heating profiles show one more time the most important features observed in the convective area, namely: i) the fact that the stratiform area heating in Tao does not change between the three simulations; ii) the much higher variability in the heating profiles characteristic for the Ferrier runs; iii). the tendency for Ferrier to produce more intense heating profiles.

The fact that the three Tao simulations did not exhibit strong sensitivity to the choices affecting the cloud ice fields could be explained by the following reasons: i) in Tao cloud ice is never present in big amounts due to its continuous depletion and conversion to snow via the Bergeron process. This limits the cloud ice depositional growth and the associated elevated heating. Furthermore, depositional growth of snow does not help much since snow is also found in very small amounts and the depositional growth is considered last from all microphysical processes; ii). as a consequence of the ice–water saturation adjustment, cloud ice is always grown in Tao regardless of the assumptions for the availability of ice nuclei. This assures that the latent heating associated with the cloud ice initiation will not vary a lot from one simulation to another since the cloud ice initiation does not vary that much. It also assures that the level of maximum heating will not change much.

The stronger sensitivity to the microphysical parameters shown by the Ferrier–produced heating profiles is related to the fact that Ferrier allows for significant amounts of cloud ice to remain as such and not to be converted into precipitation–sized particles. Since upper–level latent heating is related to the depositional growth of cloud ice, the more cloud ice there is, the stronger the upper–level heating even though the surface

precipitation is reduced. Hence, if two realizations have different precipitation efficiency they will also have different mean and precipitation-scaled mean profiles. Indeed, while OF-HI and MF-HI have the same precipitation intensity (same mean graupel and rain amounts), OF-HI has a lot more upper-level cloud ice in the mean. This leads to the production of a latent heating profile that has a lot more upper-level heating for nearly the same mid-to-low level cooling (Fig. 2.9c) and, hence, more upper-level heating per unit near-surface precipitation (Fig. 2.9d). This situation illustrates an important limitation on the accuracy of the latent heating retrievals from microwave observations of precipitation. It suggests that without a proper account for the precipitation efficiency of the observed systems, our latent heating estimates will be impaired since the observations are not sensitive to the cloud ice amounts that are closely related to the upper-level latent heating in both the convective and the stratiform areas.

A second limitation in the retrieval of latent heating profiles comes from the fact the vertical distribution of the cloud ice is not known from observations. At the same time, the Ferrier simulations illustrate that the height of the maximum heating can vary significantly (up to 1.5 km in the stratiform area between OF-HI and MF-LI) dependent upon at what levels there are ice nuclei in sufficient quantities to allow intense cloud ice initiation and growth. When significant amounts of cloud ice nuclei are present at lower levels (just above 6 km in the MF-HI and OF-HI cases as illustrated by the sharp increase in the cloud ice amounts at this altitude), this is where the maximum stratiform heating is found. On the other hand, when the environment has a more limited supply of ice nuclei (MF-LI), the cloud ice initiation and growth are

more intense only at upper levels (just above 8 km) and this is where the maximum heating level is found. Because of that type of sensitivity present in Ferrier and absent in Tao, when the two microphysical schemes (Tao and Ferrier) are initiated with the same set of parameters (the limited ice nuclei case), their stratiform areas have mean heating maximum at different altitudes. Furthermore, in that case Ferrier produces more intense precipitation-scaled heating at levels above 7 km in the stratiform area even though their convective area heating profiles are very similar. This, as already discussed, is probably related to the fact that in Ferrier, when cloud ice nuclei are not present at lower levels in the convective area, cloud ice is not initiated and less water vapor is used leaving the water vapor at closer to water saturation values. This water vapor is transported backward into the stratiform area and is used there for cloud ice initiation and growth once it reaches high enough levels where more ice nuclei are present. In turn, this additional latent heat release invigorates the stratiform area.

The fact that the two microphysical schemes (Ferrier and Tao) when set with the exact same microphysical parameters produce very similar convective area structures but different stratiform area sizes and mean heating and hydrometeor profiles further illustrates the point that the philosophical differences between the two schemes are important and lead to the simulation of different storms.

The above discussed sensitivity of the storm produced latent heating to the microphysical parameters and schemes that are used in cloud-resolving models suggests that physically based retrievals of heating from microwave observations of precipitation that use cloud-radiation databases should be affected by the assumptions that were made when building these cloud-radiation databases. Both the intensity and the height

of the retrieved latent heating profiles can be affected. In turn, global-scale circulation models have shown important sensitivity to the height and intensity of the diabatic heating produced by tropical convection (e.g. Hartmann et al., 1984; Chang and Lim, 1988; Sui and Lau, 1989).

d. Impact on remotely-sensed characteristics

As it was already shown the microphysical parameterizations impact the structure of the mean hydrometeor profiles. From a precipitation retrieval point of view the important question, however, is how the remotely-sensed characteristics (radar reflectivity and microwave brightness temperatures) are affected and whether similar precipitation structures would result in similar microwave characteristics. If this would be the case then the impact of the microphysical parameterizations on the precipitation retrieval would be negligent even though the different microphysical schemes might simulate different storms. However, if the relationship between precipitation structure and microwave (passive and active) characteristics is not unique in the framework of the discussed microphysical variations, then apparently the microphysical assumptions that went into building the cloud-radiation database would also impact the precipitation retrievals. While in this paper we will not look at the uncertainty of the retrievals, we address the same basic question by investigating the sensitivity of the simulated microwave storm characteristics to the microphysical parameterizations. For that purpose we used the model-generated hydrometeor fields to compute the radar reflectivity in the Rayleigh regime and the brightness temperatures at five microwave frequencies (10.7, 19.35, 22.235, 37.0 and 85.6 GHz) for each one of the six

microphysical realizations. The brightness temperatures were computed at nadir and over an ocean surface.

1) Radar reflectivity

The mean vertical profiles of radar reflectivity (not shown here) exhibit little difference among the six simulations. This is especially true in the convective region. In the stratiform region the difference in the profiles is bigger. The two simulations that encompass the range of the observed variability are the OT-LI and the MF-LI cases. They show differences not only in the intensity but also in the vertical structure of the mean stratiform area reflectivity profiles with OT-LI depicting a lower intensity near-surface precipitation (about 5 dBz smaller reflectivity at levels below 3 km) but higher intensity precipitation at levels above 9 km with a difference of 5 dBz at 12 km altitude. This translates into ~ 0.8 dB/km weaker vertical decrease in reflectivity between the melting level and 12 km altitude in OT-LI than that in MF-LI.

In order to obtain a better appreciation of the variability in the reflectivity structures within each of the six simulations, we used the methodology developed by Yuter and Houze (1995) and known as CFAD (Contoured Frequency by Altitude Diagrams). At each height level the frequency distribution of reflectivity was computed and the reflectivity bin size was 3 dBz. As pointed out by Yuter and Houze (1995), the contours in the CFADs do not represent the percentage of the data points but rather the percentage of points per unit variable per kilometer. In our case, the frequency distributions are contoured every 2% of data per dBz per kilometer. The statistics for the convective and the stratiform regions for each of the six simulations are presented in Figs. 2.10 and 2.11 respectively.

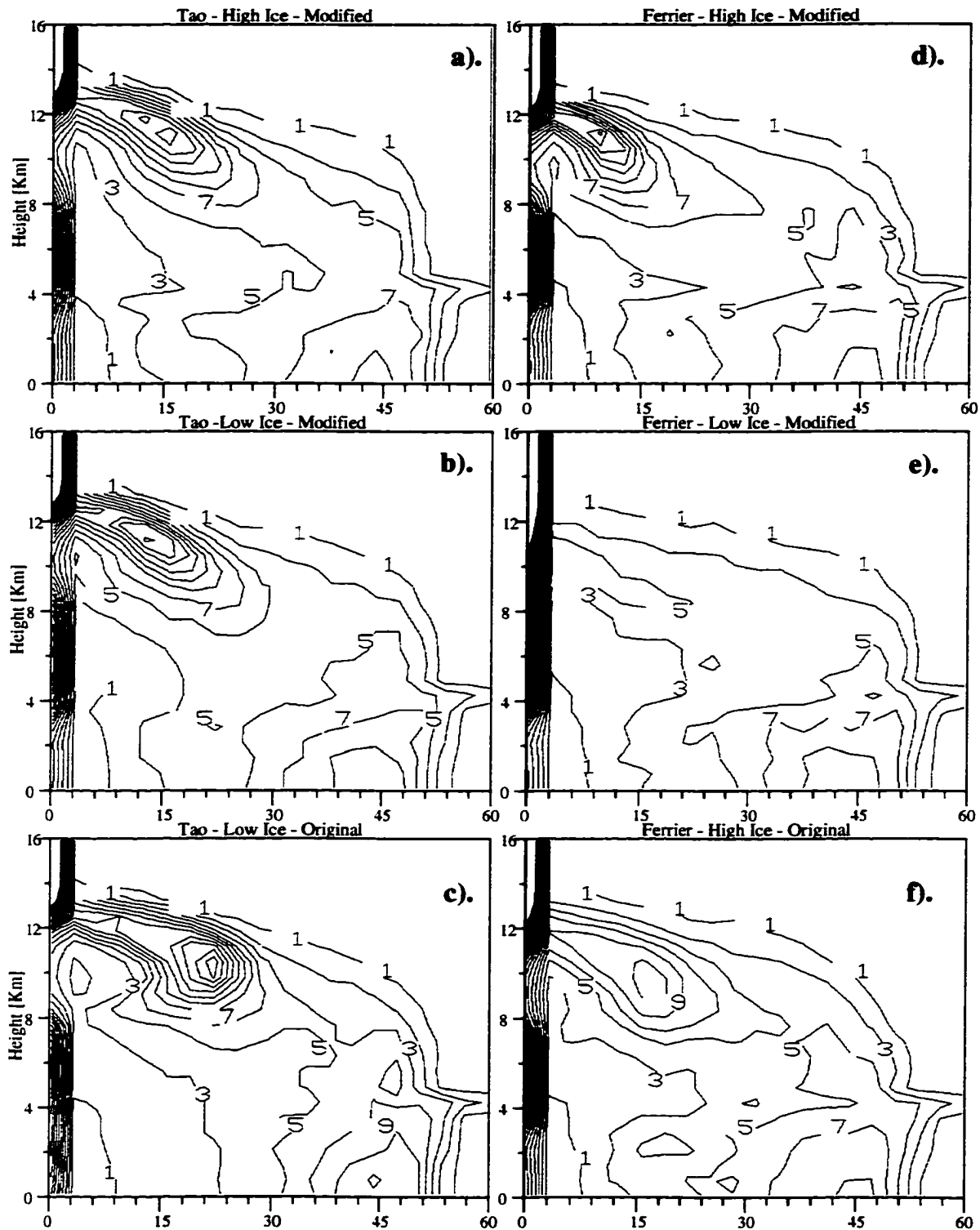


Figure 2.10. Contoured frequency by altitude diagrams (CFADs - Yuter and Houze, 1995) of reflectivity for each of the six simulations: (a) MT-HI, (b) MT-LI, (c) OT-LI, (d) MF-HI, (e) MF-LI, (d) OF-HI. CFAD statistics were computed over the convective area and during the mature stage of the storm. Contours are every 2 % of data per dBz per km. The frequency distribution of reflectivity was computed at each model level (every ~700 m) and the reflectivity bin size was 3 dBz.

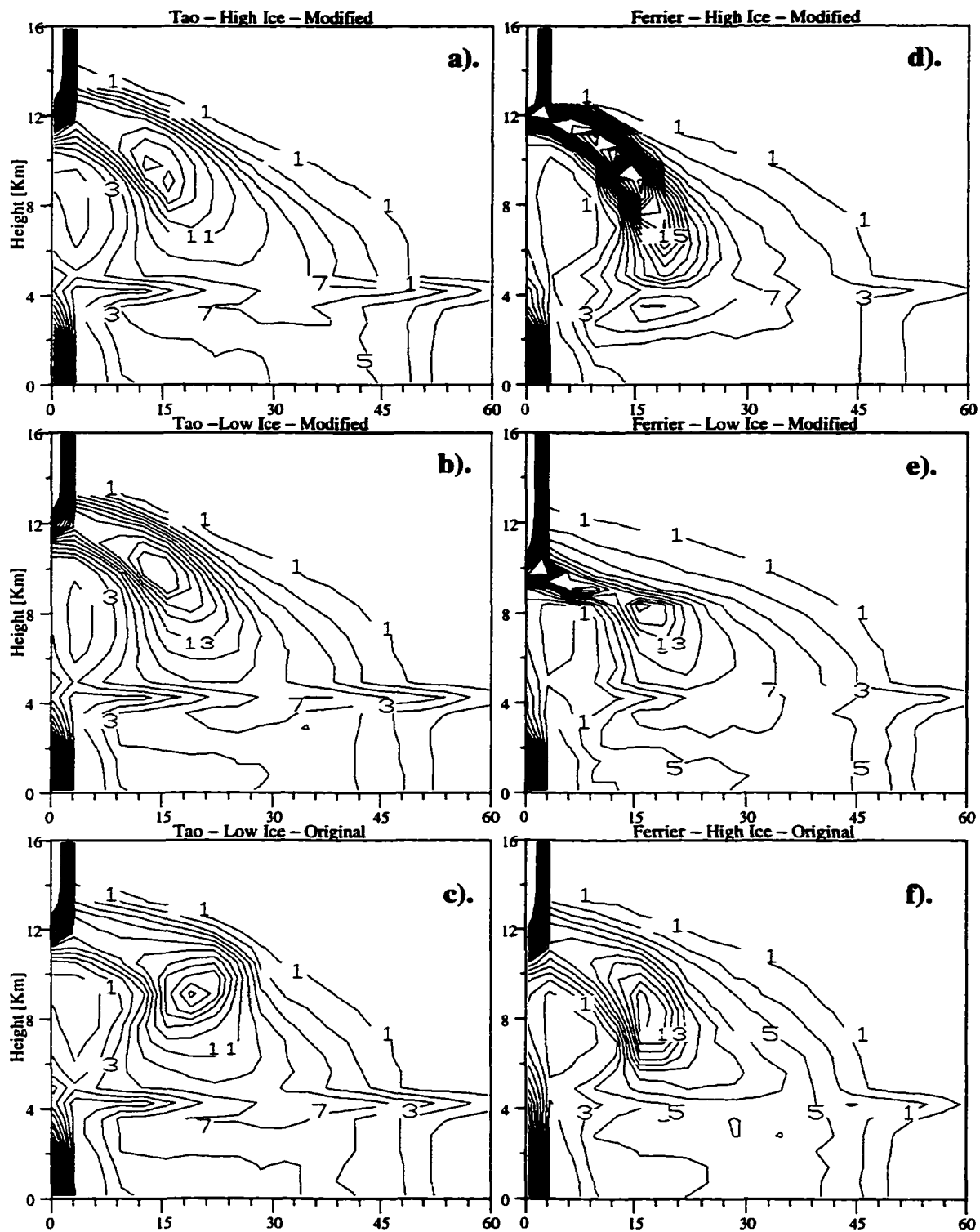


Figure 2.11. Same as in Fig. 2.10 except for CFAD statistics were computed over the stratiform area.

Figure 2.10 reveals that even though the mean convective area reflectivity profiles differed very little between the six simulations, these six simulations had different frequency distributions of reflectivity. The two most different simulations are OT-LI (Fig. 2.10c) and MF-LI (Fig. 2.10e). OT-LI case presents the simulation with the most uniform reflectivity cores as depicted by the narrow shape of the area encompassed by the 5% $\text{dBz}^{-1} \text{ km}^{-1}$ contour while MF-LI present the simulation with the highest variability in reflectivity structures within the convective area. Indeed, while at 3 km altitude the most common reflectivity values (as depicted by the 5% $\text{dBz}^{-1} \text{ km}^{-1}$ contour) in the OT-LI case vary between 30 and 52 dBz, in the MF-LI case this range extends between 21 and 52 dBz reflectivity. Even bigger is the difference in reflectivity structure at upper levels. While in OT-LI there appears to be almost no variability in reflectivity at 10 km altitude (note the bulls eye in the contour plot which indicates that 22 dBz is the most common value at these level), in MF-LI the variability in reflectivity values at this level is very big (there is no value that will happen with frequency higher than 5% $\text{dBz}^{-1} \text{ km}^{-1}$). The differences in the upper-level reflectivity structures clearly points to the snow filed distribution as the possible culprit. Indeed, the OT-LI simulation was the one with highest snow amounts at levels above 9 km while MF-LI was the one with the lowest amounts of snow at these levels. This notion is further strengthened by the fact that when the upper-level snow amounts increased in MF-HI and especially in OF-HI, their CFADs exhibited an upper-level narrowing of the distribution similar to that found in OT-LI. On the other hand, when in MT-LI and MT-HI the amount of upper-level snow decreased, their upper-level reflectivity structures also showed sings of increased variability (broadening of the distributions).

At lower levels Ferrier shows a tendency to produce higher variability in the reflectivity structures than Tao. In Tao the variability increases from OT-LI to MT-LI to MT-HI. It appears that the smaller the mean graupel and rain amounts the higher the variability in the low level reflectivity structure in the convective area.

When the two microphysical schemes were ran with the exact same set of parameters (MT-LI and MF-LI) they produced reflectivity structures with different upper-level variability. At lower levels the convective area reflectivity structures were rather similar. The two high ice realizations (MT-HI and MF-HI) produced the most closely comparing reflectivity structures in term of their convective area variability.

The stratiform area CFADs of all six simulations show the commonly observed in stratiform precipitation diagonalization and narrowing of the distribution (Yuter and Houze, 1995) representing a nearly homogeneous at each level reflectivity that steadily increases with decreasing altitude until just above 4 km altitude. At this level a strong enhancement of reflectivity is found that is associated with melting producing the radar bright band. Below that reflectivity decreases again indicating the collapse of ice particles into smaller drops and their subsequent evaporation. While these are the common features of the six simulations, the main differences are in the degree of narrowing and diagonalization. MF-LI and MF-HI show the best pronounced features and seem to compare better to the limited number of published observations than the other four simulations. Again, when the two schemes were ran with the exact set of parameters (MT-LI and MF-LI) they produced rather different reflectivity distributions at upper levels with MF-LI producing more horizontally uniform (narrower distribution) and much shallower profiles. This is illustrated by the fact that at 10 km

altitude the most common reflectivity value is 15 dBz in MT-LI but only 3 dBz in MF-LI.

2) Brightness temperatures

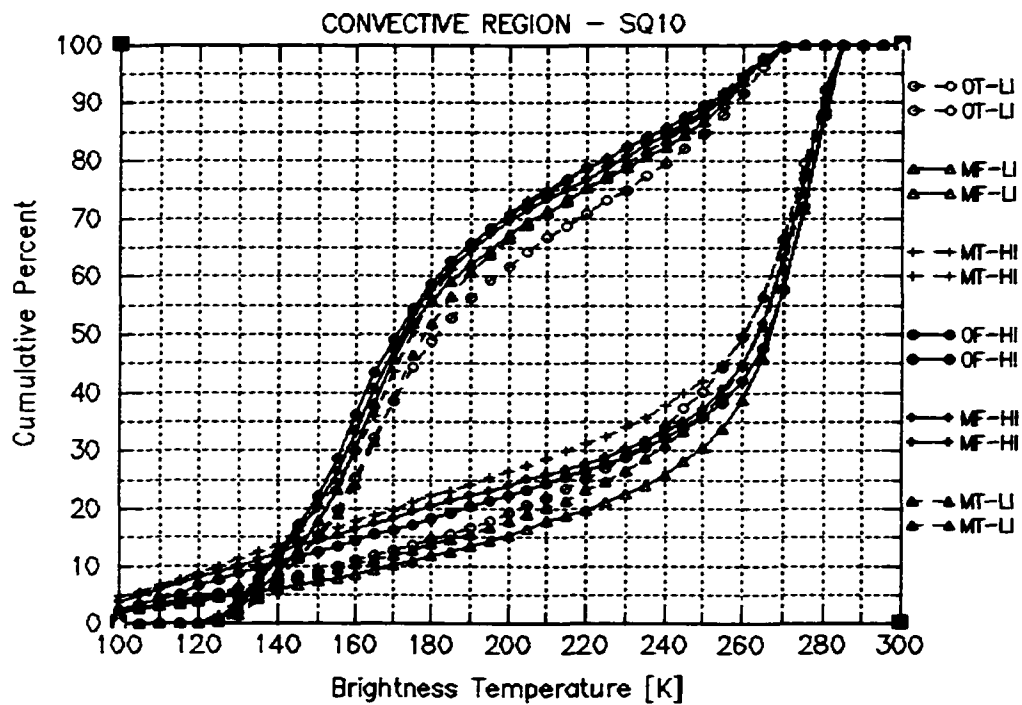
Figure 2.12 presents the cumulative frequency distributions of brightness temperatures computed at nadir and at two channels. The statistics are computed separately over the convective and the stratiform regions.

(i) Cumulative frequency distributions

In the convective region the 85.6 GHz channel exhibits the highest sensitivity. The more important things to note are: i). the three Low Ice (LI) cases appear to be warmer than the three High Ice (HI) cases. This is illustrated by the fact that the curves increase more slowly at the cold end and, hence, a higher percentage of the data are warmer than a certain temperature. It appears strange at first that the LI cases produce warmer distributions since they are the ones that generate more graupel in the convective area and, hence, should be expected to produce stronger scattering and, thus, colder 85.6 GHz Tbs. We will discuss this shortly. ii). the similarities in the distributions are stronger between the HI cases and between the LI cases than within each microphysics, i.e. MF-LI and MF-HI show more differences than MF-HI and MT-HI. This is particularly well illustrated by the brightness temperature of the 20th percentile which is 220° for MF-LI, 210° for MT-LI but only 180° for MF-HI and 170° for MT-HI.

At 10.7 GHz the three HI cases have virtually identical distributions in the convective area while the three LI cases are warmer and different from the HI cases and from each other.

a). Frequency Distribution – 10.7 and 85.6 GHz



b). Frequency Distribution – 10.7 and 85.6 GHz

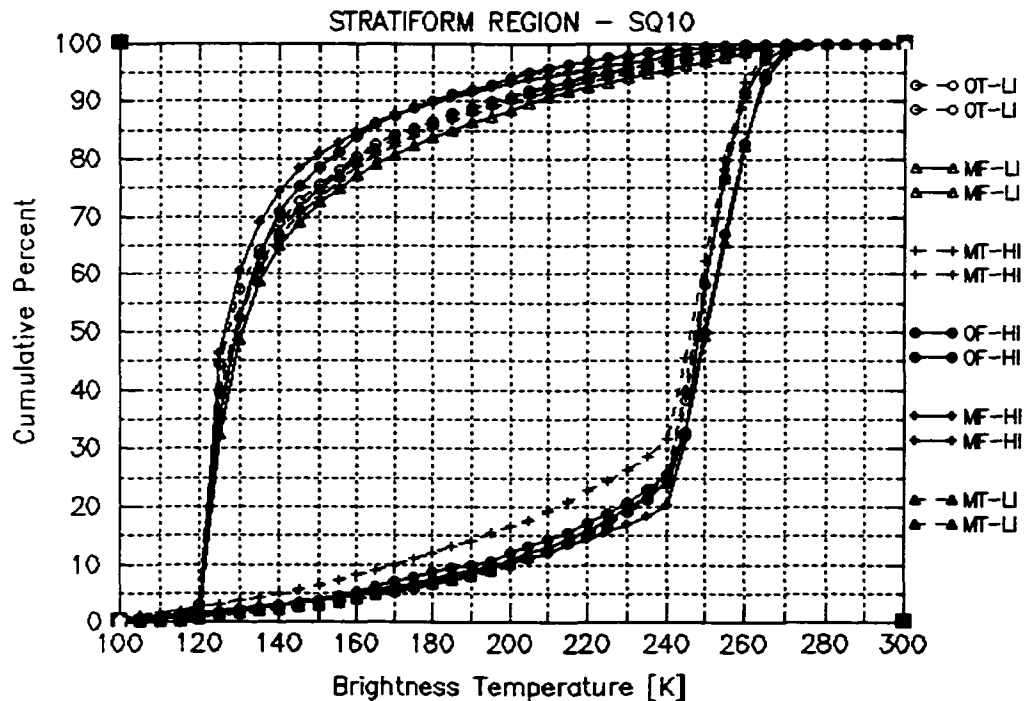


Figure 2.12. Cumulative frequency distributions of brightness temperatures (Tbs). Tbs were computed from the model-generated hydrometeors at nadir and over an ocean background. The statistics were computed separately over the convective (a) and the stratiform (b) regions. Presented are the distributions of the Tbs at 10.7 GHz and at 85.5 GHz.

In the stratiform region at 85.6 GHz the most notable fact is that MT-HI is a cold outlier while the other five distributions are identical. At 10.7 GHz the three Tao simulations appear to have very similar distributions while MF-HI and MF-LI lay on either side of Tao's distributions. OF-HI appears very similar to MF-HI.

The fact that two microphysical realizations can have essentially the same brightness temperatures at one channel and different distributions at another clearly implies that the choice of the microphysical parameterization should have implications for the retrieval of hydrometeor profiles and the associated rainfall and latent heating. However, if the distributions are different in both 10.7 and 85.6 GHz channels and show reverse structures (i.e. warmer 10.7 GHz are associated with colder 85.6 GHz) then it is not very obvious whether the two realizations could be looked as identical from the standpoint of retrieval algorithms or not (e. g. OT-LI and MF-LI). To look further into this issue we computed the 85 GHz brightness temperature frequency distributions as functions of the total liquid in the column. We used the same methodology applied in computing CFADs, however, here the frequency distributions were computed not as functions of altitude but as functions of the total liquid in the column (TLW – the sum of the cloud water and rain water). The total columnar liquid was bined every 0.5 kg/m**2 and the brightness temperatures were bined every 10 deg. Figures 2.13 and 2.14 presents the Contoured Frequency Liquid Diagrams (CFLD) computed separately over the convective and the stratiform regions.

Inspection of the convective region CFLDs reveals again that: i). the difference between the LI and the HI realizations of each of the two microphysics are bigger than the difference between the respective versions (e.g. LI) of the two microphysics. ii) the

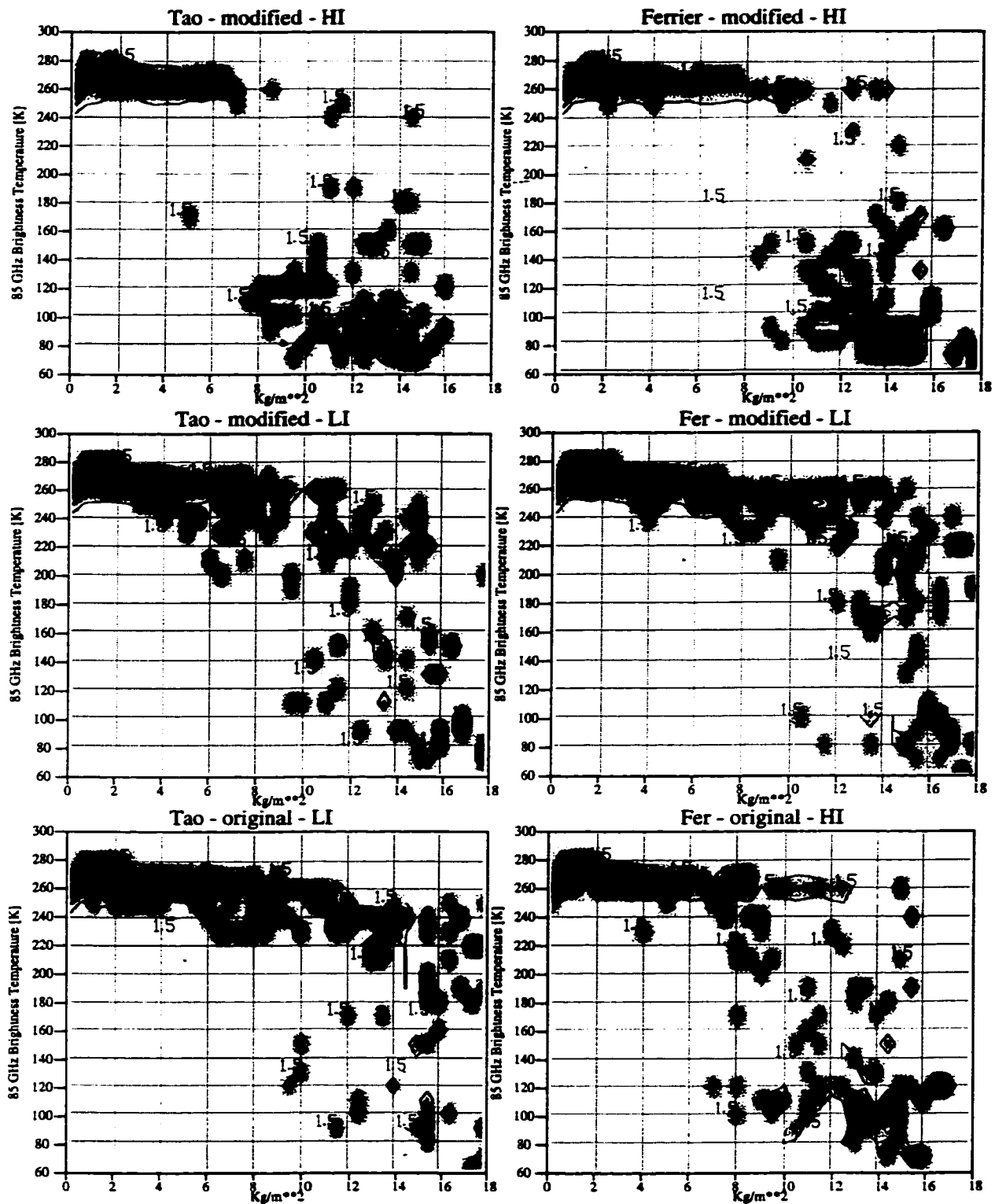


Figure 2.13. Contoured frequency liquid diagrams (CFLD) computed over the convective region. CFLDs are like CFADs except for the frequency distributions are computed not as functions of altitude but as functions of the total liquid in the column (the sum of the cloud water and rain water). The total columnar liquid was binned every 0.5 kg/m² and the brightness temperatures were binned every 10 degrees. Presented are the CFLDs of the 85.5 GHz brightness temperature computed over the convective regions of the six simulations. Contoured are the 1.5, 3.5 and 5.5 % of the data per kg/m² per degree.

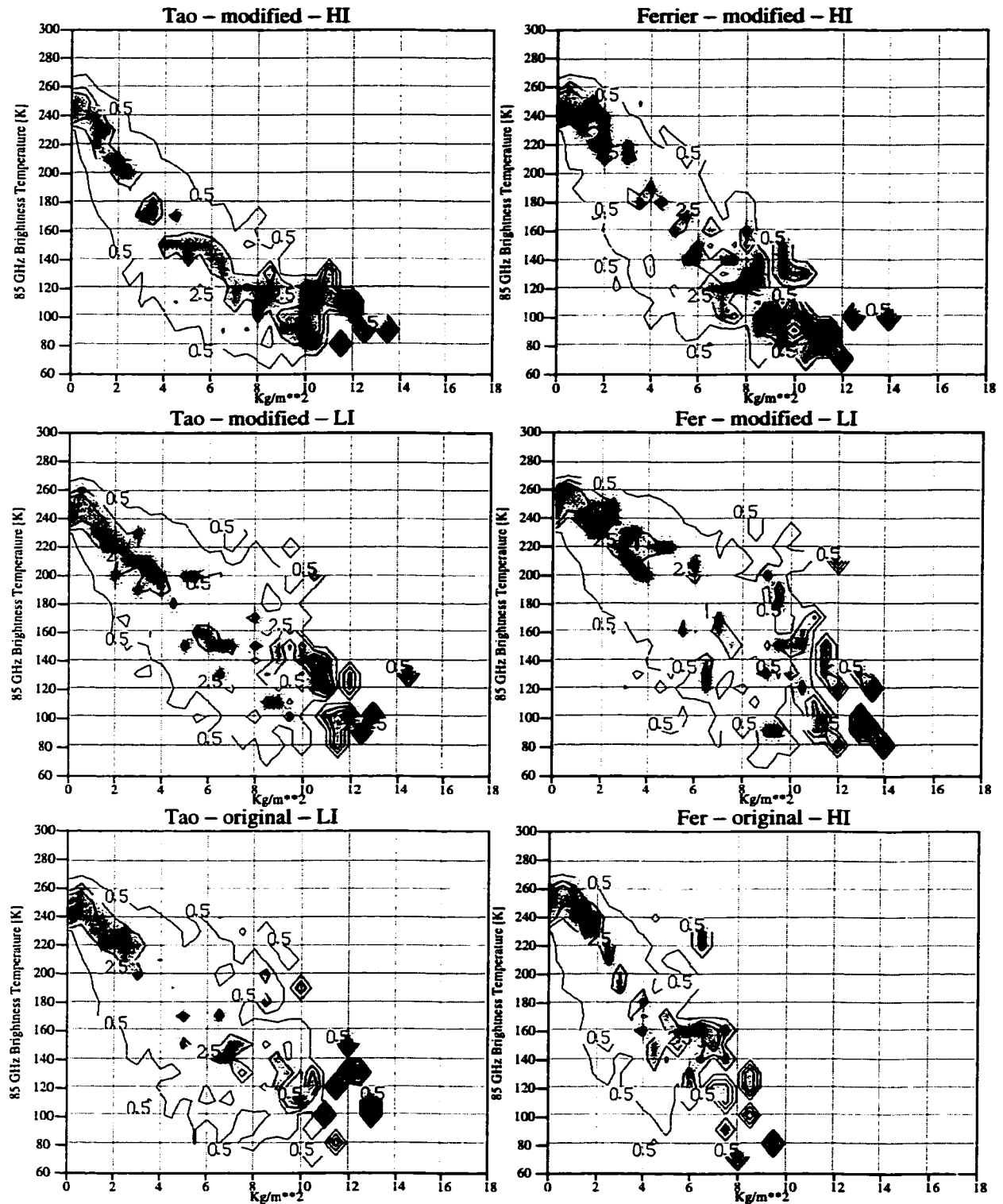


Figure 2.14. Same as in Fig. 2.13 except for statistics are computed over the stratiform regions of the six simulations.

three LI cases have warmer 85.6 GHz brightness temperatures for the same amount of total liquid in the column than the three HI cases. This is illustrated by the fact that a more significant part of the brightness temperature population is found at the warmer sector of the diagram as depicted by the 1.5 level contour. Considering that the convective area columnar liquid-to-graupel ratio appears to be the same for all six microphysical realizations (not shown here) it seems strange at first that the LI cases have the warmer 85.6 GHz Tbs. The key to understand this as well as the fact that the major contrast is between the LI and the HI cases lies in the hydrometeor profiles discussed earlier. As already mentioned the LI cases, while having the most graupel, also have significant amounts of supercooled cloud water in the graupel levels. As explained by Adler et al. (1991), the co-existence of graupel and supercooled cloud water has a significant warming impact upon the radiance emerging at the top of the atmosphere. In the presence of supercooled cloud water some of the surface radiation scattered by the graupel particles in directions away from the radiometer is absorbed by the cloud water and then re-emitted, thus increasing the amount of radiation which reaches the top of the atmosphere and decreasing the scattering signal of the graupel. Hence, in the absence of supercooled cloud water in the graupel levels the scattering signal is not altered and the coldest 85.6 GHz Tbs are produced by the microphysical realization which is associated with the most graupel. A deeper layer of graupel and the lowest amounts of cloud water in the mixed-phase layers both explain why MT-HI has the coldest 85.6 GHz distributions among the six simulations as depicted by the 1.5 level in the CFLD. Indeed, while in MF-HI the warm branch of the 1.5 level extends all the way to 11 kg/m², in MT-HI it ends at ~ 8 kg/m² and the higher amounts of total liquid

are dominated by much colder temperatures in the range of 140° to 70° . The three LI cases appear rather indistinguishable even though there are indications that MF-LI produces slightly warmer 85.6 GHz Tbs for the same amount of total liquid in the intermediate range of values for the TLW content. This is illustrated by the fact the the warm (260°) branch of the 3.5 level extends to only about 6 kg/m^2 of total liquid in the case of OT-LI and the MT-LI cases while it reaches all the way to $\sim 10 \text{ kg/m}^2$ in the case of MF-LI. The smaller amounts of graupel for the same amounts of TLW in MF-LI as compared to OT-LI and MT-LI (not shown here but illustrated by the ratio of maximum graupel to maximum rain in the mean profiles) is consistent with the above finding of slightly warmer 85.6 GHz Tbs in the MF-LI case.

The stratiform area CFLD show the same basic features. The fact that the three LI cases are warmer than the three HI cases is even better illustrated and is evident from the more gentler slope of the 2.5 contour and from the colder end of the 0.5 contour at TLW of 4 kg/m^2 , which is at or warmer then 120° in the LI cases but goes down to 100° in the HI cases. In addition, it is clearly evident that for a given amount of total columnar liquid the LI cases produce much wider distributions of brightness temperatures. This is particularly true for values of TLW > 4 and is illustrated by the wider area encompassed by the 0.5 contour. It is probably noteworthy that the widening of the distribution is mainly due to the increase in the frequency of warmer Tbs for the same TLW while at the same time the frequencies of the colder Tbs remain rather unchanged. This tendency for wider distributions in the LI cases is also illustrated by the 37 vs 85.6 GHz brightness temperature relationships (Fig. 2.15) which show a lot more scatter (less well defined features) in the LI cases. All of the above effects could

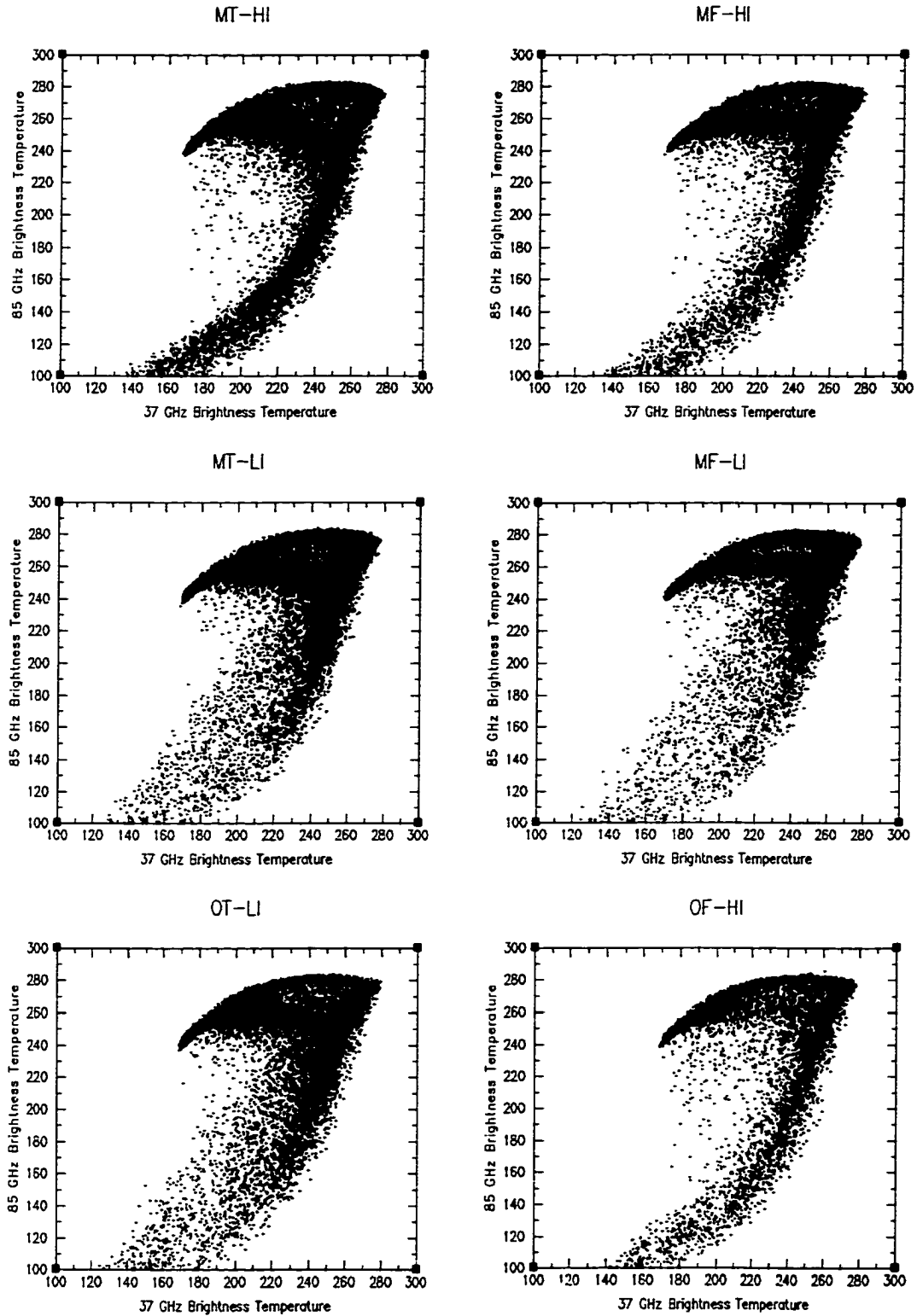


Figure 2.15. Scatterplots of the 37 GHz versus the 85.5 GHz brightness temperatures for each of the six simulations. Presented are the data from the convective and the stratiform regions and over the period 5:40 to 7:50 hours of simulation time.

be explained with the fact that the LI cases have supercooled cloud water present in the graupel levels. As Adler et al. (1991) pointed out the presence of cloud water not only warms the brightness temperatures in the scattering channels but also increases their deviations. The importance of the cloud water impact on the 85.6 GHz Tbs is further emphasized by the fact that MF-LI is significantly warmer than MT-LI in the range 0–4 kg/m² of TLW, while at the same time their ratio of total graupel-to-total liquid are very similar. While the average amount of supercooled cloud water is rather small in the stratiform areas, MF-LI has also almost double the amount of MT-LI. Hence, even small amounts of cloud water when collocated with the graupel could produce significant warming effect. Finally, while the contrast between the Ferrier cases (MF-LI, MF-HI and OF-HI) is not that big, the contrast between the LI and HI Tao cases is really strong (see the warm temperature value of the 0.5 level contour). This is not surprising at all since in Ferrier the LI case has more graupel but also more supercooled cloud water and the two effects counteract each other. In Tao, on the other hand, the LI cases have less graupel in addition to the cloud water warming effect while the HI case has more graupel and no cloud water in the graupel levels, both of these leading to much stronger scattering effect.

In summary, from the radiometric point of view the single, most important factor in determining the 85.6 GHz–total liquid in the column relationship is the presence or absence of cloud liquid water in the mixed-phase region where graupel is most abundant; the LI cases are rather indistinguishable, still MF-LI appears to produce slightly warmer 85.6 GHz brightness temperatures for the same amount of total columnar liquid; the HI cases, even though quite similar, show some important

differences: MT-HI has colder 85.6 GHz Tbs for the same amount of total liquid in the column; MT-HI has narrower 85.6 GHz Tb distribution in the stratiform region; OF-HI produces the lowest of all six simulations amounts of total liquid in the column in the stratiform region.

e. Impact on storm structure and dynamics

As already discussed, all six simulations produced leading convection-trailing stratiform type mesoscale convective systems. Furthermore, at 5:30 hours in to the simulation all six realizations show some degree of asymmetry illustrated by the fact that the stratiform precipitation is more preferentially found in the north-central portion of the line than in the southern (Fig. 2.2). Despite these similarities there are also some important differences in the orientation of the convective line. While three of the realizations (OF-HI, OT-LI and MT-LI) show a tendency for bowing out in the southern portion of the system, the other three (MF-LI, MF-HI and MT-HI) have a bit more linear structure and will be referred hereafter as the "linear" cases. This is best illustrated by their smaller tendency to bulge out and by having the north-central portion of the line located further eastward as compared to the other three simulations. Analysis of the 3 km pressure perturbation field (Fig. 2.16) shows that these three simulations (MF-LI, MF-HI and MT-HI) also had a better defined and larger midlevel mesolow which was more separated from the northern end of the line as compared to the other three simulations. Figure 2.17 presents the storm-relative flow at 3 km altitude. A well defined cyclonic circulation is found in the northern end of the storm system in all six simulations. Bartels and Maddox (1991) and Johnson and Bartels (1992) found that stretching of earth's rotation in association with midlevel convergence into the

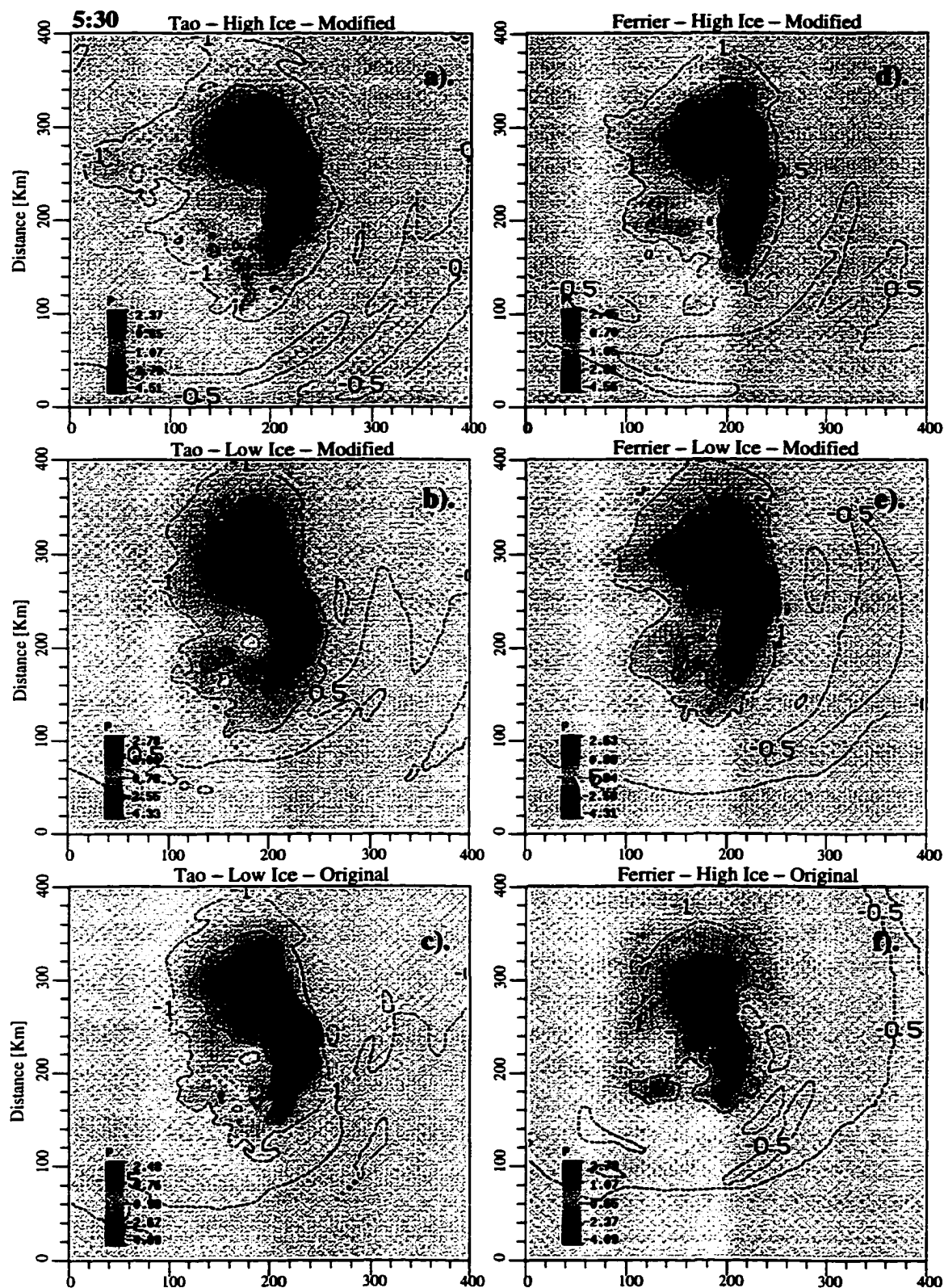


Figure 2.16. Same as in Fig. 2.2 except for presented are the pressure perturbations from the initial conditions at 3 km altitude. Contours are every 0.5 mb.

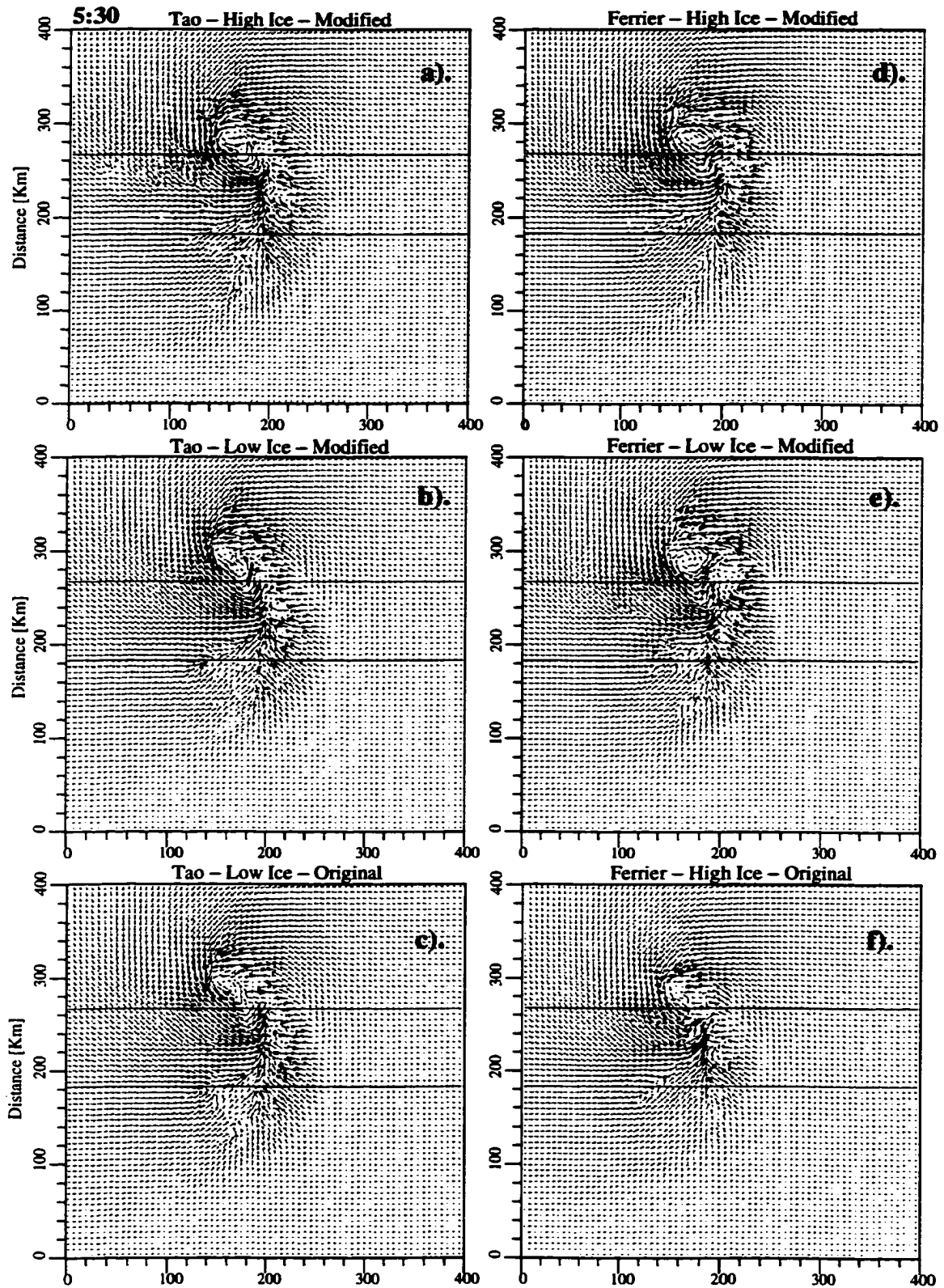


Figure 2.17. Same as in Fig. 2.2 except for presented is the storm-relative flow at 3 km altitude.

stratiform region mesolow was sufficient to generate the observed there vortex even in the absence of significant background vertical vorticity (as is the case in our simulations). Figure 2.17 reveals that there are differences in the vortex structure produced by the six simulations. The three "linear" simulations that had a better defined mesolow (MF-LI, MF-HI and MT-HI) also had a more circular and somewhat bigger vortex structure. This altered the southern part of the vortex, the Rear-to-Front (RTF) branch, in such a way as to produce a Rear Inflow (RI) with stronger westerly component. In contrast, the other three simulations that had less defined mesolow, also had more elongated vortices. This resulted in a RTF branch of the circulation having more NW-SE orientation. The low-level mesoscale outflow (Fig. 2.18) reflected the just described differences in the midlevel vortex structure in the following way: the elongated vortices were associated with low-level outflow that was strongest in the south-central portion of the storm and was apparently responsible for the bulging observed there; on the other hand, the three "linear" cases that had larger vortices with more westerly RI produced low-level outflow that was stronger in the north-central portion of the system and the enhanced convergence there aided in stronger convective development and faster eastward propagation of the northern ends. This led to the more "linear" outlook of the systems.

The midlevel mesolow affected not only the mid- to low-level circulations but also the structure of the upper-level convective outflow. Indeed, Fig. 2.19 illustrates that the 7 km storm-relative flow of the three "linear" cases had a better defined streak of southerly flow located at approximately $x=170$ and $y=220$ km, while in the other three cases the flow in this area was broader (not that well confined streak) and more

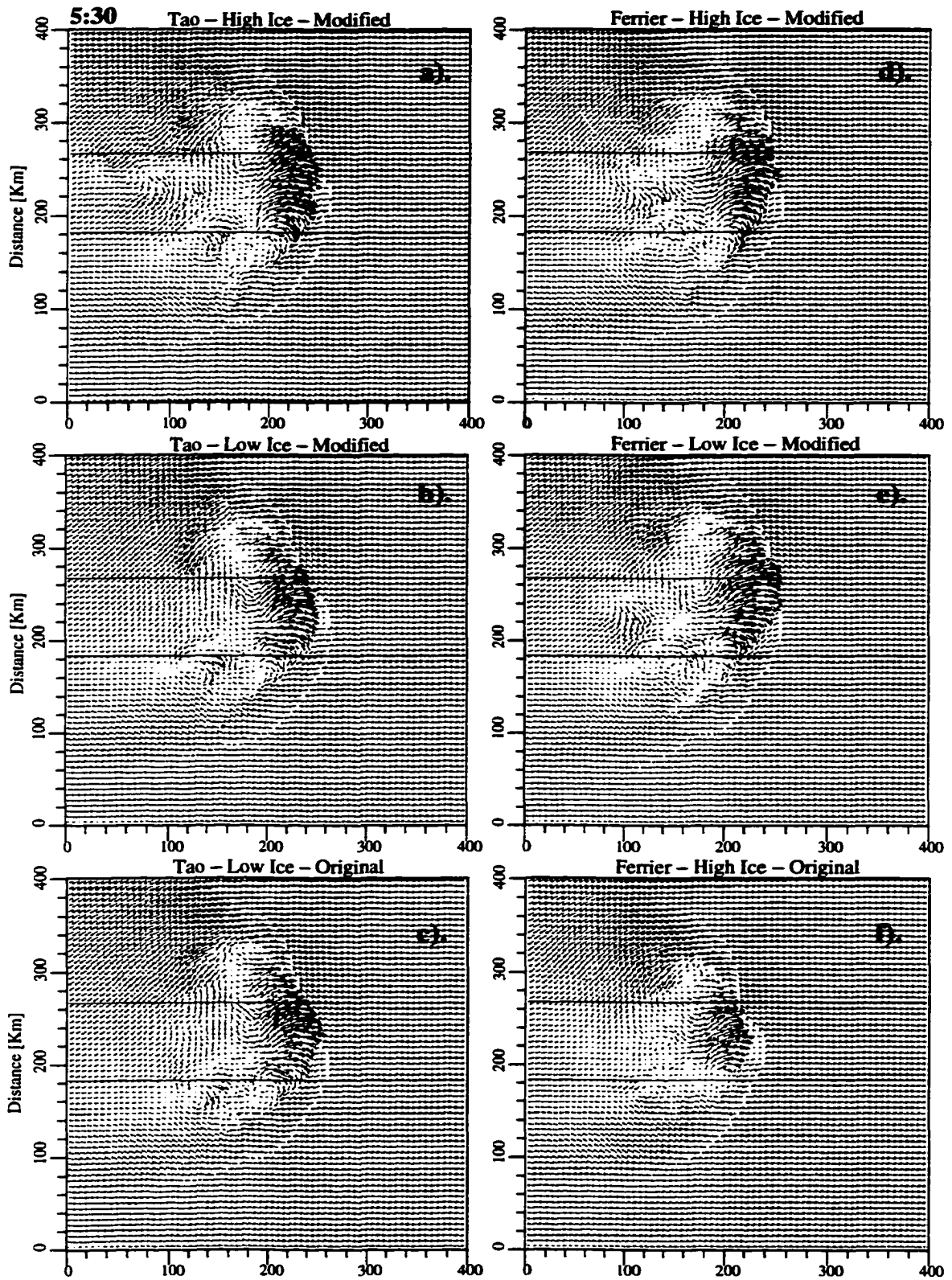


Figure 2.18. Same as in Fig. 2.2 except for presented is the storm-relative flow at 1 km altitude.

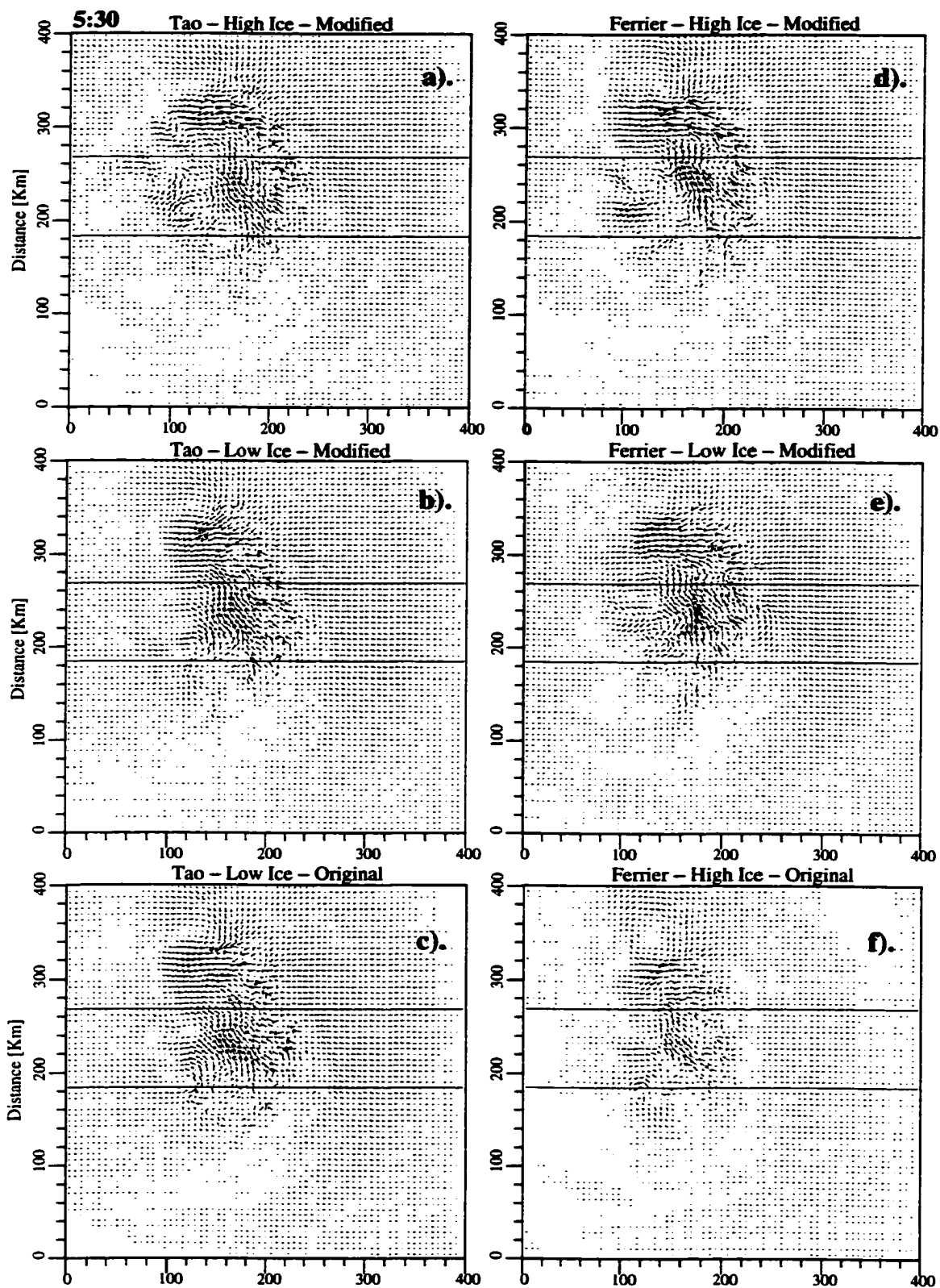


Figure 2.19. Same as in Fig. 2.2 except for presented is the storm-relative flow at 7 km altitude.

south–easterly going to NW in direction parallel to the leading line. The discussed flow represents the upper–level outflow from the convective region. We suggest that in the cases of a well–defined midlevel mesolow (the three "linear" cases) the low level inflow that enters the convective area and rises up in the convective cores experiences a stronger northward acceleration during its rise due to the stronger midlevel pressure gradient. This deflects this rising flow in such a way that when it exits the convective area at upper levels it forms a more focussed outflow with stronger northward component.

An important point to make is that this upper–level outflow is still buoyant and rising. Hence, the midlevel pressure perturbation field will be altered by the location and the intensity of the upper–level outflow and will respond with lowering of the pressure underneath the upper–level flow. This is an example of a positive feedback that will further intensify the midlevel mesolow. More importantly, the location of the midlevel mesolow will be altered and it will continue its separation from the northern end of the convective line and relative traveling backward and southward in response to the location of the strongest upper–level heating which is associated with the location of the upper–level outflow. In other words, the upper–level outflow will "pull" the midlevel mesolow further south and back, away from the northern–end convection.

Indeed, inspection of the 3 km pressure perturbation fields at 7:20 (Fig. 2.20) shows exactly that kind of evolution . The three "linear" cases now have midlevel mesolows that are positioned further backward and southward as compared to the "bowing–out" cases for which the midlevel mesolow remains more tightly connected to the northern end of the convective area.

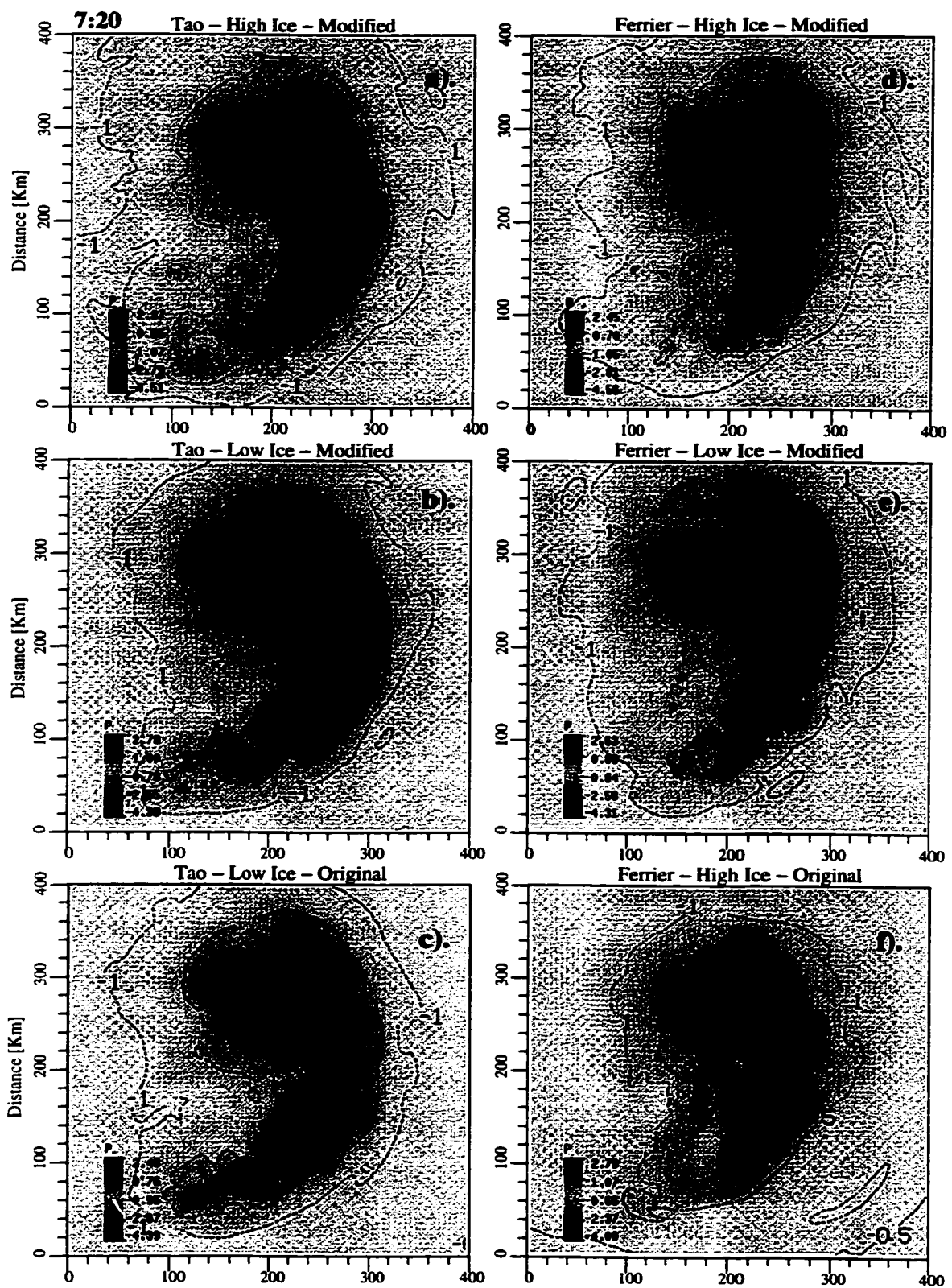


Figure 2.20. Same as in Fig. 2.16 except for presented are the pressure perturbations at 7 hours and 20 minutes into the simulation time.

The two Ferrier simulations (MF-LI and MF-HI) illustrate this best.

The 3 km storm-relative flow at 7:20 is presented in Fig. 2.21. It shows that the three "linear" case had not only bigger size vortices but also stronger RI in the central portion of the system. Furthermore, it appears that the center of the circulation is further back from the north end of the leading convective line.

In association with the further back positioned mesolow and mesovortex, there is a low-level outflow (Fig. 2.22) which has much weaker forward component in the northern end of the "linear" cases as compared to the outflow of the "bowing-out" cases. This is again best illustrated by the MF-LI simulation.

Finally, the upper-level outflow (Fig. 2.23) illustrates again that the interaction between the midlevel mesolow and the upper-level outflow appears to be stronger in the three "linear" cases as depicted by the more focussed flow that at these upper levels that appears to be converging just above the midlevel mesolow.

The interesting question now is how the observed evolution in the structure of the flow affects the structure and the evolution of the simulated storms. To investigate this we look at the reflectivity fields at 7:20 as depicted by the maximum reflectivity in the column (Fig. 2.24). A quick inspection reveals that by 7:20 the stratiform region in all six simulations became even more asymmetric, with most of the stratiform echo confined to the north-central portion of the line. This asymmetry in the distribution of the stratiform precipitation was associated with both the rapid expansion of the southern end of the convective line and the intensification of the midlevel mesovortex which continuously evaporated hydrometeors in the rear-inflow branch of the circulation.

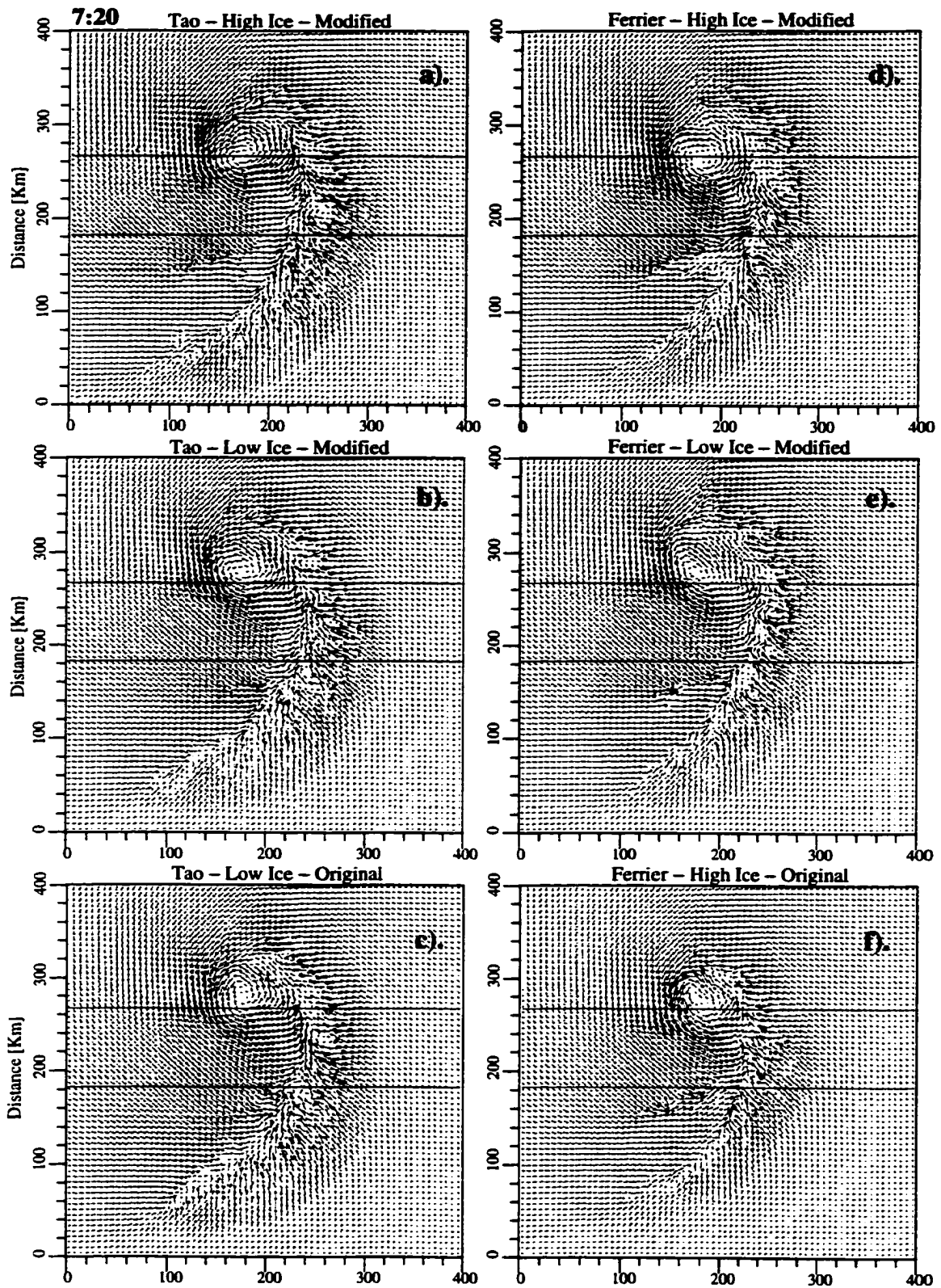


Figure 2.21. Same as in Fig. 2.17 except for presented is the storm–relative flow at 7 hours and 20 minutes into the simulation time.

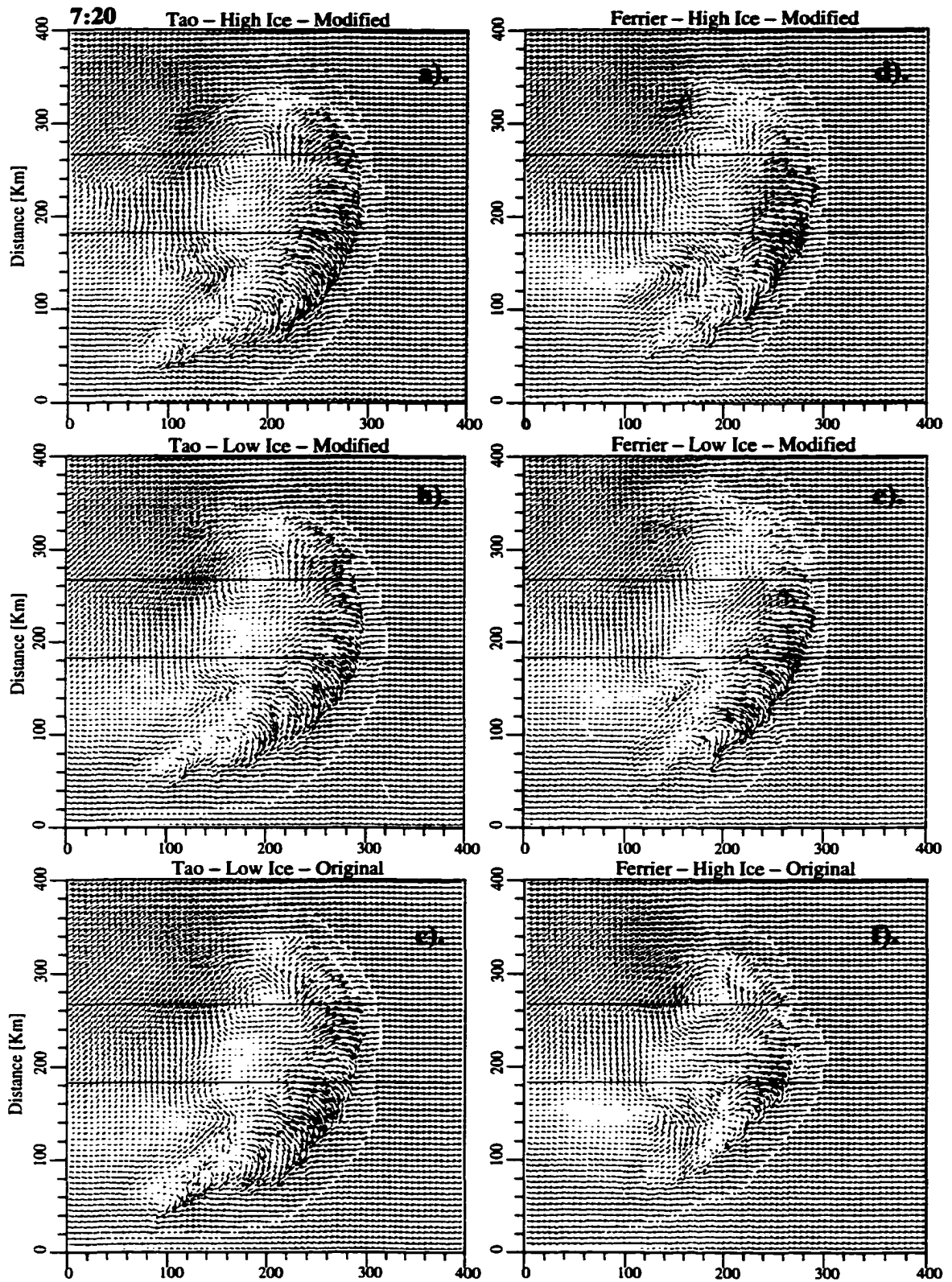


Figure 2.22. Same as in Fig. 2.18 except for presented is the storm-relative flow at 7 hours and 20 minutes into the simulation time.

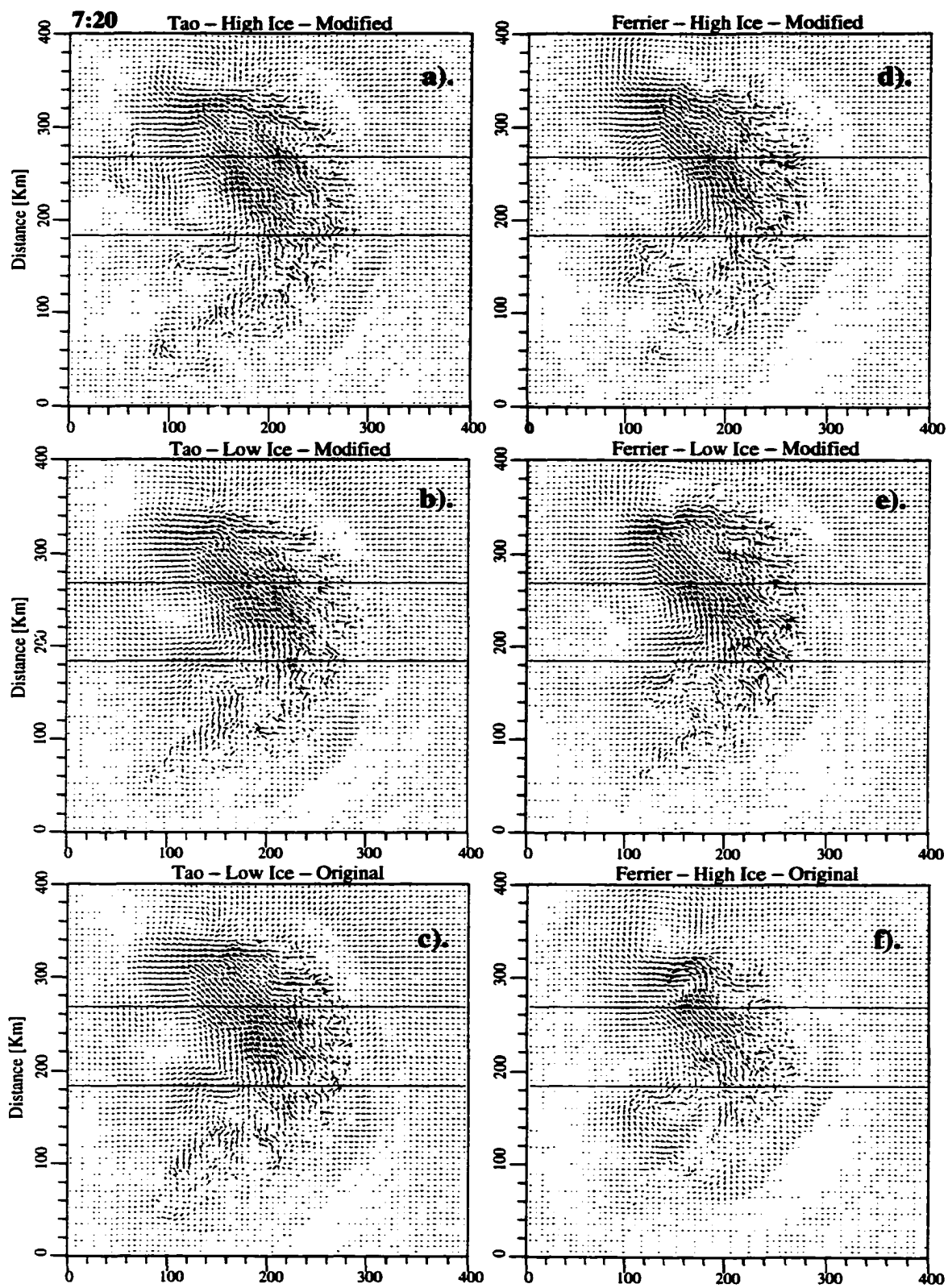


Figure 2.23. Same as in Fig. 2.19 except for presented is the storm–relative flow at 7 hours and 20 minutes into the simulation time.

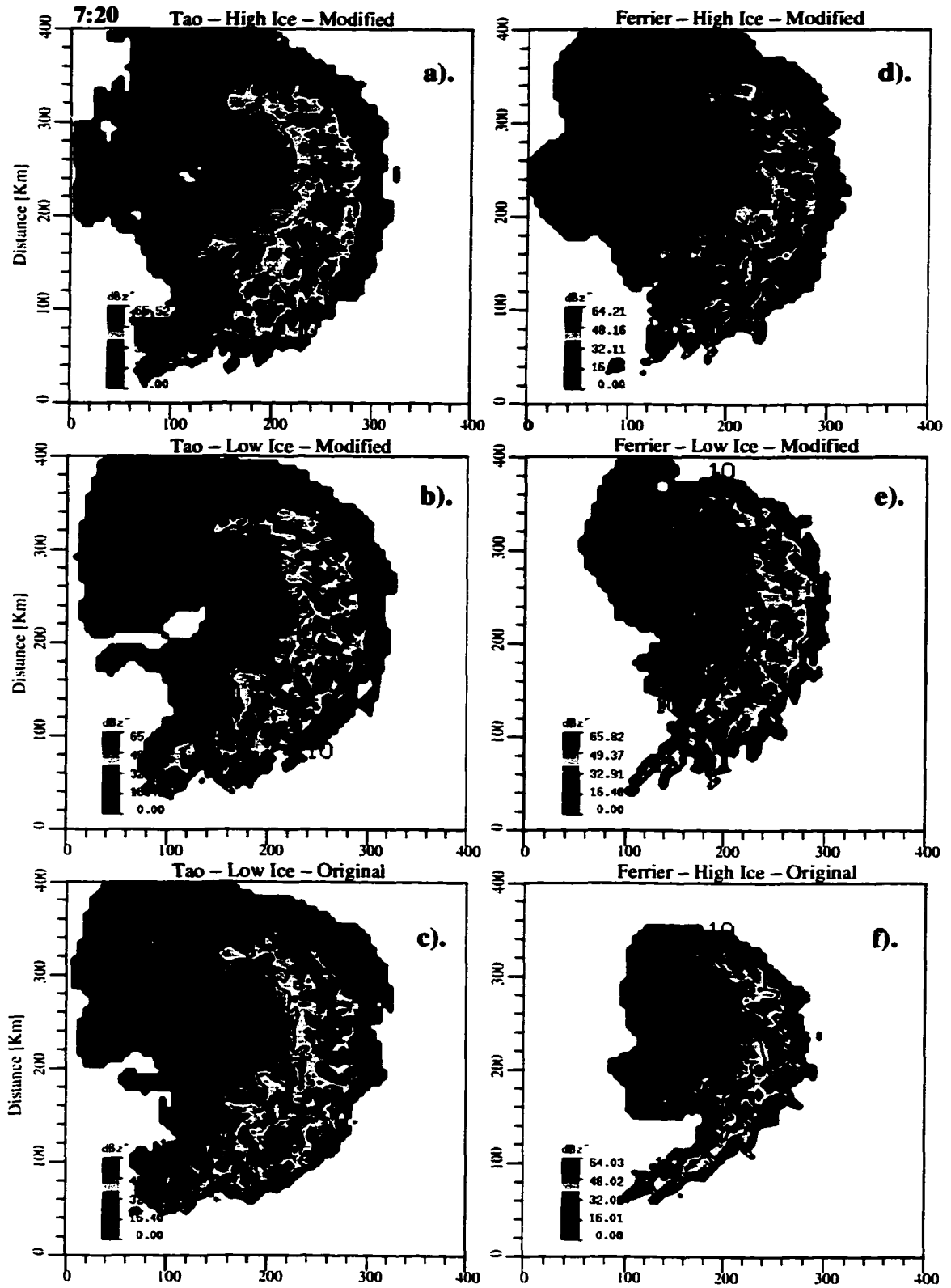


Figure 2.24. Same as in Fig. 2.2 except for presented is the reflectivity field at 7 hours and 20 minutes into the simulation time.

Indeed, the location of this branch is clearly evident from the reflectivity notch found in the back of the stratiform area.

While by 7:20 the differences in the bowing out of the convective line are somewhat less pronounced, still, MF-LI, MF-HI and MT-HI show a bit more linear structure than the other three simulations. What is more interesting is that the three "linear" cases show a stronger tendency for weakening of the convection in the northern end of the line while at the same time the convection in the central portion remains very intense and the southern end continues to expand. This is best illustrated by the structure of MF-LI. While the other three (the "bowing-out") simulations also show a tendency for southward expansion, they do not show a tendency for weakening of the northern end convection. OF-HI in particular shows even a tendency to have stronger convection in the northern ends as compared to the central portions which continues to bow out. Apparently, the the quicker separation of the midlevel mesolow in the "linear" cases that led to the reduced support of the low-level mesoscale outflow for the convergence in the northern end of the convective line eventually resulted in weakening of the convective activity there.

Hence, an early development of well-defined and separated from the convective area midlevel mesolow plays a role in determining the structure and the evolution of the reflectivity cores. But what determines the ability of a simulation to more easily produce midlevel mesolow in the stratiform area? An inspection of the scale and intensity of the stratiform area of all six simulations reveals that the three that were more capable of producing stronger midlevel circulations were the ones that either had the most intense or the biggest stratiform area in the framework of each microphysical

schemes. It appears then that the development of midlevel mesolow in the trailing stratiform region is facilitated not only by the latent heating that takes place in the still rising buoyant convective outflow that is transported backward from the convective line and into the stratiform area but also by the lower level melting and evaporative cooling that are stronger in the cases with more precipitation in the stratiform area. The important role of the low-to-mid level cooling in the production of the midlevel mesolow is illustrated by the fact that the OF-HI simulation which had very intense upper-level heating still failed to produce a well defined mesolow early into the simulation apparently due to its very limited precipitation production.

To summarize, the early development of well-defined and separated from the convective area midlevel mesolow leads to a more linear structure in the earlier times by providing a stronger low-level convergence in the northern end of the line. Having a more linear structure and a better defined mesolow in these early times helps the further separation of the midlevel mesolow and its traveling southward and backward with respect to the convective line through the interaction between the midlevel mesolow and the upper-level outflow from the convective area. In this interaction, the midlevel mesolow focusses the upper-level outflow which, in turn, alters the midlevel pressure field and "pulls" the midlevel mesolow further south and back from the northern end convection. As the midlevel mesolow travels southward and backward, the low-level divergence maximum also travels southward and backward and the mesoscale outflow stops supporting strong convergence in the the northern end of the line which leads to the observed weakening of the convective intensity in this portion of the system. At the same time, the convergence in the central portion of the storm remains very strong and

this results in the maintenance of strong and steady (slowly evolving) convection there. The anticyclonically curving mesoscale outflow found in the south–central portion of the system alters the direction of propagation of the embedded in it convective scale outflows and promotes the southward expansion of the system by forcing the convective outflow to spread southward.

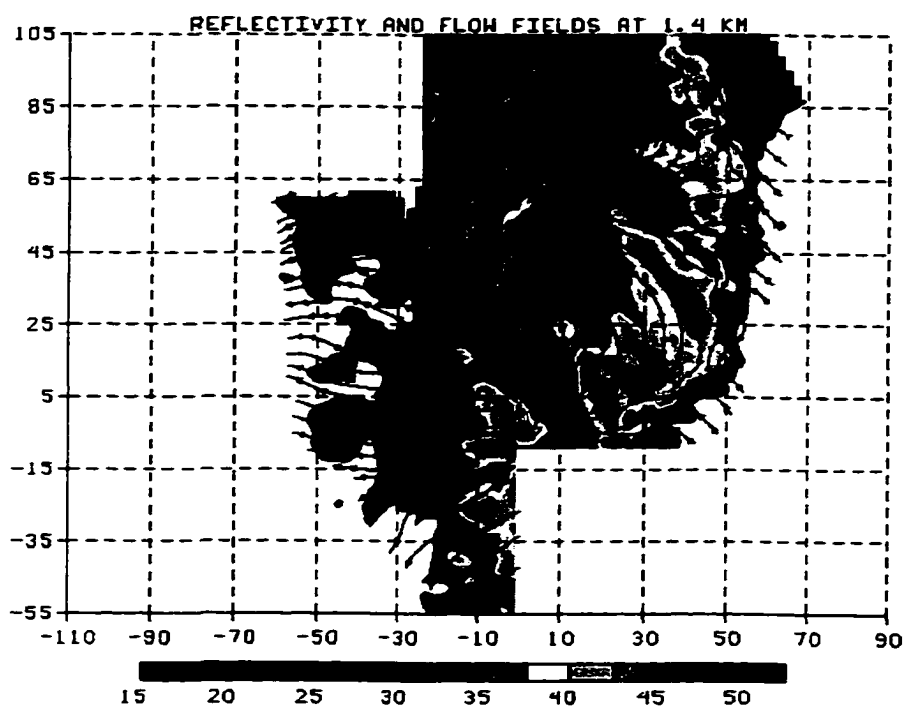
The described interaction between the midlevel mesovortex and the convective activity along the leading line was first proposed by the modeling study of Skamarock et al. (1994) and the observational study of Hristova–Veleva and Biggerstaff (1994). Based on dual–Doppler analyses of the 28 May 1985 PRE–STORM asymmetric squall line Hristova–Veleva and Biggerstaff (1994) developed a conceptual model of the mechanism through which the convectively generated midlevel mesovortex found in the stratiform region of the observed storm affected the convective characteristics and led to along–line variability in storm structure and evolution. In this model, the mesovortex is thought to be responsible for focusing the midlevel rear inflow in its rear–to–front branch and, thus, altering the structure of the low–level mesoscale outflow by producing cyclonically curving outflow in the northern portion of the system, beneath the midlevel mesovortex, and anticyclonically curving divergent outflow in the central region and southern flank. The along–line variability in the mesoscale outflow in turn affected the leading–line convective activity by: i) enhancing the convergence in the central and southern portions of the line, where the outflow directly opposes the environmental inflow, while at the same time it contributes much less to the northern flank convergence, where the mesoscale outflow is more confluent with environmental inflow; ii). altering the direction of propagation of the convective downdrafts embedded

in the mesoscale outflow. Convective outflows embedded in the northern-portion cyclonically curving mesoscale out flow are free to spread northward and backward. At the same time convective outflows embedded in the central and southern portion anticyclonically curving mesoscale outflow are forced to spread forward and southward, thus contributing to enhanced convergence in the central portion of the storm and to the production of deep southward spreading along-line flow that appears responsible for the southward expansion of convective activity with time. This could explain the strong and sustained convective activity in the central portion of the line. Finally, the weaker convergence in the northern end of the line was thought responsible for the observed weakening in time of the convective activity there.

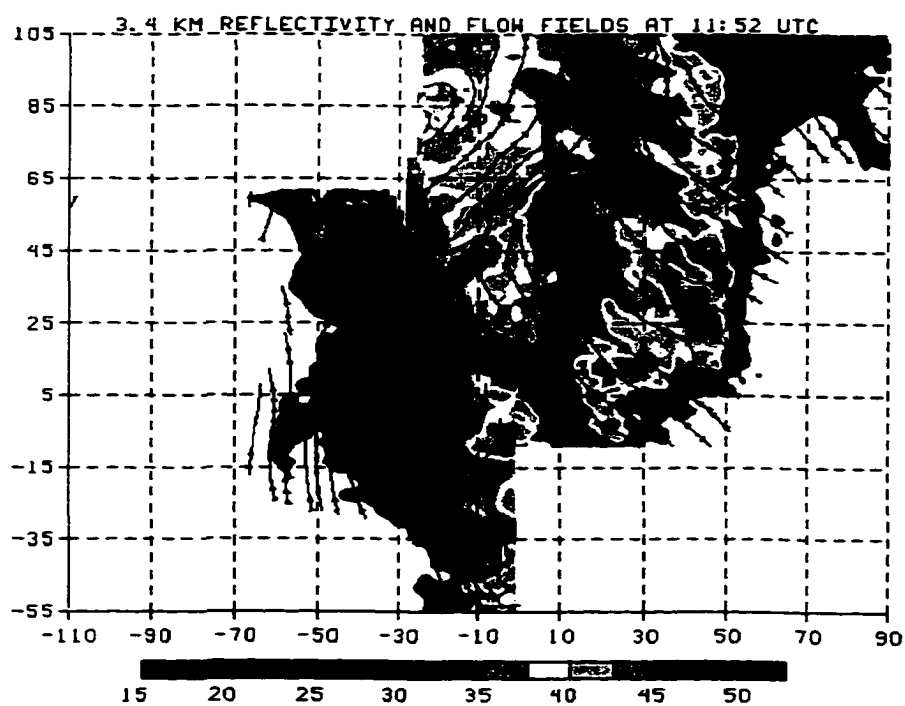
All six simulations presented here produced the basic structures that were observed, i.e. the asymmetric reflectivity structure, the midlevel mesovortex, the associated asymmetry in the low-level mesoscale outflow and the southward expansion of the storm with time. However, only three of the simulations seem to produce also the observed in reality weakening of the northern end convective activity. As discussed, these three simulations also had a midlevel mesolow which traveled backward with respect to the leading convection in time. Indeed, a similar tendency was observed in flow structure of the the 28 May 1985 squall line. This further supports the idea that the relative position of the mesolow with respect to the convective line plays a role in determining the convective line structure and evolution.

While a direct comparison between the 28 May 1985 squall line system and the six simulations presented here should not be made (since the environmental sounding was not the same) the similarities in structure and evolution are very strong especially

for the three "linear" simulations. Of them, the MF-LI case seems to compare best. Indeed, the similarities in structure and evolution are striking. To illustrate this point, Figure 2.25 presents dual-Doppler analyses of the low- and midlevel flow and reflectivity of the 28 May 1985 case for direct comparison to the simulations. Note the along-line variability in the structure of the convective cores. The southern and central portions of the leading convective line were characterized by large, somewhat isolated reflectivity cores elongated in direction of storm propagation. At the same time the northern flank is dominated by smaller, more closely spaced, weaker cores, organized in a line perpendicular to the storm motion. The MF-LI simulation at 7:20 (Fig. 2.24) presents a remarkably similar along-line variability in the intensity, size and orientation of the convective cores! This includes not only the strong elongated reflectivity cores in the central portion of the storm and the small, closely spaced northern end convective cores but even the triangular reflectivity feature found in the area where the low-level mesoscale outflow splits into cyclonically and anticyclonically curving portions (at approximately $x=260$ km and $y=265$ km). The fact that the other two "linear" cases show very similar (even though less pronounced) reflectivity structures indicates that the production of such convective organization is not accidental but it is determined by the flow structure. While the three "bowing out" cases also produce elongated reflectivity cores, such cores are found along the entire line and their orientation is somewhat radial. Furthermore, they are more quickly evolving as opposed to the "linear" cases for which it appears that the convective cores in the central portion of the line are more steady in nature and easily recognizable during periods of up to 40 minutes.



a).



b).

Figure 2.25. Reflectivity and storm-relative flow fields at 1.4 km (a) and 3.4 km (b) altitude as inferred from dual-Doppler analyses of the PRE-STORM squall line system observed on 28 May 1985. The size of the domain is 200x160 km².

The 28 May 1985 observational case also revealed that the along-line variability in the convective structure and evolution was associated with along-line variability in the storm-relative cross-line and along-line flow (Fig. 2.26). The northern end of the line was characterized by very weak gently sloping toward the surface cross-line (Rear-to-Front) storm-relative flow and by the absence of southward along-line flow in the vicinity of the convective line. The cross-line wind component in the central portion of the line revealed storm-relative Rear-to-Front (RTF) flow descending to the surface ~ 50 km behind the leading convective line. The along-line flow depicts a wedge-type structure of southward spreading flow which appears to be confined to the leading convective line by the near-surface RTF cross-line flow. Finally, the southern portion of the storm is characterized by a RTF flow which remains elevated to a very-close proximity with the convective line and apparently does not contribute much to the local production of the near-surface RTF.

For comparison with observations, Fig. 2.27 presents cross-line and along-line flow components at 7:20 hours averaged in the northern, central and southern portions of the convective line that was simulated by the MF-LI realization. The resemblance in structure and along-line variability in the flow between the observational case and the simulation is very good. Furthermore, inspection of the flow structures at 5:30 hours (Fig. 2.28) shows that while the flow in the central and southern portions of the convective line did not change much between the two times, the northern area RTF was apparently stronger in the earlier time and the convection was more intense as illustrated by the more upright front-to-rear component of the flow. This further supports the idea that the separation with time of the midlevel mesolow from the

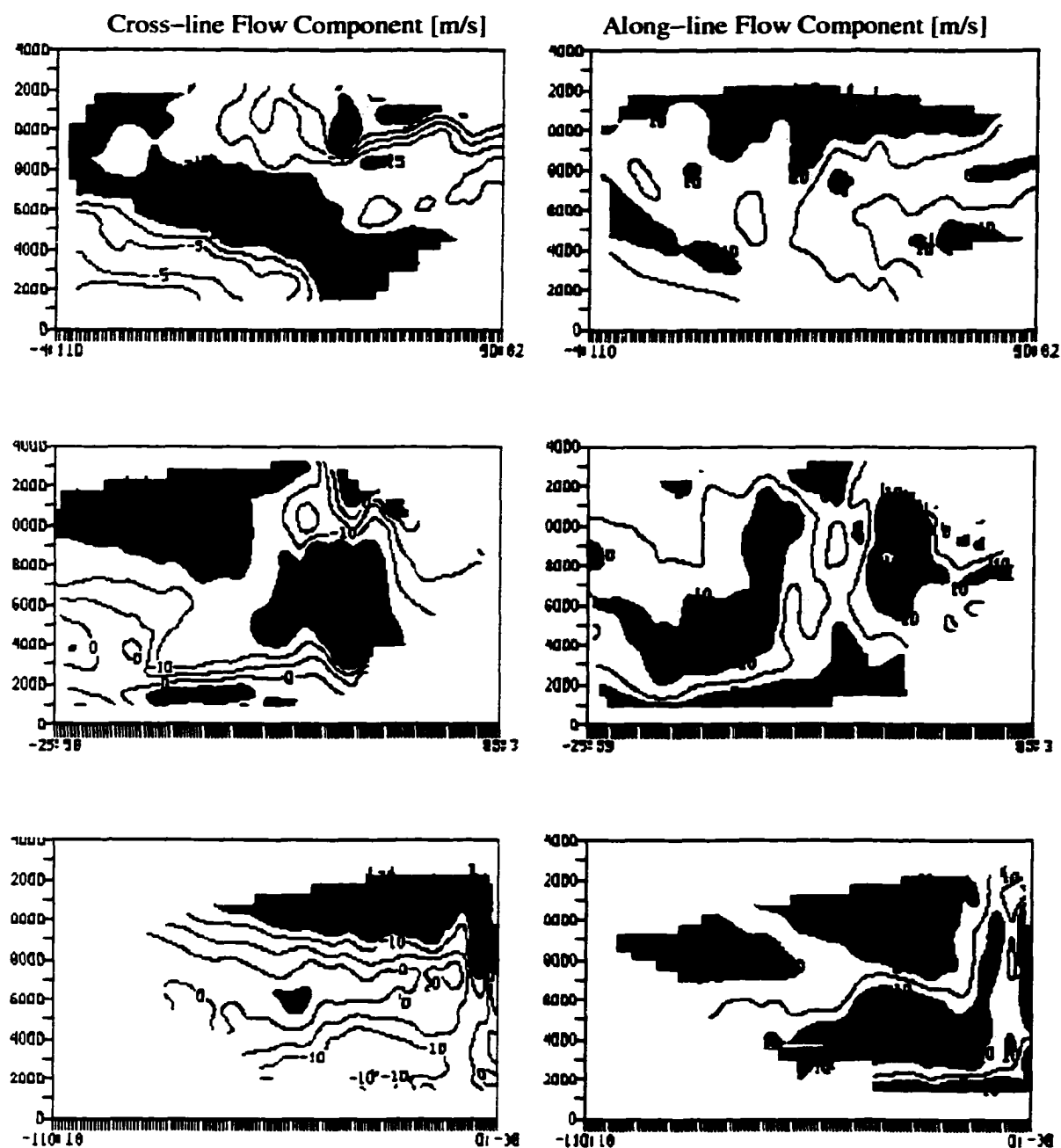


Figure 2.26 Cross-line and along-line storm-relative flow at 11:52 UTC as inferred from dual-Doppler analyses of the asymmetric squall line system observed on 28 May 1985 during PRE-STORM. The top, central and bottom panel represent the flow structure respectively in the north, central and southern portions of the storm. The horizontal distance of the cross-sections is 120 km and the height of the plots is 14 km. Contours are every 5 m/s. In the cross-line flow panels, the positive values (Rear-to-Front flow) are shaded in yellow and red, starting at 0 m/s. Negative values (Front-to-Rear Flow) are shaded in blue and purple starting at -15 m/s. In the along-line flow panels positive values (northward flow) are shaded in warm colors starting at 5 m/s. Negative values (southward flow) are shaded in cold colors, starting at 0 m/s

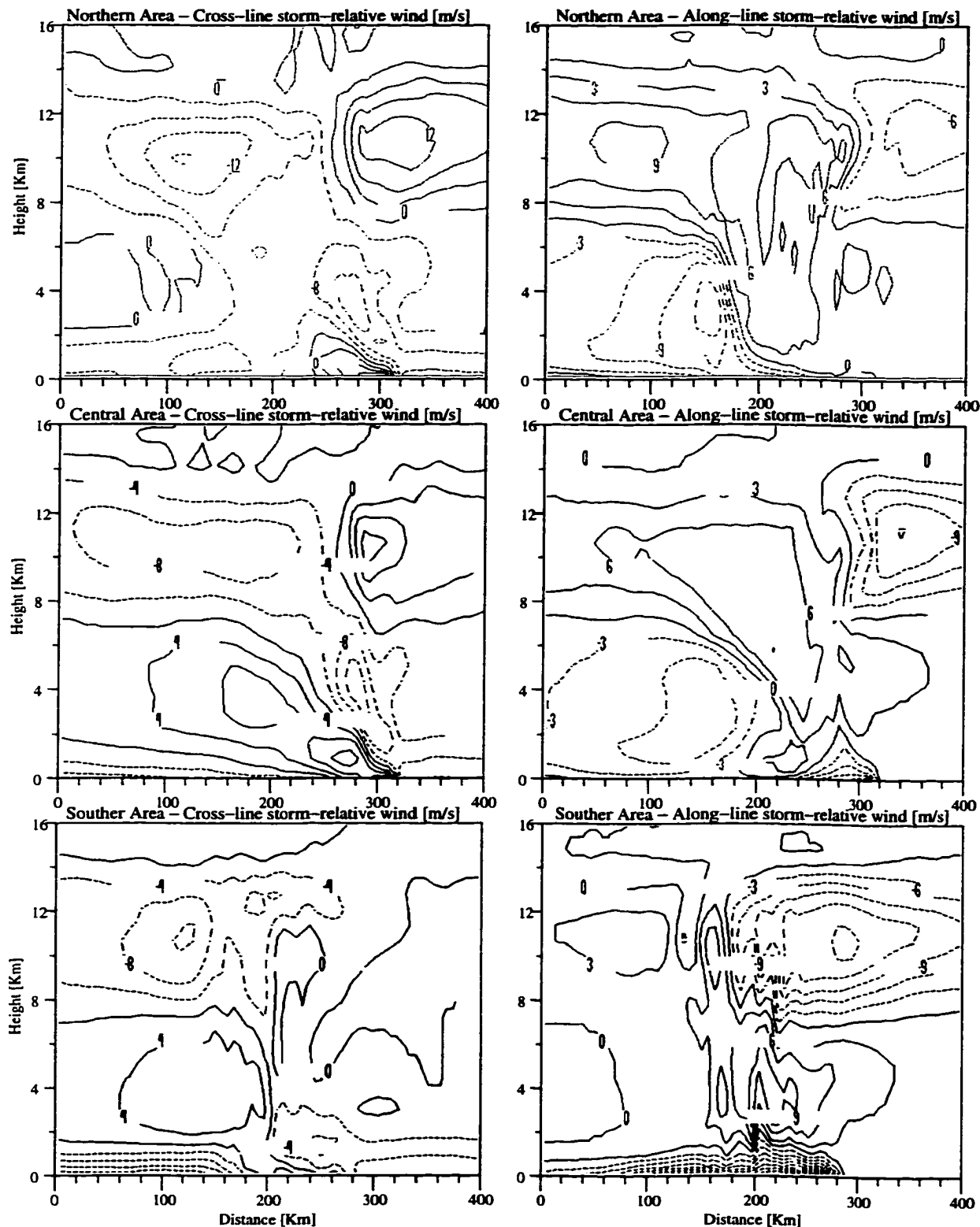


Figure 2.27. Cross-line (left panels) and along-line (right panels) storm-relative flow at 7:20 hours into the MF-LI simulation. Top, central and bottom panel present along-line averages taken in the northern, central and southern portion of the simulated storm. The central averaging area is the area between the two lines in Figs. 2.21, 2.22 and 2.23. The northern and the southern portions are slightly smaller and positioned on the two sides of the central area.

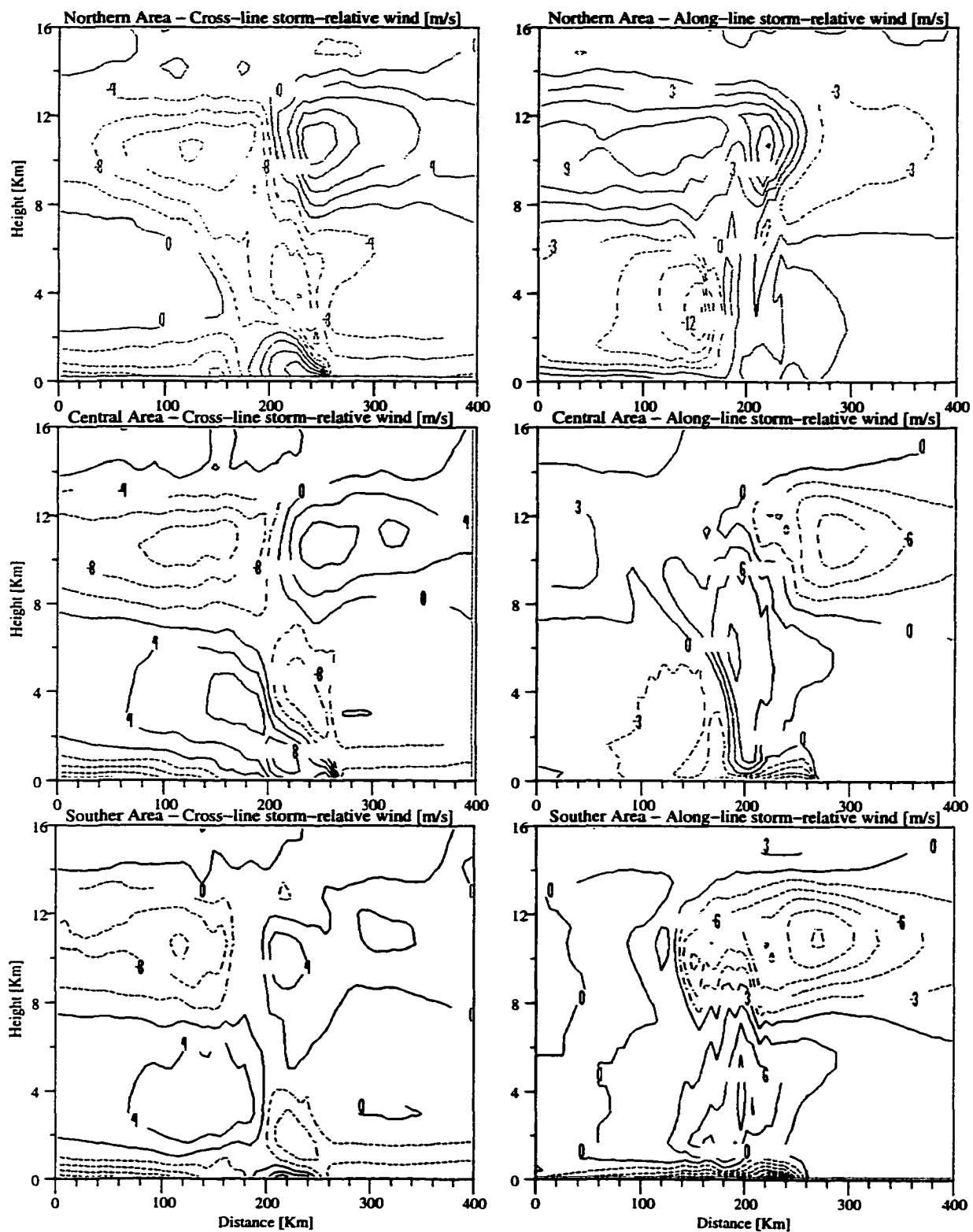


Figure 2.28. Same as in Fig. 2.27 except for the storm-relative flow at 5:30 hours into the simulation. The central averaging area is illustrated in Figs. 2.3, 2.17, 2.18 and 2.19

northern end convection leads which leads to weakening of the mesoscale RTF is in turn responsible for the decrease in the low-level convergence there and results in weakening in the convective activity. Finally, Fig. 2.29 presents northern and central portion averaged cross-sections of the cross-line and along-line flow component in the MT-LI simulation at 7:20 hours into the simulation. A comparison with the MF-LI structures at this time (Fig. 27) reveals that while the central portion flow structures were very similar between the two simulations, their northern areas were different. Indeed, the RTF was stronger in the MT-LI case as compared to the MF-LI case. This is another indication that the midlevel mesolow was located closer to the northern end convective line in the MT-LI case. The result was enhanced low-level convergence and more upright and apparently stronger northern end convection in the MT-LI case as compared to the MF-LI.

3. Summary

This study investigated the sensitivity of the simulated storms and their remotely sensed characteristics, namely radar reflectivity and microwave brightness temperatures, to the microphysical parameterizations used in a non-hydrostatic adaptive-grid three-dimensional cloud model. Unlike previous studies that examined widely different parameterization schemes, this study focused on two sets of microphysical parameterizations that are very similar – a graupel version of Tao et al. (1993a) and the single-moment three-ice version of Ferrier (1994). Both employ a two-class liquid (cloud water and rain) and three-class ice-phase (cloud ice, snow and graupel) set of parameterizations.

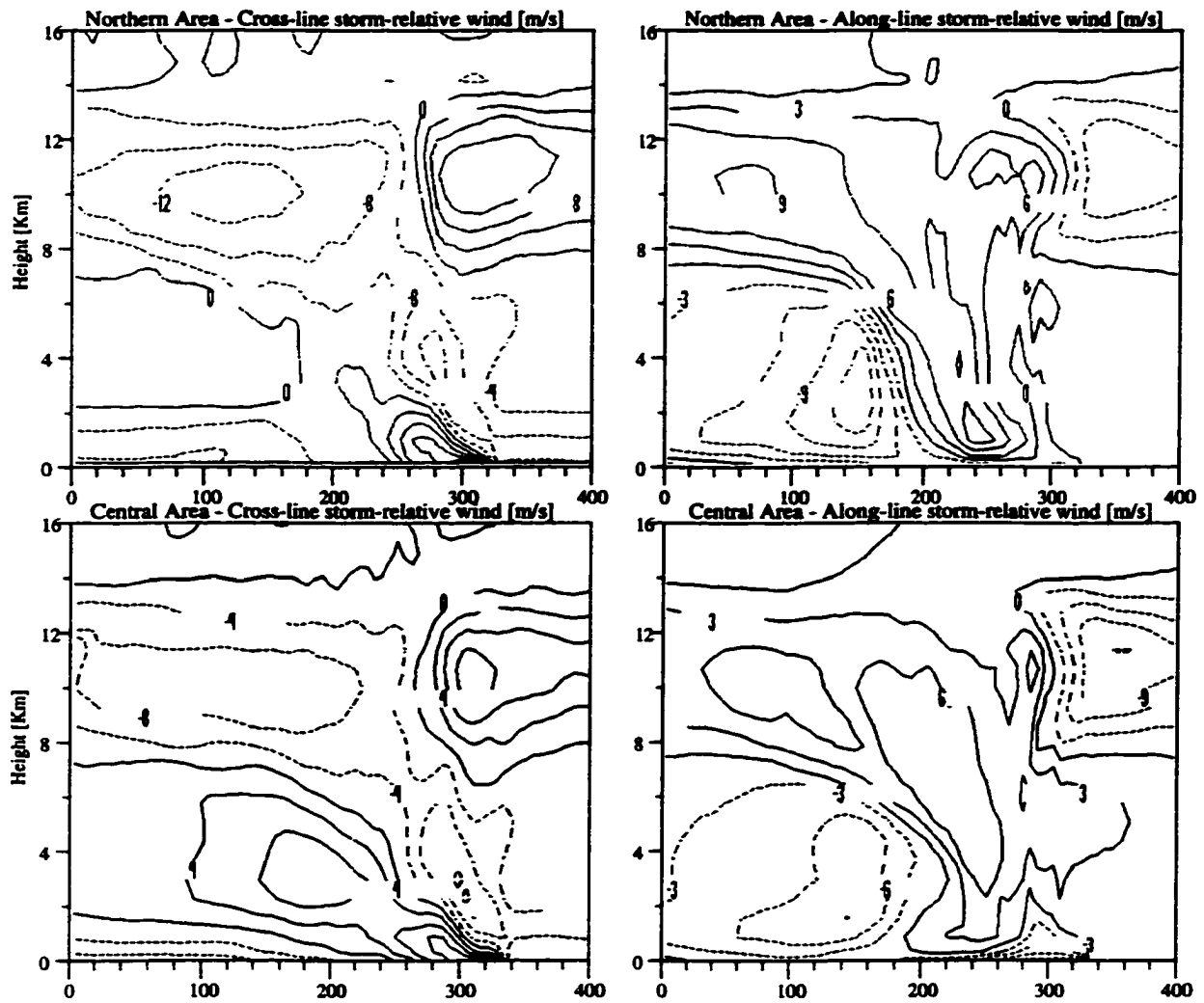


Figure 2.29. Same as in Fig. 2.27 except for presented is the storm-relative flow produced by the MT-LI simulation. The southern area flow is not presented.

An environment conducive for the formation of a non-severe midlatitude squall line system was selected to allow examination of both convective and stratiform rain regions. One set of simulations was performed using the original graupel, three-ice versions of Tao et al. (1993a) and Ferrier (1994) microphysical schemes. To determine the impact of differences in parameter values versus differences in the implementation of microphysical processes in the two schemes, a second set of simulations was performed in which all the common parameters were set to equivalent values representative of midlatitude conditions with limited abundance of cloud ice nuclei. In that set of simulations the primary differences that remained were related to cloud ice initiation, Bergeron growth for snow and the saturation adjustment procedure. Finally, a third set of simulations was conducted in which it was assumed that the environment had sufficient amount of cloud ice nuclei so as to absorb almost all of the ice-supersaturated water vapor provided by the updrafts and to severely limit the condensation of supercooled cloud water. This choice has been justified by the results from recent field campaigns that have indicated the presence of significant amounts of ice particles and the relative absence of supercooled cloud water in tropical convection. Furthermore, conducting this third set of simulations helped to further separate the impact of the assumptions about the cloud ice nuclei concentrations (NCI and NCIO) from the impact of the assumptions about the collection efficiencies of the colliding ice particles. Both of these sets of parameters (NCIO and collection efficiencies) proved to play important roles in determining the structure of the simulated storms and their remotely-sensed characteristics. Unfortunately, the limited observational studies of these parameters are

still insufficient in providing adequate guidance in the selection of parameter values for the purpose of numerical cloud modeling.

Even though the original parameterization schemes follow the same basic paradigm, the differences between them were enough to significantly impact the simulated storm dynamics and remotely sensed characteristics. After the modifications and in the case of the low cloud ice nuclei environment (low NCIO) the storm dynamics became more similar. Still, the storm sizes, radar reflectivity structures and stratiform area heating profiles remained very different. Finally, the two microphysics produced the most similar storm structures in their high-ice-nuclei mode (the MT-HI and the MF-HI cases which had high NCIO). Even then the two simulations differed significantly in their stratiform area mean precipitation intensity and precipitation-scaled latent heating profiles. For the set of simulations conducted here, the two microphysical schemes could not be tuned to simultaneously produce agreement in storm dynamics, effect upon the environment (latent heating and surface precipitation) and remotely-sensed characteristics (radar reflectivity structure and the passive microwave brightness temperature relations). In terms of remote-sensing retrievals of precipitation and latent heating this indicates sufficient level of uncertainty associated with the assumptions made in building the cloud-radiation databases. It also suggests that attention to these assumptions should be made and that cloud-radiation databases should be made more comprehensive by the inclusion of simulations with different microphysical schemes and parameters.

Following is a summary of the more specific conclusions of this study.

The choice for collection efficiency and autoconversion thresholds plays a role in determining the size and intensity of the simulated systems. Higher collection efficiencies for the colliding ice particles result in more intense convective and stratiform areas. The two extremes are represented by the choices in OT-LI and OF-HI. While OT-LI (highest efficiencies) produced the most intense convective area of all six simulations, OF-HI (smallest efficiencies) produced not only the weakest but also the smallest system. Apparently, giving preference to the production of non-precipitating cloud ice at the expense of precipitation (snow, graupel and rain) limited the development of the stratiform region and resulted in a smaller and less intense cold pool which in turn inhibited faster up-scale growth. Even during the early stages of the simulation, the lack of strong evaporative cooling in the OF-HI model run led to slower upscale growth and relatively weak convection in the southern part of the squall line. In contrast, the other simulations had stronger evaporative cooling which produced larger cold pool, correspondingly faster upscale growth, and stronger cells in the central and southern portion of the system.

The assumptions about the availability of cloud ice nuclei in the environment (NCIO) controls the production of supercooled cloud water (versus that of cloud ice). When supercooled cloud water is produced (low NCIO) the graupel and rain production is stimulated and this leads to the generation of more intense convective area precipitation. Stronger convective area is associated with weaker stratiform area in Tao and a *relatively* smaller system. In Ferrier, a stronger convective area that is produced in the presence of supercooled cloud water is associated with smaller but also stronger stratiform area as compared to the case of no supercooled cloud water. This different

behavior in response to NCIO changes between Tao and Ferrier can be attributed to the additional graupel growth mechanisms that Ferrier has. These mechanisms are activated in the presence of supercooled cloud water and higher ice-supersaturations and result in faster production of precipitation-sized particles, thus, speeding up the fall out of the condensate and increasing the intensity but limiting the size of the stratiform area.

The full impact of the philosophical differences between the two microphysical schemes is revealed in comparing the two simulations which used equal microphysical parameters and where ran under the assumption of limited cloud ice nuclei availability (low NCIO) resulting in the production of abundant supercooled cloud water – MT-LI and MF-LI. In that case Ferrier and Tao produced similar in size and intensity convective areas but their stratiform areas were very different in both size and intensity, with Tao producing larger stratiform region but with less intense mean precipitation, vertical velocity and latent heating profiles. These are possible reasons for the observed differences: i) storage differences – a very important factor limiting the size of the stratiform area in Ferrier is that cloud ice is allowed to stay to the prescribed amounts and is actually accumulated there (as illustrated by larger stratiform means as compared to the convective ones). In Tao, on the other hand, the cloud ice is continuously converted to snow (this explains the very low amounts of cloud ice in Tao) and, thus, forced to precipitate out, increasing the size of the stratiform area; ii) production differences – the second reason is probably related to the fact that Tao always uses more of the convective area water vapor to produce cloud ice there. This results from the *continuous* ice initiation and the use of the ice-water saturation adjustment. This condensate quickly converts to snow and is transported backward into the stratiform area

where it contributes to the stratiform precipitation production. Both the higher cloud ice production and depletion rates in Tao as compared to Ferrier explain the relative insensitivity of the Tao simulations to the choices for NCIO parameter. In Ferrier, in the case of low NCIO, less water vapor is used in the convective area since cloud ice is not produced in significant amounts at lower levels and this leaves the water vapor at closer to water-saturation values. Furthermore, less snow is produced in the convective area. This limits the amount of cloud ice and snow exported from the convective into the stratiform area and, hence, further limits the possible size of the stratiform area. However, the water vapor which remained unused in the convective area is also transported backwards and is used in the stratiform area where it enhances the cloud ice and snow growth. The additional latent heat that is released, as compared to that in MT-LI, gives rise to stronger vertical velocities and the subsequent production of stronger ice-supersaturations and more supercooled cloud water. This, in turn, leads to increased production of graupel (due to the additional graupel growth mechanisms that Ferrier has) and speeds up the precipitating out of the condensate, thus even further limiting the extent of the stratiform area but increasing its intensity.

The storm dynamics is also affected by the microphysical parameterization philosophies and by the choice of microphysical parameters. Realizations which produce large or intense stratiform areas show a tendency to develop a well defined midlevel mesolow earlier in their lifetime. This mesolow alters the orientation and the shape of the convective line by modifying the orientation of the midlevel rear inflow and the subsequent production of stronger low-level mesoscale outflow in the northern end of the line as compared to the cases with less developed mesolow. The increased

northern end convergence associated with this mesoscale outflow aids the northern end convective development and this leads to a more linear (as compared to "bowing out") structure during these early mature stages. A linear structure and a well defined midlevel mesolow alter the upper-level buoyant outflow by focussing it into a streak that spreads backward from the convective line. In turn, this modified upper-level outflow alters the midlevel pressure field "pulling" it southward and backward and, thus, contributing toward its even faster separation from the northern convective end. The separation of the midlevel mesolow leads to weakening its support of the northern-end convection while the central portion of the convective line remains strong and the southern end continuous to grow and expand. All this illustrates the importance of the scale interactions between the convective and the stratiform regions of the mesoscale convective systems and highlights the impact which microphysical parameterizations can have on the dynamics of the simulated storms. It also points to the fact that proper representation of both the convective and the stratiform regions is very important for simulating realistic storm structures and evolution.

While the presented simulations are not of a particular storm, they reproduced strikingly well the important characteristics of observed MCCs (Houze et al., 1990; Hristova-Veleva and Biggerstaff, 1994). In particular, the along-line variability in structure and evolution of the convective line with the most intense convection located at the southern end of the line, the asymmetric precipitation structure with the stratiform area located behind the northern portion of the convective line, the structure of the mesoscale flow at all levels, the development of a midlevel Mesoscale Convective

Vortex (MCV) and its interaction with the leading convective line, all are remarkably similar to observed over the central United States.

The upper-level reflectivity means and distributions were mostly affected by the amount of snow at these levels. Since Tao gives preference to the snow production at the expense of the cloud ice, it tends to produce stronger upper-level reflectivity. Differences of up to 5 dB were found in the area and time-averaged vertical profiles of radar reflectivity at levels above 8 km (the most different at these levels were OT-LI and MF-LI).

Microwave brightness temperatures for the scattering frequencies (37 and 85.6 GHz) and their relationship with the underlying columnar liquid water were most strongly affected by the amount of supercooled cloud water in the graupel layers (which amount is dependent upon the choices for NCIO). This supercooled cloud water absorbs some of the energy scattered by graupel and re-emits it. This process warmed the 85.6 GHz brightness temperatures by as much as 40° in this set of simulations (Seo et al, 2000) and also widened the distribution of 85.6 GHz brightness temperatures that were associated with a given amount of columnar liquid water. When Ferrier and Tao were ran with the same set of parameters and in the case of super cloud water production, Ferrier produced slightly warmer 85.6 GHz brightness temperatures for the same amount of total liquid water in the column. This is likely related to the fact that in the case of low NCIO Ferrier tends to produce more supercooled cloud water than Tao.

For the passive microwave frequencies examined here, snow and cloud ice did not contribute significantly to any of the brightness temperatures (Seo et al., 2000).

Tuning the model microphysics to ensure similar brightness temperature relations does not imply that the distribution of all hydrometeors will be the same.

For simulated storms with similar brightness temperature relations, it was found that differences in cloud ice production affected the magnitude and altitude of the maxima in area and time-averaged latent heating profiles, especially in the stratiform region. In Ferrier, the altitude of the peak shifted in accordance with the level where intense cloud ice production was allowed. This level dependent upon the cloud ice nuclei availability (NCIO) assumptions. In Tao cloud ice was always produced at levels closer to freezing and not allowed to accumulate. This resulted in the simulation of latent heating profiles with constant altitude of the peak and only its intensity dependent upon the NCIO assumptions. In both microphysics, production of higher amounts of cloud ice per unit rain led to mean latent heating profiles with stronger upper-level peaks. In that sense, microphysical schemes that produce storms with different precipitation efficiency will also produce different heating profiles. Retrievals of latent heating from passive microwave observations may suffer large uncertainties at upper levels due to insensitivity of most brightness temperature observations to cloud ice.

In addition to uncertainty in latent heating retrievals, the different brightness temperature relations associated with the different amounts of supercooled cloud water produced in the model will also impact retrievals of rain from passive microwave measurements. This uncertainty will be largest for retrievals over land where the strong and non-uniform surface emissivity limits the retrievals to using only the higher frequencies associated with scattering and most strongly affected by the unknown amounts of supercooled cloud water.

CHAPTER III

IMPACT OF PARTICLE TERMINAL VELOCITY AND SIZE DISTRIBUTION PARAMETERS ON SIMULATED STORM STRUCTURE, DYNAMICS AND REMOTELY-SENSED CHARACTERISTICS. SIMULATION OF A TROPICAL SQUALL LINE

1. Background

In their study of the impact of microphysical parameterizations on simulated storm characteristics McCumber et al. (1991) showed that the choice for the descriptive parameters (i.e. density, terminal velocity and the intercept parameter of the assumed reverse exponential particle size distribution) of the large ice category in three-ice-class microphysical schemes has the most profound effect upon the modeled storms, while the impact of the different parameterization of the microphysical processes was much less significant. Furthermore, they suggested that a cloud ice-snow-graupel combination should be preferred when simulating tropical convection. They suggested that selecting graupel instead of hail as the large-ice category should be more appropriate to represent the large stratiform precipitation that is often observed in association with tropical convection. The smaller terminal velocity, lower density and the assumed large number of graupel particles resulted in large amounts of graupel being suspended by the strong convective updrafts. This allowed the graupel to enter the anvil region of the storm system where it became an important constituent of the anvil cloud and led to the simulation of the melting level radar bright band that is commonly found in stratiform

clouds. While many studies have inarguably shown that the inclusion of smaller and more slowly falling ice particles contributes to the development of more realistic stratiform precipitation in modeled storms, what the particular choices for particle parameters should be remains still an area of active research.

Indeed, Ferrier (1995) questioned the choice for the descriptive parameters for graupel that was made in McCumber et al. (1991). In particular, he pointed out that the parameterized graupel was low density and had slow terminal velocity despite the fact that a non negligible portion of the graupel was initiated by the freezing of supercooled raindrops, which should result in much denser, faster falling ice than parameterized by graupel. He further supported the idea of using faster falling denser graupel in model simulations by referring to observations using video cameras on radiosondes that indicated that frozen raindrops were the dominant ice class in the convective portions of Micronesian rainbands at temperatures warmer than -10°C .

Furthermore, Ferrier (1995) suggested that the intercept of the assumed graupel size distribution might have been too small resulting in the simulation of fewer but larger graupel particles. Indeed, when he used the same parameters in the simulation of a GATE squall line, the simulated bright band was stronger than the observed. an indication of the presence of very large melting particles in the simulation. Once again, observations of tropical convection seem to indicate that, indeed, the number concentrations of ice particles are much larger than it was previously thought. Indeed, studying two-dimensional images of ice particles observed during the Summer Monsoon Experiment (SMONEX), Gamache (1990) found that the mean size distributions of total particle concentration in the -10 to -22°C interval in convective

clouds could be represented with an inverse exponential function with intercept parameter on the order of 10^8 (see his Fig. 1). The total number of particles in this case included, of course, not only graupel particles but also branched and column particles (representative of snow and ice crystals). However, the contribution to the total sample of the later two types was very small while the majority of the particles were aggregates or indeterminable (likely heavily rimed crystals) which are represented as graupel in the model. Furthermore, recent observations from tropical field campaigns in support of TRMM seem to suggest the same, namely, that in tropical convection there are large numbers of ice particles even at levels just a few degrees below freezing. This finding is consistent with the small quantities of supercooled cloud water that were independently measured in situ and could also be inferred from the measured microwave brightness temperature relations. All this presents a picture of nearly completely glaciated convective updrafts. Gamache (1990) pointed out that the high ice particle concentration in convective updrafts and the absence of supercooled liquid water would inhibit the production of large particles and few would fall out in the convective area while many small particles would be transported into the stratiform region. This could explain the observed low convective precipitation efficiency of tropical squall lines as well as the presence of deep stratiform clouds.

Measurement of rain Drop Size Distributions (DSDs) has an even longer history to that of ice particle distributions. However, observational studies have provided widely different distributions depending on the experiments created to measure them. Measurement from many geographical regions and rain types have shown that the reverse exponential distribution tends to be the limiting form when individually

observed drop size distributions are averaged (Rogers, 1979) even though each individual sample can show significant deviations from that form. Because of that, the most commonly used distribution is the reverse exponential distribution that was observed by Marshall and Palmer (M-P) (1948). Still, it appears that in the observations there are fewer of the very small and fewer of the large drops than that predicted by M-P. Indeed, many of the more recent studies have indicated that the DSDs are probably multi-peaked, as a result of the drop breakup processes, and that the peaks decrease the number of the large drops as compared to that predicted by M-P DSD (Valdez and Young, 1985). Furthermore, observations taken during TOGA COARE have indicated that convective and stratiform precipitation had different mean drop diameters with the convective region being characterized by a smaller mean diameter (Tokay and Short, 1994; Haddad et al., 1997). All this suggests that tropical convective rain would be better represented in cloud models by an exponential distribution with a larger intercept as compared to that of M-P so as to decrease the number of the large drops in accordance with observations. These large drops, which appear not to be commonly found in observations, would have the strongest negative impact on both the simulated radar reflectivity and microwave brightness temperatures. Indeed, Tesmer and Wilhelm (1998) found an improved agreement between observations and simulations of microwave brightness temperatures when they used a DSD with intercept five times larger than that of M-P which effectively decreased the opacity of the rain layer.

The sensitivity of modeled storms and their remotely sensed characteristics to the assumed parameters of the hydrometeors and their size distributions has been well

recognized. On the other hand, observational studies have indicated a wide variability in these parameters and, to date, have not been able to provide clear guidance in the selection of parameters for the purpose of cloud modeling and the development of rainfall retrieval algorithms from remotely sensed microwave observations. This study is conducted with the intent to shed more light on how the hydrometeor parameter choices affect not just a particular storm characteristic but the storm's micro- and macro-structure and evolution. Being able to reproduce the storm in its integrity will indicate that the complex intercorrelations between the different processes and scales are, indeed, properly represented by the model. This in turn, will give a high fidelity in the rainfall and latent heating retrieval algorithms using such databases (Panegrossi et al., 1998).

2. Experimental setup

a. Model setup and initialization

The microphysical parameterization scheme used here was taken from Tao and Simpson (1993) and is a hybrid version of Lin et al. (1983) (LFO) parameterization. In the current application the hail density, terminal velocity and intercept parameter of the assumed reverse exponential size distribution (Nog) were modified to values more typical of graupel parameters. Graupel was chosen as the large-ice category in this sensitivity study since a tropical convective system is simulated and tropical environments are generally not conducive for the development of strong vertical velocity and, hence, could not support the growth of very large and dense ice particles (hail). Furthermore, based on their modeling study, McCumber et al. (1991) suggested

that the use of graupel instead of hail leads to the simulation of more realistic stratiform precipitation.

A set of six simulations was designed to study the sensitivity of the simulated storm's structure, dynamics and remotely sense characteristics to the microphysical choices concerning the selection of the rain drop size distribution parameters and the selection of the graupel parameters (density, terminal velocity and size distribution). The choices of parameters for each of the six runs are given in Table 3.1. Two different formulas were used to compute the graupel terminal velocity – one was that given by Rutledge and Hobbs (1984) (RH) and the other by Lin et al. (1983). When applied to the graupel density and number concentrations assumed in this study, the two formulas resulted in computing mass-weighted mean terminal velocities which differed by about a factor of two on the average, with Lin et al. (1983) formula producing the faster falling particles. Philosophically, the selection of the one or the other formula reflects the underlying assumptions about what the "graupel" represents in a given simulation. If large aggregates are represented as "graupel", then the RH formulation of lower terminal velocity is more appropriate. On the other hand, if "graupel" represents highly rimed particles, then the LFO formulation should be more appropriate.

The initial model environment is horizontally homogeneous and given by the thermodynamic sounding (Fig. 3.1) taken from Trier et al., 1996. It is based on a composite of P-3 aircraft data and rawinsonde observations from Honiara, Guadalcanal taken in the environment just ahead of the squall line system that developed on 22 February 1993. The system's mature stage was well observed by many in-situ and remote-sensing instruments and its structure and evolution over a four hour period have

Table 3.1. Drop size distribution parameter for rain (Nor), density, terminal velocity and particle size distribution parameter for graupel (Nog) that are varied between the six simulations of the tropical squall line.

Simulation	400_8_4_	400_8_4	600_8_4	600_22_10	600_60_30	600_60_60
	<i>RHvt</i>					
Graupel						
<i>Density</i>	400 [kg/m ³]	400 [kg/m ³]	600 [kg/m ³]	600 [kg/m ³]	600 [kg/m ³]	600 [kg/m ³]
<i>Vt-formula</i>	RH*	LFO**	LFO**	LFO**	LFO**	LFO**
<i>Nog [m⁻⁴]</i>	4.10 ⁶	4.10 ⁶	4.10 ⁶	10.10 ⁶	30.10 ⁶	60.10 ⁶
Rain						
<i>Nor [m⁻⁴]</i>	8.10 ⁶	8.10 ⁶	8.10 ⁶	22.10 ⁶	60.10 ⁶	60.10 ⁶

* – graupel terminal velocity as given by Rutledge and Hobbs, 1984 (RH)

** – hail terminal velocity as given by Lin et al., 1983 (LFO) – here the graupel density and number concentrations are used instead of that of hail used by LFO

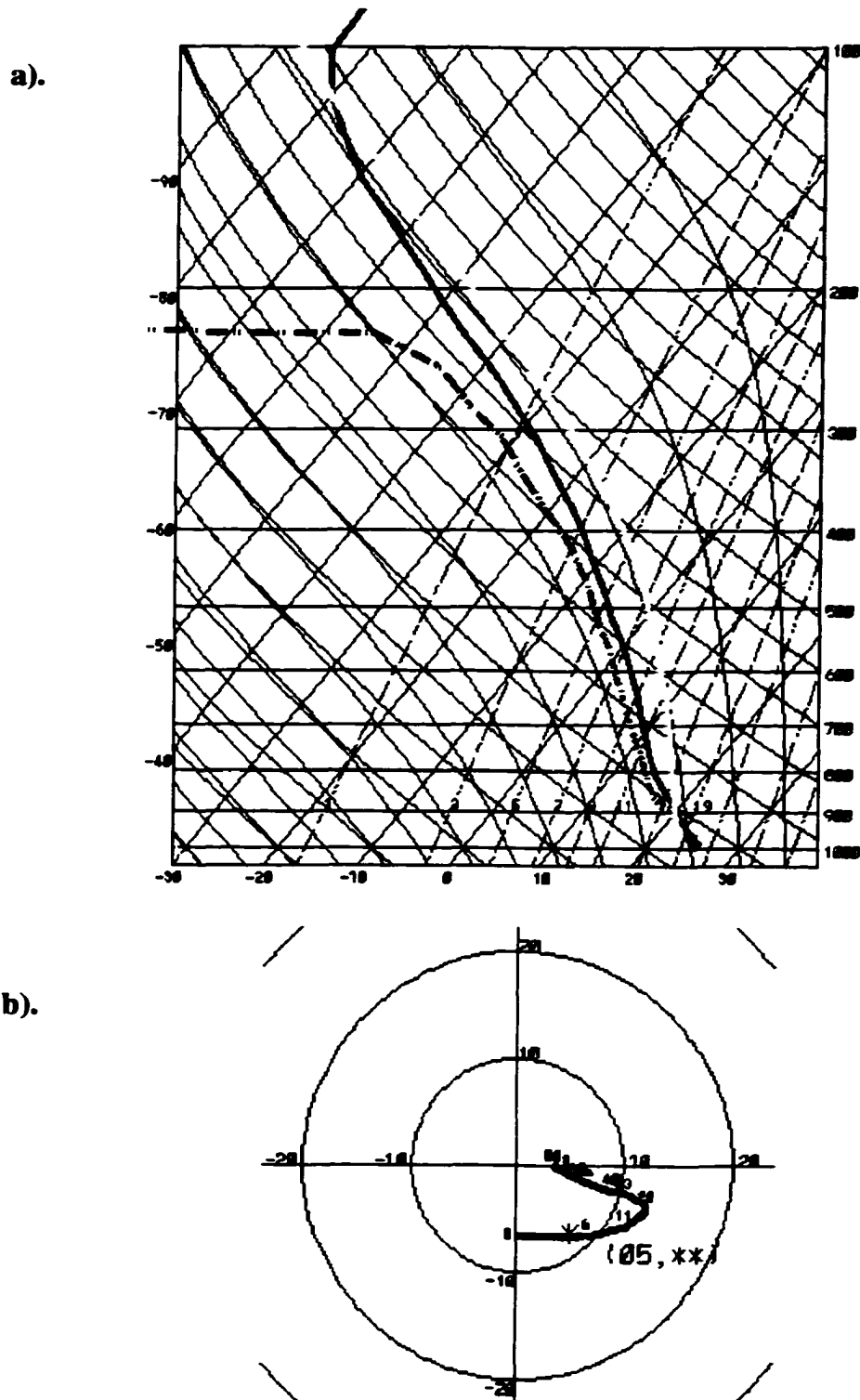


Figure 3.1. The tropical environmental conditions used to initialize the cloud model. (a) skew-T, log-P profile of temperature (red curve), and dewpoint (blue curve) in $^{\circ}\text{C}$, with path of an idealized parcel ascent given by the yellow curve. (b). hodograph (m/s). In (b), numbers indicate pressure levels.

been documented by Jorgensen et al., 1997. Furthermore, its passive microwave signatures and stratiform area reflectivity structure have been studied by McGaughey and Zipser (1996a, 1996b). The environmental conditions of 22 February 1993 squall line system have been used in several modeling studies (Trier et al., 1996; Trier et al., 1997; Olson et al., 1996; Olson et al., 1999). The fact that this squall line system has been the focus of many observational and modeling studies makes it a particularly good choice for our sensitivity modeling study.

Convection is initiated in the model by putting four warm bubbles in a 330° – 150° oriented line. Each of the bubbles was 3° warmer than the environment and had 20 km horizontal and 2.8 km vertical dimensions. The bubbles were placed 25 km apart.

The model domain has a horizontal extent of 900x900 km and a vertical extent of 23.35 km. The vertical resolution is 200 m at the surface and stretching to 700 m at levels above 1 km. Three levels of grid refinement were used. The coarse grid had a horizontal resolution of 18 km. The refinement ratio is 3:1 resulting in a grid spacing of 2 km on the finest grid where convection is resolved. The model generated variables were recorded at 6×6 km² horizontal resolution and with a temporal resolution of 10 minutes. Radar reflectivity was calculated from the hydrometeor fields under an assumption of 10 cm wavelength. Using the radiative transfer model, microwave brightness temperatures were computed at five different frequencies and two polarizations. The data presented here were computed at nadir and over an ocean background. The ocean surface was assumed to be specular as suggested by Tesmer and Wilheit (1998). The temperature and the wind at the lowest model level were used to compute the surface emissivity. All points containing precipitation somewhere in the

vertical were classified as convective, stratiform or non-precipitating anvil (virga) following the criteria given in Chapter II.

3. Results

a. Overview of the storm structure and the convective/stratiform partitioning

Figure 3.2 presents the maximum reflectivity in the column for each of the six simulations at six hours into the simulation time. Figure 3.3 gives the results of the convective/stratiform separation. A quick comparison among the six simulations reveals that the storm organization, scale and convective/stratiform separation are very sensitive to the selection of Particle Size Distribution (PSD) parameters and the terminal velocity of the large-ice particles. It appears that varying the graupel density in the range of 400 to 600 kg/m³ does not have a significant impact.

The impact of the terminal velocity selection for the graupel particles is evident from the comparison of the simulations in Figs. 3.2a and 3.2b. It appears that the overall system scale does not change much. Furthermore, in both cases the convection seems to be organized in isolated, highly three-dimensional cores. However, what is different between the two simulations is the size of the convective cores. While in the case of the low graupel terminal velocity (Fig. 3.2a) the convective cores are large, they become much smaller and more numerous in the case of the higher terminal velocity (Fig. 3.2b). Indeed, in his comparative study Ferrier (1995) found the same tendency for simulation of broader reflectivity cores when lower graupel terminal velocities are used and attributed this to the graupel falling over a larger area due to its lower fall speeds in that case. A better appreciation of the impact of the graupel parameter

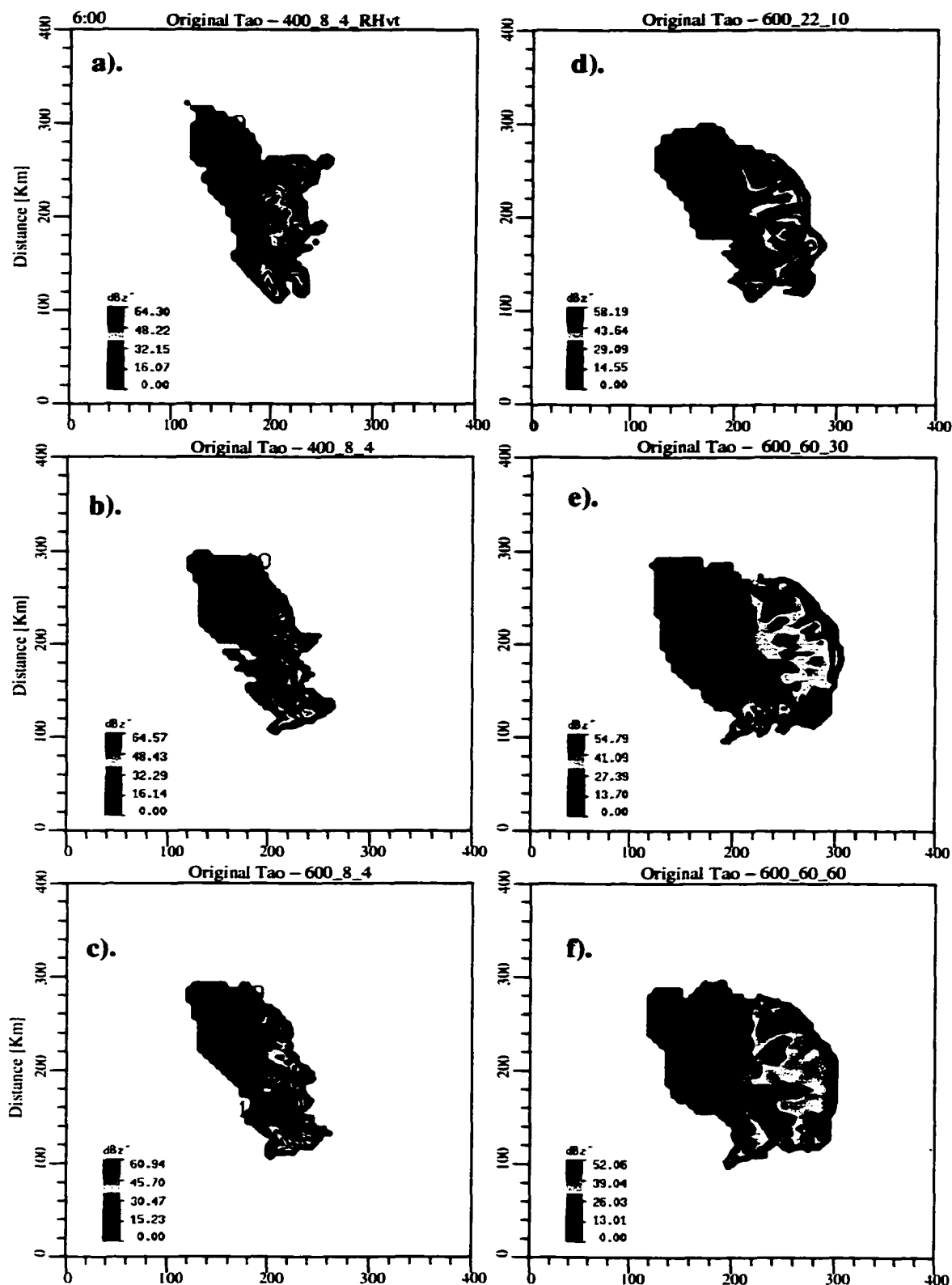


Figure 3.2. Radar reflectivity (in dBz) computed from the hydrometeor fields generated by the cloud model at 6 hours into the simulation time. Presented is the maximum reflectivity in each 6x6 km² column. Model domain is 400x400 km². Each of the six panels presents the reflectivity field that corresponds to a particular model run: (a) 400_8_4_RHvt; (b) 400_8_4; (c) 600_8_4; (d) 600_22_10; (e) 600_60_30; (f) 600_60_60. See Table 3.1 for details on the model setup.

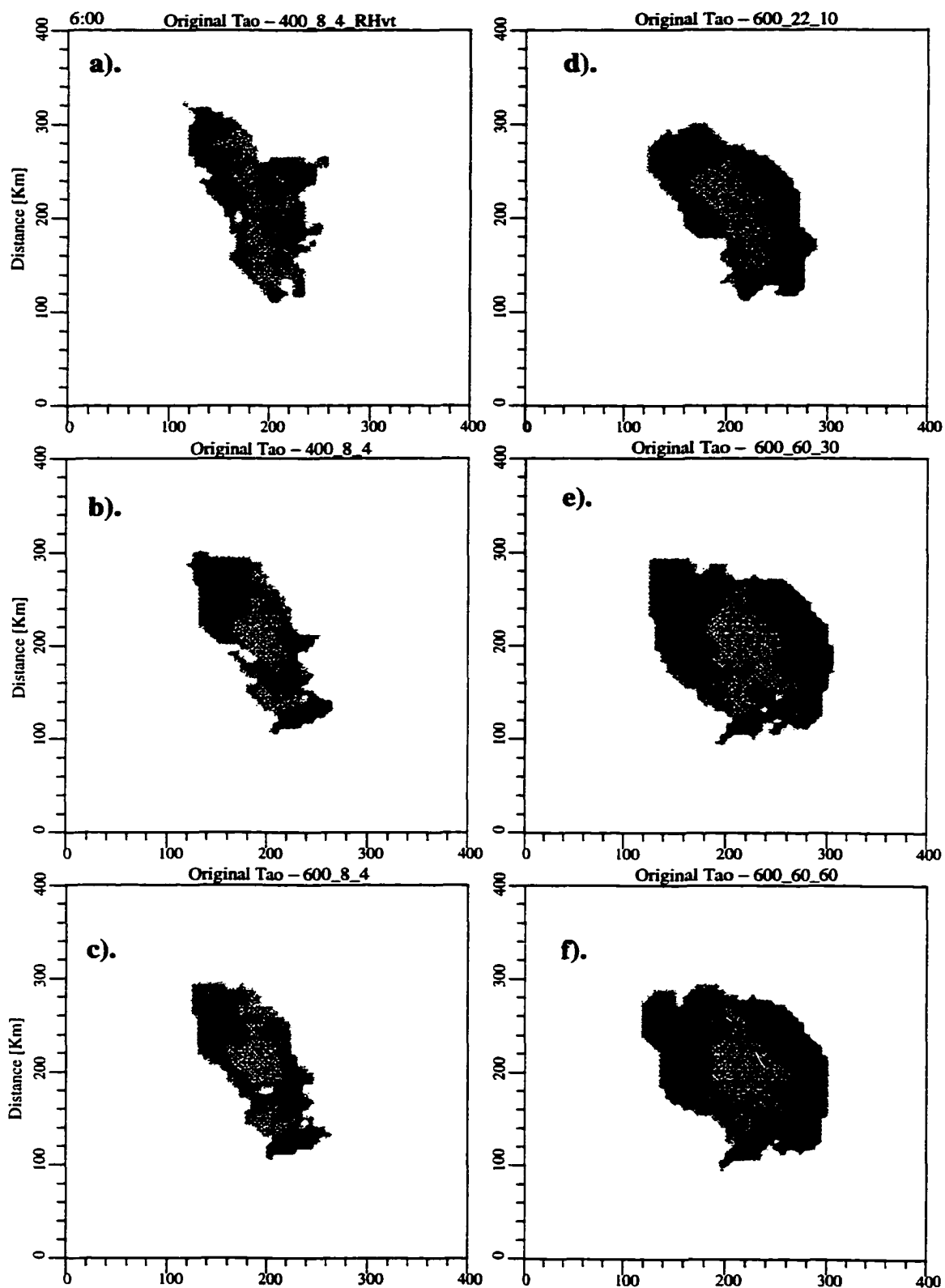


Figure 3.3. Same as in Fig. 3.2 except for presented are the results of the convective / stratiform/ non-precipitating anvil separation. The convective region is plotted in black, the stratiform region - in light gray and the non-precipitating anvil - in darker gray.

selection (terminal velocity, density and number concentration, as specified by the intercept of the graupel particle size distribution – N_{og}) can be obtained by investigating the CFADs (Contoured Frequency by Altitude Diagrams – Yuter and Houze, 1995) of reflectivity over the convective region (Fig. 3.4). A comparison of the upper level reflectivity structures is particularly revealing. When the graupel terminal velocity was chosen to be very small (the 400_8_4_RHvt simulation – Figs. 3.2a, 3.3a and 3.4a) the most common reflectivity value at 8 km altitude was 45 dBz. This reflectivity value is too high for that altitude according to observations which show that in tropical convection reflectivity decreases quickly with height at levels above freezing (Zipser and Lutz, 1994) and that the 30 dBz contour rarely exceeds 6 km altitude even in the Pacific warm pool area (DeMott and Rutledge, 1998) where deep convection is often found. Apparently, selecting a small terminal velocity for the graupel particles resulted in significant amounts of graupel being suspended at higher altitudes by the convective updrafts. Indeed, when the terminal velocity was increased by about a factor of two (the Lin et al., 1983 formulation except for using the graupel density and number concentrations as given by Rutledge and Hobbs, 1984) the most common reflectivity value at 8 km altitude rapidly dropped to ~21 dBz in much closer agreement with observations. Furthermore, assuming that the graupel mass was distributed among a higher number of smaller graupel particles (i.e. increasing the N_{og} value) led to further decrease in the reflectivity at levels above freezing. For example, while in the $N_{og}=4.10^6 \text{ m}^{-4}$ case (Fig. 3.4c) the 1% $\text{dBz}^{-1}\text{km}^{-1}$ contour is at ~49 dBz at 8 km, this value drops to ~46 dBz in the $N_{og}=10.10^6 \text{ m}^{-4}$ case (Fig. 3.4d) and further on to ~42

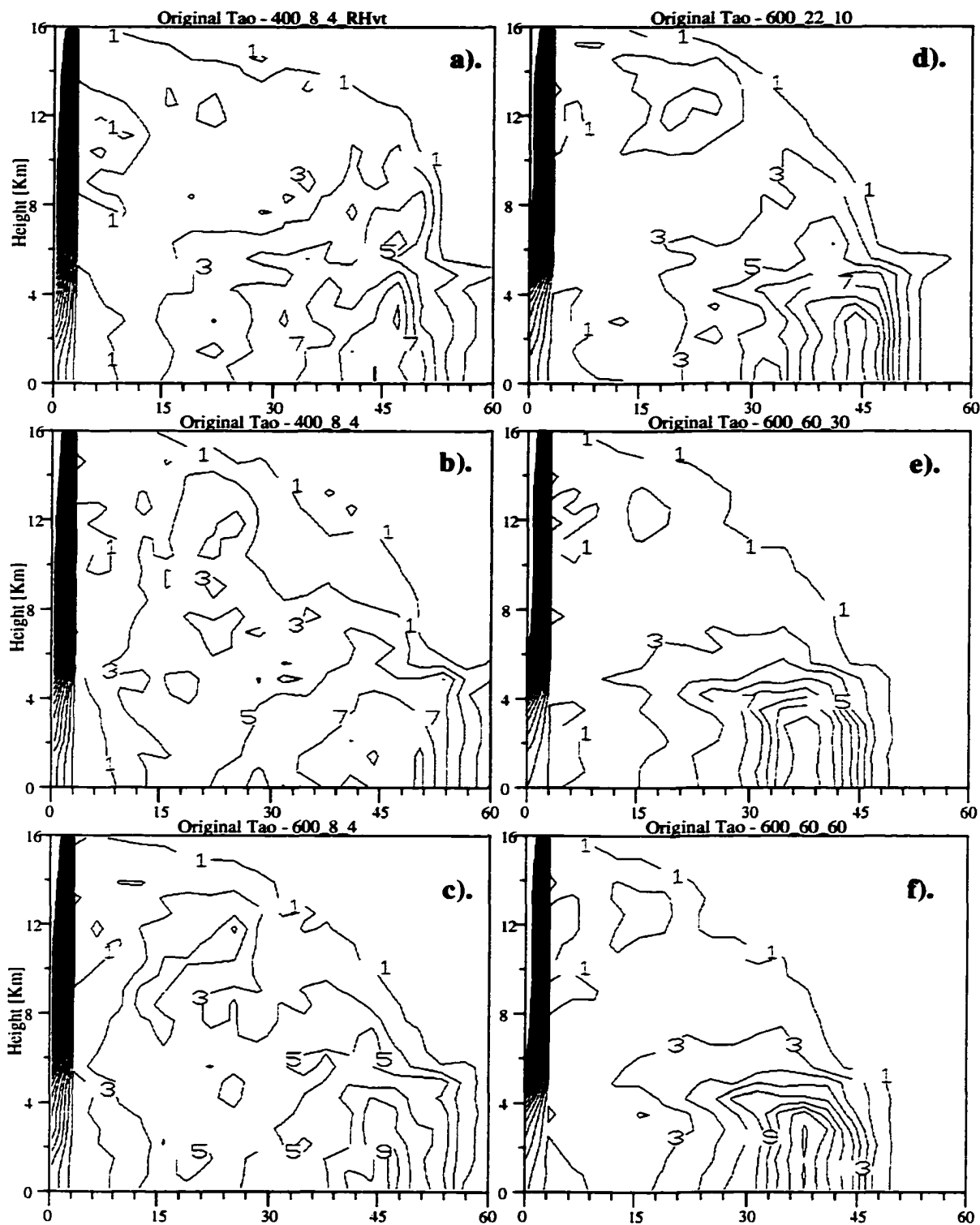


Figure 3.4. Contoured frequency by altitude diagrams of reflectivity for each of the six simulations presented in Fig. 3.2. CFAD statistics were computed separately over the convective ((a)-(f)) and the stratiform regions ((g)-(l)). Contours are every 2 % of data per dBz per km. The frequency distribution of reflectivity was computed at each model level (every ~700 m) and the reflectivity bin size was 3 dBz.

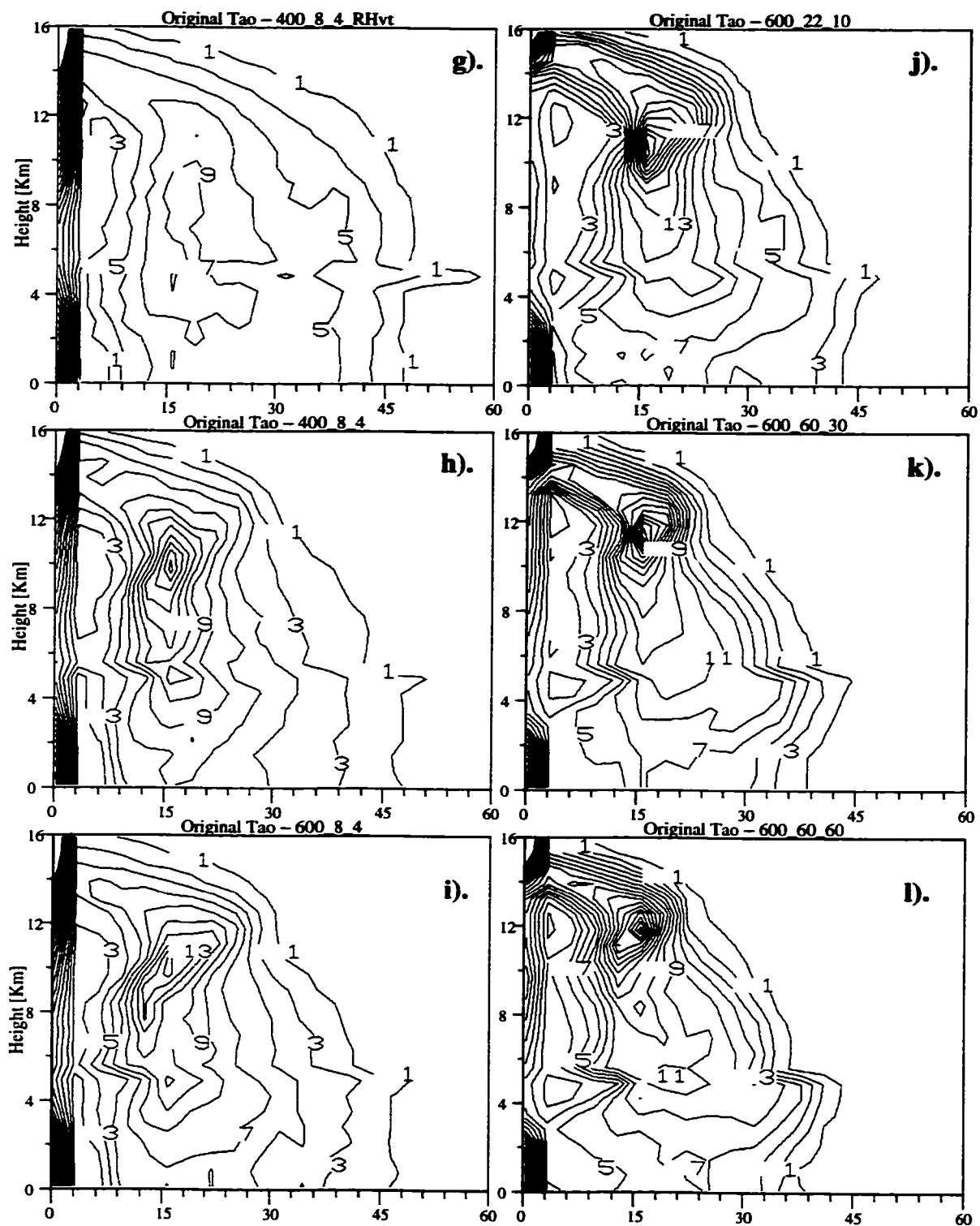


Figure 3.4. (Continued)

dBz in the $Nog=30.106 \text{ m}^{-4}$ (Fig. 3.4e), and to ~ 39 dBz in the $Nog=60.106 \text{ m}^{-4}$ case (Fig. 4f).

A closer look at the reflectivity structure (Fig. 3.2) shows that both the scale of the system and the organization of the convective cores changed rather drastically when the parameters of the particle size distributions changed. In particular, modifying the rain DSD to represent a larger number of smaller drops by changing the intercept parameter from the M–P value of $Nor=8.10^6 \text{ m}^{-4}$ to $Nor=22.10^6 \text{ m}^{-4}$ resulted in the production of a larger system (compare Fig. 3.2c and 3.2d). Further increase in the Nor parameter (Figs. 3.2e,f) led to the production of even larger systems. Maybe even more importantly, the structure of the convective region changed when the Nor was increased from the M–P value. All three simulations which used the M–P value (Figs. 3.2a–c) exhibited convective organization of isolated, rather strong but relatively small (with the exception of 2a) convective cores. In contrast, when the Nor value was increased (and the number of large rain drops decreased) the convective area became progressively more homogeneous and two–dimensional. This is clearly illustrated by the 40 dBz contour line which was highly fractionated in the first three simulations (the M–P cases) but became a rather continuous, unbroken area in the later three. The transition to a more homogeneous convective area with the increase in the number of small drops in the rain distribution is further illustrated by the CFADs of reflectivity over the convective region (Fig. 3.4). Indeed, the three M–P simulations (400_8_4_RHvt, 400_8_4 and 600_8_4 – Figs. 3.4a–c) had wider distributions signifying a higher variability in the reflectivity values at each level and, hence, a higher diversity in the structure of the reflectivity region. On the other hand, with the increase in the Nor value

for the rain distribution, the convective regions of the resulting simulations had progressively narrower CFADs of reflectivity (Figs. 3.4d–f), indicating that a particular value of reflectivity was the most common at a given altitude. Furthermore, the CFADs illustrate that when the N_{or} increased, the most common reflectivity value at levels below melting dropped from ~ 47 dBz in the M–P case (Fig. 3.4c), to ~ 44 dBz when $N_{or}=22.10^6 \text{ m}^{-4}$ (Fig. 3.4d), to ~ 38 dBz in the cases of $N_{or}=60.10^6 \text{ m}^{-4}$ (Figs. 3.4e–f). Of course, this is to be expected since the reflectivity is proportional to sixth power of the particle diameters and, hence, not having many large particles in the last three simulations should result in lower reflectivity values even if the total amount of rain remains the same or is slightly higher as will be later shown to be the case here.

In comparing the storms between Figs. 3.2c, 3.2d and 3.2e, it might be a bit difficult at first to attribute all the changes in the storm structure and scale to only the changes in the rain distribution parameters, since the graupel distribution parameters were also changed between these simulations. However, a comparison between Figs. 3.2e and 3.2f reveals that, when only the graupel distribution parameters were changed, the storm structure did not change much and only the reflectivity behind the leading convective line slightly increased. This gives more credibility to our interpretation that the rain distribution parameters, instead of that of the graupel, play the controlling role in determining the convective organization and the scale of the system.

This notion is further supported when examining the cold pool structure. Indeed, the differences in the cold pool size and intensity between the six simulations are particularly revealing and provide the key to understand the observed changes in storm structure. Figure 3.5 presents the potential temperature perturbations from the

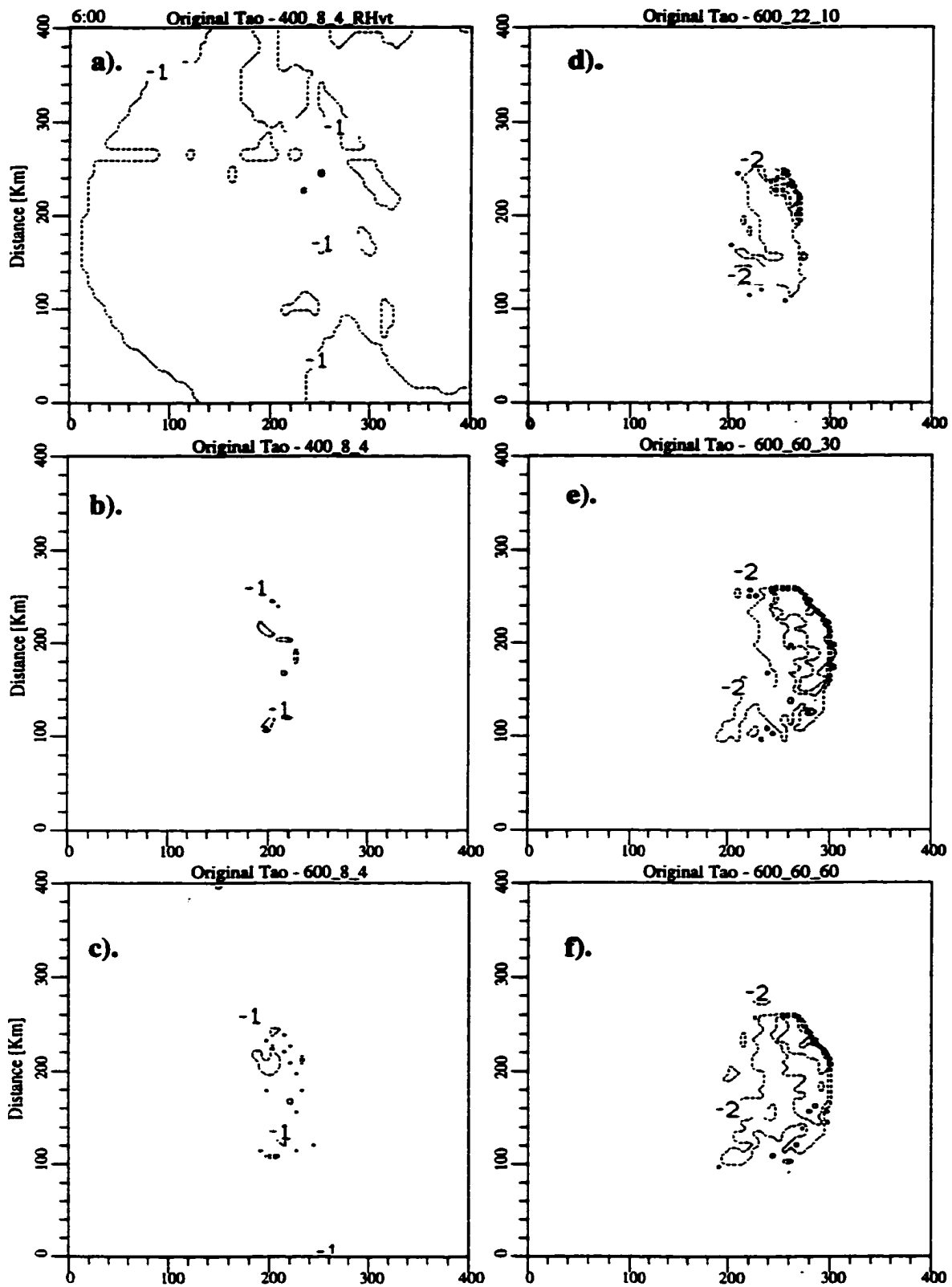


Figure 3.5. Same as in Fig. 3.2 except for plotted are the potential temperature perturbations from the initial conditions at 500 m above sea level.

environment (initial conditions) at 500 m (just above the second vertical model level) Above Sea Level (ASL). There is a stark difference between the three simulations that used a M-P DSD ($N_{or}=8.10^6 \text{ m}^{-4}$ – Figs. 3.5a–c) on the one side, and the three other simulations that used DSDs with larger number of smaller drops ($N_{or}=22.10^6$ and $N_{or}=60.10^6 \text{ m}^{-4}$ – Figs. 3.5d–f) on the other. Apparently in the three M-P simulations either the near surface rain was not too much or the assumed drops were too big to provide for significant rain evaporation and low level cooling in this moist tropical environment. The result was a very weak cold pool which lacked in spatial coherence. It is to no surprise that the convection occurred in isolated small cores, only in places where the convectively-produced cold pool was sufficient to trigger enough lifting. An interesting case is the one with the slow-falling graupel (the 400_8_4_RHvt case in Fig. 3.5a). In that case the cold pool was rather extensive but uniform and weak. New convection seems to have been triggered at the temperature gradients produced not by the convective low-level cooling but by the hydrostatically induced low-level warming that was induced by the upper-level subsidence right ahead of the strongest convection. To the contrary of the three M-P cases, when the assumed rain DSD was such as to represent a significant number of small drops, the simulated storms produced rather extensive and much stronger cold pools. These cold pools were apparently sufficiently strong along the entire leading edge of the storm system and, thus, were able to trigger new convection in a more spatially continuous fashion. This resulted in a much more two-dimensional and homogeneous appearance of the leading convective line.

Composite radar reflectivity patterns from the P-3's lower fuselage C-band radar, observed over the 22 February 1993 TOGA COARE squall line system (Fig. 3.6),

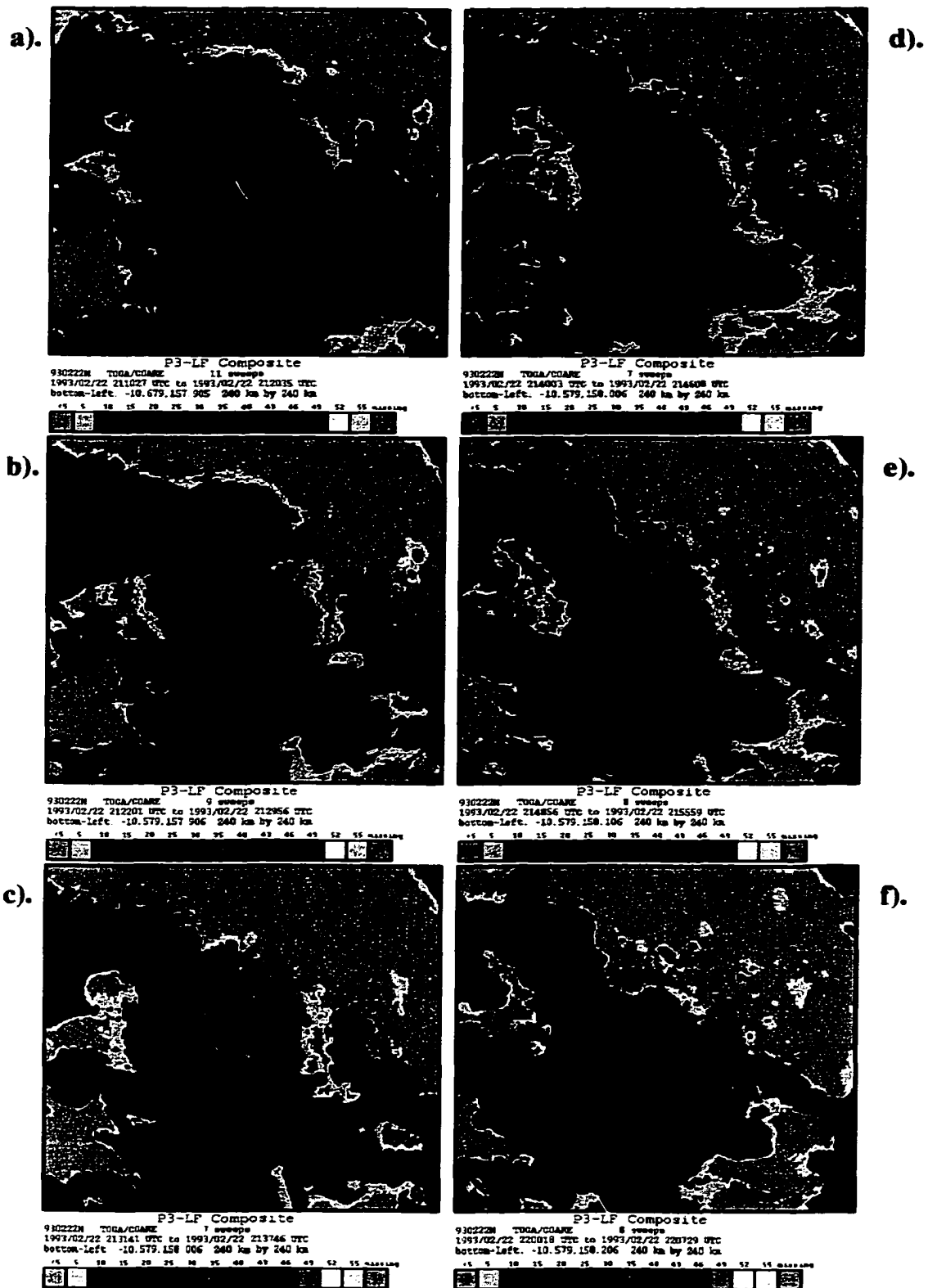


Figure 3.6. Composite radar reflectivity (dBZ) over the periods (a) 2110–2120 UTC, (b) 2122–2130 UTC, (c) 2131–2137 UTC, (d) 2140–2146 UTC, (e) 2149–2156 UTC, and (f) 2200–2207 UTC from the P-3's lower fuselage C-band radar, observed over the 22 February 1993 TOGA COARE squall line. Color scale for radar reflectivity is shown at the bottom of each panel. The domain of analysis is 240x240 km².

clearly indicate that in reality the leading convective line was, indeed, quite two-dimensional and rather homogeneous as illustrated by the 35 dBz contour line. This suggests that the smaller-raindrop size distributions might be more appropriate to use in simulating this particular storm. This cloud-model based finding is in agreement with the ground-based DSD observations taken during TOGA-COARE which indicated that tropical convection was, indeed, characterized by rather small mean drop diameters (Tokay and Short, 1994; Haddad et al., 1997). Indeed, the mass-weighted rain-rate independent mean diameter was ~ 1 (the convective value of D^* in Haddad et al., 1997) which would translate to $N_{or} = 90 \cdot 10^6 \text{ m}^{-4}$, under the assumptions of a reverse exponential distribution (Haddad, personal communications).

Further support for the appropriateness of the smaller-mean diameter DSDs for the simulation of this case comes from the comparison of the simulated cold pool intensity and that observed during in-situ measurements of the 22 February 1993 system. Jorgensen et al. (1997) have presented such measurements taken at 150 m ASL at the leading edge and 50 km behind the convective line. They indicate that under the intense convection in the northern bowing-out portion of the line the cold pool was about 3° C colder than the environment, while the temperature perturbation 50 km behind the convection was about 2° C colder than the environment. Again, the smaller-mean diameter DSD simulations are in much better agreement with these observations. Moreover, the agreement is remarkably good!

To further emphasize the importance of the cold pool forcing and its impact on the structure of the simulated convective organization, we would like to refer to a simulation of the same system (same initial environment) with the GCE model (Olson et

al., 1996; Olson et al., 1999). Their choice of microphysical parameters (graupel and rain density, terminal velocity and intercept of the reverse exponential particle size distributions) is equivalent to the one which we used in the 400_8_4 simulation (Fig. 3.2b). However, the structure of the storm in their simulations (see Fig. 3 in Olson et al., 1996 and Figs. 1 and 2 in Olson et al., 1999) is very different than the one which our corresponding simulation produced. In fact, their simulation appears to compare much better to reality and to our three simulations that had smaller-mean-diameter rain DSDs. The key to understand why that happened lies in the fact that they initialized their model with a pre-existing cold pool, while we initialized it with warm bubbles. Their pre-existing cold pool was apparently strong and extensive enough to hinder the fact that their choice of microphysical parameters would not have otherwise led to the production of such a cold pool. Their resulting simulation compared well to the reality in terms of storm structure (since in reality the system, indeed, produced extensive cold pool) but that does not necessarily mean that the simulated vertical hydrometeor structure and microwave characteristics would compare also so well.

The result of the convective/stratiform separation for each of the six simulations at 6 hours into the simulation were presented in Fig. 3.3. Before we continue with presenting the mean vertical profiles of hydrometeors over each of these two dynamically and microphysically different regions we would like to illustrate how the statistics of the convective/stratiform separation differed among the six simulations. Figure 3.7 presents the number of convective, stratiform and non-precipitating anvil points and their proportions. The more important things to note are the following: i). the convective area did not change at all in size between the three M-P simulations.

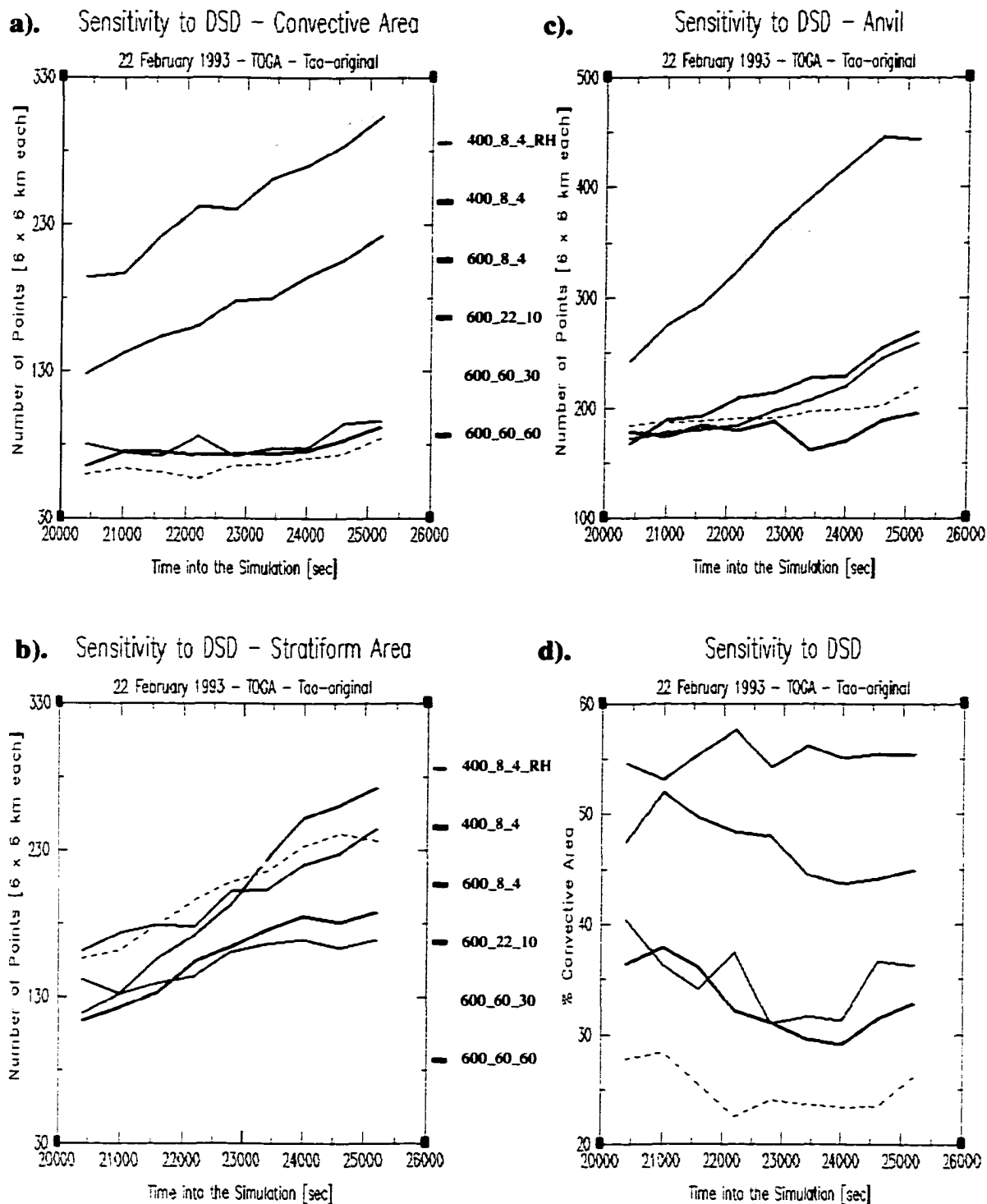


Figure 3.7. Convective (a), stratiform (b), and anvil (c) number of points between 5 h 30 min and 7 h simulation time for each of the six simulations presented in Fig. 3.2. Presented is also the % convective area (d) which is the ratio of the convective area to the combined convective and stratiform area.

Instead, it started to rapidly increase when the DSDs were of smaller-mean-diameter drops. Furthermore, when only the graupel particle size distribution was modified (the 600_60_30 vs. the 600_60_60 simulation), the convective area did not change in size. Hence, the size of the convective area seems to be closely related to the choice of the rain DSD parameters. It appears that the DSD parameters alter the cold pool structure, as already discussed, which in turn is responsible for determining the size of the convective area. Inspection of Fig. 3.3 indicates that the increase in the size of the convective area can be attributed to two different trends: the first is the development of a more continuous and longer leading convective line; the second trend is illustrated by the backward growth of the convective area. In other words, as the mean drop diameter decreased and the cold pool increased in strength, the convective area became not only longer but also wider. ii) the size of the stratiform area does not change as much between the six simulations. This statement is a bit misleading, though, since it appears that the size of the non-precipitating anvil is rather sensitive to the selection of the DSD parameters. The two very small-mean-diameter DSD (the 600_60_30 and 600_60_60) simulations produced a much more extensive (and of equal size between the two) non-precipitating anvil as compared to the other four simulations. This is easily understood in the light of the fact that the very small rain drops apparently evaporated readily even in this very moist environment. Hence, in these two cases, the stratiform area (as defined by the area where stratiform precipitation reaches the surface) represented a rather limited portion of the entire stratiform cloud that trails the convective line. Indeed, this was only the most intense portion of the stratiform cloud. This should be taken into account when discussing the intensity of the mean vertical profiles in the

stratiform area. However, it is worth noting that the 600_22_10 simulation had the same stratiform/non-precipitating anvil proportions and sizes as the three M-P simulations. Hence, a comparison in terms of mean stratiform intensity among these four simulations (400_8_4_RHvt, 400_8_4, 600_8_4 and 600_22_10) is more meaningful. iii). in terms of percent convective area, the 400_8_4_RHvt had the smallest percent convective area. While its convective area was the same size as that of the other two M-P simulations, its stratiform area was larger. Apparently, the lower graupel terminal velocity in this case resulted in a bigger portion of the graupel particles being advected rearwards from the convective area and into the stratiform area where they fall out and contribute to the stratiform rain production. Again, the graupel density did not have an effect on the percent convective area, as it did not affect significantly any of the already described structures. The decrease in the mean-drop-diameter of the rain distribution resulted in an increase in the percent convective area, consistent with the fact that the smaller the rain drops, the more readily they evaporated in the stratiform area and, hence, the relative increase in the area covered by stratiform rain was smaller as compared to the increase in the size of the convective area. In other words: when the rain drops are smaller, the resulting cold pool is larger and stronger; the convective area becomes longer and wider; at the same time, the stratiform area becomes more limited in terms of backward extent as a result of the increased evaporation.

b. Mean vertical profiles over the convective and the stratiform areas

When considering the mean hydrometeor profiles (Fig. 3.8 a-h), we will focus our attention mainly on the changes in the graupel and the rain fields that resulted from

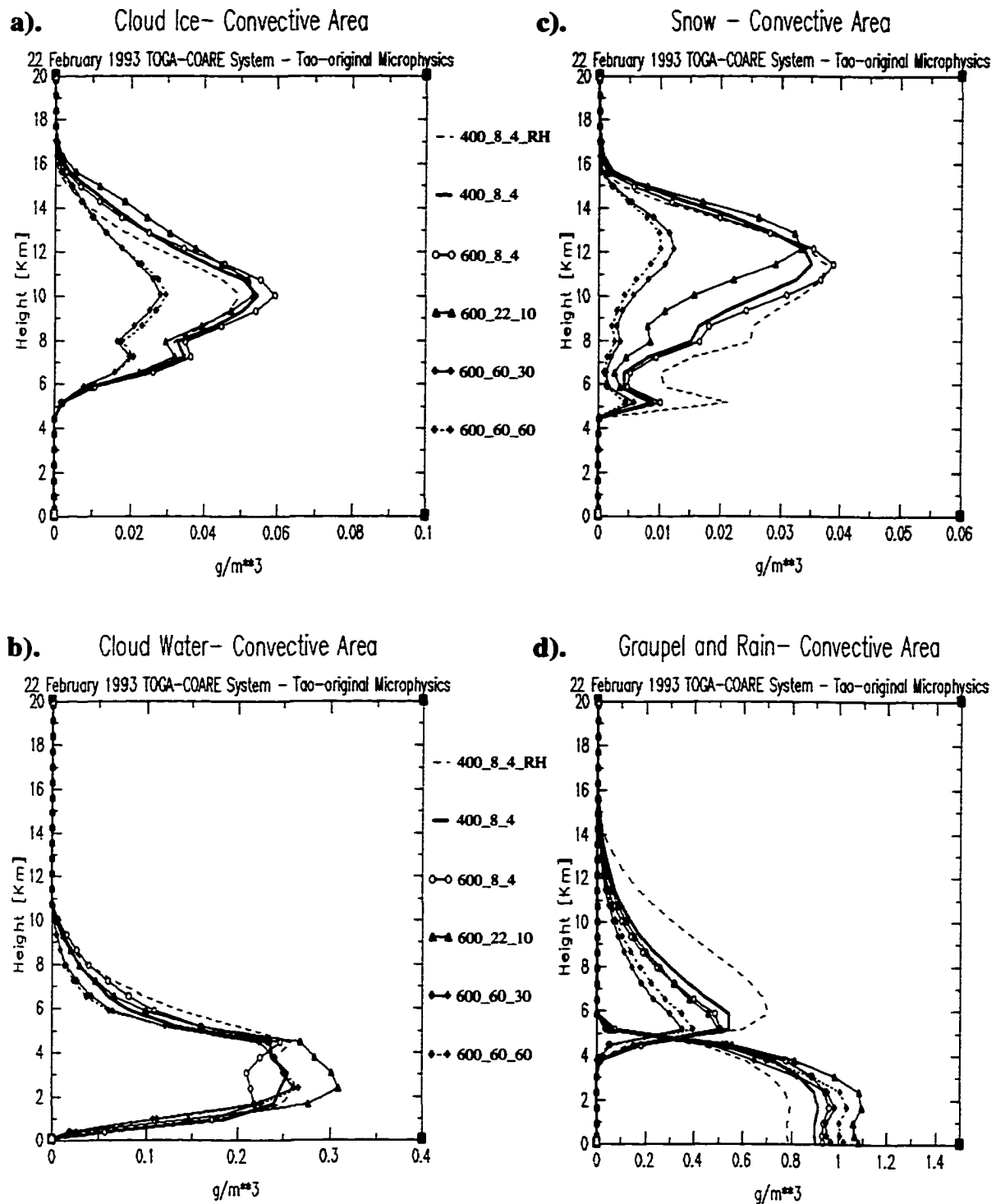


Figure 3.8. Mean vertical profiles of hydrometeors (g/m^3) over the convective (a)–(d) and the stratiform (e)–(h) area for each of the six simulations presented in Fig. 3.2. The means were computed over the period from 5:30 to 7 hours model time that presents the mature stage of the simulated storms. The results from all six simulations are presented in one plot in the following manner: (a) and (e) – cloud ice; (b) and (f) – cloud water; (c) and (g) – snow; and (d) and (h) – graupel and rain.

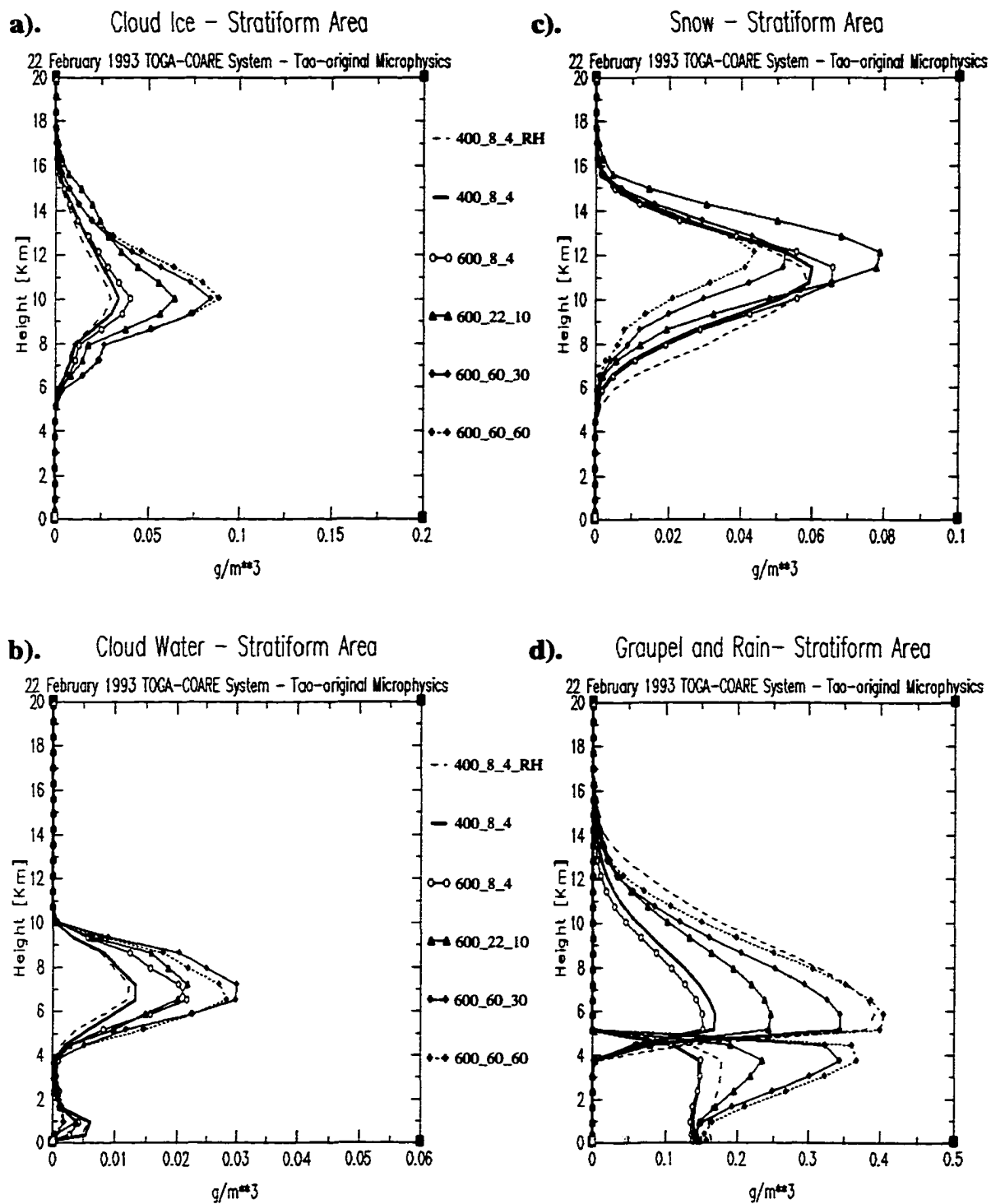


Figure 3.8. (Continued)

the different choices for the descriptive parameters of the particles. We will discuss the other hydrometeor fields only when illustrating a particular idea.

Lets first consider how the graupel terminal velocity affected the simulations. We already saw that the scale of the simulated system was not particularly sensitive to the graupel terminal velocity formulation. This is not the case when considering the mean hydrometeor structure. Indeed, an inspection of the convective region profiles (Fig. 3.8d) clearly illustrates the significant impact which the graupel terminal velocity has on the graupel-to-rain ratio. The low terminal velocity simulation (400_8_4_RHvt) had the highest amount of graupel among the six simulations at all levels. At the same time this simulation had the lowest amount of convective rain! This illustrates that when the terminal velocity is small, significant amounts of graupel are suspended at upper levels and the precipitation efficiency of the storm is decreased. The lack of strong and spatially coherent cold pool production in this case (compare Figs. 3.5a and 3.5b) limited the low-level convective forcing to only isolated pockets. The well-separated, highly three-dimensional cores were apparently not competing strongly and this is probably why this simulation produced the strongest low-level mean vertical velocity in the convective area (Fig. 3.9a) and also the strongest mean convective latent heating (Fig. 3.10 a-b). Furthermore, the weaker cooling by melting, as should be expected in the case of not too much graupel falling out, also contributed to a more intense low-level latent heating. Indeed, while the other five simulations all showed to a different degree a melting-level minimum in the latent heating profile, that minimum was absent in the case when low-terminal velocity were assumed for the graupel particles.

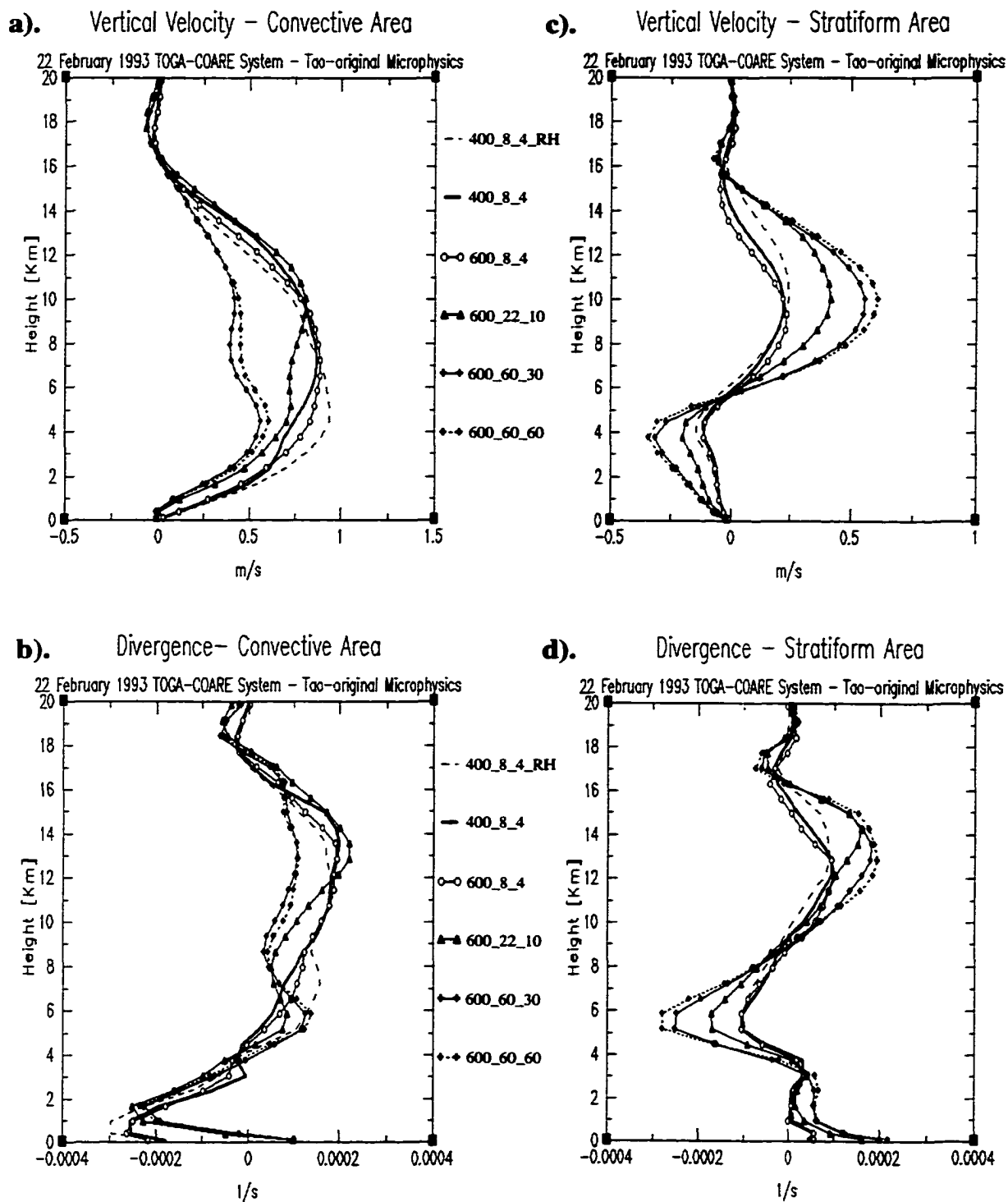


Figure 3.9. Mean vertical profiles of vertical velocity (m/s) computed over the mature stage of the simulated storms for each of the six simulations presented in Fig. 3.2. The means were computed separately over the (a) convective and (c) stratiform regions. Mean vertical profiles of divergence (1/s) computed over the convective (b) and the stratiform (d) regions.

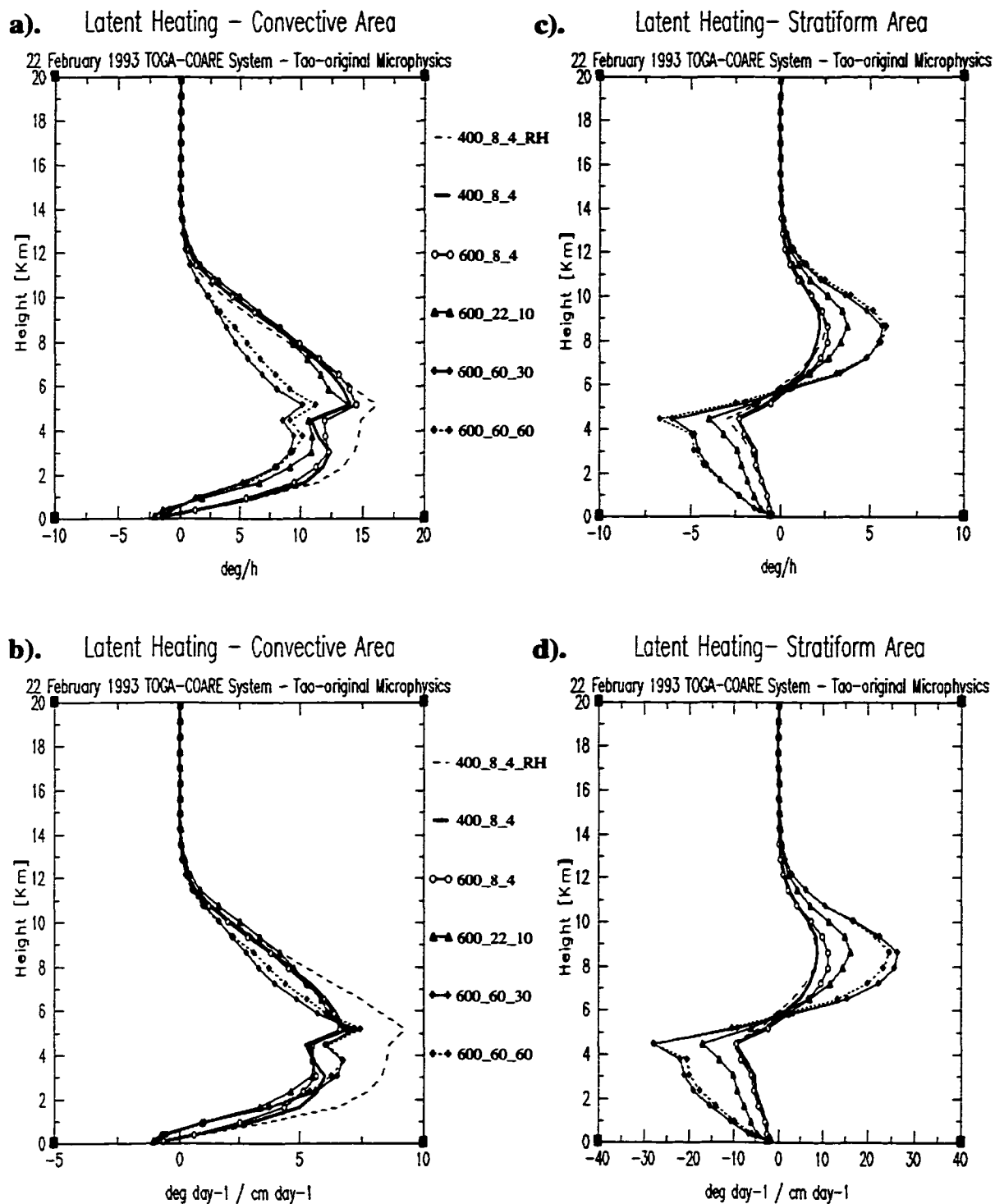


Figure 3.10. Same as in Fig. 3.9 except for presented are the area and time-averaged means of latent heating (a) and (c) and latent heating scaled by the average precipitation in the lowest 2 km - (b) and (d).

The impact of terminal velocity selection on the graupel-to-rain ratio is most dramatically illustrated in analyzing the mean hydrometeor profiles computed over the stratiform area. While in the stratiform area the ratio was just below 1 (~ 0.9), it became almost 2.7 in the stratiform area! Hence, a significant amount of graupel was allowed to accumulate there without contributing much to the rain production. This undoubtedly should have a pronounced impact on the microwave brightness temperatures at the higher (scattering) frequencies. We will come back to this issue later.

Increasing the graupel terminal velocity by about a factor of two, by using the Lin et al., 1983 formulation instead of that of Rutledge et al., 1984, resulted in a drastic change in the graupel-to-rain ratio in both the convective and the stratiform regions (see the 400_8_4 simulation in Figs. 3.8 d and h). In the convective region this ratio became ~ 0.6 and ~ 1.1 in the stratiform region. Furthermore, while the mean convective area rain increased in the case of the faster-falling graupel, the stratiform area mean rain decreased in addition to the stratiform area decreasing in size (Fig. 3.7). This is of no surprise since the faster-falling graupel should fall out in closer proximity to the convective area and, hence, contribute less to the stratiform area rain production. Finally, the case of the faster falling graupel clearly illustrates that significant portion of the rain was apparently produced through coalescence of rain and cloud drops and without the help of the ice-related processes. This is referred to as the "warm rain" production and is typical of tropical environments where the parcel's buoyancies are low and the associated lower vertical velocities result in rain drops remaining longer at levels below freezing. This, in addition to the higher altitude of the tropical freezing level and the significant amount of moisture, all stimulate the growth by coalescence and the

production of rain without the participation of the ice-phase processes. That the effectiveness of the "warm rain" process is closely related to the environmental characteristics is clearly evident from the fact that a simulation of a midlatitude squall line system that used the same microphysical set-up (Hristova-Veleva et al., 2000) did not result in "warm rain" production. However, it is not only the environmental temperature and humidity that are responsible for the effectiveness of the "warm rain" processes. The storm structure and the rain size distribution parameters seem to play an important role as well. In the case of the slower-falling graupel, for example, the "warm rain" process seems to have been suppressed simply because the *convective* cold pool production was diminished and the subsequent rather isolated convective forcing appears to have favored the development of stronger vertical velocity in the convective area. Maybe even more importantly, the decreased cooling by melting (since less graupel is falling out) should have helped the development of stronger buoyancy and vertical velocity. In turn, the stronger vertical velocity decreased the residence time of droplets at levels below freezing and, thus, diminished the role of growth by coalescence.

A further illustration of how the storm dynamics and the particle size distributions could affect the "warm rain" processes intensity is given when comparing the changes in the mean graupel and rain profiles and the changes in the graupel-to-rain ratio that occur with the changing assumptions for the DSD distribution. In particular, as the rain drops become progressively smaller from the 600_8_4 case, to the 600_22_10 case, to the 600_60_30 case, the graupel-to-rain ratio also continues to drop signifying a more intense "warm rain" processes. The possible explanations are three –

two dynamical and one microphysical. Let's first present the dynamical considerations. As we already saw, the smaller the mean drop diameter, the more spatially coherent the convectively-produced cold pool, the more continuous and uniform the convective area. The increased two-dimensionality of the convective area was exemplified by the increasingly more continuous band that is encompassed by the 40 dBz line in the maximum reflectivity field (Fig. 3.2c-f), while the higher homogeneity was illustrated by the progressively more narrow CFADs of reflectivity in the convective area (Fig. 3.4c-f). Another clear illustration of the fact that the convective area was becoming ever more homogeneous with decreasing mean particle diameter is given by the CFADs of vertical velocity (Fig. 3.11). More importantly, both the CFADs of vertical velocity and the convective area mean vertical velocity profiles (Fig. 3.9a) show also that the convective area vertical velocity was decreasing with decreasing mean-diameter drops. From a dynamical standpoint, two are the possible reasons: i). in terms of buoyancy, the more two-dimensional and extensive the leading convective line, the lower the buoyancy of the individual parcels since now they are rising not in the undisturbed environment but in an environment in which there is latent heat release everywhere; the lower the buoyancy, the lower the vertical velocity; ii). the second dynamical explanation of why the vertical velocity decreases with the decrease of the mean diameter of the drops is as follows: the smaller the drops, the stronger the evaporational low-level cooling, the stronger the cold pool. A stronger cold pool for the same environmental vertical shear of the horizontal wind would result in a more pronounced rearward (relative to the direction of squall line motion) tilt of the updrafts according to the theory of Rotunno et al. (1988). Indeed, analyses of the 1.5 km and the 6 km vertical velocity

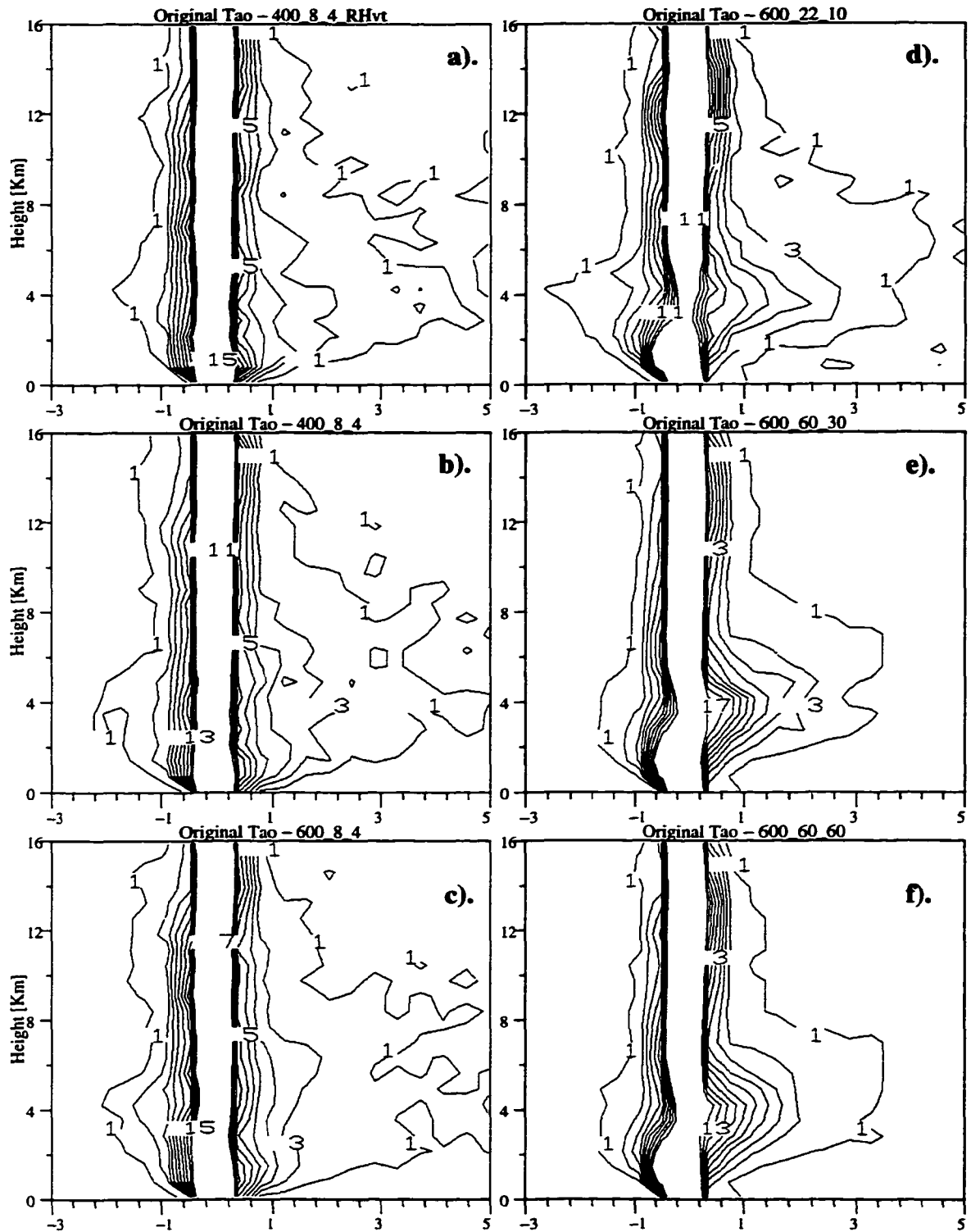


Figure 3.11. Same as in Fig. 3.4 except for presented are the CFADs of vertical velocity. The frequency distribution of vertical velocity was computed at each model level (every ~ 700 m) and the velocity bin size was 0.4 m/s. Contours are every 2% of data per m/s per km. Values greater than 19% per m/s per km are not plotted.

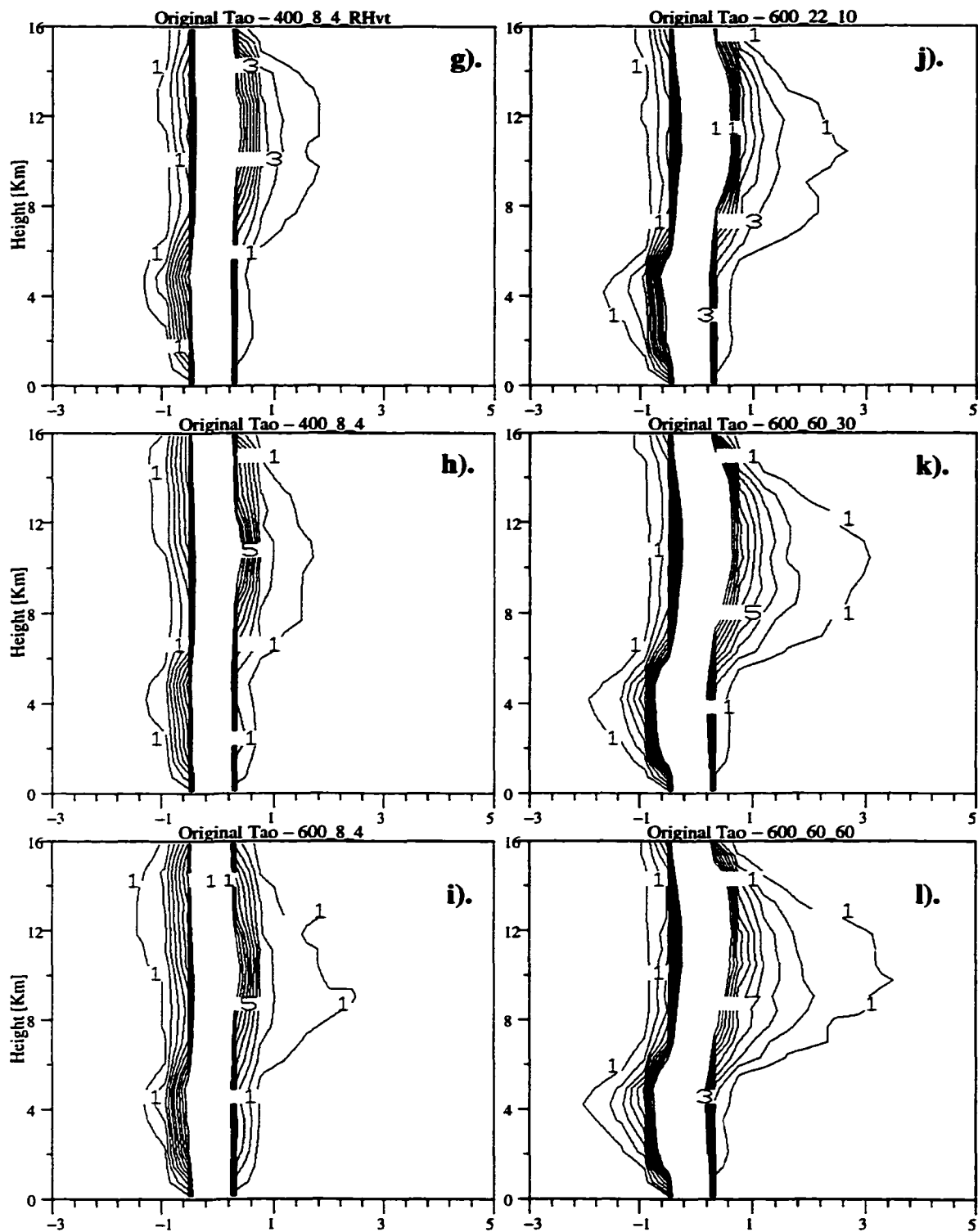


Figure 3.11. (Continued)

fields show exactly that. As the leading edge cold pool became stronger, especially in the northern bowing out portion of the convective line, the rearward tilt of the convective cores became much more pronounced. Indeed, the increase of updraft tilt explains the observed broadening of the convective area in this portion of the storm. Increased slope of the updrafts with height would result in increased entrainment and, hence, decreased buoyancy and vertical velocity. In turn, decreased vertical velocity increases the residence time of the rain and cloud droplets at levels below freezing and, thus, gives higher chance of the growth by coalescence to produce large enough particles that will fall out as rain without involving ice production.

The third explanation comes from more microphysical considerations. In particular, having smaller-mean diameter drops means having *more* drops that also fall out *slower*. Both of these factors would increase the relative importance of the growth by coalescence and the rain formation below freezing. Furthermore, since fewer drops will enter the levels above freezing, the ice-processes intensity would decrease in the case of very small rain drops. That could explain the observed decrease of the upper-level vertical velocity for the very small mean diameter drops used in the 600_60_30 and the 600_60_60 simulations (Fig. 3.9a). The decreased upper-level vertical velocity would lead to a decrease in the convective area intensity in general. Indeed, the mean near-surface convective rain in these two cases decreased as compared to the larger-mean-drop simulation of the 600_22_10 case.

The 600_22_10 simulation is a special case in the transition from larger to smaller mean drop diameter distributions. While the cold pool in this case is large and strong enough to force new convection along the entire leading line, the most intense

parts of it are still rather small as compared to the 600_60_30 and the 600_60_60 simulations (Fig. 3.5). As a result, equally intense convection is not forced everywhere and the convective structure is still a bit more cellular. Hence, the competition among the convective cores is a bit weaker and this leads to stronger vertical velocities and higher importance of the ice processes in this case as compared to the other two. Furthermore, the rearward tilt of the convective updrafts is not as strong in the 600_22_10 simulation as that in the other two cases. As a result, the 600_22_10 produces the most intense convective area in terms of mean rain intensity. The upper-level heating remains important in the convective area as opposed to the two very small mean rain drop diameter simulations. Furthermore, the 600_22_10 simulation produces a very large and intensive stratiform area. All the leads to the 600_22_10 simulation producing the system with the most intense upper-level heating maximum and, thus, the most elevated heating source (Fig. 3.12).

While some of the differences in the "warm rain" intensity among the six simulations could be partially attributed to the changes in the graupel size distribution which was also taking place, it appears that its importance is smaller. Indeed, when only the graupel particle distribution was changed between the 600_60_30 and the 600_60_60 simulations, with the later having twice as large an intercept, the changes were very small not only in the storm structure, size and convective/stratiform/anvil proportions but also the differences in the mean vertical profiles of hydrometeors, vertical velocity and latent heating were very small. It does appear that the two simulations were identical with the only more important difference between them being in the mean graupel amounts in the stratiform area. Apparently the smaller, and, hence,

Sensitivity to DSD – SYSTEM SCALE HEATING

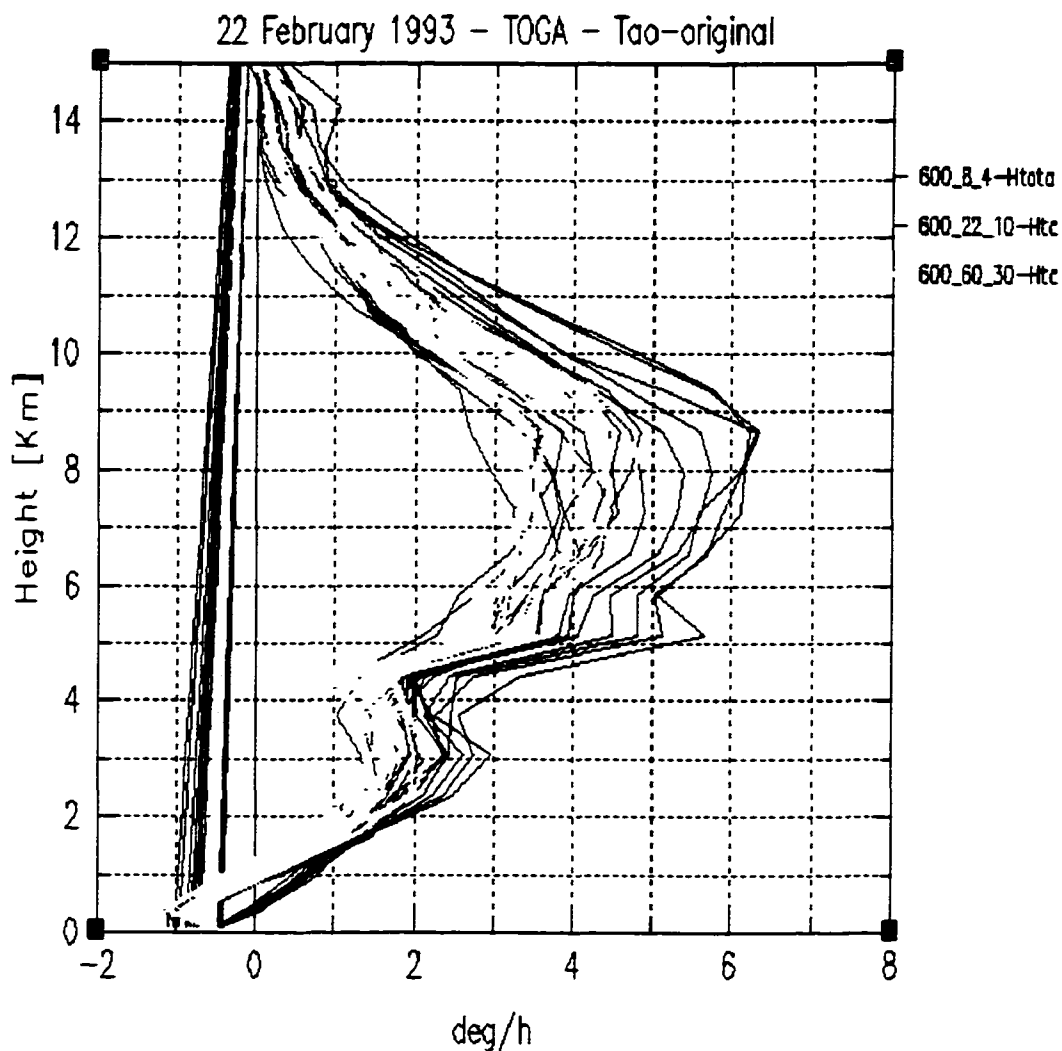


Figure 3.12. Mean vertical profile of the latent heating (deg/h) computed over the combined convective, stratiform and non-precipitating anvil regions. Presented are nine mean latent heating profiles (10 minutes apart) for each of the three simulations: 600_8_4 (red), 600_22_10 (blue) and 600_60_30 (yellow). The time period that is covered by the 9 profiles is from 5:40 to 7 h into the simulation time.

more slowly falling graupel particles in the 600_60_60 simulation were more effective in collecting the upper-level snow (due to their increased residence time in the levels occupied by snow) and that helped produce more graupel which accumulated in bigger quantities above the melting level also as a result of its lower terminal velocity.

The stratiform area mean hydrometeor profiles (Fig. 3.8e–h) clearly illustrate how the decrease in the mean rain drop diameter results in increased evaporation at levels below melting. This significantly alters the graupel-to-rain ratio. With ever decreasing mean drop diameter distributions the stratiform area appears to become more and more intense (Figs. 3.8e–h, 3.9c–d, 3.10c–d). However, as already pointed out, this is at least partially an artifact, which results from the increased rain evaporation that severely limits the backward extent of the stratiform area. What is sampled here then, is only the most intense part of the stratiform area that follows immediately behind the leading convective line.

c. Brightness temperatures relations

It is clear from the above discussions that the columnar graupel-to-rain ratio changes as a function of the assumed in the cloud model particle terminal velocity and size distribution parameters. Since the microwave brightness temperatures that emerge at the top of the atmosphere are a reflection of the complex interactions of the radiation emitted by the earth surface with the multi-layered hydrometeor structure, it is obvious that Brightness Temperature–Rain Rate (Tb–RR) relations will also be a function of all these assumptions. Indeed, Fig. 3.13 shows exactly that. In the convective area the choice of the DSD parameters modifies the 10 GHz Tb–RR relationship in such a way that the smaller mean drop diameter distributions produce colder 10 GHz Tb for the

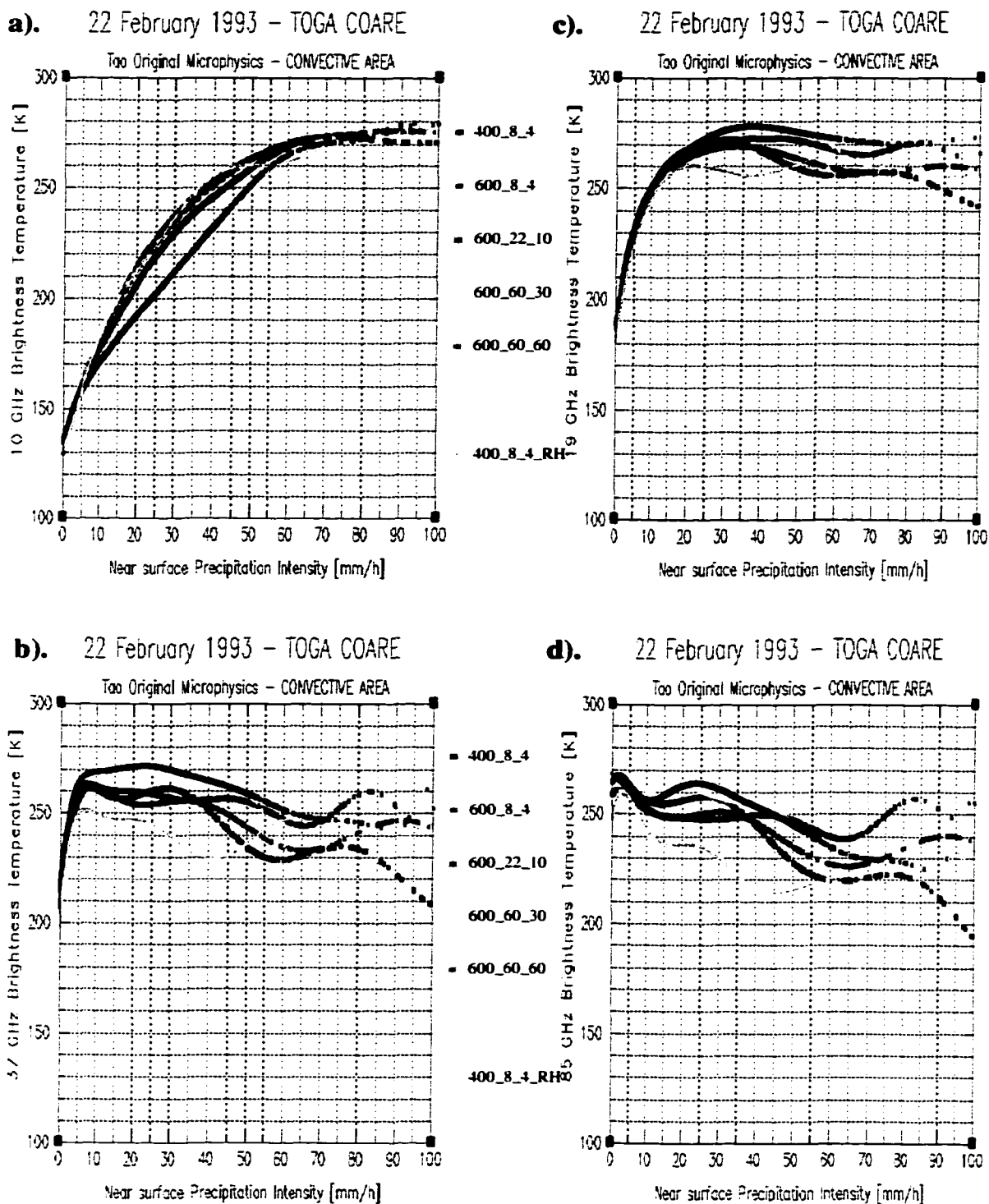


Figure 3.13. Convective area relationship between the model-produced near surface rain rate (mm/h) and the microwave brightness temperatures computed from the model hydrometeors at four frequencies: 10 GHz – (a); 19 GHz – (c); 37 GHz – (b), and 85 GHz – (d). Presented are the 10th degree polynomial fits to the data points that encompassed the mature stage of the system (5:30 to 7h into the simulation). The results for each of the six simulations presented in Fig. 3.2 are color-coded according to the legend. The stratiform area relationships are presented in the same manner in panel (e)–(h).

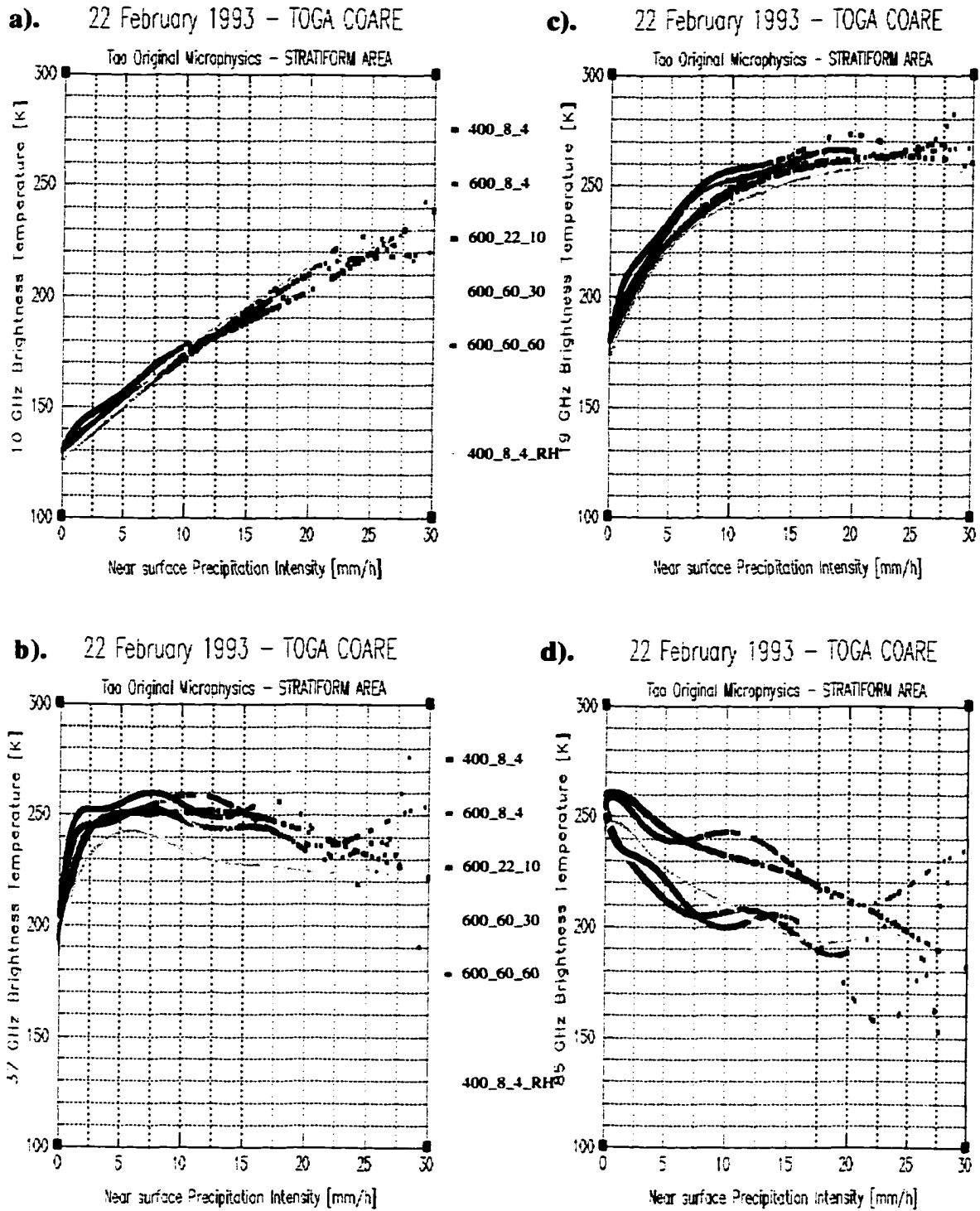


Figure 3.13. (Continued)

same near-surface rain rate. This is especially true for rain rates in the range of 10 to 55 mm/h (Fig. 3.13a). It appears that at 19 GHz the T_b -RR relationships are affected the least by the DSD parameter selection as also reported by Wilheit et al., (1977). This is especially true for rain rates below 35 mm/h (Fig. 3.13c). For higher rain rates, it appears that even the 19 GHz T_b -RR relationships are slightly affected, with the smaller mean-diameter (D_{mean}) DSDs now producing slightly warmer 19 GHz brightness temperatures for the same near-surface rain rate as compared to the larger D_{mean} DSDs. This trend, however, becomes much more pronounced at the higher frequencies, that are affected more strongly by the scattering (Fig. 3.13b and d). In our case, the smaller D_{mean} DSDs produced also smaller amount of graupel for a given amount of rain in the convective area (the more intense "warm rain" processes) and that, in addition to having smaller mean diameter ice particles, could explain to a high degree the warmer scattering frequencies but would not explain the colder emission-based frequencies like the 10 GHz brightness temperatures. However, Coppens and Haddad (2000) found a similar behavior, namely colder 10 and warmer 85 GHz for the same amount of average rain rate in the level below melting when they assumed smaller D_{mean} DSDs. In their case the amount of upper-level graupel was not modified at all and only the rain-rate independent mass-weighted mean diameter of the rain distribution was changed (the D'' parameter in Haddad et al., 1997). They attributed the contrary trends at low and higher frequencies to the fact that the lower frequencies are dominated by absorption while scattering starts to dominate as the frequency (and rain rate) increase. Both effects are more significant for larger drops and, hence, the opposite trends. This conclusion is further supported by the finding of Tesmer and Wilheit (1998) that the assumption of

smaller D_{mean} DSDs, in addition to modifications of the integrated water vapor content, made their cloud more transparent (and, hence the radiometrically colder background more prominent) at frequencies below 37 GHz.

As for the impact of the graupel terminal velocity assumptions, clearly, the slower falling graupel produced much colder higher frequency brightness temperatures for the same amount of near-surface rain-rate. This is to no-surprise, considering the increased scattering effect of the significant amounts of graupel that remained suspended at levels above melting in that case.

In the stratiform area (Fig. 3.13e-h), the 10 GHz T_b -RR relationships appear not to have been affected by any of the particle parameter selections. The 85 GHz T_b -RR relationships also present an interesting result. While in the convective area the smaller D_{mean} DSDs had warmer 85 GHz T_b s for a given amount of near-surface rain rate than the larger D_{mean} DSDs, in the stratiform region this does not hold. Here the small D_{mean} DSDs are relatively very cold. The explanation comes from considering the vertical hydrometeor profiles in the stratiform region (Fig. 3.8h). The intense rain evaporation, that was characteristically found in the case of the small-particle distributions, resulted in much lower near-surface rain rates for a significant amount of graupel (and rain, for that matter) at levels about freezing. This explains the increased amount of scattering and the lower 85 GHz T_b s in that case. This finding comes, even though from a different perspective, in support of the conclusion made by McGaughey and Zipser (1996b) that the vertical profile of the rain distribution could play an important role in determining the upwelling brightness temperatures.

The 22 February 1993 TOGA COARE squall line system was well observed by several instrumental platforms and this has been one of the primary reasons to chose this particular case for our sensitivity studies. In particular, the Advanced Microwave Precipitation Radiometer (AMPR) collected microwave brightness temperatures at 10.7, 19.35, 37.1 and 85.5 GHz that emerged at the top of the system. In this study, we analyzed the radiances measured at nadir. They are presented in terms of scatterplots of brightness temperature relations between the different channels (Fig. 3.14) and in terms of frequency distributions for each of the four channels separately (Fig. 3.15). For comparison, we present in the same manner the brightness temperature computed for each of our six simulations – Fig. 3.16 and Fig. 3.17.

Lets first look at the scatterplots of brightness temperature relations (T_b – T_b correlations) for each of the six simulations (Fig. 3.16). A quick comparison to the observational data (Fig. 3.14) reveals that each of the six simulations produced a lot stronger scattering in the plots (less well defined features indicative of weaker correlations) than it was seen in the observations. The very well defined features of the observational data, especially in the 85 versus 37 GHz plot seem to suggest that in reality there must have been very little supercooled cloud water since it is know that the supercooled cloud water, that is found in the graupel layers, increases the variability of brightness temperatures at the higher frequencies. The set-up in the microphysical scheme used in the six simulations here was such that significant amounts of supercooled cloud water had been generated (OT–LI from Chapter II) and this could partially explain the scatter in the plots. The situation was the worst for the slower–falling graupel simulation in which also both the graupel and the rain were assumed to

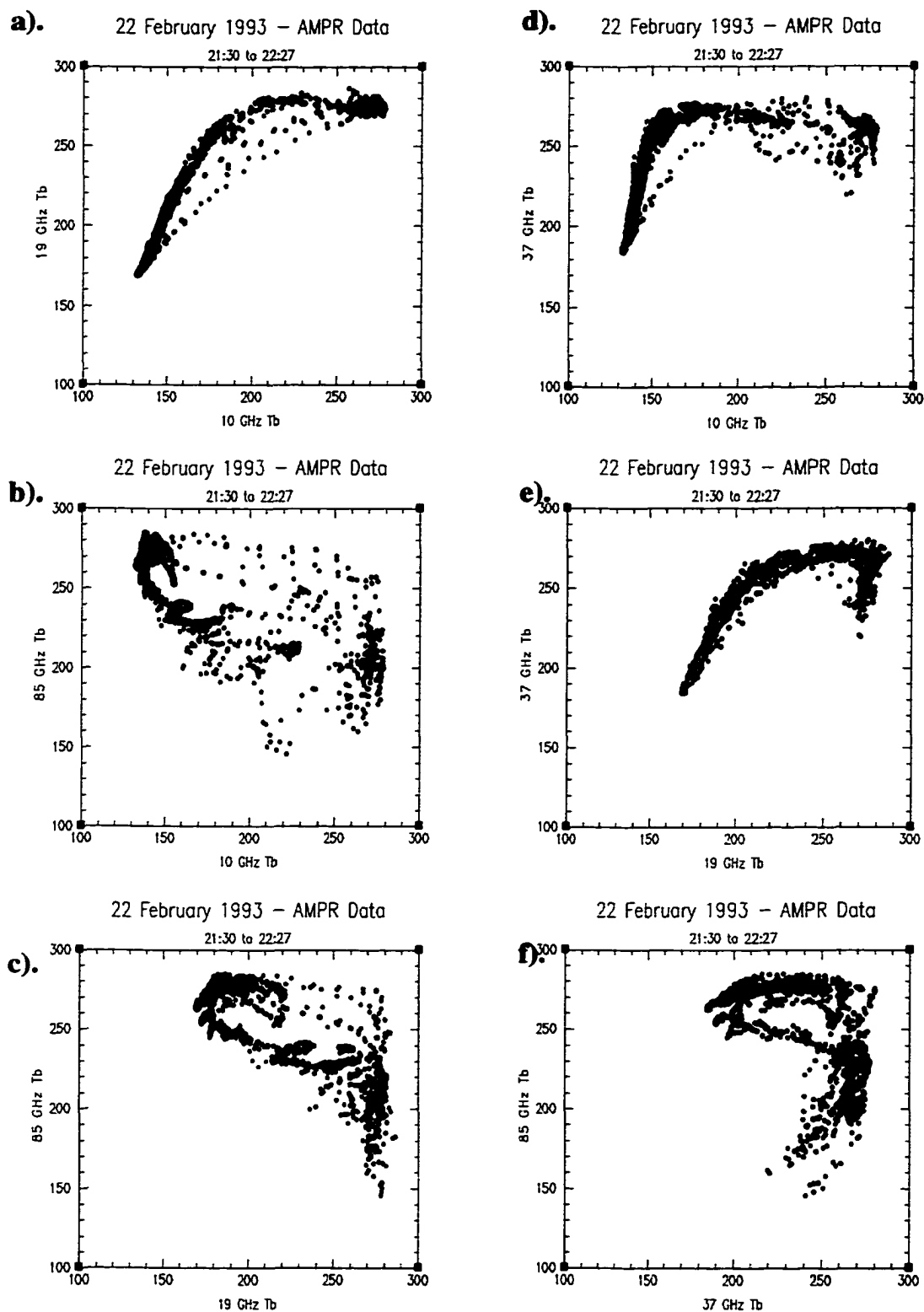


Figure 3.14. Brightness temperature scatterplots for (a) 10.7 GHz vs. 19.35 GHz, (b) 10.7 GHz vs. 85.5 GHz, (c) 19.35 GHz vs. 85.5 GHz, (d) 10.7 GHz vs. 37.1 GHz, (e) 19.35 GHz vs. 37.1 GHz and (f) 37.1 GHz vs. 85.5 GHz. Data were observed by AMPR as it flew over the 22 February 1993 TOGA-COARE squall line system. The resolution of the data is $2.8 \times 2.8 \text{ km}^2$.

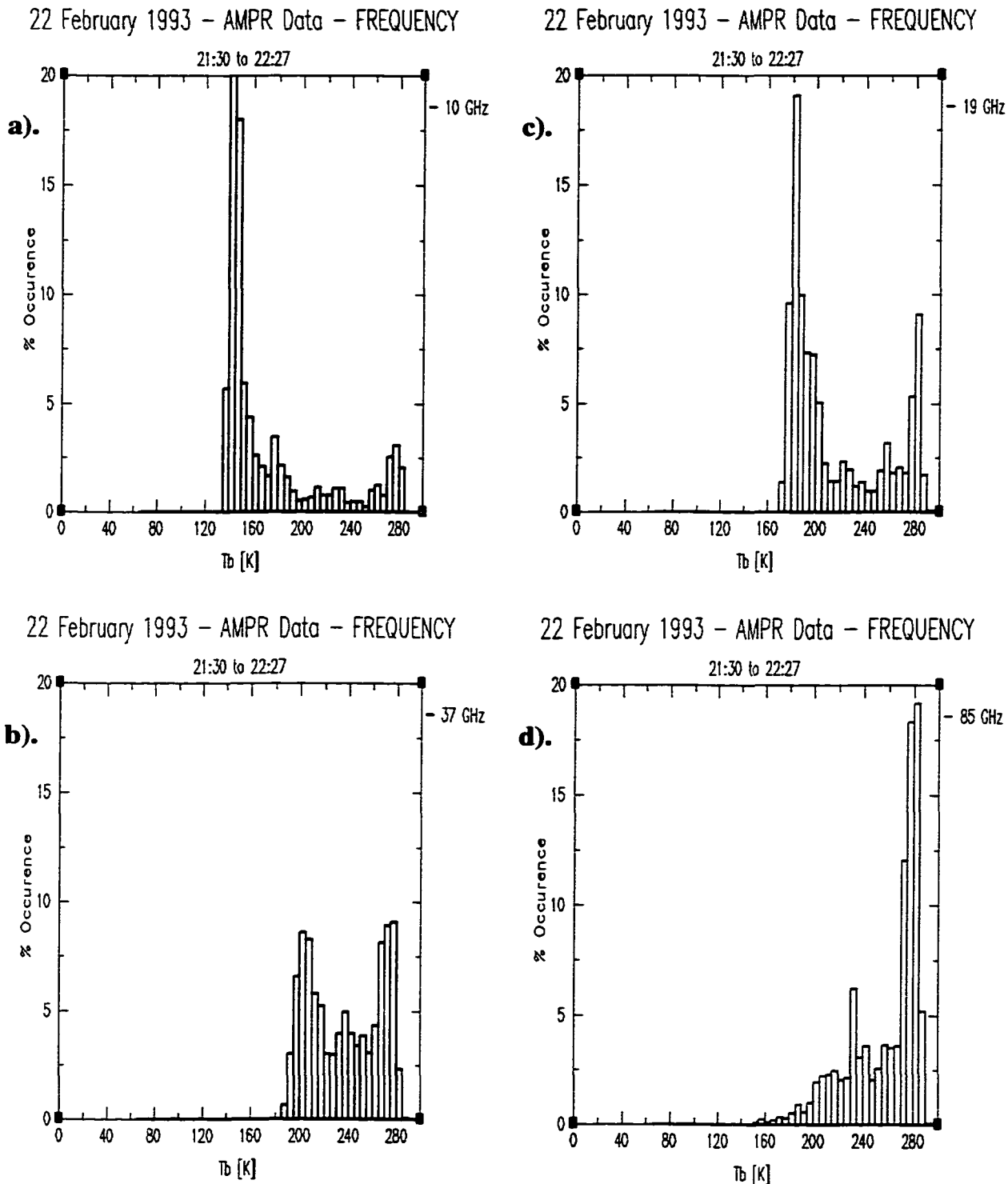


Figure 3.15. Frequency distribution for each of the four microwave channels (10.7 GHz, 19.35 GHz, 37.1 GHz and 85.5 GHz) of the brightness temperatures observed by AMPR as it flew over the 22 February 1993 TOGA-COARE squall line system.

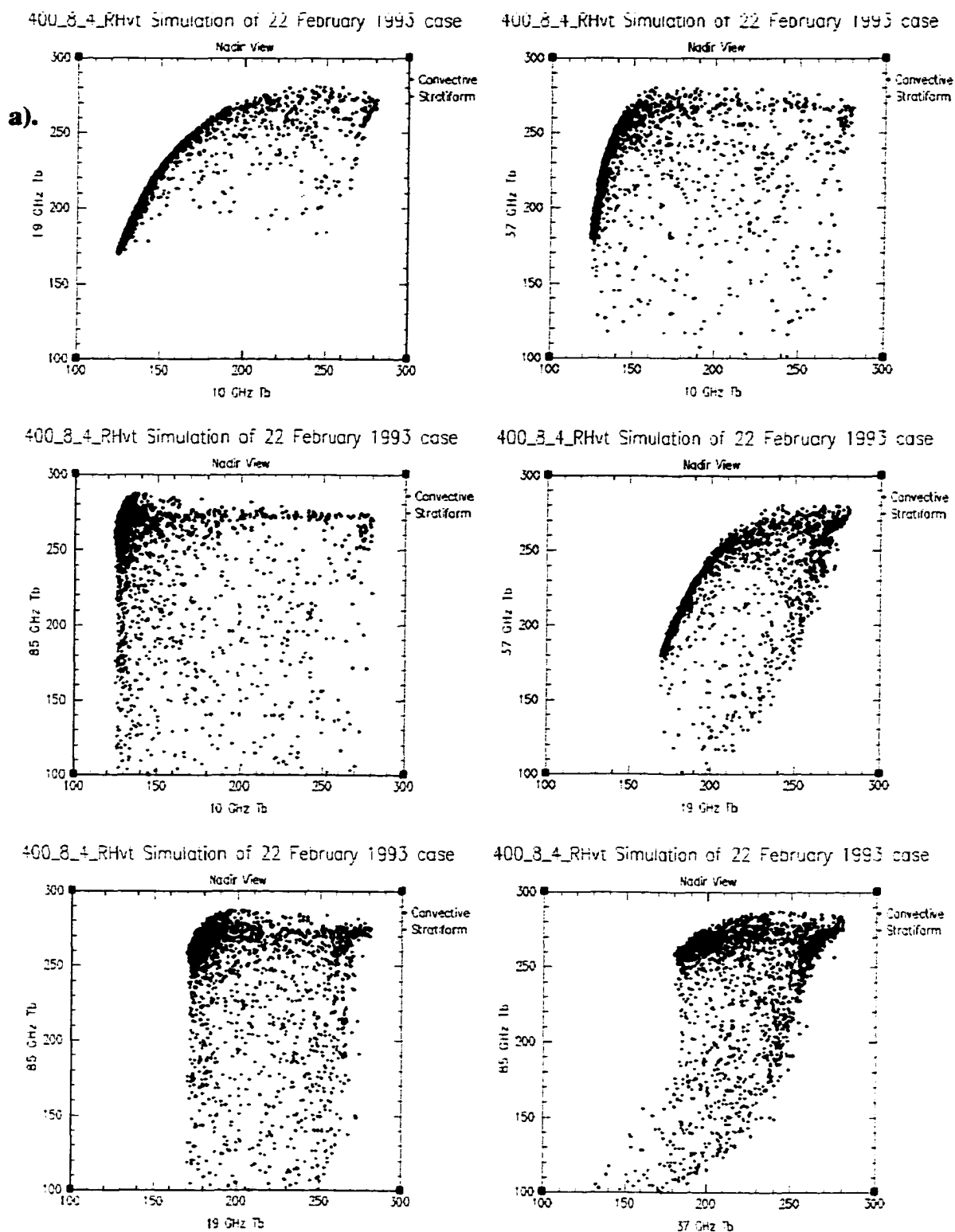


Figure 3.16. Same as in Fig. 3.14 except for scatterplots of the brightness temperatures computed from the hydrometeor fields produced by each of the six simulations: (a) – 400_8_4_RHvt simulation; (b) – 400_8_4 simulation; (c) – 600_8_4 simulation; (d) – 600_22_10 simulation; (e) – the 600_60_30 simulation; (f) – the 600_60_60 simulation. The convective area brightness temperatures are plotted in black and the stratiform area ones – in red.

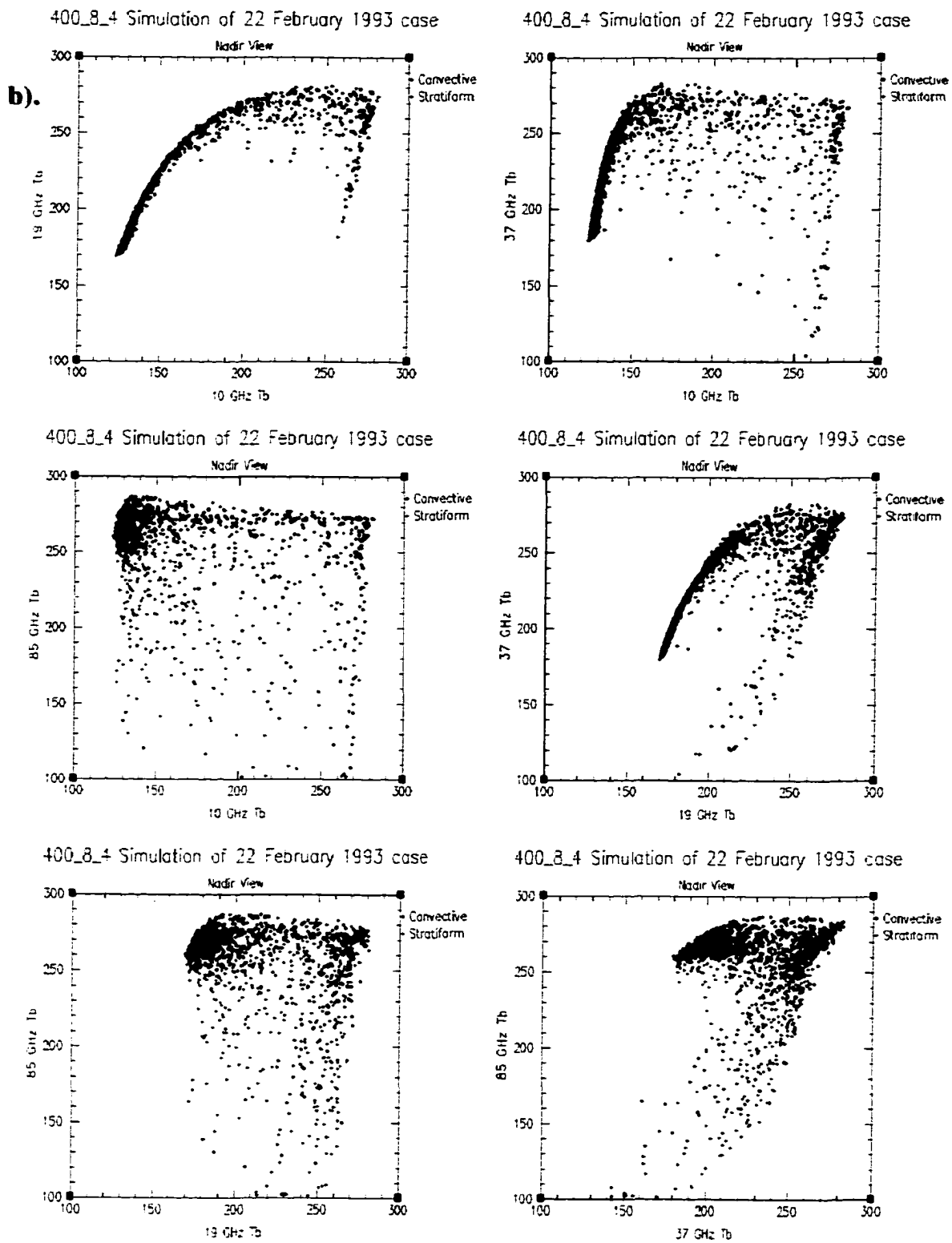


Figure 3.16. (Continued)

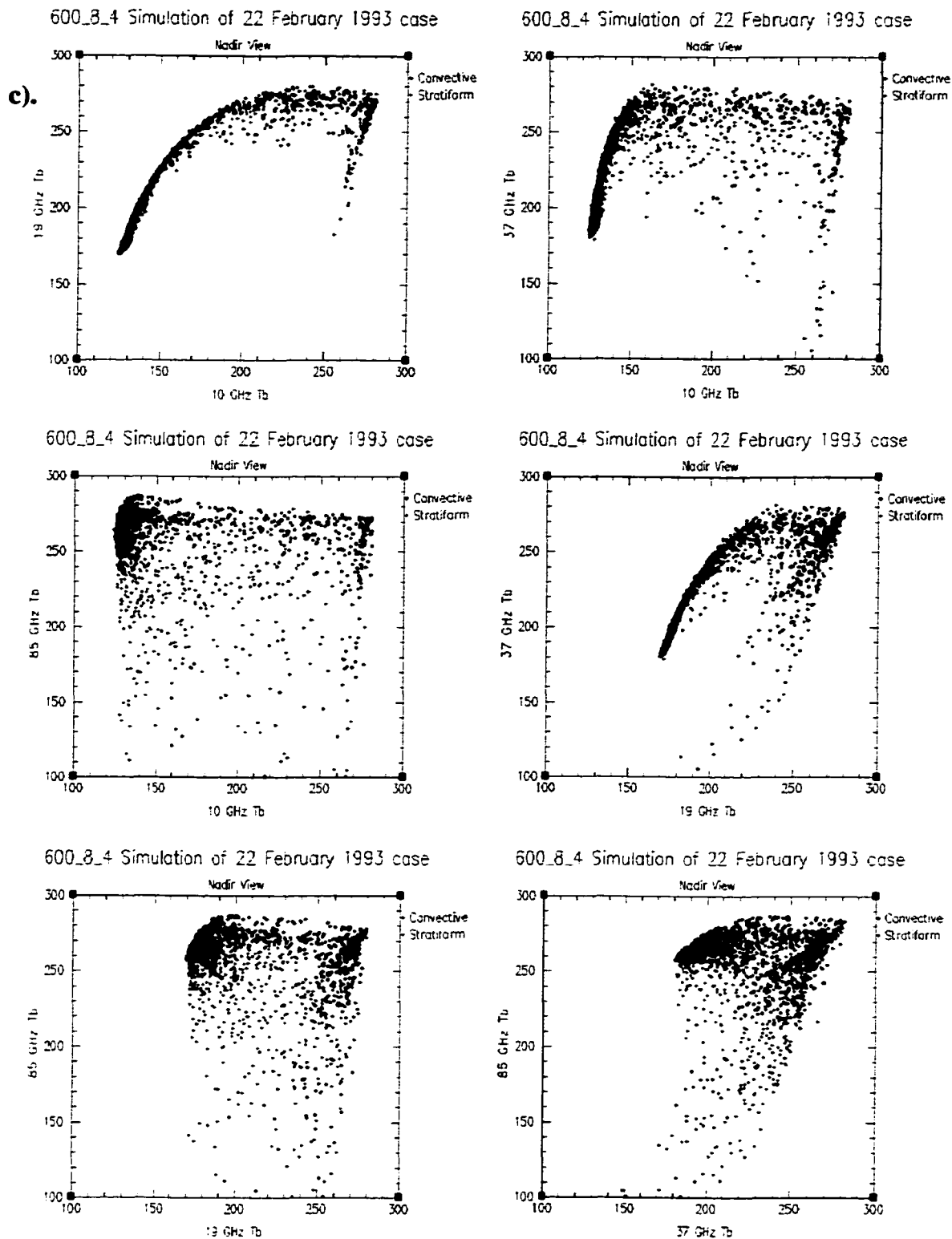


Figure 3.16. (Continued)

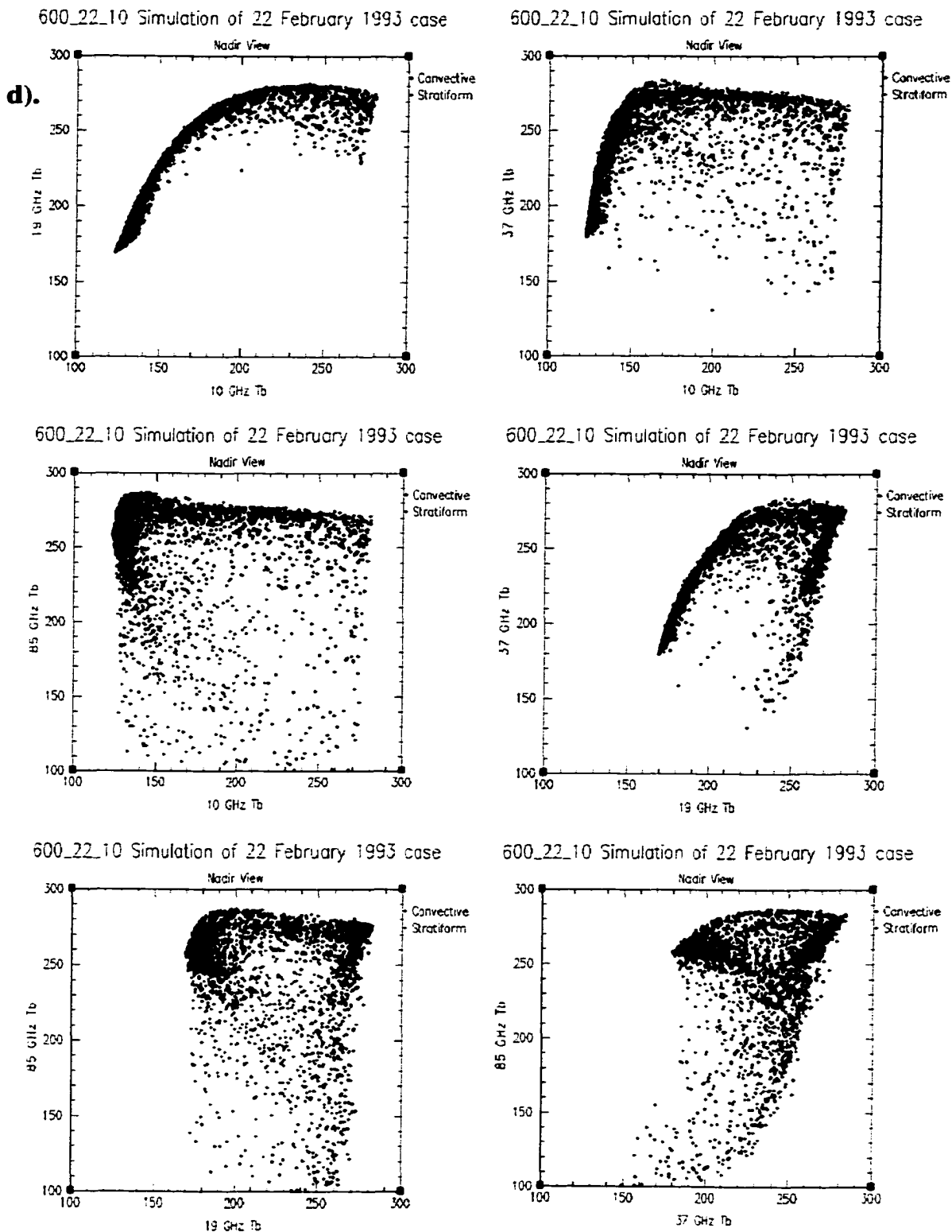


Figure 3.16. (Continued)

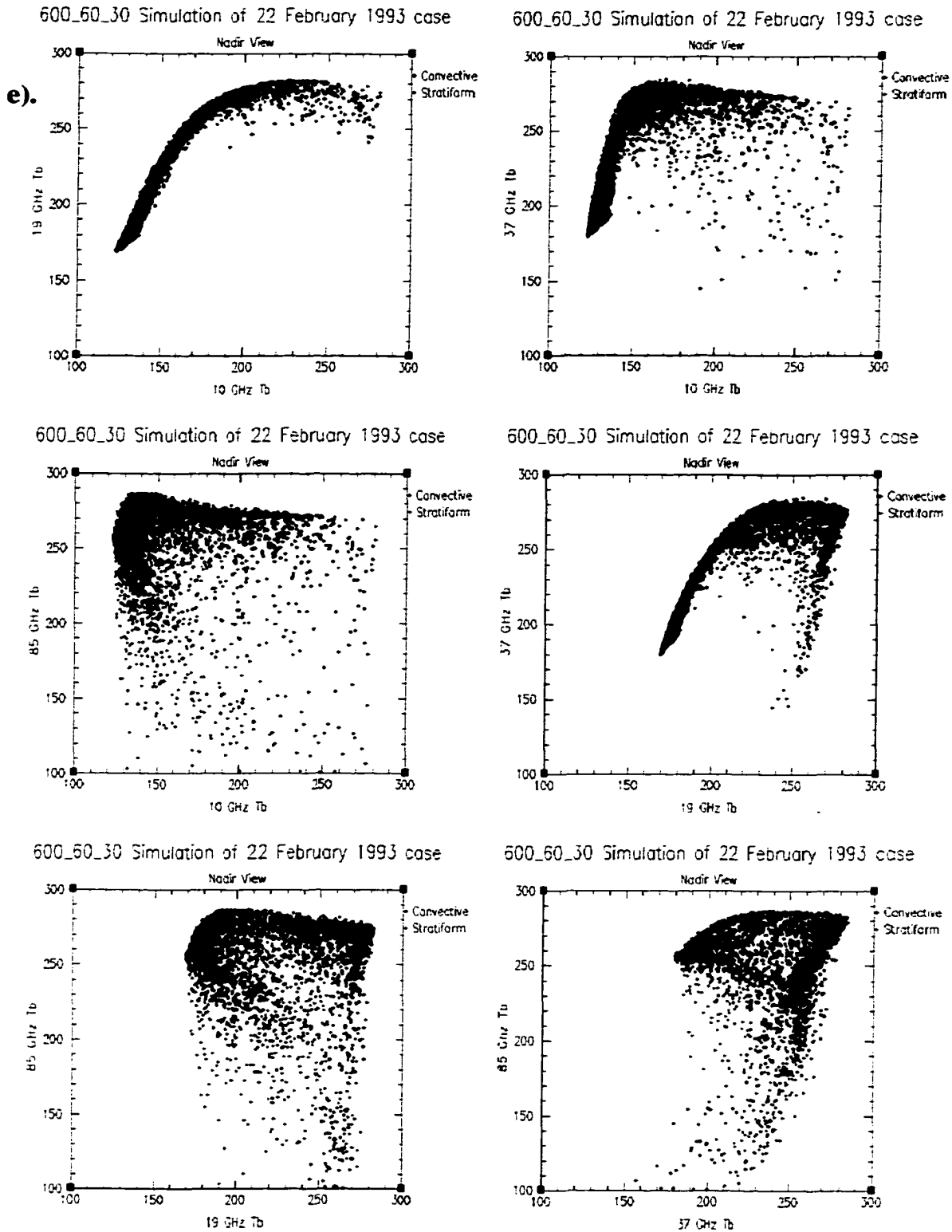


Figure 3.16. (Continued)

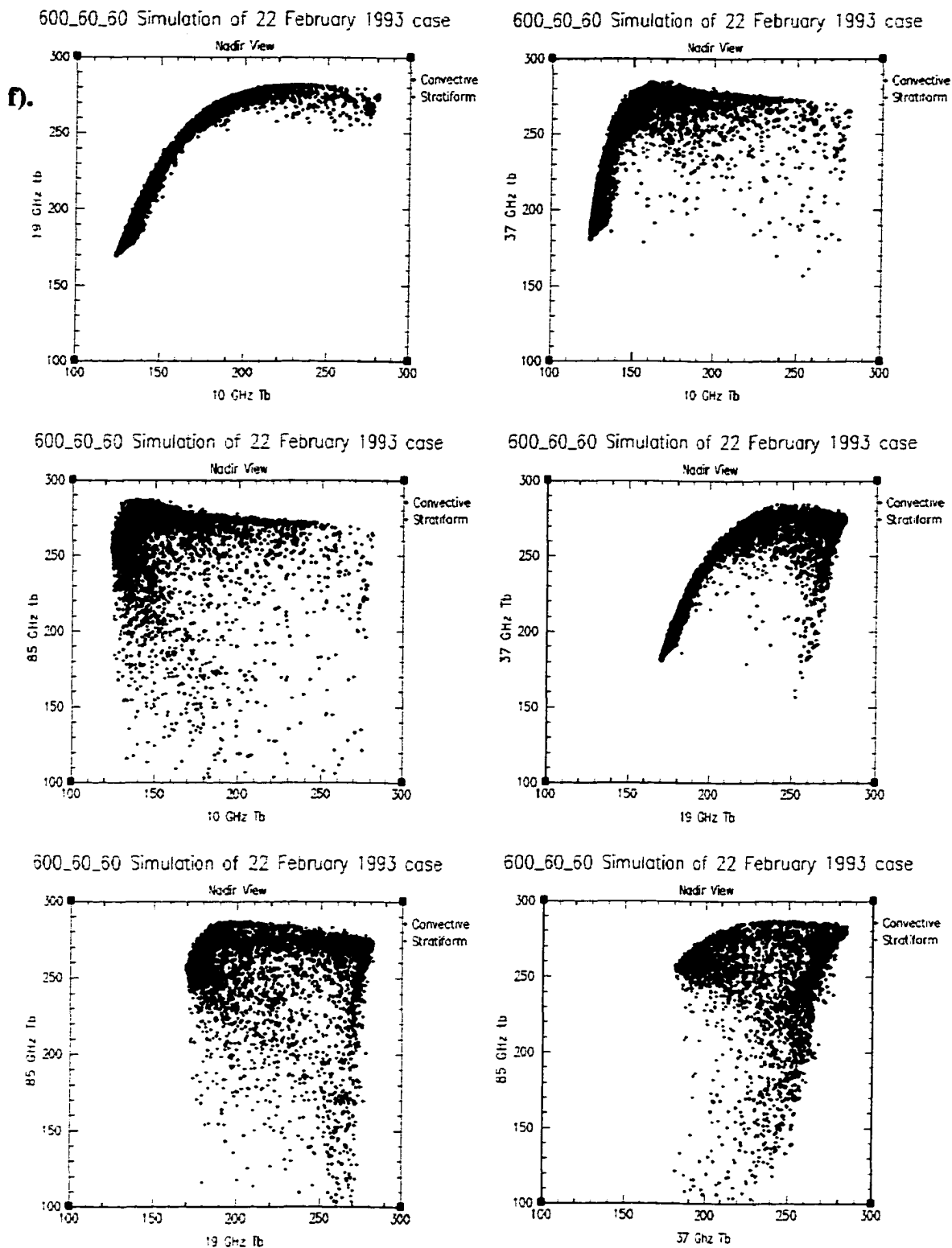
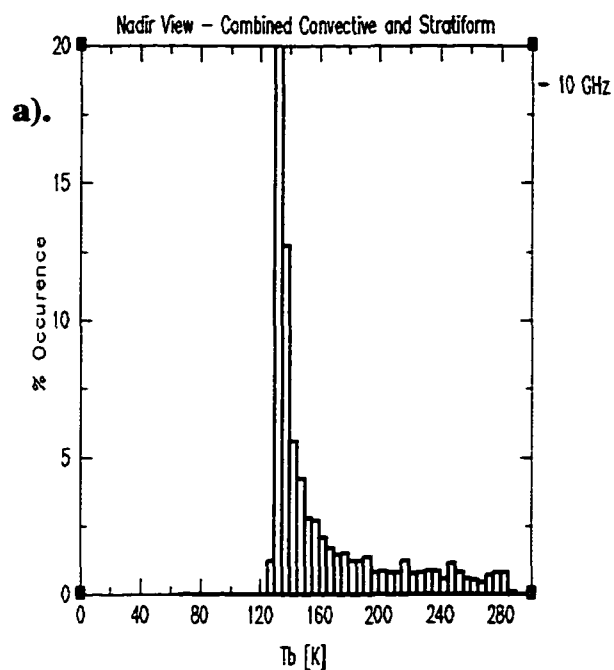
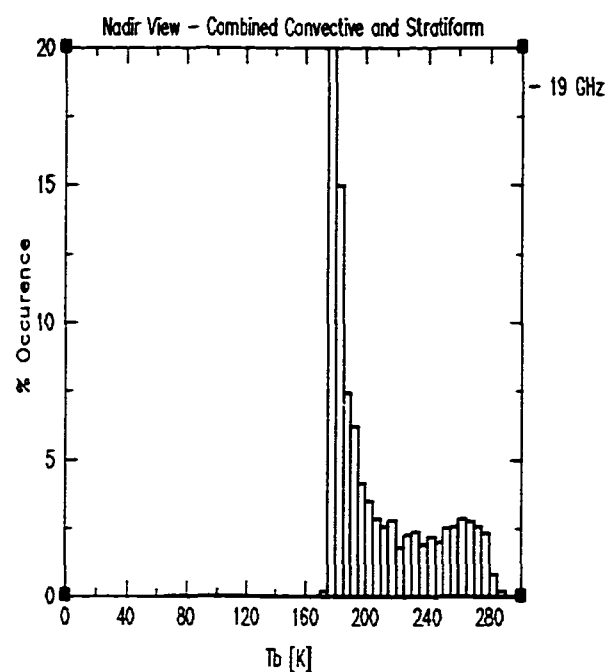


Figure 3.16. (Continued)

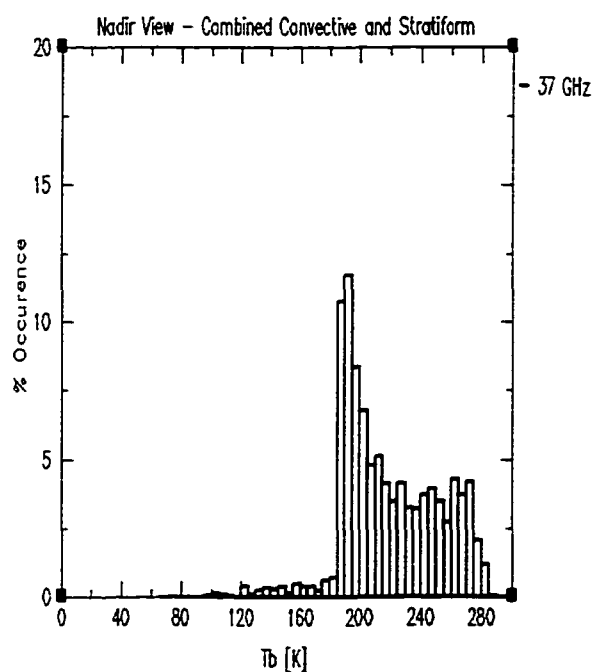
400_8_4_RHvt Simulation of 22 February 1993 case



400_8_4_RHvt Simulation of 22 February 1993 case



400_8_4_RHvt Simulation of 22 February 1993 case



400_8_4_RHvt Simulation of 22 February 1993 case

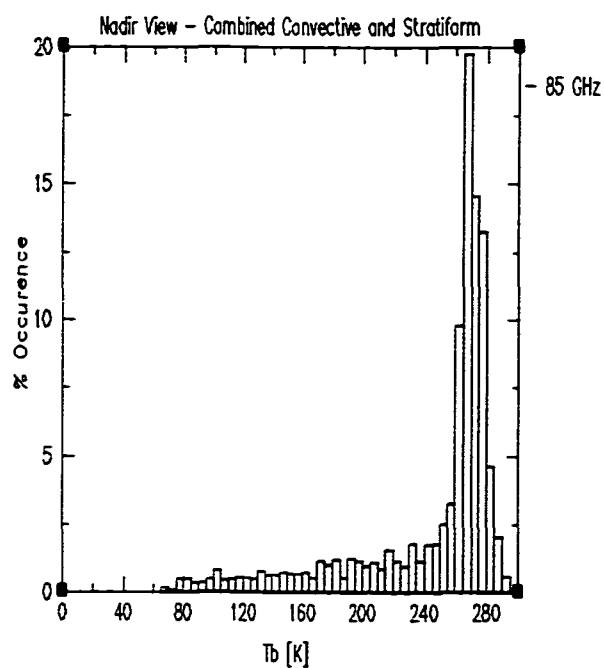


Figure 3.17. Same as in Fig. 3.15 except for frequency distribution of the brightness temperatures computed from the hydrometeor fields produced by each of the six simulations: (a) – the 400_8_4_RHvt simulation; (b) – the 400_8_4 simulation; (c) – the 600_8_4 simulation; (d) – the 600_22_10 simulation; (e) – the 600_60_30 simulation; and (f) – the 600_60_60 simulation. Statistics are computed over the combined convective and stratiform regions.

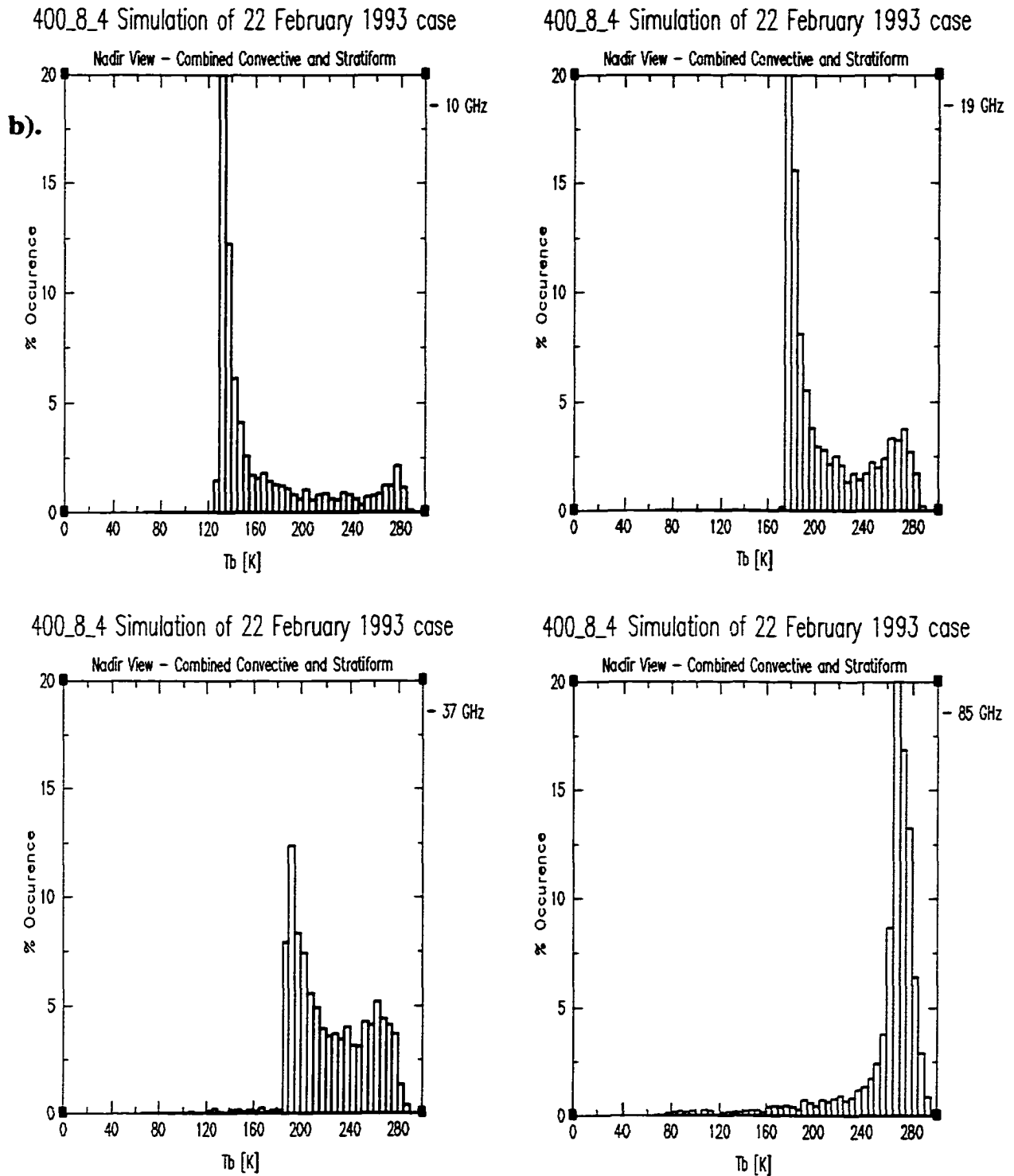


Figure 3.17. (Continued)

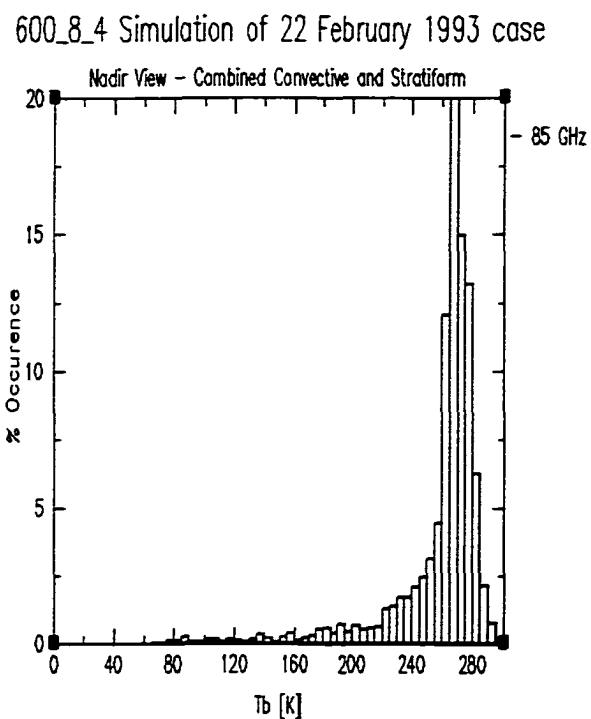
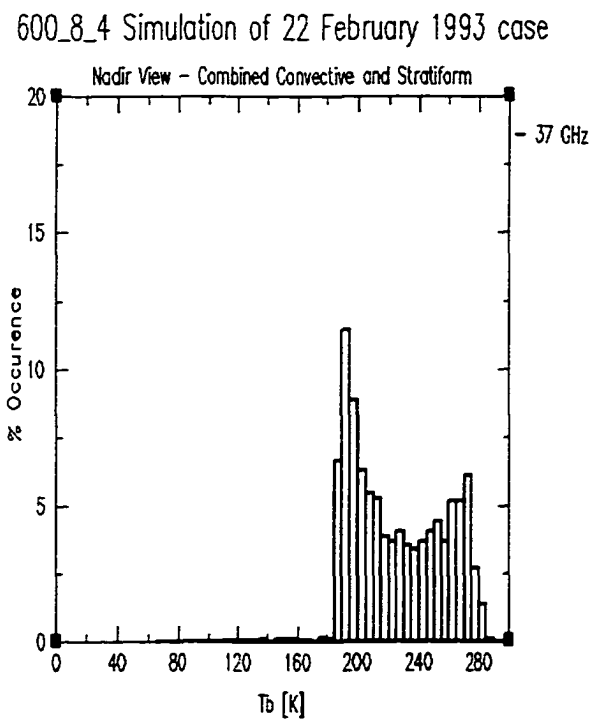
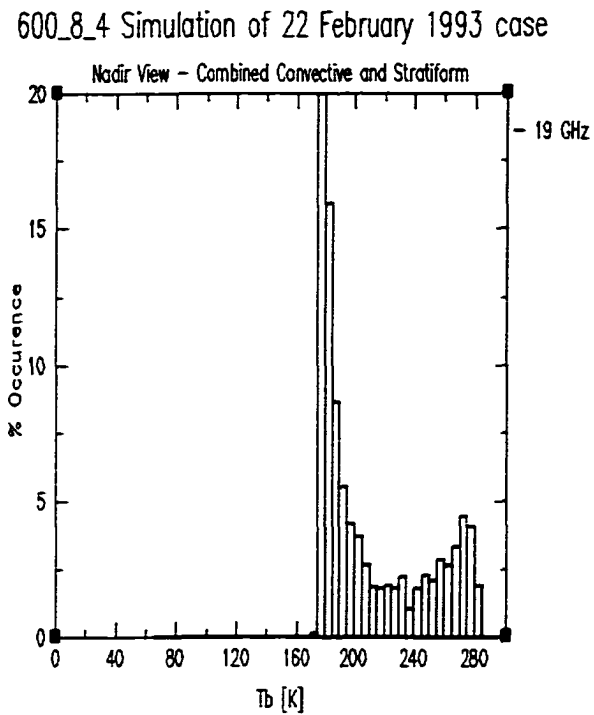
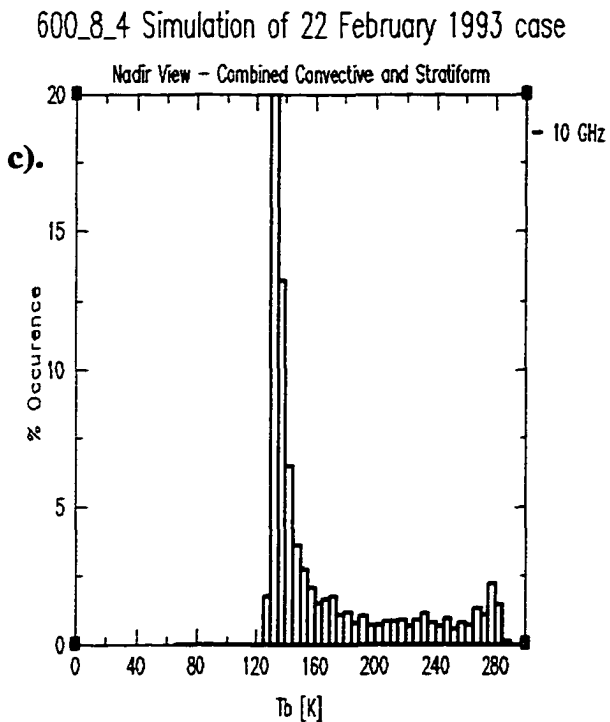
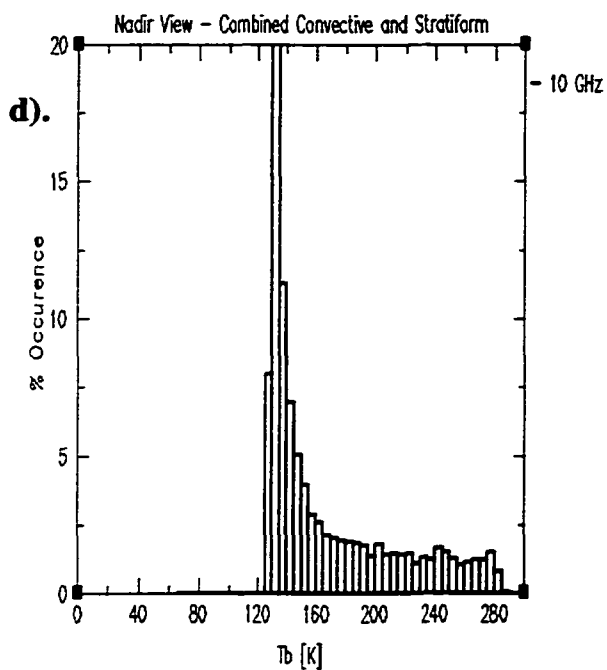
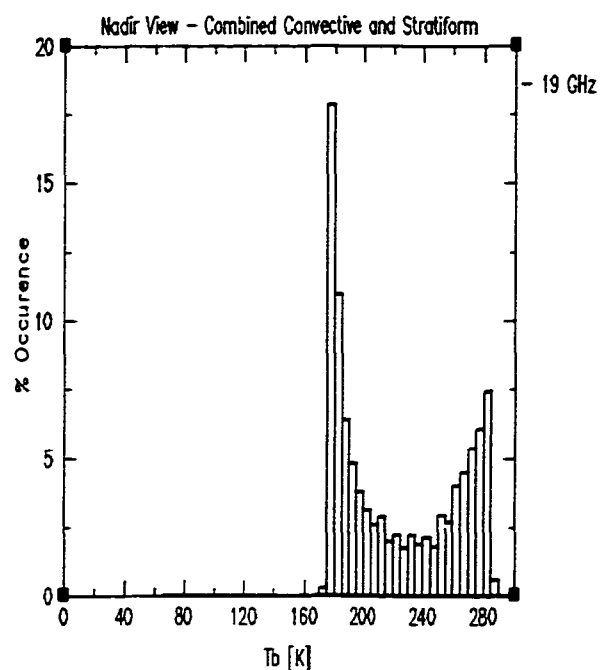


Figure 3.17. (Continued)

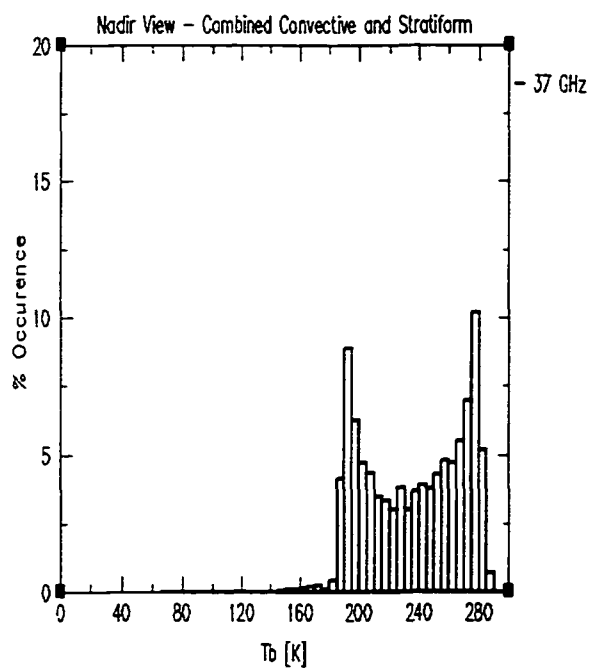
600_22_10 Simulation of 22 February 1993 case



600_22_10 Simulation of 22 February 1993 case



600_22_10 Simulation of 22 February 1993 case



600_22_10 Simulation of 22 February 1993 case

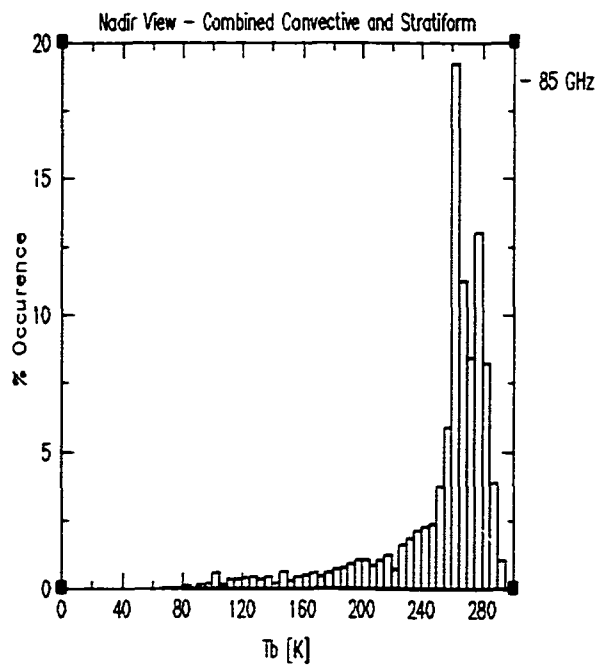
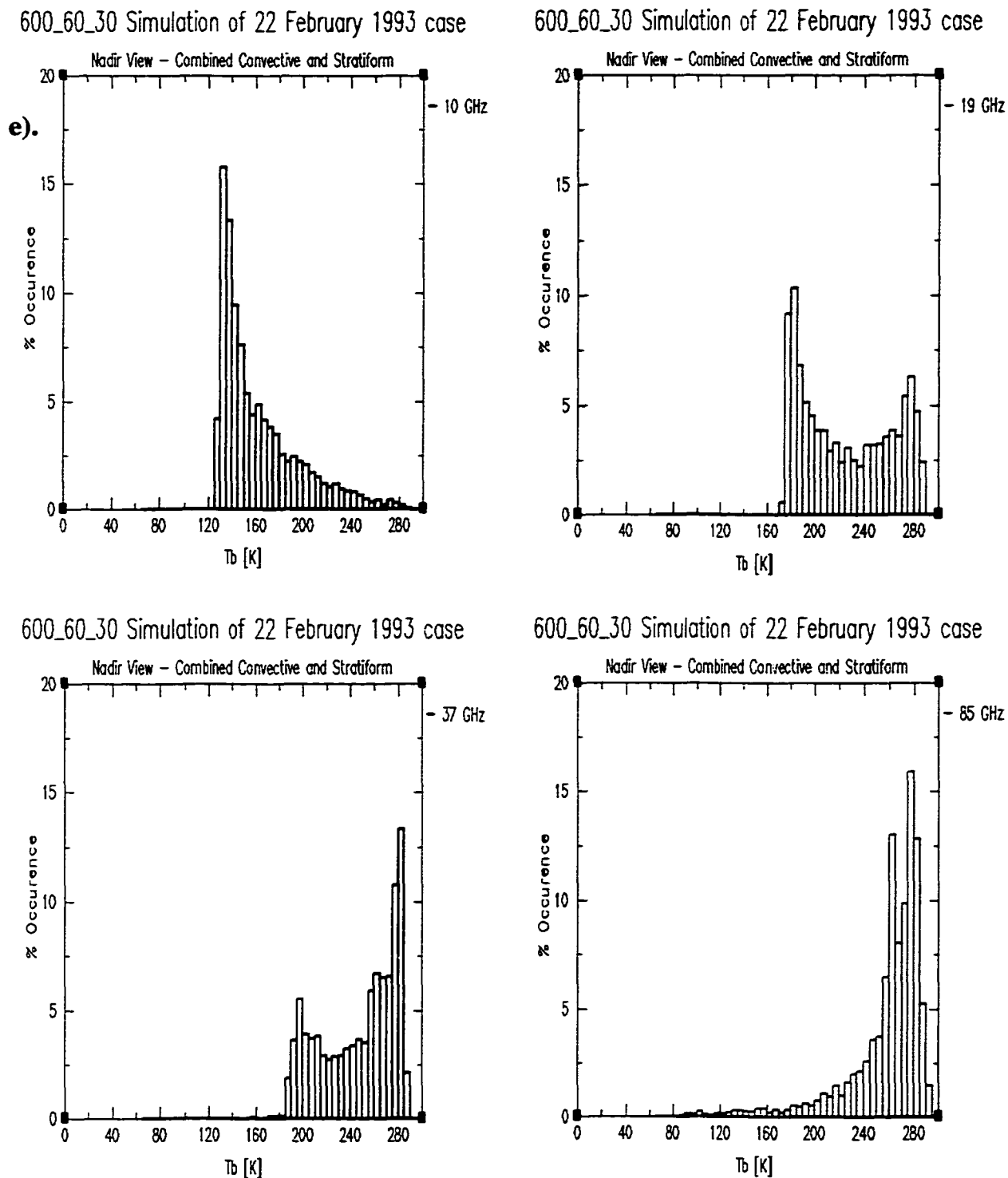


Figure 3.17. (Continued)



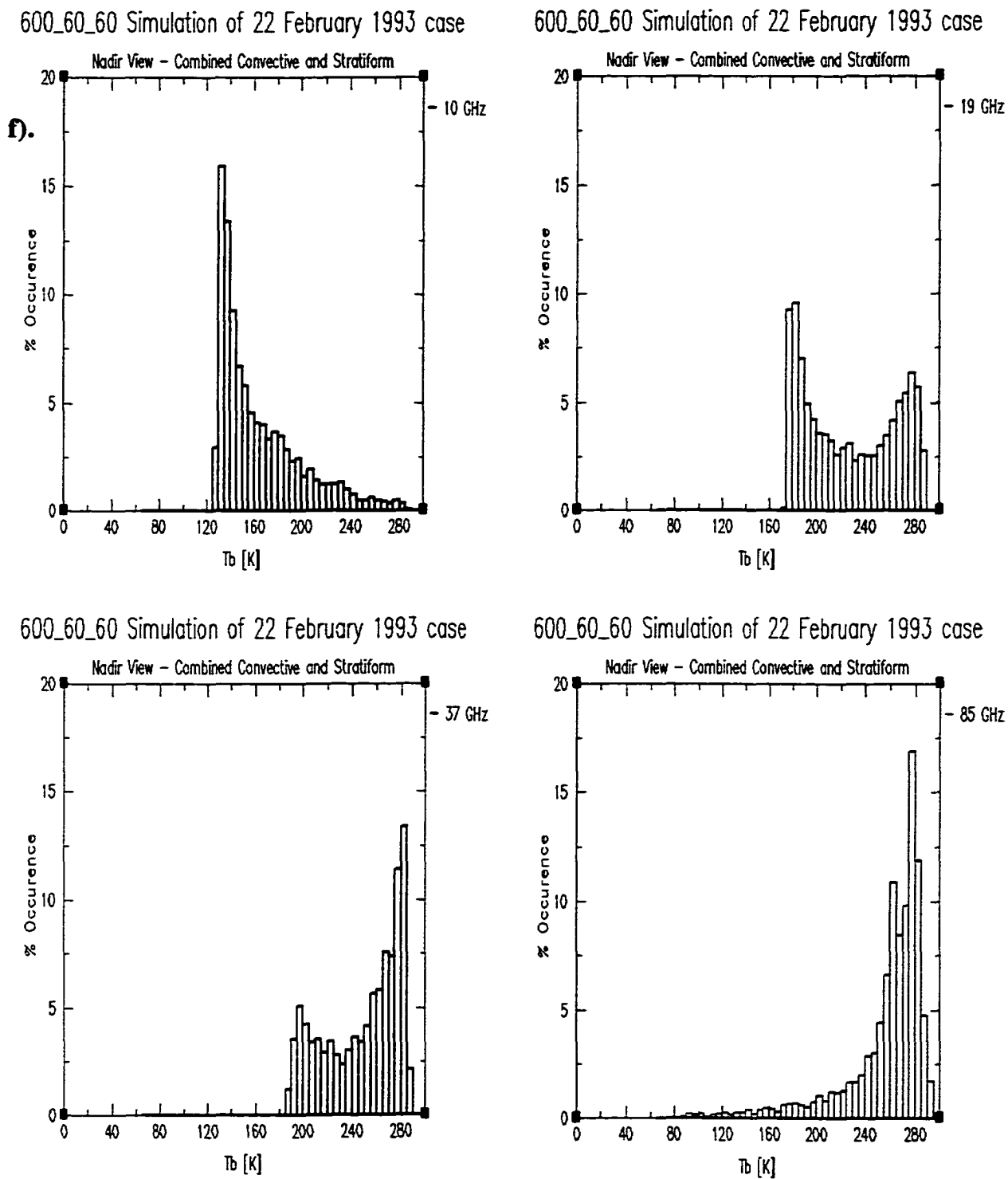


Figure 3.17. (Continued)

have been distributed among smaller number of larger particles (the 400_8_4_RHvt simulation – Fig. 3.16a). Particularly exemplifying are the scatter plots of 85 vs 10 GHz and 85 vs 37 GHz. As the graupel terminal velocity was increased and the assumed particle size distributions moved toward distributions of smaller mean diameter, a tendency for the development of much "cleaner" features became obvious (compare Figs. 3.16a to 3.16b ... to 3.16f). Especially interesting is the development in the features of the stratiform area. Not only did they become better defined but also became more distinct from that of the convective region (see especially the development of the 85 vs 37 GHz relations). While the observations could not be separated into convective and stratiform Tb relations, an investigation of the observational scatterplots (Fig. 3.14) does indicate that two distinct regimes were present. It does appear that as the model particle size distributions moved toward smaller mean diameter particles, the Tb–Tb relations moved closer to the observations. Indeed, the 600_60_30 simulation seems to compare rather well to the reality not only in the clarity and distinctiveness of both the convective and the stratiform features, but also in the fact that the modeled 37 and 85 GHz Tbs seemed to have warmed slightly in comparison to the other simulations and in closer agreement with observations. The examined scatterplots would seem to suggest that the 600_60_30 simulation is the ideal choice of parameters (among the ones tested here) if not for the fact that the high rain rates that were found in the observations (see the clustering in the warm end of the 19 vs 10 GHz scatterplot in Fig. 3.14) had apparently disappeared in the simulations that used progressively smaller DSDs.

This disappearance of the higher rain rates and the associated warmer 10 GHz brightness temperatures is especially well illustrated in the frequency distributions for

each of the four channels and each of the six simulations (Fig. 3.17). The very warm 10 GHz Tbs (on the order of 275° K) were most frequently observed in the 400_8_4 and the 600_8_4 simulations and gradually disappeared as the drops became smaller. Instead, the frequency of the colder 10 GHz increased indicating more widespread but weaker rain rates. Figure 3.18 illustrates especially well the changes in the 10 GHz frequency distribution over the convective region that took place with the decreasing mean diameter distributions. Two are the likely reasons that led to the observed changes in the 10 GHz frequency distributions: i). as the drop size distributions moved toward smaller drops, the convective regions became more uniform due to the production of more extensive and strong cold pool and the associated larger-scale convective forcing. The stronger, more localized convective cores disappeared as it was illustrated by the reflectivity and the vertical velocity fields; ii). the smaller mean diameter drops had less pronounced warming effect on the 10 GHz brightness temperatures even for the same near-surface rain-rates. Both of these effects worked in the same direction and this resulted in rather pronounced changes in the 10 GHz brightness temperatures distribution.

With this in mind, it now appears that the 600_22_10 simulation compares closest to the observations. Furthermore, a comparison of the frequency distributions for the 19 and 37 GHz brightness temperatures for each of the six simulations to the frequency distributions of the observations (Fig. 3.15) in these two channels also suggests the same conclusion. Indeed, the size and the relative proportions of the two peaks that are characteristic for the Tb distributions at these two frequencies seem to

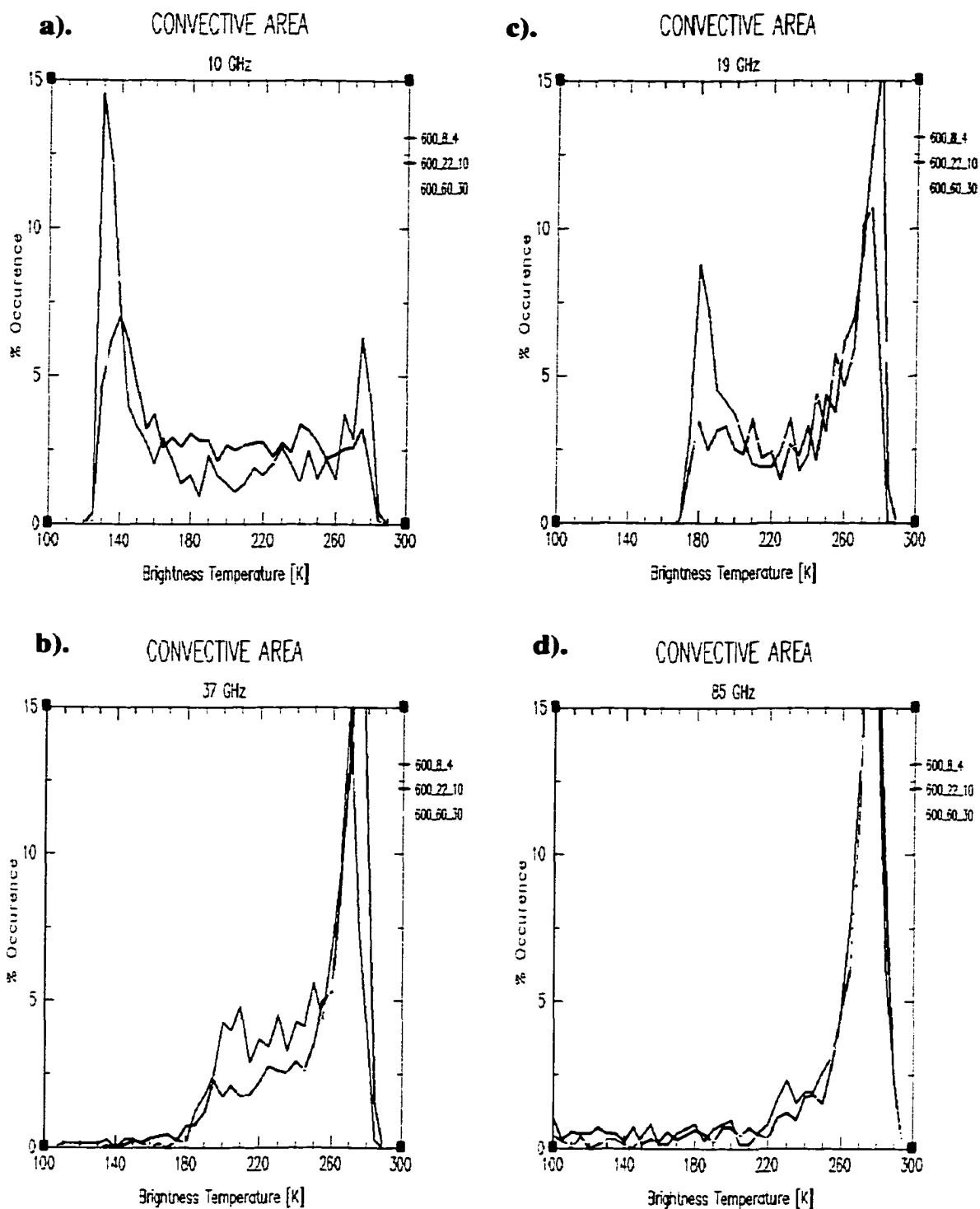


Figure 3.18. Same as in Fig. 3.17 except for statistics are computed separately over the convective (a)–(d) and stratiform (e)–(h) regions. Presented are the data from three simulations: 600_8_4 (red), 600_22_10 (blue) and 600_60_30 (yellow).

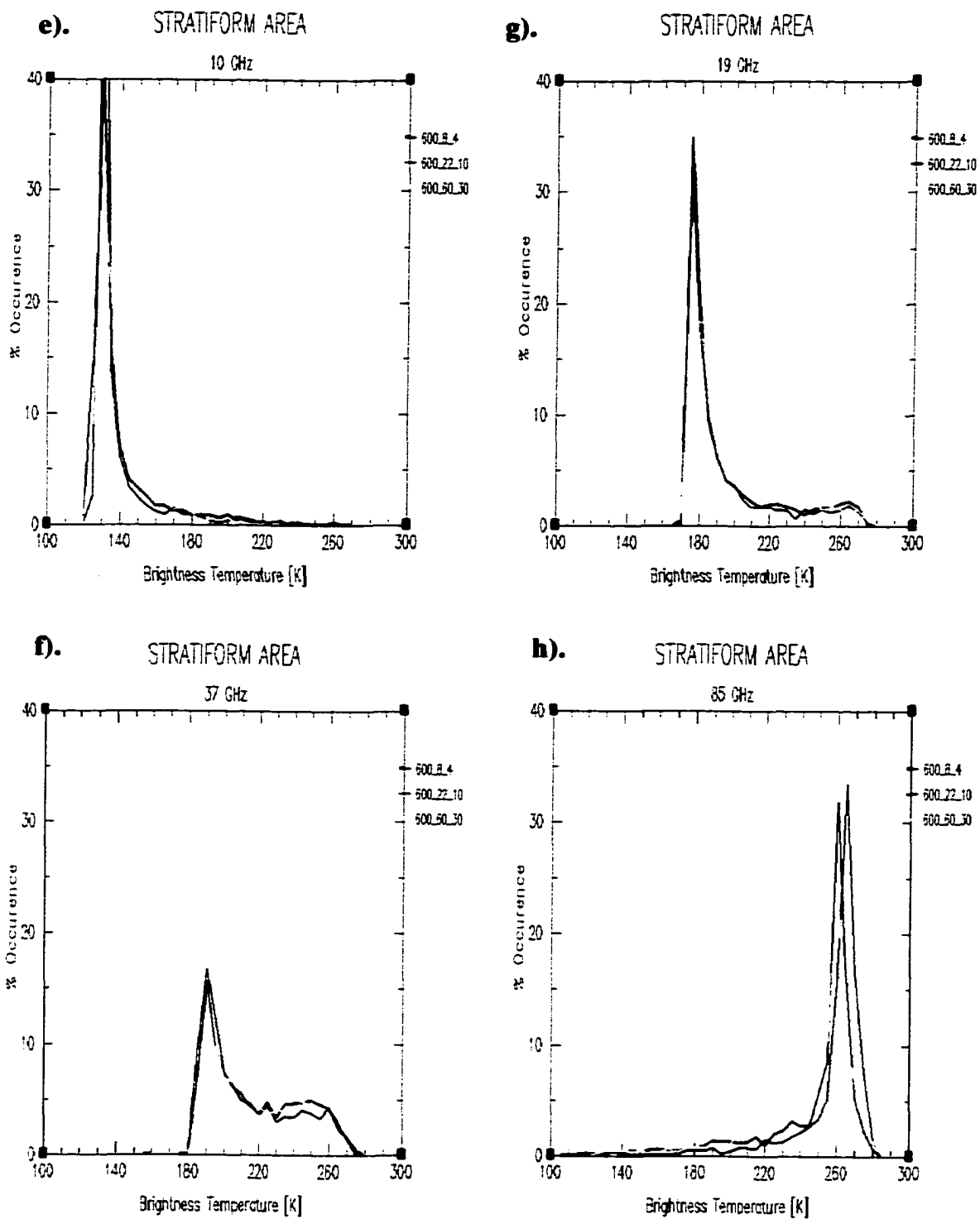


Figure 3.18. (Continued)

indicate that the convective/stratiform proportions of the 600_22_10 simulation are likely rather close to that of the observed squall line system.

4. Summary

Even rather small variations in the largely unknown particle terminal velocity and size distribution parameters have a significant effect on the storm organization, dynamics and evolution. Furthermore they affect the vertical hydrometeor profiles and the resultant latent heating profiles and microwave signatures. All these imply a high sensitivity of the rainfall and latent heating retrievals to the assumptions that went into building the cloud–radiation databases used in the retrieval algorithms.

In particular, while changing the terminal velocity of the large–ice particles by a factor of two did not change significantly the size of the cloud–model simulated convective storm, it had a significant impact on the vertical hydrometeor profiles and on the microwave remotely–sensed characteristics. The assumption of slower–falling graupel particles, that is probably more appropriate for low–density large aggregates but not for particles formed by riming in the convective updrafts, results in significant amounts of graupel being suspended at levels above melting. This affects the simulated storm in three ways: i). significant amount of the convectively–produced graupel is allowed to enter in the stratiform area and to contribute to the precipitation production there instead of adding to the convective area precipitation. This changes the convective/stratiform proportions leading to the simulation of the smallest percent convective area among the six simulations studied here; ii). since the graupel remains largely suspended, the graupel–to–rain ration is rather large (~ 1 in the convective area and ~ 2.6 in the stratiform area). This indicates that the "warm rain" processes is not

very efficient in the rain production, and results in the simulation of strong reflectivities at upper levels and weak decrease of reflectivity with height – all of these features being rather uncharacteristic for tropical convection as indicated by observations. Furthermore, the increased amount of graupel at upper levels leads to simulation of very low brightness temperatures in the higher frequency channels (37 and 85 GHz) and to poorly defined T_b – T_b relations especially in the stratiform region. This does not seem to compare well to passive microwave observations of tropical convection; iii). finally, the storm structure and evolution is altered since the suspended graupel does not contribute much to the low–level cold pool production. The resulting cold pool is large but weak and lacks in spatial coherence which affects the forcing of new convection and prevents the development of convective lines. Instead, convection happens in more isolated and larger–scale cores. The higher three–dimensionality of the convective cores and the lower cooling by melting (since the graupel is not readily falling out), both appear to be favorable for the generation of more intense convection (as determined by the stronger vertical velocity) which, in turn, limits the relative importance of the "warm rain" production by decreasing the residence time of the cloud and rain drops at levels below freezing.

Changing the density of the graupel particles from 400 to 600 kg/m³ had a very small effect upon the structure and the size of the simulated tropical storm, the convective/stratiform proportions, or the mean hydrometeor profiles and microwave signatures. Still, for the denser particles the ratio of graupel–to–rain is slightly smaller, especially in the convective area, signifying a more intense "warm rain" processes. This probably occurs because the denser particles should fall off faster, thus, contributing

more to the cooling by melting and, hence, to the production of weaker buoyancy and vertical velocity in the convective cores.

A word of caution, the sensitivity of the modeled storms to the graupel density and terminal velocity might change with the buoyancy of the environment since the particle-size-sorting by the updrafts would change as a function of the updraft velocity.

The storm structure and evolution are most strongly altered by the choices pertaining to the particle size distribution parameters. The assumptions about the rain drop size distributions appear to have the strongest impact upon the simulated storm organization. Modifying twice the intercept parameter of the assumed reverse exponential distributions by a factor of 2.7 each time led to the production of very different systems. Assuming rain drops with smaller than M-P mean diameter, in accordance with ground observations of drop size distributions in tropical convection, resulted in significant changes in the structure and the intensity of the evaporatively generated near-surface cold pool, which in turn, altered the subsequent storm structure and development. This suggest an important limitation on the use in retrieval algorithms of cloud-radiation databases in which the model was initialized with a pre-existing cold pool. In that cases, the simulated storm structure and evolution might appear realistic if the cold pool that was used for the initialization compares well to the one produced by the real storm. However, the microphysical structure of the simulated storm might still remain inaccurate since, in that case, it was not the microphysical processes but the initial conditions, that controlled the cold pool structure and the subsequent storm evolution. Hence, a potentially very useful peace of observational information, namely the storm structure and evolution, might remain uninformative when trying to decide

whether a particular microphysical set-up, indeed, reproduces well the storm's micro- and macro-characteristics.

The results of our sensitivity tests indicate that the smaller the assumed rain drops, the more effective the evaporation, the stronger and more spatially coherent the cold pool. This leads to forcing of convection over a larger and more continuous area. The increased competition for low-level moisture, the decreased buoyancy of the individual convective cores, that are rising not in the unperturbed environment but in an environment in which there is latent heating everywhere, and the increased upper-level entrainment that is associated with the more rearward tilted updrafts, all result in the production of weaker mean vertical velocity and more uniform convective area. As the mean drop diameter decreases, the "warm rain" processes increase in importance as signified by the decreasing graupel-to-rain ratio. This happens for two reasons: i) the dynamically induced weakening of the vertical velocity results in increased residence time for the rain drops at levels below freezing which, in turn, favors the growth by coalescence and the rain production without the participation of the ice processes. Furthermore, the less drops enter the levels above freezing, the weaker the ice-related processes, the further the decrease of the upper-level, and subsequently, the lower-level, vertical velocity; ii). the increased number and the slower falling out of the particles that result from the assumption of smaller mean diameter drops, would also lead to increase in the importance of the growth by coalescence.

In the simulation that assumed reverse exponential rain distribution with and intercept parameter of $22 \cdot 10^6 \text{ m}^{-4}$ the cold pool was still somewhat localized and the convective area rather intense. The more intense vertical velocity (as compared to the

simulations with intercept of 60.10^6 m^{-4}) and the fact that the number of rain drops was apparently not enough to efficiently collect the available cloud water (this simulation had the highest value of cloud water in the convective area) resulted in still very active ice-related processes. This, in addition to an intense and extensive stratiform area, resulted in the simulation that produce the most elevated latent heating profile. The system-generated latent heating profiles will apparently be affected by the intensity of the "warm rain" processes. The stronger the "warm rain" production, the lower the altitude of the latent heating maximum.

Finally, the vertical reflectivity profiles and the microwave brightness temperature of the simulations that used smaller mean diameter particles related much better to the observations of the storm, which environmental sounding was used to initialize the model. The smaller mean diameter particles produce storms with a pronounced drop of reflectivity with height at levels above freezing – a frequently observed characteristic of tropical convection. This in addition to better defined correlations between microwave brightness temperatures at various channels, closer correspondence of the frequency distributions of the brightness temperatures to the observed, and a generally good reproduction of the storm structure and evolution, all pointed to 600_22_10 simulation as the best match to the observations from the set of simulations that we studied here.

CHAPTER IV

CONCLUSIONS

Latent heat released in tropical convective systems not only drives the circulation in the tropical atmosphere but also impacts the midlatitude circulations by modifying the storm tracks via teleconnection patterns. However, currently the large-scale models of the atmospheric circulation have resolution much coarser than needed to resolve the convective processes. Hence, an accurate estimation of the observed convectively-produced tropical diabatic heating is needed during the initialization and the data-assimilation stages of the large-scale model runs in order to improve their performance. Cloud-resolving models are used to address the problem of relating satellite-observed brightness temperatures and radar reflectivities to the four-dimensional distribution of the hydrometeors and the diabatic heating associated with their production. These cloud-radiation databases have been extensively used over the last decade in the development of physically-based algorithms for retrieval of rainfall and latent heating from passive and active microwave satellite observations of precipitating systems. However, to achieve the goal of improving the large-scale models and their short-term climate predictions, the estimates of rainfall and latent heating have to be highly accurate and this depends critically on the degree of sophistication which went into building the cloud-radiation databases and on their representativeness of the nature. Furthermore, the uncertainties associated with the estimates are of critical importance. Hence, a good understanding of the behavior of the cloud-resolving models is important

for improving the parameterization and initialization of the large-scale models. Thus, an essential step toward achieving our goal of improving the long-term forecasts lies in evaluating the performance of the cloud-scale models by assessing the sensitivity of the modeled storms to the use of different models and parameterizations. Of them, the representation of the complex microphysical processes has probably the most crucial impact upon the modeled storms.

In this study a three-dimensional cloud model was used in conjunction with a radiative transfer model to address the two basic questions of how to assure the accuracy and determine the uncertainty of the estimates. The first question is addressed by identifying the storm characteristics that show sensitivity to particular microphysical parameter choices. Identifying these characteristics will then help develop a set of constraints by which to judge whether a particular storm simulation is indeed representative of the system it simulated. Assuring the representativeness of the cloud-radiation database will then give high fidelity to the rainfall and latent heating estimates that use the database. While quantifying the uncertainty in the estimates is not part of this study, the same basic question is addressed by studying the degree of sensitivity of the storm characteristics and their correlations to the microphysical parameter choices.

Three types of sensitivity tests were performed. The first set of tests evaluated the sensitivity to the choice of microphysical parameterization scheme. For that purpose two microphysical schemes were used – Tao's and Ferrier's. Both schemes share the same basic paradigm of two-class liquid water (cloud water and rain) and three-class ice-phase (cloud ice, snow and graupel) set of parameterizations. Their main differences are in the treatment of the cloud ice initiation processes and the subsequent

growth of snow. Furthermore, the two schemes differ to a certain degree in the parameterization of the graupel growth. While these later differences are not first order, it appears that they slightly impact simulated storms.

The second set of tests evaluated the sensitivity of modeled storms to the selection of ice aggregation parameters and to the assumed number of ice crystals that are activated at 0° C. The third set of tests evaluated the sensitivity of simulated storms to the selection of the hydrometeor's descriptive parameters (density, terminal velocity, and particle size distributions).

While many studies have recognized the importance of the above parameters in cloud modeling, no study thus far has tried to approach the problem of identifying and quantifying the sensitivity of the simulated storms by looking at the sensitivity of more than one or two storm characteristics at a time. This study is conducted with the intent to shed more light on how the microphysical parameter choices affect not just a particular storm characteristic but the storm's micro- and macro-structure and evolution. Being able to reproduce the storm in its entirety will indicate that the complex intercorrelations between the different processes and scales are, indeed, properly represented by the model. This in turn, will give a high fidelity in the rainfall and latent heating retrieval algorithms using such databases.

Following are some of the more important conclusions. The comparison between the two microphysical parameterization schemes reveals that they show different degree of sensitivity to the selection of microphysical parameters. In particular, Ferrier's scheme is more sensitive to the assumptions about the ice particle aggregation efficiencies and the assumption about the availability of ice nuclei in the

environment, while Tao's scheme is less sensitive. When Ferrier's microphysical scheme is used, the storm scale, the convective/stratiform proportions, the magnitude and the altitude of the mean heating profile, and the mean stratiform characteristics all are altered when different microphysical parameters are used. This is because in Ferrier's scheme the precipitation efficiency (the partitioning between the anvil and the precipitation) appears to be more readily modified by the parameter choices. In turn, a higher precipitation efficiency results in the production of bigger and stronger cold pool which leads to the upscale growth of the simulated storm. Furthermore, when the precipitation efficiency is higher there is less cloud ice in the anvil which leads to decreased depositional growth and, thus, to smaller and lower altitude peak in the vertical heating profile. On the other hand, when Tao's scheme is used in the cloud model the precipitation efficiency appears to be less sensitive to the parameter choices. This can be explained with the fact that Tao's scheme has a built-in mechanism for cloud ice production and its conversion to precipitation-sized particles. That mechanism operates somewhat independently from the assumptions about the ice nuclei availability and the assumptions about the cloud ice-snow interactions.

The full impact of the philosophical differences between the two microphysical schemes is revealed in comparing the two simulations which used equal microphysical parameters and where ran under the assumption of limited cloud ice nuclei availability resulting in the production of abundant supercooled cloud water. In that case, Ferrier and Tao produced similar in size and intensity convective areas. However, their stratiform areas were very different in both size and intensity with Tao producing larger stratiform region but with less intense mean precipitation, vertical velocity, and latent

heating profiles. Furthermore, the stratiform area latent heating profiles peaked at different altitudes with Tao producing a lower-level heating maximum.

When the two microphysical schemes were ran under the assumption of cloud ice nuclei abundance, they produced systems with similar size stratiform areas but with very different mean rain, graupel, and latent heating profiles.

The storm dynamics are also affected by the microphysical parameterization philosophies and by the choice of microphysical parameters. Realizations which produce large or intense stratiform areas show a tendency to develop a well defined midlevel mesolow earlier in their lifetime. This mesolow alters the orientation and the shape of the convective line and affects the subsequent storm evolution. Furthermore, the production of intense stratiform area precipitation appears to play an important role in determining the overall storm scale.

It becomes obvious from the above results that the stratiform area characteristics of the simulated storms are particularly sensitive to the choice of microphysical scheme. Hence, the satellite-retrieved stratiform area characteristics would be very sensitive to the assumptions that went into building the cloud-radiation database used in the retrieval.

While our study suggests that the uncertainty in the stratiform area retrievals would be high, it also illustrates that by comparing simulated to observed stratiform area characteristics one could rather effectively discriminate between different microphysical simulations. Hence, a carefully designed field program could provide the means to narrow down the uncertainty.

The upper-level reflectivity means and distributions were mostly affected by the amount of snow at these levels. Since Tao gives preference to the snow production at the expense of the cloud ice, it tends to produce stronger upper-level reflectivity.

Microwave brightness temperatures for the scattering frequencies (37 and 85.6 GHz) and their relationship with the underlying columnar liquid water were most strongly affected by the amount of supercooled cloud water in the graupel layers. When Ferrier and Tao were ran with the same set of parameters and in the case of supercooled cloud water production, Ferrier produced slightly warmer 85.6 GHz brightness temperatures for the same amount of total liquid water in the column. This is likely related to the fact that in the case of low NCIO Ferrier tends to produce more supercooled cloud water than Tao.

For the passive microwave frequencies examined here, snow and cloud ice did not contribute significantly to any of the brightness temperatures. Tuning the model microphysics to ensure similar brightness temperature relations does not imply that the distribution of all hydrometeors will be the same.

For simulated storms with similar brightness temperature relations, it was found that differences in cloud ice production affected the magnitude and altitude of the maxima in area and time-averaged latent heating profiles, especially in the stratiform region. In Ferrier, the altitude of the peak shifted in accordance with the level where intense cloud ice production was allowed. This level depended upon the cloud ice nuclei availability (NCIO) assumptions. In Tao, cloud ice was always produced at levels closer to freezing and not allowed to accumulate. This resulted in the simulation of latent heating profiles with constant peak altitude. Only its intensity depended upon

the NCIO assumptions. In both microphysics, production of higher amounts of cloud ice per unit rain led to mean latent heating profiles with stronger upper-level peaks. In that sense, microphysical schemes that produce storms with different precipitation efficiency will also produce different heating profiles. Retrievals of latent heating from passive microwave observations may suffer large uncertainties at upper levels due to the insensitivity of most brightness temperature observations to cloud ice.

In addition to uncertainty in latent heating retrievals, the different brightness temperature relations associated with the different amounts of supercooled cloud water produced in the model will also impact retrievals of rain from passive microwave measurements. This uncertainty will be largest for retrievals over land where the strong and non-uniform surface emissivity limits the retrievals to using only the higher frequencies associated with scattering and most strongly affected by the unknown amounts of supercooled cloud water.

Finally, we focus our attention on the impact of the descriptive parameters (i.e. density, terminal velocity and the intercept parameter of the assumed reverse exponential particle size distribution). While previous studies have pointed out to the significant importance of these choices, these studies investigated vastly different paradigms. This study, on the other hand investigates the sensitivity of the simulated storms to rather small changes in the largely unknown descriptive parameters. This set of simulations was performed using the environmental sounding of a well-observed tropical convective system.

The graupel terminal velocity assumption modifies the simulated storms in several ways by altering the amount of graupel that could be suspended by the updrafts.

In particular, slower falling particles remain suspended in larger quantities. This changes the graupel-to-rain ratio in favor of the graupel and, thus, affects the vertical profiles of radar reflectivity and the microwave brightness temperatures in a way that compares unfavorably to observations of tropical convection. Furthermore, the convective/stratiform proportions change in favor of the stratiform area since the slower-falling particles that are produced in the convective area enter more easily into the stratiform area and contribute to the precipitation production there. Finally, the slower-falling graupel particles contribute less to the rain production in general since they remain suspended in larger quantities. The result is simulations that have weaker cooling by evaporation and melting. In turn, the less coherent cold pool leads to the generation of more isolated three-dimensional cores. All of the above factors favor the production of stronger vertical velocity.

Changing the density of the graupel particles from 400 to 600 kg/m³ had very small effect upon the structure and the size of the simulated tropical storm, the convective/stratiform proportions, or the mean hydrometeor profiles and microwave signatures. A word of caution, the sensitivity of the modeled storms to the graupel density and terminal velocity assumptions might change with the buoyancy of the environment since the particle-size-sorting by the updrafts would change as a function of the updraft velocity.

The storm structure and evolution are most strongly altered by the choices pertaining to the particle size distribution parameters. The assumptions about the rain drop size distributions appear to have the strongest impact upon the simulated storm organization. Assuming rain drops with smaller than M-P mean diameter, in

accordance with ground observations of drop size distributions in tropical convection, resulted in significant changes in the structure and the intensity of the evaporatively generated near-surface cold pool, which in turn, altered the subsequent storm structure and development. This suggests an important limitation on the use in retrieval algorithms of cloud-radiation databases in which the model was initialized with a pre-existing cold pool. In that case, the simulated storm structure and evolution might appear realistic if the cold pool that was used for the initialization compares well to the one produced by the real storm. However, the microphysical structure of the simulated storm might still remain inaccurate since, in that case, it was not the microphysical processes but the initial conditions, that controlled the cold pool structure and the subsequent storm evolution. Hence, a potentially very useful piece of observational information, namely the storm structure and evolution, might remain uninformative when trying to decide whether a particular microphysical set-up reproduces the storm's micro- and macro-characteristics.

The results of our sensitivity tests indicate that the smaller the assumed rain drops, the more effective the evaporation, and the stronger and more spatially coherent the cold pool. This leads to forcing of convection over a larger and more continuous area. The increased competition for low-level moisture, the decreased buoyancy of the individual convective cores that are rising not in the unperturbed environment but in an environment in which there is latent heating everywhere, and the increased upper-level entrainment that is associated with the more rearward tilted updrafts all result in the production of weaker mean vertical velocity and more uniform convective area. As the mean drop diameter decreases, the "warm rain" processes increase in importance as

signified by the decreasing graupel-to-rain ratio. This happens for two reasons: i) the dynamically induced weakening of the vertical velocity results in increased residence time for the rain drops at levels below freezing which, in turn, favors the growth by coalescence and the rain production without the participation of the ice processes. Furthermore, the less drops enter the levels above freezing, the weaker the ice-related processes, the further the decrease of the upper-level, and subsequently, the lower-level, vertical velocity; ii). the increased number and the slower falling out of the particles that result from the assumption of smaller mean diameter drops, would also lead to increase in the importance of the growth by coalescence.

Investigation of the overall storm structure and evolution, the structure of the vertical profiles of reflectivity, and the microwave brightness temperature relations all signify that the simulation that used smaller than Marshall-Palmer mean diameter particles related much better to the observations of the tropical storm. This illustrates how a set of simultaneous observations could help determine the set of microphysical parameters that, when used in a cloud model, would result in a simulation that best captures the micro- and macro- structure of the storm that is represented.

In conclusion, this study indicates significant sensitivity in many storm characteristics to the selection of the microphysical parameters and schemes. This, in addition to the fact that observational and laboratory studies are still insufficient and their sometimes contradictory results have not been able so far to provide clear guidance in the development of microphysical parameterizations, implies that satellite-based estimations of rainfall and latent heating that use cloud-radiation databases might carry significant uncertainty.

REFERENCES

- Adler, R. F, H.-Y. Yeh, N. Prasad, W.-K. Tao and J. Simpson, 1991: Microwave simulations of a tropical rainfall system with a three-dimensional cloud model. *J. Appl. Meteor.*, **30**, 924–953.
- Arakawa, A., 1971: A parameterization of cumulus convection and its application to numerical simulation of the tropical general circulation. Paper presented at the *7th Tech. Conf. Hurricanes and Tropical Meteorology*, Barbados, Amer. Meteor. Soc.
- Augustine, J. A. , and E. J. Zipser, 1987: The use of wind profilers in a mesoscale experiment. *Bull. Amer. Meteor. Soc.*, **68**, 4–17.
- Bartels, D. L., and R. A. Maddox, 1991: Midlevel cyclonic vortices generated by mesoscale convective complexes. *Mon. Wea. Rev.*, **119**, 104–118.
- Bennetts, D. A., and F. Rawlins, 1981: Parameterization of the ice-phase in a model of mid-latitude cumulonimbus convection and its influence on the simulation of cloud development. *Quart. J. R. Met. Soc.*, **107**, 477–502.
- Biggerstaff, M. I., and R. A. Houze, Jr., 1993: Kinematics and microphysics of the transition zone of the 10–11 June 1985 squall line. *J. Atmos. Sci.*, **50**, 3091–3110.
- _____, and _____, 1991: Kinematic and precipitation structure of the 10–11 June 1985 squall line. *Mon. Wea. Rev.*, **119**, 3034–3065.
- Chang, C.-P. and Lim, H., 1988: Kelvin Wave-CISK: A possible mechanism for the 30–50 day oscillations. *J. Atmos. Sci.*, **45**, 1709–1720.
- Chen, T. C. and M. C. Yen, 1991: A study of the diabatic heating associated with the MADDEN–JULIAN oscillation. *J. Geophys. Res.–ATMOSPHERES*, **96(D7)**, 13163–13177.
- Coppens, D., and Z. S. Haddad, 2000: Effects of rain drop size distribution variations on microwave brightness temperature calculations. *J. Geophys. Res.*, submitted.
- Cotton, W. R., M.-S. Lin, R. L. McAnelly and C. J. Tremback, 1989: A composite model of mesoscale convective complexes. *Mon. Wea. Rev.*, **117**, 765–783.
- _____, G. J. Tripoli, R. M. Rauber and E. A. Mulvihill, 1986: Numerical simulation of the effects of varying ice crystal nucleation rates and aggregation processes on orographic snowfall. *J. Climate Appl. Meteor.*, **25**, 1658–1680.

- DeMaria, M., 1985: Linear response of a stratified tropical atmosphere to convective forcing. *J. Atmos. Sci.*, **42**, 1944–1959.
- DeMott, C. A., and S. A. Rutledge, 1998: The vertical structure of TOGA COARE convection. Part I: Radar echo distributions. *J. Atmos. Sci.*, **55**, 2730–2747.
- Ferrier, B. S., W. –K. Tao, and, J. Simpson, 1995: A double–moment multiple–phase four–class bulk ice scheme. Part II: Simulations of convective storms in different large–scale environments and comparisons with other bulk parameterizations. *J. Atmos. Sci.*, **52**, 1001–1033.
- _____, 1994: A double–moment multiple–phase four–class bulk ice scheme. Part I: Description. *J. Atmos. Sci.*, **51**, 249–280.
- Fritsch, J. M. and R. A. Maddox, 1981: Convectively driven mesoscale weather systems aloft. *J. Appl. Meteor.*, **20**, 9–19.
- Gallus, W. A., Jr., and R. H. Johnson, 1991: Heat and moisture budgets of an intense midlatitude squall line. *J. Atmos. Sci.*, **48**, 122–146.
- Gamache, J. F., 1990: Microphysical observations in summer MONEX convective and stratiform clouds. *Mon. Wea. Rev.*, **118**, 1238–1249.
- Haddad, Z. S., D. A. Short, S. L. Durden, E. Im, S. Hensley, M. B. Grable, and R. A. Black, 1997: A new parameterization of the rain drop size distribution. *IEEE Transactions on Geoscience and Remote Sensing*, **35**, No. 3, 532–539.
- Hallgren, R. E., and C. L. Hosler, 1960: Preliminary results on the aggregation of ice crystals. *Geophys. Monogr., Am. Geophys. Union*, **5**, 257–263.
- Halverson J., M. Garstang, J. Scala, and W.–K. Tao, 1996: Water and energy budgets of a Florida mesoscale convective system: A combined observational and modeling study. *Mon. Wea. Rev.*, **124**, 1161–1180.
- Hartmann, D. L., H. H. Hendon, and R. A. Houze, Jr., 1984: Some implications of the mesoscale circulations in tropical cloud clusters for large–scale dynamics and climate. *J. Atmos. Sci.*, **41**, 113–121.
- Hosler, C. L., and R. E. Hallgren, 1961: Ice crystal aggregation. *Nubila*, **4**, No. 1, 13–19.
- _____, and _____, 1960: The aggregation of small ice crystals. *Discuss. Faraday Soc.*, **30**, 200–208.

- _____, D. C. Jensen and L. Goldshlak, 1957: On the aggregation of ice crystals to form snow. *J. Meteor.*, **14**, 415–420.
- Houze, R. A., Jr., B.F. Smull and P. Dodge, 1990: Mesoscale organization of springtime rainstorms in Oklahoma. *Mon. Wea. Rev.*, **118**, 613–654.
- _____, 1982: Cloud clusters and large-scale vertical motions in the tropics. *J. Meteor. Soc. Japan*, **60**, 396–410.
- _____, P. V. Hobbs, P. H. Herzegh and D. B. Parsons, 1979: Size distributions of precipitation particles in frontal clouds. *J. Atmos. Sci.*, **36**, 156–162.
- Hristova–Veleva, S. M., and M. I. Biggerstaff, 1994: Interactions between the convective region and a mesoscale vortex in a midlatitude squall line system. *Sixth Conf. on Mesoscale Processes*, 18–22 July 1994, Portland, OR by the American Meteorological Society, 399–402.
- Johnson, D. E., P. K. Wang, and J. M. Straka, 1993: Numerical simulations of the 2 August 1981 CCOPE supercell storm with and without ice microphysics. *J. Appl. Meteor.*, **32**, 745–759.
- Johnson, R. H., and D. L. Bartels, 1992: Circulations associated with a mature-to-decaying midlatitude mesoscale convective system. Part II: Upper-level features. *Mon. Wea. Rev.*, **120**, 1301–120.
- _____, 1984: Partitioning tropical heat and moisture budgets into cumulus and mesoscale components: Implications for cumulus parameterization. *Mon. Wea. Rev.*, **112**, 1590–1601.
- Jorgensen, D. P., M. A. LeMone, and S. B. Trier, 1997: Structure and evolution of the 22 February 1993 TOGA COARE squall line: Aircraft observations of precipitation, circulation and surface energy fluxes. *J. Atmos. Sci.*, **54**, 1961–1985.
- Kessler, E., III, 1969: *On the Distribution and Continuity of Water Substance in Atmospheric Circulations*. *Meteor. Monogr.*, No. **32**, Amer. Meteor. Soc., 84 pp.
- Klemp, J. B., and R. B. Wilhelmson, 1978: The simulation of three-dimensional convective storm dynamics. *J. Atmos. Sci.*, **35**, 1070–1096.
- Krueger, S. K., Q. Fu, K. N. Liou, and H.-N. Chin 1995: Improvements of an ice-phase microphysics parameterization for use in numerical simulations of tropical convection. *J. Appl. Meteor.*, **34**, 281–287.

- Kummerow, C., 1993: On the accuracy of the Eddington approximation for radiative transfer in the microwave frequencies. *J. Geophys. Res.*, **98**, 2757–2765.
- _____, and Wienmann, 1988: Determining microwave brightness temperatures from precipitating horizontally finite and vertically structured clouds. *J. Geophys. Res.*, **93 (D4)**, 3720–3728.
- Lau, K. -M., and L. Peng, 1987: Origin of low-frequency (intra-seasonal) oscillations in the tropical atmosphere. Part I: The basic theory. *J. Atmos. Sci.*, **42**, 950–972.
- Leary, C.A., and R. A. Houze, Jr., 1979: The structure and evolution of convection in a tropical cloud cluster. *J. Atmos. Sci.*, **36**, 437–457.
- Lin, Y. L., R. D. Farley, and H. D. Orville, 1983: Bulk parameterization of the snow field in a cloud model. *J. Climate and Appl. Meteor.*, **22**, 1065–1092.
- Liu, C. H., M. W. Moncrieff, and E. J. Zipser, 1997: Dynamical influence of microphysics in tropical squall lines: A numerical study. *Mon. Wea. Rev.*, **125**, 2193–2210.
- Lord, S. J., H. E. Willoughby, and J. M. Piotrowicz, 1984: Role of a parameterized ice-phase microphysics in an axisymmetric non-hydrostatic tropical cyclone model. *J. Atmos. Sci.*, **41**, 2836–2848.
- Maddox, R. A., 1983: Large-scale meteorological conditions associated with midlatitude, mesoscale convective complexes. *Mon. Wea. Rev.*, **111**, 1475–1493.
- Marshall, J. S. and W. M. Palmer, 1948: The distribution of raindrops with size. *J. Meteor.*, **5**, 165–166.
- McCumber, M., W. -K. Tao, J. Simpson, R. Penc, and S. T. Soong, 1991: Comparison of ice-phase microphysical parameterization schemes using numerical simulations of tropical convection. *J. Appl. Meteor.*, **30**, 985–1004.
- McGaughey, G., and E. J. Zipser, 1996a: High-resolution passive microwave observations of convective systems over the tropical Pacific ocean. *J. Appl. Meteor.*, **35**, 1921–1947.
- _____, and _____, 1996b: Passive microwave observations of the stratiform regions of two tropical oceanic mesoscale convective systems. *J. Appl. Meteor.*, **35**, 1949–1962.
- Meyers, M. P., P. J. DeMott and W. R. Cotton, 1992: New primary ice-nucleation parameterizations in an explicit cloud model. *J. Appl. Meteor.*, **31**, 708–721.

- Mugnai, A., E. A. Smith, and G. J. Tripoli, 1993: Foundations for statistical–physical precipitation retrieval from passive microwave satellite measurements. Part II: Emission source and generalized weighting function properties of a time–dependent cloud–radiation model. *J. Appl. Meteor.*, **32**, 17–39.
- _____, and _____, 1988: Radiative transfer to space through a precipitating cloud at multiple microwave frequencies. Part I: Model description. *J. Appl. Meteor.*, **27**, 1055–1073.
- Olson, W. S., C.D. Kummerow, Y. Hong and W.–K. Tao, 1999: Atmospheric latent heating distributions in the tropics derived from satellite passive microwave radiometer measurements. *J. Appl. Meteor.*, **38**, 633–664.
- _____, _____, G. M. Heymsfield, and L. Giglio, 1996: A method for combined passive–active microwave retrievals of cloud and precipitation profiles. *J. Appl. Meteor.*, **35**, 1763–1789.
- Panegrossi, G., S. Dietrich, F. S. Marzano, A. Mugnai, E. A. Smith, X. Xiang, G. J. Tripoli, P. K. Wang, and J. P. V. P. Baptista, 1998: Use of cloud model microphysics for passive microwave–based precipitation retrieval. Significance of consistency between model and measurement manifolds. *J. Atmos. Sci.*, **55**, 1644–1673.
- Pruppacher, H. R., and J. D. Klett, 1978: *Microphysics of Clouds and Precipitation*, D. Reidel, 714 pp.
- Rogers, R. R., 1979: *A Short Course in Cloud Physics*, 2nd ed., Pergamon Press, 235 pp.
- Rotunno, R., J. B. Klemp, and M. L. Weisman, 1988: A theory for strong, long–lived squall lines. *J. Atmos. Sci.*, **45**, 463–485.
- Rutledge, S. A., and P. V. Hobbs, 1984: Mesoscale and microscale structure and organization of clouds and precipitation in midlatitude cyclones. XII: A diagnostic modeling study of precipitation development in narrow cold–frontal rainbands. *J. Atmos. Sci.*, **41**, 2949–2972.
- _____, and _____, 1983: The Mesoscale and microscale structure and organization of clouds and precipitation in midlatitude cyclones. VIII: A model for the "Seeder–Feeder" process in warm–frontal rainbands. *J. Atmos. Sci.*, **40**, 1185–1206.
- Schlesinger, R. E., 1994: Heat, moisture, and momentum budgets of isolated deep midlatitude and tropical convective clouds as diagnosed from three–dimensional model output. Part I: Control experiments. *J. Atmos. Sci.*, **51**, 3649–3673.

- Seo, E.-K., M. I. Biggerstaff, S. M. Hristova-Veleva, and K. -Y. Kim, 2000: Sensitivity of hydrometeor profiles and microwave brightness temperatures to cloud microphysics for a MCS over land. Part I: Model comparison using EOF analysis. *J. Atmos. Sci.*, submitted.
- Simpson, J. R., and W.-K. Tao, 1993: The Goddard Cumulus Ensemble Model. Part II: Applications for studying cloud precipitating processes and for NASA TRMM. *Terrestrial, Atmospheric and Oceanic Sciences*, **4**, 73–116.
- _____, R. Adler, and G. R. North, 1988: A proposed tropical rainfall measuring mission (TRMM). *Bull. Amer. Meteor. Soc.*, **69**, 278–295.
- Skamarock, W. C., M. L. Weisman and J. B. Klemp, 1994: Three dimensional evolution of simulated long-lived squall lines. *J. Atmos. Sci.*, **51**, 2563–2584.
- _____, and J. B. Klemp, 1993: Adaptive grid refinement for two-dimensional and three-dimensional nonhydrostatic atmospheric flow. *Mon. Wea. Rev.*, **121**, 788–804.
- Smith, E. A., A. Mugnai, H. J. Cooper, G. J. Tripoli, and X. Xiang, 1992: Foundations for statistical-physical precipitation retrieval from passive microwave satellite measurements. Part I: Brightness temperature properties of a time-dependent cloud-radiation model. *J. Appl. Meteor.*, **31**, 506–531.
- _____, and A. Mugnai, 1988: Radiative transfer through a precipitating cloud at multiple microwave frequencies. Part II: Results and analyses. *J. Appl. Meteor.*, **27**, 1074–1091.
- Smull, B. F., and R. A. Houze, Jr., 1985: A midlatitude squall line with a trailing region of stratiform rain: Radar and satellite observations. *Mon. Wea. Rev.*, **113**, 117–133.
- Soong, S. -T., and Y. Ogura, 1973: A comparison between axisymmetric and slab-symmetric cumulus cloud models. *J. Atmos. Sci.*, **30**, 879–893.
- Sui, C.-H. and K.-M. Lau, 1989: Origin of low-frequency (intra-seasonal) oscillations in the tropical atmosphere. Part II: Structure and propagation of mobile wave-CISK modes and their modification by lower boundary forcings. *J. Atmos. Sci.*, **46**, 37–56.
- Tao, W. -K. and J. Simpson, 1993a: Goddard Cumulus Ensemble Model. Part I: Model description. *Terrestrial, Atmospheric and Oceanic Sciences*, **4**, No. 1, 35–72.
- _____, _____, C. H. Sui, B. Ferrier, S. Lang, J. Scala, M. D. Chou, and K. Pickering, 1993b: Heating, moisture, and water budgets of tropical and midlatitude squall

- lines: Comparisons and sensitivity to longwave radiation. *J. Atmos. Sci.*, **50**, 673–690.
- _____, S. Lang, J. Simpson, and R. Adler, 1993c: Retrieval algorithms for estimating the vertical profiles of latent heat release: Their applications for TRMM. *J. Meteor. Soc. Japan*, **71**, 685–700.
- _____, J. Simpson and S. T. Soong, 1991: Numerical simulations of a subtropical squall line over the Taiwan Strait. *Mon. Wea. Rev.*, **119**, 2699–2723.
- _____, _____, S. Lang, M. McCumber, R. Adler, and R. Penc, 1990: An algorithm to estimate the heating budget from vertical hydrometeor profiles. *J. Appl. Meteor.*, **29**, 1232–1244.
- _____, and _____, 1989a: Modeling study of a tropical squall-type convective line. *J. Atmos. Sci.*, **46**, 177–202.
- _____, _____, and M. McCumber, 1989b: An ice-water saturation adjustment. *Mon. Wea. Rev.*, **117**, 231–235.
- Tesmer, J. R., and T. T. Wilheit, 1998: An improved microwave radiative transfer model for tropical oceanic precipitation. *J. Atmos. Sci.*, **55**, 1674–1688.
- Tokay, A., and D. A. Short, 1994: Case studies of convective vs stratiform rain over Kapingamarangi atoll during TOGA-COARE. Preprints, *Sixth Conf. On Mesoscale Processes*, Portland, OR, Amer. Meteor. Soc., 85–88.
- Trenberth, K. E., G. W. Branstator and P.A. Arkin, 1988: Origins of the 1988 North American drought. *Science*, **242**, 1640–1645.
- Trier, S. B., W. C. Skamarock, and M. A. LeMone, 1997: Structure and evolution of the 22 February 1993 TOGA COARE squall line : Organization mechanisms inferred from numerical simulation. *J. Atmos. Sci.*, **54**, 386–407.
- _____, _____, _____, D.B. Parsons, and D.P. Jorgensen, 1996: Structure and evolution of the 22 February 1993 TOGA COARE squall line: Numerical simulations. *J. Atmos. Sci.*, **53**, 2861–2886.
- Valdez, M. P., and K. C. Young, 1985: Number fluxes in equilibrium raindrop populations: A Markov chain analysis. *J. Atmos. Sci.*, **42**, 1024–1036.
- Weisman, M. L., and J. B. Klemp, 1982: The dependence of numerically simulated convective storms on vertical wind shear and buoyancy. *Mon. Wea. Rev.*, **110**, 504–520.

- Wicker, L. J., and R. B. Wilhelmson, 1995: Simulation and analysis of tornado development and decay within a three-dimensional supercell thunderstorm. *J. Atmos. Sci.*, **52**, 2675–2703.
- Wilheit, T. T., and Coauthors, 1994: Algorithms for the retrieval of rainfall from passive microwave measurements. *Remote Sensing Reviews*, **11**, 163–194.
- Yanai, M., S. Esbensen, and E. J. Chu, 1973: Determination of bulk properties of tropical cloud clusters from large-scale heat and moisture budgets. *J. Atmos. Sci.*, **30**, 611–627.
- Yang, M. –J. And R. A. Houze, Jr., 1995: Sensitivity of squall-line rear inflow to ice microphysics and environmental humidity. *Mon. Wea. Rev.*, **123**, 3175–3193.
- Yang, S. and E. A. Smith, 1999a: Four-dimensional structure of monthly latent heating derived from SSM/I satellite measurements. *J. Climate*, **12**, 1016–1037.
- _____ and _____, 1999b: Moisture budget analysis of TOGA COARE area using SSM/I-retrieved latent heating and large-scale Q2 estimates. *J. Atmos. Ocean. Techn.*, **16**, 633–655.
- Yuter, S. E., and R. A. Houze, Jr., 1995: Three-dimensional kinematic and microphysical evolution of Florida cumulonimbus. Part II: Frequency distributions of vertical velocity, reflectivity, and differential reflectivity. *Mon. Wea. Rev.*, **123**, 1941–1963.
- Zipser, E. J., and K. R. Lutz, 1994: The vertical profile of radar reflectivity of convective cells: A strong indicator of storm intensity and lightning probability? *Mon. Wea. Rev.*, **122**, 1751–1759.

VITA

SVETLA M. HRISTOVA – VELEVA

5613 Freeman Av.
 La Crescenta, CA 91214
 e-mail: veleva@mcsys.jpl.nasa.gov
 phone: (818) 354-7314

EDUCATION

- 1994 – September Entered the doctoral program in Atmospheric Sciences at Texas A&M University.
- 1994 – May Master of Science, Texas A&M University. Her thesis was an observational study of the structure and evolution of a midlatitude mesoscale convective system. Based on dual-Doppler flow analyses, she developed a conceptual model of the scale interaction between a stratiform area midlevel mesovortex and the variability along the leading convective line.
- 1991 – 1994 Graduate student in the Department of Meteorology, Texas A&M University.
- 1992 – June Summer Colloquium on Observational Techniques in the Atmospheric Sciences – sponsored by the National Center for Atmospheric Research (NCAR)
- 1980 B.Sc. Degree in Physics with a specialization in Meteorology, SOFIA UNIVERSITY "Kliment Ohridski", Sofia, Bulgaria
- 1975 Graduated with golden medal (GPA – 4.0) from 7th High School "George Dimitrov", Sofia, Bulgaria

EMPLOYMENT

- 1999 – 2000 Research Associate, Texas A&M University
- 1998 – 2000 No-fee consultant – Jet Propulsion Laboratory
- 1991 – 1999 Graduate Research Assistant, Texas A&M University
- 1989 – 1990 Research Assistant – Cooperative Institute for Applied Meteorological Studies (CIAMS), Texas A&M University.
- 1980 – 1988 Meteorologist – Department of Networks, Head Office of Hydrology and Meteorology, Bulgarian Academy of Science.

PROFESSIONAL MEMBERSHIPS AND RECOGNITIONS

- Chi Epsilon Pi – Meteorology Honor Society
 Phi Kappa Phi – National Honor Society. Initiated on April 18 1997.
 1997-1998 Graduate Women Research Scholarship Finalist